

**ALMA MATER STUDIORUM - UNIVERSITÀ DI BOLOGNA**

---

**SCUOLA DI INGEGNERIA E ARCHITETTURA**

*DICAM*

*Dipartimento di Ingegneria Civile, Chimica, Ambientale e dei Materiali*

**DOTTORATO DI RICERCA**

in

**INGEGNERIA CIVILE, CHIMICA, AMBIENTALE E DEI MATERIALI**

Ciclo XXX

**Settore concorsuale di afferenza: 08/B3** Tecnica delle Costruzioni

**Settore scientifico-disciplinare: ICAR 09**

**EXPERIMENTAL AND NUMERICAL INVESTIGATIONS ON  
THE SHEAR BEHAVIOR OF EXISTING MASONRY  
STRUCTURES**

Candidata:

**Francesca Ferretti**

Supervisore:

**Prof. Ing. Marco Savoia**

Coordinatore:

**Prof. Ing. Luca Vittuari**

Co-supervisor:

**Prof. Ing. Claudio Mazzotti**

**Prof. Jan G. Rots**

**Prof. Ing. Barbara Ferracuti**

---

**Esame finale anno 2018**



## Table of Contents

List of Figures .....	7
List of Tables.....	13
Abstract .....	15
1 Introduction.....	17
1.1 Masonry structures.....	18
1.1.1 Materials and masonry typologies.....	18
1.1.2 Structural typologies.....	19
1.2 Failure mechanisms of masonry structures.....	22
1.2.1 In-plane shear strength of masonry piers .....	23
1.2.2 Shear verifications in Building Codes.....	26
1.3 Seismic vulnerability assessment procedures .....	27
1.4 Objectives and scope of the thesis .....	30
2 Experimental techniques for the mechanical characterization of existing masonries .....	32
2.1 Slightly-destructive tests.....	34
2.1.1 Single and double flatjack tests .....	34
2.1.2 Shove test .....	35
2.1.3 Splitting test on masonry cores with inclined mortar joint .....	38
2.2 Destructive tests.....	40
2.2.1 Diagonal compression test.....	40
2.2.2 Shear compression test .....	41
3 Experimental campaign on rural masonries in Emilia-Romagna .....	45
3.1 Experimental Program .....	48
3.2 Slightly-destructive tests.....	51
3.2.1 Splitting test on masonry cores with inclined mortar joint .....	51
3.2.2 Shove test .....	53
3.2.3 Calibration of Mohr-Coulomb's failure domain through slightly-destructive test results	55
3.3 Destructive tests.....	59

---

3.3.1	Diagonal compression test.....	59
3.3.2	Shear-compression test.....	63
3.4	Discussion on the calibrated failure criteria .....	68
3.4.1	Mohr-Coulomb’s failure criterion from slightly-destructive tests .....	69
3.4.2	Turnšek and Čačovič’s failure criterion for destructive tests.....	70
3.4.3	Mann and Müller’s failure criterion for destructive tests.....	71
3.4.4	Comparison between failure criteria and shear-compression test results.....	72
3.5	Conclusions.....	73
4	Numerical studies on the shear-sliding behavior of masonry .....	75
4.1	Numerical modeling of masonry .....	79
4.1.1	Modeling strategies .....	79
4.1.2	Constitutive models.....	81
5	Numerical simulations of triplet test.....	87
5.1	Standard triplet test .....	88
5.1.1	Experimental campaign.....	88
5.1.2	Numerical model .....	93
5.1.3	Numerical results.....	94
5.1.4	Influence of boundary conditions.....	98
5.2	Modified triplet test .....	99
5.2.1	Experimental campaign.....	99
5.2.2	Numerical model .....	103
5.2.3	Numerical results.....	104
5.2.4	Influence of dilatancy parameters .....	107
5.2.5	Influence of the elastic properties of the head joint .....	108
5.3	Discussion.....	109
6	Numerical simulations of shove test.....	111
6.1	Shove test – Method A .....	112
6.1.1	Testing procedure .....	112
6.1.2	Numerical model .....	113
6.1.3	Numerical results.....	114

---

6.1.4	Parametric studies on dilatancy.....	125
6.1.5	Correction factors for vertical loads.....	132
6.2	Shove test – Method B.....	135
6.2.1	Testing procedure.....	135
6.2.2	Numerical model.....	135
6.2.3	Numerical results.....	136
6.2.4	Parametric studies on dilatancy.....	146
6.2.5	Correction factors for vertical loads.....	153
6.3	Results comparison and discussion.....	156
6.3.1	Shove test – Method A vs Shove test – Method B.....	156
6.3.2	Shove test vs Triplet test.....	157
7	Case study.....	159
8	Conclusions.....	167
8.1	Summary.....	167
8.2	Future works.....	168
	Acknowledgements.....	171
	References.....	173



## List of Figures

Figure 1.1. Examples of abaci for the identification of masonry typologies: (a) GNDT Manual; (b) Abacus of masonry typologies, Emilia Romagna Region, 2009. ....	19
Figure 1.2. Classification of masonry buildings: (a) first class; (b-c) second class; (d) third class (Preite, 1986) .....	20
Figure 1.3. Masonry structural typologies, characteristics and critical issues: (a) first class buildings; (b) second class buildings; (c) third class buildings (Pagano, 1990).....	22
Figure 1.4. Typical out-of-plane failure mechanisms (Reluis document). ....	23
Figure 1.5. Typical failure modes of masonry piers: (a) crushing associated to rocking; (b) sliding; (c) diagonal cracking (Calderini et al. 2009). ....	24
Figure 1.6. Diagonal cracking failure mechanism: (a) stair-stepped crack; (b) brick tensile failure (Magenes 2000). ....	25
Figure 2.1. Flatjack test testing procedure: a) single flatjack test; b) double flatjack test. ....	35
Figure 2.2. Single (a) and double (b) flatjack test setups. ....	35
Figure 2.3. Shove test setups: (a) Method A; (b) Method B; Method C.....	36
Figure 2.4. Typical shove test results ( <i>Method A</i> ): (a) load-displacement curve; (b) Coulomb friction failure domain. (Atkinson et al. 1988).....	37
Figure 2.5. Setup of the shove test, <i>Method B</i> . ....	37
Figure 2.6. Splitting test on a masonry core with inclined mortar joint. ....	39
Figure 2.7. Setup of the diagonal compression test. ....	40
Figure 2.8. Mohr circles for the two different interpretations of the stress state in the diagonal compression test. ....	41
Figure 2.9. Shear-compression test: Setup A.....	42
Figure 2.10. Shear-compression test: Setup B.....	42
Figure 2.11. Structural schemes of the shear-compression test: (a) <i>Setup A</i> ; (b) <i>Setup B</i> . ....	43
Figure 2.12. Shear-compression test: Mohr circle at failure.....	44
Figure 3.1. Structural deficiencies associated to out-of-plane mechanisms. ....	46
Figure 3.2. Structural deficiencies associated to in-plane mechanisms. ....	47
Figure 3.3. Location of the investigated buildings. ....	48
Figure 3.4. Investigated masonry buildings.....	49
Figure 3.5. Location of the experimental tests, building B01.....	50
Figure 3.6. Slightly-destructive tests: (a) core extraction; (b) preparation for the shove test. ....	51
Figure 3.7. Splitting test on masonry cores with different mortar layer inclinations: (a) building B01; (b) building B02. ....	52
Figure 3.8. Shove test: (a) at ground floor (max vertical stress); (b) below window openings (zero vertical stress) ....	53
Figure 3.9. Shove test: load-displacement curve with the identification of the first sliding load.....	54
Figure 3.10. Determination of the Mohr-Coulomb's failure domain: (a) building B01, (b) building B02.....	57
Figure 3.11. Setup of the diagonal compression test. ....	60
Figure 3.12. Setup of the diagonal compression test, details.....	60
Figure 3.13. Diagonal compression test: mean diagonal deformations. ....	61

Figure 3.14. Diagonal compression test: failure modes.....	62
Figure 3.15. Shear-compression test: Setup A.....	63
Figure 3.16. Shear-compression test: Setup B.....	63
Figure 3.17. Shear-compression test: failure modes.....	65
Figure 3.18. Shear-compression test: mean diagonal deformations in the lower half of the masonry panel.....	66
Figure 3.19. Shear-compression test: shear stress vs horizontal displacement in the lower half of the masonry panel.....	67
Figure 3.20. Shear-compression test - Deformed shapes of the panels: (a) elastic phase; (b) maximum load.....	67
Figure 3.21. Comparison of failure criteria for the investigated buildings.....	69
Figure 3.22. Comparison between crack inclinations for building B04: (a) CD test; (b) NT test.....	71
Figure 3.23. Definition of the parameter $\phi$ for different type of masonry (Calderini et a. 2010).....	71
Figure 4.1. Shear test setups for the evaluation of the masonry shear strength: (a) Schubert test; (b) DIN test; (c) Hamid & Drysdale test; (d) Hoffman & Stöckl test; (e) Triplet test, Riddington & Jukes; (f) Van der Pluijm test; (g) Popal & Lissel test; (h) Atkinson test.....	76
Figure 4.2. Shear test: typical diagram and mechanical properties to be derived. (Rots 1997).....	78
Figure 4.3. Shear tests: (a) triplet test (EN 1052-3); (b) shove test (ASTM C1531).....	79
Figure 4.4. Modeling strategies for masonry structures: (a) masonry sample; (b) detailed micro-modeling; (c) simplified micro-modeling; (d) macro-modeling. (Lourenço 1996).....	80
Figure 4.5. Combined cracking-shearing-crushing model for nonlinear interface elements. (Diana Manual).....	82
Figure 4.6. Stress-displacement diagrams for interface elements according to the different failure modes: (a) tensile behavior; (b) shear behavior; (c) compressive behavior. (Lourenco, 1996).....	83
Figure 4.7. Dilatant displacement normal to the joint upon plastic shear displacement – Curves from experiments by Van der Pluijm. (Van Zijl 2004a).....	84
Figure 5.1. Typical shear stress vs shear displacement curves for different values of pre-compression applied. (Rots 1997).....	87
Figure 5.2. Specimen geometry: (a) standard triplet specimen (stacked bond); (b) modified triplet specimen (running bond).....	88
Figure 5.3. Standard triplet test: experimental setup.....	89
Figure 5.4. Standard triplet test: typical failure mode.....	90
Figure 5.5. Standard triplet test: shear failure involving mortar.....	90
Figure 5.6. Standard triplet test results: (a) shear stress vs relative displacement of the central brick (LVDTs readings); (b) shear stress vs pre-compression stress.....	91
Figure 5.7. Standard triplet test results: mode-II fracture energy vs pre-compression stress.....	92
Figure 5.8. Standard triplet test results: normal displacement vs tangential displacement.....	92
Figure 5.9. Standard triplet test: finite element model.....	93
Figure 5.10. Standard triplet test, shear stress vs tangential displacement.....	95
Figure 5.11. Standard triplet test, normal displacement vs tangential displacement.....	95
Figure 5.12. Standard triplet test at pre-compression $0.20 \text{ N/mm}^2$ – Principal stress distributions: (a) pre-peak ( $\delta_v = 0.02 \text{ mm}$ ); (b) post-peak ( $\delta_v = 0.08 \text{ mm}$ ).....	96
Figure 5.13. Standard triplet test at pre-compression $0.20 \text{ N/mm}^2$ , normal stress evolution along the nonlinear interface.....	97

Figure 5.14. Standard triplet test at pre-compression $0.20 \text{ N/mm}^2$ , tangential stress evolution along the nonlinear interface.....	97
Figure 5.15. Standard triplet test with restrained lateral displacement, shear stress vs tangential displacement...	99
Figure 5.16. Standard triplet test, shear stress vs tangential displacement – Free vs restrained lateral displacement conditions.....	99
Figure 5.17. Modified triplet test: experimental setup.....	100
Figure 5.18. Modified triplet test: typical failure mode.....	100
Figure 5.19. Modified triplet test: “bridging” failure mode.....	101
Figure 5.20. Modified triplet test: shear failure involving the head joint.....	101
Figure 5.21. Modified triplet test results: (a) shear stress vs relative displacement of the central brick (LVDTs readings); (b) shear stress vs pre-compression stress.....	102
Figure 5.22. Modified triplet test results: mode-II fracture energy vs pre-compression stress.....	102
Figure 5.23. Modified triplet test results: normal displacement vs tangential displacement.....	103
Figure 5.24. Modified triplet test: finite element model.....	104
Figure 5.25. Modified triplet test, shear stress vs tangential displacement.....	105
Figure 5.26. Modified triplet test, normal displacement vs tangential displacement.....	105
Figure 5.27. Modified triplet test at pre-compression $0.20 \text{ N/mm}^2$ , normal stress evolution along the nonlinear interface.....	106
Figure 5.28. Modified triplet test at pre-compression $0.20 \text{ N/mm}^2$ , tangential stress evolution along the nonlinear interface.....	106
Figure 5.29. Modified triplet test at pre-compression $0.20 \text{ N/mm}^2$ , normal stress evolution along the head joint.....	107
Figure 5.30. Modified triplet test, normal displacement vs tangential displacement.....	108
Figure 5.31. Modified triplet test at pre-compression $0.20 \text{ N/mm}^2$ , normal stress evolution – Intact vs weak head joint.....	109
Figure 6.1. Shove test: wall geometry and test setup. (TU Delft).....	111
Figure 6.2. Shove test – <i>Method A</i> : wall geometry and test location.....	112
Figure 6.3. Shove test – <i>Method A</i> , finite element model: (a) entire wall panel; (b) detail of the flatjack pressure application; (c) detail of the shear load application.....	113
Figure 6.4. Model A1 – Numerical results: shear load $F$ vs tangential displacement $\delta v$ diagram.....	115
Figure 6.5. Model A1 – Numerical results: shear stress $\tau$ vs tangential displacement $\delta v$ diagram.....	115
Figure 6.6. Model A1 – Numerical results: orthogonal displacements $\delta u$ vs tangential displacement $\delta v$ .....	116
Figure 6.7. Model A1 – Principal stress distributions: (a) self-weight; (b) overburden application; (c) execution of the first cut.....	118
Figure 6.8. Model A1 – Principal stress distributions: (a) execution of the second cut; (b) removal of bricks; (c) application of the flatjack pressure.....	119
Figure 6.9. Model A1 – Principal stress distributions: (a) application of the shear load; (b) peak load; (c) residual branch.....	120
Figure 6.10. Model A1 – Principal stress distributions between flatjacks: (a) application of the flatjack pressure; (b) peak load; (c) post-peak phase.....	121

Figure 6.11- Model A1 – Stress evolution along the top sliding interface: (a) normal stress; (b) tangential stress. .... 123

Figure 6.12- Model A1 – Stress evolution along the bottom sliding interface: (a) normal stress; (b) tangential stress. .... 123

Figure 6.13. Numerical results – comparison: shear load  $F$  vs tangential displacement  $\delta v$  diagram. .... 124

Figure 6.14. Numerical results - comparison: shear stress  $\tau$  vs tangential displacement  $\delta v$  diagram. .... 124

Figure 6.15. Numerical results - comparison: orthogonal displacements  $\delta u$  vs tangential displacement  $\delta v$ . .... 124

Figure 6.16. Theoretical plastic orthogonal displacement  $u_{pl}$  vs plastic tangential displacement  $v_{pl}$  curves: (a) parametric studies on  $\psi_0$ ; (b) parametric studies on  $\sigma_u$ ; (c) parametric studies on  $\delta$ . .... 126

Figure 6.17. Parametric studies on  $\psi_0$ : shear load  $F$  vs tangential displacement  $\delta v$  diagram. .... 128

Figure 6.18. Parametric studies on  $\psi_0$ : shear stress  $\tau$  vs tangential displacement  $\delta v$  diagram. .... 128

Figure 6.19. Parametric studies on  $\psi_0$ : orthogonal displacements  $\delta u$  vs tangential displacement  $\delta v$ . .... 128

Figure 6.20. Parametric studies on  $\sigma_u$ : shear load  $F$  vs tangential displacement  $\delta v$  diagram. .... 129

Figure 6.21. Parametric studies on  $\sigma_u$ : shear stress  $\tau$  vs tangential displacement  $\delta v$  diagram. .... 129

Figure 6.22. Parametric studies on  $\sigma_u$ : orthogonal displacements  $\delta u$  vs tangential displacement  $\delta v$ . .... 129

Figure 6.23. Parametric studies on  $\delta$ : shear load  $F$  vs tangential displacement  $\delta v$  diagram. .... 130

Figure 6.24. Parametric studies on  $\delta$ : shear stress  $\tau$  vs tangential displacement  $\delta v$  diagram. .... 130

Figure 6.25. Parametric studies on  $\delta$ : orthogonal displacements  $\delta u$  vs tangential displacement  $\delta v$ . .... 130

Figure 6.26. Parametric studies - comparison: shear load  $F$  vs tangential displacement  $\delta v$  diagram. .... 131

Figure 6.27. Parametric studies - comparison: shear stress  $\tau$  vs tangential displacement  $\delta v$  diagram. .... 131

Figure 6.28. Parametric studies - comparison: orthogonal displacement  $\delta u$  vs tangential displacement  $\delta v$  diagram. .... 131

Figure 6.29. Shove test – *Method B*: wall geometry and test location. .... 135

Figure 6.30. Shove test - *Method B*, finite element model: (a) entire wall panel; (b) detail of the shear load application. .... 136

Figure 6.31. Model B1 – Numerical results: shear load  $F$  vs tangential displacement  $\delta v$  diagram. .... 137

Figure 6.32. Model B1 – Numerical results: shear stress  $\tau$  vs tangential displacement  $\delta v$  diagram. .... 137

Figure 6.33. Model B1 – Numerical results: orthogonal displacements  $\delta u$  vs tangential displacement  $\delta v$ . .... 138

Figure 6.34. Model B1 – Principal stress distributions: (a) self-weight; (b) overburden application; (c) removal of bricks. .... 140

Figure 6.35. Model B1 – Principal stress distributions: (a) application of the shear load; (b) peak load; (c) residual branch. .... 141

Figure 6.36. Model B1 – Principal stress distributions on the tested masonry portion: (a) application of the vertical load and removal of bricks; (b) peak load; (c) post-peak phase. .... 142

Figure 6.37- Model B1 – Stress evolution along the top sliding interface: (a) normal stress; (b) tangential stress. .... 144

Figure 6.38- Model B1 – Stress evolution along the bottom sliding interface: (a) normal stress; (b) tangential stress. .... 144

Figure 6.39. Numerical results – comparison: shear load  $F$  vs tangential displacement  $\delta v$  diagram. .... 145

Figure 6.40. Numerical results - comparison: shear stress  $\tau$  vs tangential displacement  $\delta v$  diagram. .... 145

Figure 6.41. Numerical results - comparison: orthogonal displacements  $\delta u$  vs tangential displacement  $\delta v$ . .... 145

Figure 6.42. Theoretical plastic orthogonal displacement $u_{pl}$ vs plastic tangential displacement $v_{pl}$ curves: (a) parametric studies on $\psi_0$ ; (b) parametric studies on $\sigma_u$ ; (c) parametric studies on $\delta$ .....	147
Figure 6.43. Parametric studies on $\psi_0$ : shear load $F$ vs tangential displacement $\delta v$ diagram. ....	149
Figure 6.44. Parametric studies on $\psi_0$ : shear stress $\tau$ vs tangential displacement $\delta v$ diagram. ....	149
Figure 6.45. Parametric studies on $\psi_0$ : orthogonal displacements $\delta u$ vs tangential displacement $\delta v$ . ....	149
Figure 6.46. Parametric studies on $\sigma_u$ : shear load $F$ vs tangential displacement $\delta v$ diagram.....	150
Figure 6.47. Parametric studies on $\sigma_u$ : shear stress $\tau$ vs tangential displacement $\delta v$ diagram.....	150
Figure 6.48. Parametric studies on $\sigma_u$ : orthogonal displacements $\delta u$ vs tangential displacement $\delta v$ .....	150
Figure 6.49. Parametric studies on $\delta$ : shear load $F$ vs tangential displacement $\delta v$ diagram. ....	151
Figure 6.50. Parametric studies on $\delta$ : shear stress $\tau$ vs tangential displacement $\delta v$ diagram. ....	151
Figure 6.51. Parametric studies on $\delta$ : orthogonal displacements $\delta u$ vs tangential displacement $\delta v$ . ....	151
Figure 6.52. Parametric studies - comparison: shear load $F$ vs tangential displacement $\delta v$ diagram. ....	152
Figure 6.53. Parametric studies - comparison: shear stress $\tau$ vs tangential displacement $\delta v$ diagram. ....	152
Figure 6.54. Parametric studies - comparison: orthogonal displacements $\delta u$ vs tangential displacement $\delta v$ . ....	152
Figure 7.1. Case study: wall geometry and test setup. (TUDelft).....	159
Figure 7.2. Case study – Single flatjack test: (a) execution of the cut; (b) seating of the flatjack.....	160
Figure 7.3. Case study – Double flatjack test (undisturbed masonry): (a) setup; (b) $\sigma$ - $\varepsilon$ curves. ....	161
Figure 7.4. Case study – Double flatjack test (shove test configuration): (a) setup; (b) $\sigma$ - $\varepsilon$ curves. ....	162
Figure 7.5. Case study – Shove test: (a) setup; (b) failure mode.....	162
Figure 7.6. Case study – Shove test results: $\sigma$ - $\tau$ diagrams.....	164
Figure 7.7. Case study – Shove test: experimental vs numerical results: (a) tangential stress $\tau$ vs tangential displacement $\delta v$ ; (b) orthogonal displacement $\delta u$ vs tangential displacement $\delta v$ .....	165



## List of Tables

Table 1.1. Knowledge levels and confidence factors. ....	27
Table 1.2. Reference values of mechanical parameters (minimum and maximum) and mean self-weight for different masonry typologies, referred to weak mortar, uncoursed masonry, absent connections between wall leaves, texture following the “rule of the art” in case of regular elements; $f_m$ = mean compressive strength of masonry; $\tau_0$ = mean shear strength of masonry; $E$ = mean value of the elastic modulus; $G$ = mean value of the shear modulus; $w$ = mean self-weight of masonry. (NTC 2008 – Appendix C8A, section C8A.2, table C8A.2.1.) .....	29
Table 1.3. Corrective coefficients of the mechanical parameters indicated in Table 1.2 to be applied in presence of: high-quality mortar, thin mortar joints, transversal connections between wall leaves, poor internal core, strengthening interventions such as mortar injections or reinforced plaster. (NTC 2008 – Appendix C8A, section C8A.2, table C8A.2.2.).....	29
Table 3.1. Number of performed tests.....	50
Table 3.2. Slightly-destructive tests: results and Mohr-Coulomb’s failure domain parameters, buildings B01-B04. .....	55
Table 3.3. Slightly-destructive tests: results and Mohr-Coulomb’s failure domain parameters, buildings B05-B08. .....	56
Table 3.4. Diagonal compression test (CD): results. ....	60
Table 3.5. Shear-compression test (NT): results. ....	64
Table 3.6. Mann and Müller’s failure domain parameters.....	72
Table 5.1. Mechanical properties of calcium silicate masonry.....	89
Table 5.2. Shear properties of standard triplets. ....	91
Table 5.3. Standard triplet test results: dilatancy parameters. ....	92
Table 5.4. Input parameters for masonry.....	94
Table 5.5. Shear properties of modified triplets. ....	102
Table 5.6. Modified dilatancy parameters. ....	108
Table 6.1. Shove test – <i>Method A</i> : loading conditions for the numerical simulations.....	115
Table 6.2. Shove test – <i>Method A</i> : parametric studies on dilatancy. ....	125
Table 6.3. Model A1 – Results of the parametric analyses. ....	132
Table 6.4. Model A1 – Elastic joints: equivalent normal and tangential stresses.....	133
Table 6.5. Model A1 – No tension & constant shear stiffness: equivalent normal and tangential stresses. ....	133
Table 6.6. Model A1 – No tension & reduced shear stiffness: equivalent normal and tangential stresses. ....	133
Table 6.7. Model A1 – No tension & zero shear stiffness: equivalent normal and tangential stresses. ....	134
Table 6.8. Model A1 – Correction factors.....	134
Table 6.9. Shove test – <i>Method B</i> : loading conditions for the numerical simulations.....	137
Table 6.10. Shove test – <i>Method B</i> : parametric studies on dilatancy. ....	146
Table 6.11. Model B1 – Results of the parametric analyses.....	153
Table 6.12. Model B1 – Elastic joints: equivalent normal and tangential stresses.....	154
Table 6.13. Model B1 – No tension & constant shear stiffness: equivalent normal and tangential stresses. ....	154
Table 6.14. Model B1 – No tension & reduced shear stiffness: equivalent normal and tangential stresses. ....	154

Table 6.15. Model B1 – No tension & zero shear stiffness: equivalent normal and tangential stresses. ....	155
Table 6.16. Model B1 – Correction factors. ....	155
Table 7.1. Case study – Single flatjack test results. ....	160
Table 7.2. Case study – Shove test results. ....	163

## Abstract

Masonry is a composite material, whose behavior is strongly influenced by the presence of vertical and horizontal mortar joints. With reference to the shear behavior of masonry structural elements, which is crucial during a seismic event, three different failure mechanisms can be identified: rocking, sliding and diagonal cracking. The great damages experienced by existing masonry constructions during the seismic events which struck Italy in recent years, have highlighted the need of a systematic vulnerability assessment of this construction typologies. One of the crucial aspect, in this framework, is the evaluation of the mechanical properties of the materials, which can be achieved through the execution of non-destructive, slightly-destructive and destructive tests.

On existing buildings, it is often unpracticable to perform experimental tests or, when they are performed, their reduced number and local nature do not allow to obtain reliable estimation of the mechanical parameters. Therefore, it is fundamental to identify experimental procedures having the minimum impact on the construction, obtaining, at the same time, representative results. To this aim, the combination of different experimental tests can be a very powerful possibility. In parallel, the reliability of the single technique should be analyzed as well.

The scope of the present work is to investigate the shear behavior of masonry structural elements, both from the experimental and the numerical point of view. Slightly-destructive and destructive techniques were applied in the field and, starting from the observations of the typical failure mechanisms, numerical simulations of shear tests were performed.

In the first part of the research, an extended experimental campaign was conducted on existing masonry buildings. The main objective of this activity was to evaluate the most suitable techniques that can be applied to get reliable information on the material mechanical properties. Slightly-destructive and destructive tests were performed on eight masonry buildings, severely damaged by the 2012 Emilia earthquake (Italy) and intended to be demolished. Concerning slightly-destructive tests, shove tests and splitting tests on cores with inclined mortar joint were chosen. As destructive tests, diagonal compression and shear-compression tests were adopted. The tests results are here analysed and discussed, focusing on the strength parameters obtainable from each test type and on the construction of appropriate failure domains.

In the second part of the research, the shear-sliding failure mechanism was studied in detail through numerical simulations of triplet tests (EN 1052-3) and shove tests (ASTM C1531). The scope was to investigate factors that could affect the shear-sliding behavior of masonry. Among others, the influence of the boundary conditions, the development of the stress distributions along the mortar joints, the cracking formation and evolution, and the role of dilatancy were

studied. In the numerical analysis, a simplified micro-modeling strategy was adopted. Bricks were modelled as a linear, elastic and isotropic material, while the nonlinearities were concentrated in the joints, where the sliding failure was expected to take place. A composite interface model was used, including a tension cut-off, a Coulomb friction criterion and a compressive cap. The input strength parameters used to set the yield functions were selected from results of experimental tests.

The results of the numerical analyses allowed to gain a better interpretation and understanding of the outcomes of the shear tests considered. Moreover, factors that could influence the shear-sliding behavior of masonry were analyzed by performing parametric studies. The numerical models were validated through comparisons with the results from experimental tests, in terms of failure load, post-peak behavior and specimen deformability. The understanding gained from numerical simulations of shear tests allowed to propose some improvements of the testing procedure and of the results interpretation.

## 1 Introduction

Masonry can generally be defined as a composite material, made of natural or artificial elements assembled in different ways and bonded together with mortar. One of the best characteristics of a masonry construction is its simplicity. Indeed, laying pieces of stone, bricks, or blocks on top of each other, either with or without cohesion via mortar, is a simple, though adequate, technique that has been successfully used ever since remote ages (Rots 1997). In Italy, both bricks and stones were used from very ancient times until today in many types of buildings, both monumental and residential. Along the past centuries, the great variability of historical, geographic, economic and social conditions determined an extreme diversification of the construction technologies. Therefore, existing masonry buildings have not only different aesthetic qualities but also different mechanical properties and durability characteristics.

From the mechanical point of view, masonry is a non-homogeneous, plastic and anisotropic material, characterized by a very low tensile strength. It is usually described as a material exhibiting distinct directional properties due to the mortar joints, which act as planes of weakness (Lourenço 1996). Masonry can be typically unreinforced or reinforced and an understanding of the behavior of this composite material requires the characterization of its components. Indeed, the properties of masonry are strongly dependent upon the properties of its constituents. Clay bricks, stones, and mortar are quasi-brittle materials, which fail due to a process of progressive internal crack growth (Lourenço 2014). An adequate characterization of both the single components and the bond between mortar and bricks, as well as of masonry assemblages, is needed for an effective structural analysis of masonry structures and should be performed through extensive experimental testing.

The evaluation of the structural safety of existing masonry buildings is a current and a crucial issue throughout the world. In seismic prone regions, especially, the high vulnerability of these structures increases the seismic risk also for low and medium hazard levels, as the most recent earthquakes have highlighted. The situation is even more critical when dealing with old masonry constructions, either built without a proper seismic design or subjected to damages and degradation through years and decades and, therefore, particularly vulnerable to horizontal actions. Several challenges and difficulties have to be faced in the structural analysis and the safety assessment of historical constructions due to their geometrical complexity, the variability of materials and building techniques adopted, the poor knowledge on past events which might have affected the current condition of the constructions and the lack of design codes. In this context, the use of a multidisciplinary approach is strongly recommended, which is based on

four key-steps: anamnesis, diagnosis, therapy, and control (Masciotta et al. 2001). It should integrate a variety of complementary activities, such as historical investigations, use of non-destructive or slightly-destructive techniques, and monitoring (Roca et al. 2010).

## 1.1 Masonry structures

Masonry buildings are structural systems composed of vertical and horizontal structural elements, walls and floors, which have to be connected in every direction to obtain a box-like behavior. Horizontal connecting elements (e.g. steel ties or ring beams) should be provided at each floor level to connect the walls. The typical structural elements characterizing ordinary masonry buildings are: (i) vertical wall panels (piers), (ii) horizontal masonry panels (spandrels), and (iii) rigid nodes, located at the intersections of vertical and horizontal panels.

According to available materials, climatic and functional requirements, technical knowledge and traditional practice specific to different countries, a variety of masonry typologies can be found (Tomažević 1999). Indeed, a wide variety of materials, both natural and artificial, and different structural typologies have been adopted in the past centuries for the construction of traditional masonry buildings. In Mediterranean countries, typical stone or brick masonry buildings have a regular structural layout, characterized by the presence of walls distributed in two orthogonal directions. Wooden floors or brick vaults were adopted as horizontal structural elements in old constructions, while wall ties were not always present.

### 1.1.1 *Materials and masonry typologies*

The identification of the masonry quality is of crucial importance, especially when dealing with existing constructions, since it is strongly correlated to the mechanical behavior of the structural elements. It should be gained by diagnostic analyses, in which the materials characteristics should be investigated, as well as the characteristics of the masonry typology. In particular, the following features need to be analyzed:

- Type of the resisting elements: natural stones, fired clay bricks, adobe bricks, etc.;
- Shape and dimensions of the resisting elements;
- Type of mortar: cementitious mortar, lime-based mortar, pozzolanic mortar, etc.
- Type and characteristics of the texture;
- Presence of passing through stones (headers).

In the Italian Building Code (NTC 2008), the principal masonry typologies characterizing existing constructions on the national territory are listed. However, given the extreme diversification of the masonry typologies, every Italian Region can provide further

specifications to better identify and assess the masonry quality. Different classifications have been proposed in past years, such as the ones provided by the National Group for the Earthquake Protection (GNDT) and by the Emilia Romagna Region (Figure 1.1).

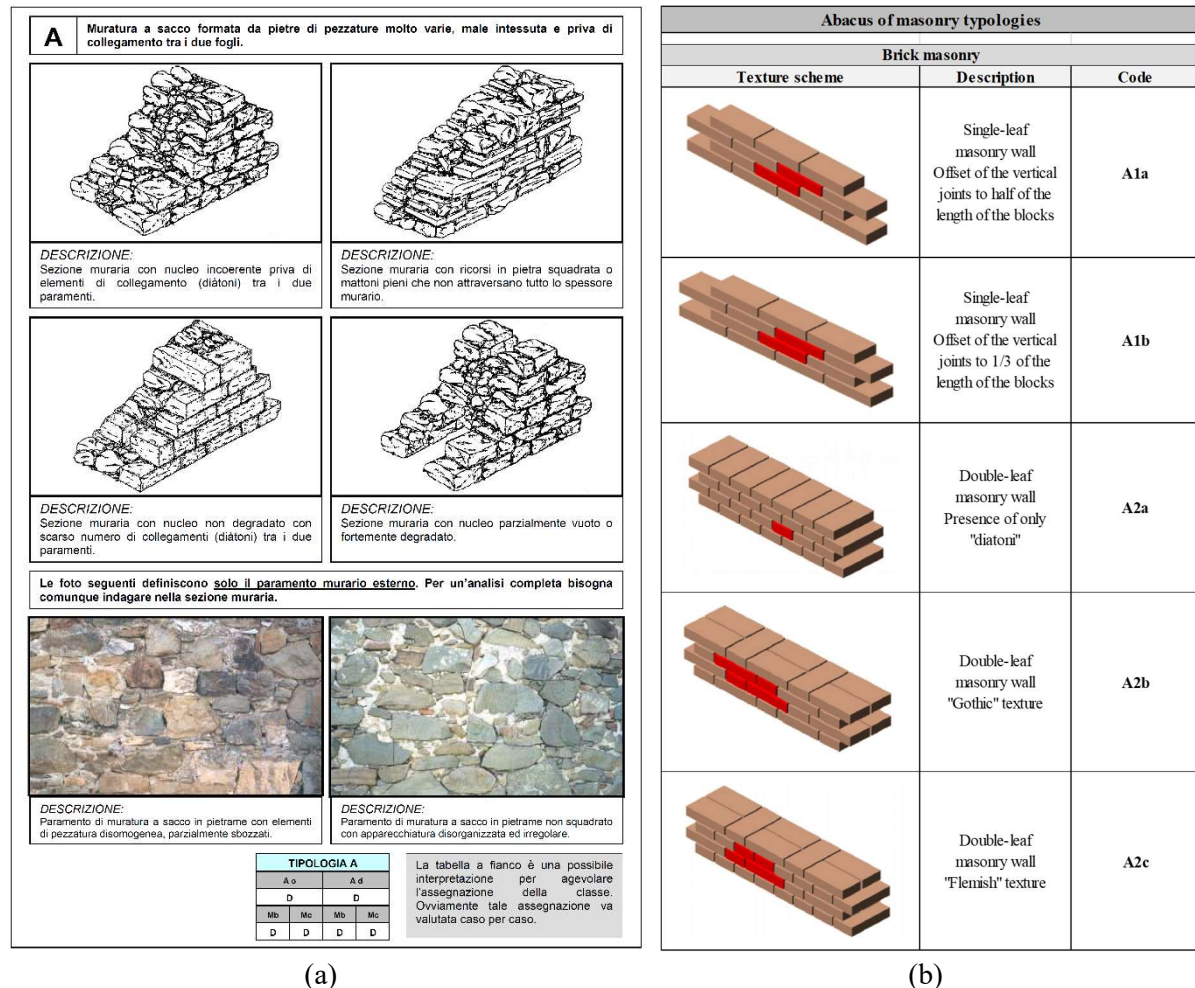


Figure 1.1. Examples of abaci for the identification of masonry typologies: (a) GNDT Manual; (b) Abacus of masonry typologies, Emilia Romagna Region, 2009.

### 1.1.2 Structural typologies

A classification based on the global behavior of a building allows to highlight the structural problems both for vertical and horizontal loads and, especially in the post-seismic surveys, it helps in bearing in mind the entire range of problems, typical of a certain class. The classification is particularly useful for a better understanding of the structural behavior of the building and of its critical issues, which are the bases to provide a first assessment of its vulnerability. Here, a quite simple but useful classification proposed by Pagano (1968) and reported by Lenza & Ghersi (2011) with some additional seismic considerations is presented. Three classes of masonry buildings were identified, as shown in Figure 1.2, having decreasing level of vulnerability from the first to the third class:

- First class: arches and vaulted systems;
- Second class: plane decks with simply supported beams;
- Third class: concrete slabs and ring beams.

In the Italian historical city centers it is possible to find the characteristics of the three classes in a single building due to the evolution of the construction along the past decades and centuries.

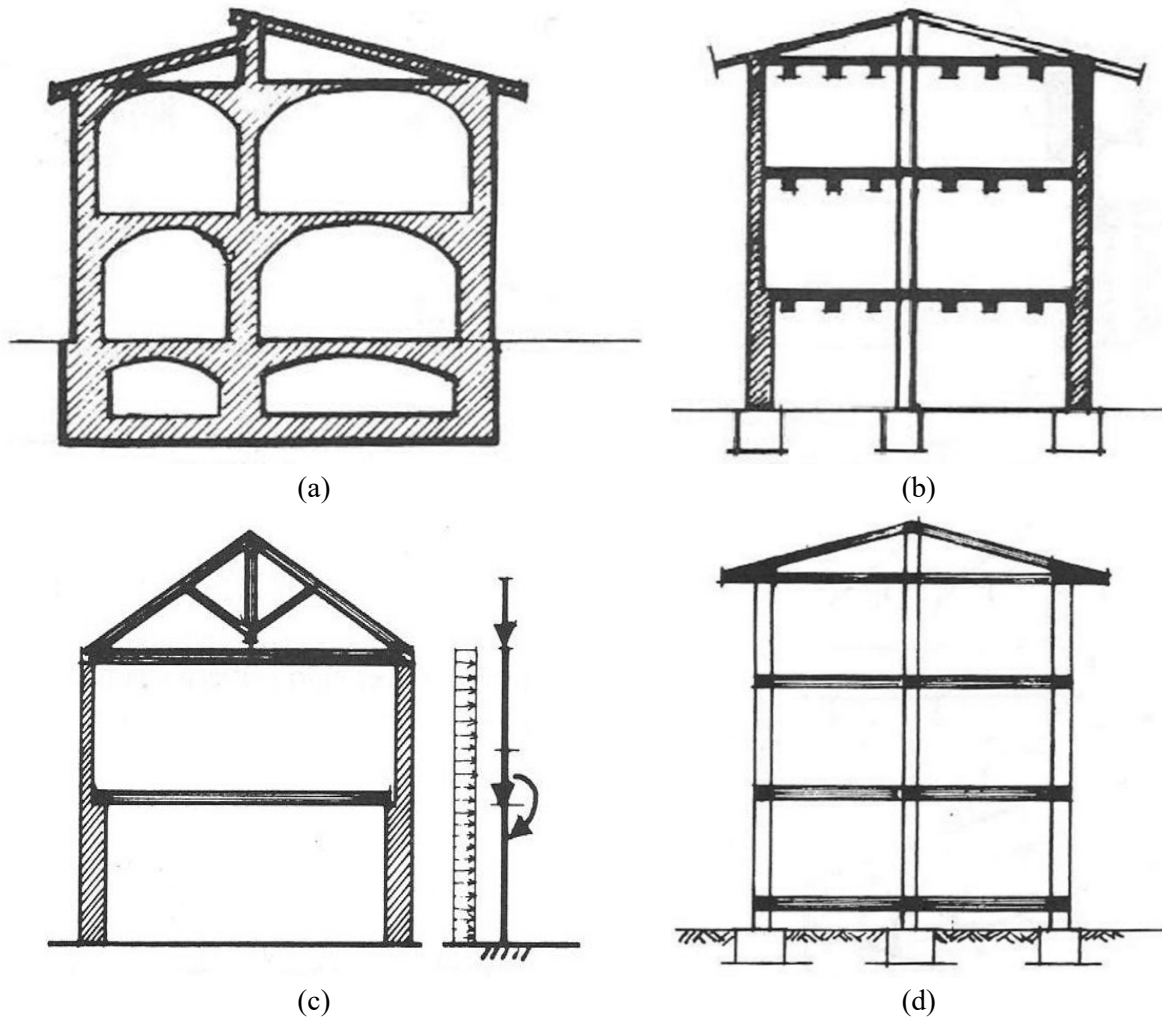


Figure 1.2. Classification of masonry buildings: (a) first class; (b-c) second class; (d) third class (Preite, 1986)

### First class buildings

Buildings belonging to the first class (Figure 1.3a) are entirely constituted by masonry and are characterized by the presence of vaulted systems. Vertical walls, continuous from the foundations to the roof, exhibit arches above the openings. The presence of arches and vaults affects the behavior of the structure under vertical loads: the thrusts are balanced in the internal nodes, but they have an overturning effect on the external walls. The combination of these

factors can determine the activation of out-of-plane overturning, which could be prevented by effective connections between orthogonal walls.

With regards to the resistance against horizontal actions, one of the crucial aspects is the absence of rigid slabs able to distribute the seismic actions to the resisting elements according to their stiffness. Therefore, each wall panel has to directly carry the seismic accelerations. With regards to actions perpendicular to the masonry walls, they can be transmitted to the orthogonal walls through the arch effect. However, the small thickness of the wall determines high thrusting actions, which are balanced in the internal nodes but difficult to be absorbed by the external walls. The presence of steel chains, parallel to the wall panel, is thus necessary.

Considering the effect of the seismic action in the plane of the walls, the horizontal forces could be tackled by a truss mechanism with compressed struts able to transfer the actions to the foundations. However, in absence of horizontal tensile resisting elements, the formation of the truss mechanism is not activated in all the panels. The walls, indeed, could behave as many independent cantilevers since the spandrel elements do not provide a sufficient coupling.

### Second class buildings

Buildings belonging to the second class (Figure 1.3b) are characterized by vertical masonry panels (piers) and by plane slabs consisting of simply supported beams. Instead of arches above the compartments or the openings, masonry or timber lintels are present. The presence of the horizontal slabs eliminates the problem of the thrusting forces given by arches and vaults in first class buildings and therefore it is common to find, in this category, buildings with a higher number of floors and thinner walls. Nevertheless, the global behavior of the building can be influenced by some phenomena that can produce the outward opening of the structure, such as: the eccentricity of the external walls, and the arch effect of the lintels, that generates thrusting actions, balanced in the internal nodes but not in the external ones. The existence of efficient connections between the structural elements can reduce the effect of the mentioned issues.

In presence of horizontal seismic actions, out-of-plane failure could be activated if good connections between the beams of the slabs and the masonry walls are not provided. External walls loaded by the slabs exhibit a safer behavior due to the effect of the weight of the floor which counteract the overturning mechanism.

### Third class buildings

Buildings belonging to the third class (Figure 1.3c) are characterized by the presence of concrete slabs and ring beams due to the increasingly widespread use of reinforced concrete starting from the beginning of the 20th century. In many cases, it can be also noticed the

presence of reinforced concrete lintels well embedded above the openings, which ensure the elimination of the thrusting actions due to the arch effect.

These buildings exhibit an improved seismic behavior and the critical issues of the other classes are reduced or eliminated. The slabs work both as a restraint for the external walls (preventing overturning mechanisms) and as a rigid diaphragm able to distribute the seismic action on the vertical structural elements. Moreover, the presence of tensile resisting elements (ring beams and lintels) allows the formation of a truss mechanism in all the masonry panels, ensuring the transmission of forces to the foundations.

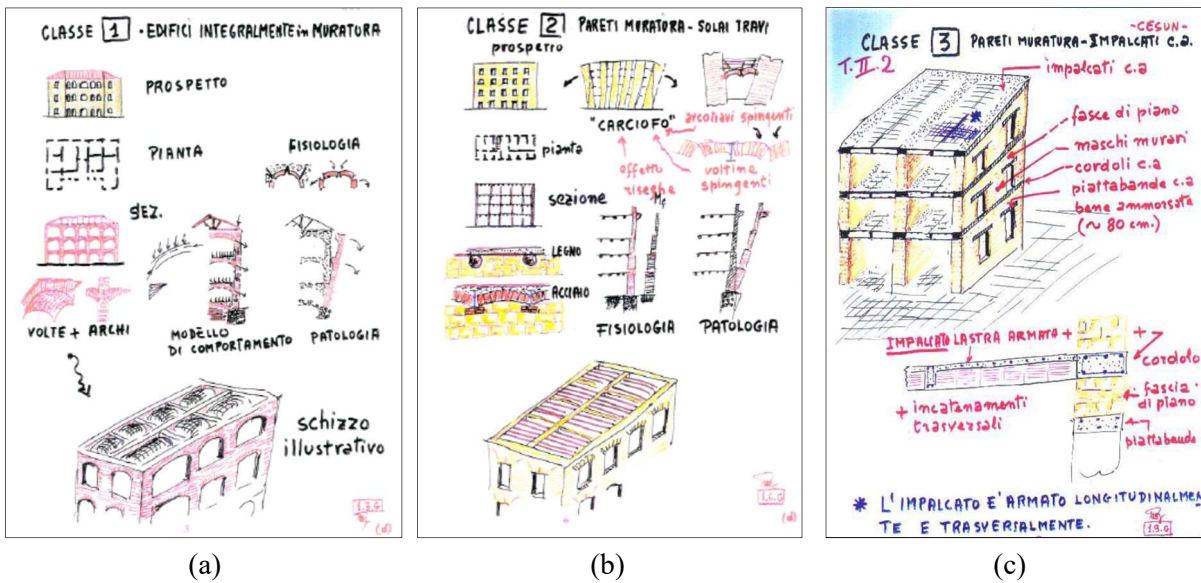


Figure 1.3. Masonry structural typologies, characteristics and critical issues: (a) first class buildings; (b) second class buildings; (c) third class buildings (Pagano, 1990).

## 1.2 Failure mechanisms of masonry structures

Failure mechanisms of masonry structures subjected to a seismic action can be associated to out-of-plane or in-plane response of the masonry walls. Usually, as demonstrated by the post-earthquake damage surveys, the main sources of vulnerability for masonry structures are associated to local out-of-plane failure modes (Magenes & Penna 2009). These mechanisms (Figure 1.4) can be activated in presence of very poor connections between orthogonal walls (e.g. lack of interlocking, absence of tie rods or ring beams) and between walls and floors (e.g. simply supported wooden floors) or in presence of thrusting roof. Once out-of-plane failure is prevented by proper measures, local mechanisms can be prevented, and a global behavior governed by the wall in-plane response can develop. In this case, the in-plane walls provide the stability necessary to avoid collapse. (Magenes & Calvi 1997).

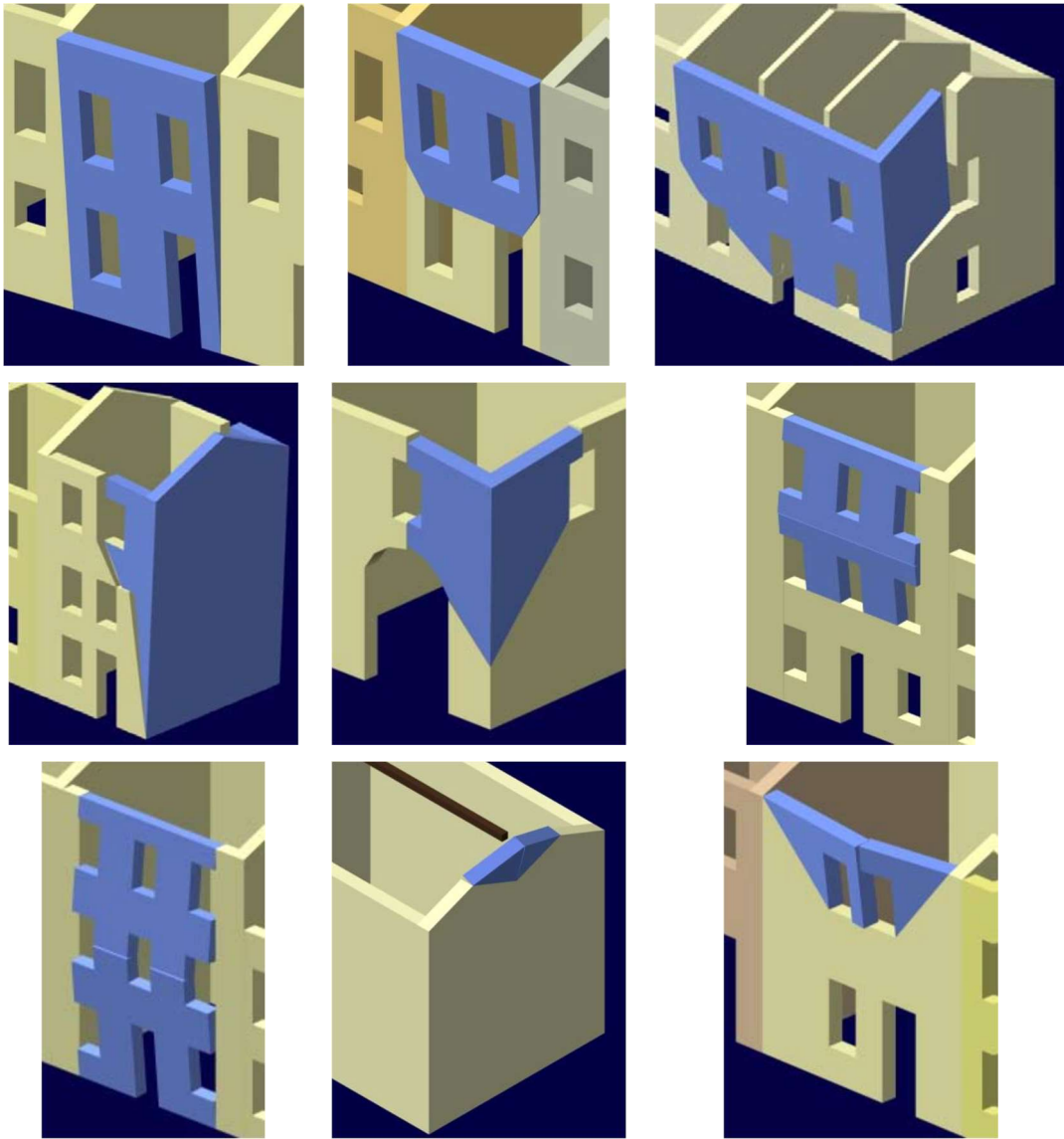


Figure 1.4. Typical out-of-plane failure mechanisms (Reluis document).

### 1.2.1 *In-plane shear strength of masonry piers*

Masonry piers can fail in shear according to three well-known mechanisms: toe crushing associated to rocking, sliding and diagonal cracking (Figure 1.5). In order to quantitatively describe these different behaviors, several models were proposed in the past (Turnšek & Čačovič 1971, Benedetti & Tomazevic 1984, Mann & Muller 1980). In this work, the attention will be focused on the sliding and the diagonal cracking failure modes only, which were investigated in the experimental campaign presented in the followings. Indeed, the toe crushing was not observed in the testing program, because it typically occurs in case of slender walls or with high levels of vertical stress, which is not typical of the analyzed types of masonry structures.

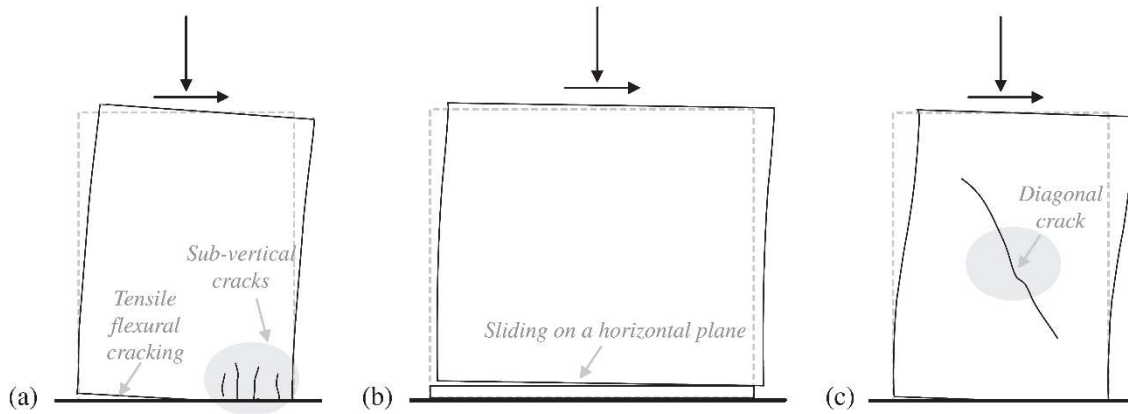


Figure 1.5. Typical failure modes of masonry piers: (a) crushing associated to rocking; (b) sliding; (c) diagonal cracking (Calderini et al. 2009).

The sliding failure takes place along a mortar joint, usually at the bottom of squat masonry piers subjected to low compressive stress. The well-recognized model for describing the sliding failure is the Mohr-Coulomb's model, in which the governing parameters of the phenomenon are the cohesion and the friction coefficient, according to the linear formulation:

$$\tau = c + \mu\sigma, \quad (1.1)$$

where  $\tau$  is the shear strength,  $\sigma$  is the compressive stress,  $c$  is the cohesion and  $\mu$  is the friction coefficient. These latter parameters can be determined from slightly-destructive tests in which the sliding along a mortar joint is investigated, as will be shown in the followings.

The diagonal cracking failure mode, typical of moderately slender masonry panels with higher compressive stress applied, is characterized by the presence of diagonal cracks, which generally develop starting from the center of the panel and then propagate towards the corners. The failure criterion proposed for the interpretation of this mechanism is based on the assumption that the crack will appear in correspondence of the reaching of the masonry tensile strength in the center of the panel. The formulation, initially proposed by Turnšek and Čačovič (1971), defines a parabolic failure domain, in which the governing parameter is the diagonal tensile strength  $f_t$ :

$$\tau = \frac{f_t}{b} \sqrt{1 + \frac{\sigma}{f_t}}, \quad (1.2)$$

where  $b$  is a shape factor which accounts for the distribution of shear stresses over the cross section of the panel. Several proposals can be found in literature (Turnšek & Čačovič 1971, Benedetti & Tomazevic 1984, Augenti 2000) for the definition of the parameter  $b$ , which in general represents the ratio between the maximum tangential stress in the centre of the panel and the mean tangential stress. According to Benedetti and Tomaževič (1984), it can range from

1 to 1.5, depending on the geometry of the panel (height  $H$  and width  $W$ ) and on the state of stress during the test. For slender panels, characterized by an aspect ratio  $H/W \geq 1.5$ , it can be assumed equal to 1.5, while for squat panels, having an aspect ratio  $H/W \leq 1$ , it can be set equal to 1; the actual value of the aspect ratio can be taken for intermediate cases.

The two models, describing the sliding failure and the diagonal cracking failure, summarized above, were modified by Mann and Müller (1980), in order to better interpret the diagonal cracking failure mode. Differently from the previous model, where masonry is assumed to be elastic, homogeneous and isotropic until failure, they analyzed masonry as a composite material. Therefore, they considered the possibility for the crack to develop according to the features of the constituents, and not rigidly along a principal stress direction. From the observation of real damages, indeed, the diagonal failure can be characterized either (i) by a “stair-stepped path”, with cracks mainly passing through mortar joints, or (ii) by a smooth diagonal crack causing the brick tensile failure (Figure 1.6).

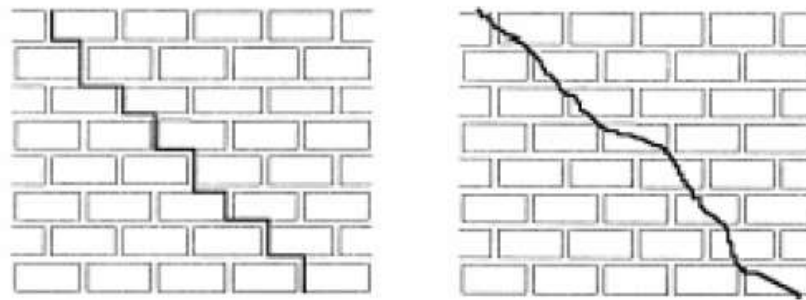


Figure 1.6. Diagonal cracking failure mechanism: (a) stair-stepped crack; (b) brick tensile failure (Magenes 2000).

The first diagonal failure mode (stair-stepped crack), typical of masonry panels with poor-quality mortars with respect to that of bricks, is characterized by a sliding mechanism and can be interpreted through a linear failure criterion, very similar to Eq. (1.1):

$$\tau = \tilde{c} + \tilde{\mu}\sigma . \quad (1.3)$$

Here, the cohesion  $\tilde{c}$  and the friction coefficient  $\tilde{\mu}$  are “global” parameters, related to the “local” parameters of the mortar, presented in Eq. (1.1), through the following formulas:

$$\tilde{c} = \frac{c}{1 + \mu\varphi} \quad (1.4)$$

$$\tilde{\mu} = \frac{\mu}{1 + \mu\varphi} , \quad (1.5)$$

where  $\varphi$  is a parameter related to the masonry pattern, for regular pattern:  $\varphi = 2h/l$ ,  $h$  and  $l$  being the height and the length of the bricks, respectively. Particular attention has to be paid on

the definition of this parameter in case of irregular pattern, because  $\varphi$  can be determined by knowing the inclination of the diagonal crack, as will be done in the interpretation of the destructive tests here presented.

According to Mann and Müller, the second diagonal failure mode, involving bricks, can be interpreted with a model built on the one proposed by Turnšek and Čačovič, by substituting the diagonal tensile strength of masonry  $f_t$  with the tensile strength of bricks  $f_{bt}$ , according to the formula:

$$\tau = \frac{f_{bt}}{b_b} \sqrt{1 + \frac{\sigma}{f_{bt}}}, \quad (1.6)$$

where  $b_b$  is a coefficient which accounts for the distribution of shear stresses on the block, taken to be equal to 2.3 (Magenes & Calvi 1997, Calderini et al. 2009).

The choice of the failure model is of fundamental importance in order to appreciate and analyse the mechanism which is more likely to be activated. Together with the theoretical knowledge of the masonry behavior, the observation of the actual failure mechanisms in experimental tests – in-situ and in laboratory – is essential in order to understand which model best fits the reality.

### 1.2.2 Shear verifications in Building Codes

In this section, a brief description of the indications contained in the Building Codes for the shear verification of masonry walls is reported. The Italian Code is here taken into consideration, together with the Eurocode.

In Eurocode 8 – Part III, the evaluation of the shear strength of an existing unreinforced masonry wall controlled by shear is based on a shear-sliding mechanism, according to Mohr-Coulomb's criterion (Eq. (1.1)). The compressive stress  $\sigma$  is evaluated considering the compressed portion of the cross section only and the friction coefficient  $\mu$  is assigned and equal to 0.4. According to Eurocode 8, the initial shear strength, corresponding to the cohesion, can be obtained from in situ tests and from additional sources of information. Alternative formulations are not reported.

The indications provided by the Italian Code (NTC 2008) for the verifications of masonry walls of existing buildings against shear are based on the evaluation of the shear strength according to the diagonal cracking mechanisms. The formulation reported in the Italian Code is the one of Eq. (1.2). It is recommended that the value of the diagonal tensile strength, if evaluated through diagonal compression tests, is calculated according to the elastic interpretation (see

Section 2.2.1). The value of the coefficient  $b$  should be determined as proposed by Benedetti and Tomažević (1984).

### 1.3 Seismic vulnerability assessment procedures

The approach proposed by the Building Codes (Eurocode 8 – Part III, NTC 2008) for the seismic vulnerability assessment of existing constructions is based on the knowledge of the building under investigation. The great variability of materials and structural typologies determines a substantial complexity in the verification process and, consequently, in the design of strengthening interventions. However, rehabilitation can be successfully accomplished only if diagnosis of the state of damage of the building has been carefully carried out (Binda et al. 2000). The best possible knowledge of the building, which is the essential requirement for any type of structural analysis and for the seismic vulnerability assessment of existing structures, can be achieved by means of historical analysis, survey operations and experimental investigations, with different levels of detail. The objective is to identify the geometry of the building, the structural elements, the constructive details, the masonry typology, the state of damage, and the quality of the materials. An accurate seismic vulnerability assessment, even if it is quite challenging and expensive, is fundamental for the analysis of the seismic response of a single building to identify its characteristics and critical issues and to design efficient strengthening intervention.

In assessing the earthquake resistance of existing structures, the input data shall be collected from a variety of sources, including: available documentation specific to the building in question, relevant generic data sources (e.g. contemporary codes and standards), field investigations and, in most cases, in-situ and laboratory tests. The Codes define three different *Knowledge Levels*, according to the level (limited, extensive, exhaustive) of inspection and testing that is reached during the investigations on a building. To these knowledge levels, confidence factors are associated, which reduces the average mechanical properties of the investigated masonry (Table 1.1).

Table 1.1. Knowledge levels and confidence factors.

<b>Knowledge Level</b>	<b>Confidence Factor</b>
Limited knowledge (KL1)	1.35
Normal knowledge (KL2)	1.2
Full knowledge (KL3)	1.0

One of the crucial aspects, in the seismic vulnerability assessment procedures, is the evaluation of the mechanical properties of the materials. Non-destructive, slightly-destructive or destructive tests can be performed with this purpose. However, the number of tests which can be carried out on an existing structure is often very limited to reduce the damages on the construction to a minimum.

Limited indications can be found in the Building Codes regarding the type and number of tests which should be executed in order to reach a certain *Knowledge Level*. Nevertheless, when destructive tests are not performed, which is typical in the engineering practice, the Italian Code provides values of the mechanical properties for different masonry typologies to be used for the structural verifications (Table 1.2). In particular, the values reported in Table 1.2 should be corrected with the coefficients of Table 1.3 if the characteristics of the investigated masonry are different from the ones to which Table 1.2 refers.

Once the mechanical characterisation of the material is achieved, it is necessary to analyse the structural system through numerical models. The masonry assessment can be based on linear and nonlinear analyses, both static and dynamic, on finite element models or using local analyses with kinematic approach. Linear static analysis, according to the Codes, may be applied to buildings whose response is not significantly affected by contributions from modes of vibration higher than the fundamental mode in each principal direction and should be used only for simple structures. Linear dynamic analysis can also be adopted and allows to obtain information on the dynamic behaviour of the structure. However, as can be easily verified, linear analysis may be very overconservative when applied to masonry structures, which, instead, typically show a strongly nonlinear behavior since the first stages of the structural response. Therefore, since the late 1970s, nonlinear analyses, and in particular pushover analyses, have been used in the seismic assessment and design of masonry structures (VV.AA. 2016). The nonlinear static analysis (pushover analysis) simulates the evolution of the condition of structures during earthquakes, through the application of incremental horizontal forces and progressive updating of the structural model until collapse. The results give information about the ultimate capacity of the structure, considering the nonlinear behaviour in the resisting elements. The displacement capacity has to be compared with the displacement demand of the earthquake. By performing nonlinear dynamic analyses (time-history analyses), the time-dependent response of the structure may be obtained through direct numerical integration of its differential equation of motion. Structural elements have to be modelled with hysteretic properties that represent the effects of yielding and cyclic response. Given the complexity and the high computational costs, nonlinear dynamic analyses are not usually performed in practice.

Table 1.2. Reference values of mechanical parameters (minimum and maximum) and mean self-weight for different masonry typologies, referred to weak mortar, uncoursed masonry, absent connections between wall leaves, texture following the “rule of the art” in case of regular elements;  $f_m$  = mean compressive strength of masonry;  $\tau_0$  = mean shear strength of masonry;  $E$  = mean value of the elastic modulus;  $G$  = mean value of the shear modulus;  $w$  = mean self-weight of masonry. (NTC 2008 – Appendix C8A, section C8A.2, table C8A.2.1.)

Tipologia di muratura	$f_m$	$\tau_0$	E	G	w
	(N/cm <sup>2</sup> )	(N/cm <sup>2</sup> )	(N/mm <sup>2</sup> )	(N/mm <sup>2</sup> )	
	Min-max	min-max	min-max	min-max	
Muratura in pietrame disordinata (ciottoli, pietre erratiche e irregolari)	100	2,0	690	230	19
	180	3,2	1050	350	
Muratura a conci sbazzati, con paramento di limitato spessore e nucleo interno	200	3,5	1020	340	20
	300	5,1	1440	480	
Muratura in pietre a spacco con buona tessitura	260	5,6	1500	500	21
	380	7,4	1980	660	
Muratura a conci di pietra tenera (tufo, calcarenite, ecc.)	140	2,8	900	300	16
	240	4,2	1260	420	
Muratura a blocchi lapidei squadrati	600	9,0	2400	780	22
	800	12,0	3200	940	
Muratura in mattoni pieni e malta di calce	240	6,0	1200	400	18
	400	9,2	1800	600	
Muratura in mattoni semipieni con malta cementizia (es.: doppio UNI foratura $\leq 40\%$ )	500	24	3500	875	15
	800	32	5600	1400	
Muratura in blocchi laterizi semipieni (perc. foratura < 45%)	400	30,0	3600	1080	12
	600	40,0	5400	1620	
Muratura in blocchi laterizi semipieni, con giunti verticali a secco (perc. foratura < 45%)	300	10,0	2700	810	11
	400	13,0	3600	1080	
Muratura in blocchi di calcestruzzo o argilla espansa (perc. foratura tra 45% e 65%)	150	9,5	1200	300	12
	200	12,5	1600	400	
Muratura in blocchi di calcestruzzo semipieni (foratura < 45%)	300	18,0	2400	600	14
	440	24,0	3520	880	

Table 1.3. Corrective coefficients of the mechanical parameters indicated in Table 1.2 to be applied in presence of: high-quality mortar, thin mortar joints, transversal connections between wall leaves, poor internal core, strengthening interventions such as mortar injections or reinforced plaster. (NTC 2008 – Appendix C8A, section C8A.2, table C8A.2.2.)

Tipologia di muratura	Malta buona	Giunti sottili (<10 mm)	Ricorsi o listature	Connessione trasversale	Nucleo scadente e/o ampio	Iniezione di miscele leganti	Intonaco armato *
Muratura in pietrame disordinata (ciottoli, pietre erratiche e irregolari)	1,5	-	1,3	1,5	0,9	2	2,5
Muratura a conci sbazzati, con paramento di limitato spessore e	1,4	1,2	1,2	1,5	0,8	1,7	2
Muratura in pietre a spacco con buona tessitura	1,3	-	1,1	1,3	0,8	1,5	1,5
Muratura a conci di pietra tenera (tufo, calcarenite, ecc.)	1,5	1,5	-	1,5	0,9	1,7	2
Muratura a blocchi lapidei squadrati	1,2	1,2	-	1,2	0,7	1,2	1,2
Muratura in mattoni pieni e malta di calce	1,5	1,5	-	1,3	0,7	1,5	1,5

## 1.4 Objectives and scope of the thesis

In the framework of the seismic vulnerability assessment of existing brick masonry structures, which constitute a great and valuable portion of the Italian building stock, this work focuses on the investigation of the shear behavior of masonry structural elements. The scope is pursued on two different levels: experimental investigations and numerical simulations. Indeed, the first objective of the thesis is the identification of the most suitable and reliable experimental techniques, which can be applied in situ for the mechanical characterization of the masonry material. The shear-sliding failure of masonry is often involved in the failure mechanisms of masonry piers, but some issues regarding the execution and interpretation of in situ shear tests have not been solved yet. Therefore, the second part of the thesis is devoted to the study of the parameters which could affect the sliding behavior of masonry, through numerical simulations of typical shear tests, to improve the current experimental techniques.

In Chapter 2, a brief review of slightly-destructive and destructive tests for the evaluation of the masonry shear strength is presented. The focus is devoted to experimental techniques which can be directly applied in situ, such as: shove test, splitting test on masonry cores with inclined mortar joint, diagonal compression, and shear-compression test.

The mentioned experimental tests were performed on existing buildings during an important experimental campaign carried out on masonry constructions severely damaged by the 2012 Emilia earthquake. The experimental program and results are described in Chapter 3. The advantages and disadvantages of each technique are analyzed and discussed, considering obtainable mechanical parameters and the definition of appropriate failure criteria, representative of the failure mechanisms characteristics of the investigated masonry. The fact that both slightly-destructive and destructive tests were performed, allowed to investigate the ability of local tests to identify the global behavior of a structural element.

Chapter 4 deals with the numerical studies of the shear-sliding behavior of masonry, which was a typical failure mode observed in the experimental campaign. The principal characteristics of an ideal shear test are presented and details about the modeling strategies and constitutive models used in the numerical simulations of Chapter 5 and 6 are reported.

In Chapter 5, numerical simulations of triplet tests (EN 1052-3) are presented. Two specimen geometries are considered, characterized by different bond patterns. The model is calibrated through experimental test results on standard triplet specimens and then validated through comparisons with experimental tests performed on both the specimen types.

In Chapter 6, numerical simulations of shove tests (ASTM C1531) are presented. Two different testing procedures, proposed in the Standard, are modeled and compared to analyze

advantages and disadvantages and verify the reliability of the results obtained by both the test methods. Moreover, comparison with the numerical results of triplet test are discussed and proposal for improvements of the experimental procedure and the results interpretation are included.

A case study is presented in Chapter 7. Results of a shove test performed in laboratory on a masonry wall are reported and then compared with the results of the numerical simulations to validate the model.

Chapter 8 contains a summary and the final conclusions that can be derived from this research work. Suggestions for future works are also included.

## **2 Experimental techniques for the mechanical characterization of existing masonries**

The reliability of the seismic vulnerability assessments, as stated in the Building Codes (Eurocode 8 – Part III, NTC 2008), strongly depends on the level of knowledge of the building under investigation. In order to improve the level of knowledge, one of the key aspects to deal with is the evaluation of the material mechanical properties. Moreover, the accuracy of the modeling results always depends on the correct identification of the mechanical parameters required to characterize masonry material (Alecci et al. 2013). However, even though there is the need of accurately estimating these parameters by performing experimental tests, very few indications are reported in the Codes regarding the number and type of tests to be executed. Moreover, the great variability of materials and construction typologies makes it difficult to define, in a unique way, the procedures and techniques to be used in experimental programs, especially considering that, in most cases, a very limited number of in-situ tests can be performed. Consequently, the choice on the investigations type and their extent has a great influence on the results reliability and an expert judgment is often needed, since the information gained from the experimental studies are then used as input data for structural models and analysis.

Several in-situ experimental techniques are now available to determine the mechanical parameters governing the failure of masonry elements. According to their invasiveness on the construction, they can basically be subdivided into three categories: non-destructive, slightly-destructive (or minor destructive) and destructive techniques. Non-destructive tests provide qualitative information on masonry and they are useful for establishing if the results obtained with destructive tests, which are usually performed on limited portions of walls, can be extended to the whole structure. The main goals of the non-destructive tests are: the identification of the hidden structural elements, the qualification of masonry and its components, the survey of the crack pattern and of the superficial damages and the verification of the physical and mechanical properties of mortar and bricks. Moreover, non-destructive tests can be applied to the same elements and structures many times and in different periods hence such methods are suitable for the diagnostic testing of buildings during both the construction and the service life. Slightly-destructive tests are mainly performed in situ on limited portion of masonry walls and they involve minor damages to the structural elements, resulting in local loss of properties and requiring repairs. Destructive tests allow the direct measures of the mechanical characteristics of full-scale structural elements, but produces a great damage on the existing construction.

Both slightly-destructive and destructive tests, which this work is focused on, have their advantages and disadvantages. Slightly-destructive tests can be very promising, considering their easy execution and low impact on the structure, even though they could provide too localized information and quite scattered results. On the other hand, destructive tests, performed on full-scale masonry panels, can be more representative of the global behaviour of the structural elements, but they are often unfeasible in the engineering practice due to their invasiveness and economic effort.

The importance of defining consistent procedures for the study of the masonry mechanical characteristics was already highlighted by other authors (Binda et al. 2000, Ceroni et al. 2012). Several researches were developed for the evaluation of both the compressive and shear strength of masonry, with the aim of analysing the reliability of slightly-destructive tests and defining non-standard alternative experimental procedures. Among others, the use of masonry cores subjected to both compressive tests and splitting tests with inclined mortar joint were proposed by Benedetti et al. (2008) and by Sassoni et al. (2013). Being these minor-destructive methods very promising, different authors performed experimental campaigns to validate the less invasive techniques on the basis of the results of the more representative destructive ones. With reference to the masonry shear behaviour, which is the topic of the present work, the results of splitting tests on masonry cores with a rotated mortar layer were compared with results obtained in laboratory by performing diagonal compression tests (Braga et al. 1993) and shear-compression tests (Mazzotti et al. 2014). Specific studies on the combined state of stress induced in the mortar joint in the splitting test were also conducted, with the aim of evaluating a failure criterion for mortars (Marastoni et al. 2016). Moreover, different works were focused on comparisons between diagonal compression tests and standard moderately destructive laboratory tests, such as triplet tests and shear tests (Incerti et al. 2016, Alecci et al. 2013). In most of these works, a good agreement between the different experimental techniques was found.

It should be noticed that the cited testing programs were all executed under laboratory conditions, on specimens purposely built in a controlled environment. These, of course, are the optimal conditions in which calibrate and validate the proposed testing procedures. However, the mechanical behaviour in-situ can be very different and could have a significant influence on the test outcomes. Indeed, the materials composition, their load history and state of conservation can hardly be exactly reproduced in laboratory. As a consequence, there is the need of comparing the above-mentioned techniques also in the field. This is the reason why an experimental campaign, which will be presented in Section 3, was conducted on existing

masonry buildings. In the followings, a brief review of some in-situ slightly-destructive and destructive techniques for the evaluation of the shear strength of masonry is reported.

## 2.1 Slightly-destructive tests

### 2.1.1 Single and double flatjack tests

The single and double flatjack tests are performed to determine the in-situ compressive stress level of the masonry and to study its deformability characteristics. Even if they are not performed to evaluate the masonry shear strength, the testing procedure is here reported since it will be used in the shove test on the case study (Section 7).

The single flatjack test (Figure 2.1a), according to the Standard ASTM C1196-14, is carried out by introducing a thin flatjack in a horizontal cut executed in correspondence of a bed joint. Gauge points have to be positioned above and below the cut and measurements of the initial (pre-cut) distances between these points must be made using a removable extensometer. After the cutting, due to the release of the compressive stress, the distance between the edges of the slot decreases. Post-cut measurements have to be carried out in order to obtain initial deviation from the original gage distances. In general, the values of the displacements measured at the reference points are not constant; but they tend to be greater in the center of the cut due to the new distribution of stresses (Binda & Tiraboschi 1999). The flatjack, made with thin welded steel plates, is then inserted into the slot and the pressure is gradually increased to restore the initial distance between the gauge points. The average compressive stress  $\sigma$  in the masonry can be calculated as:

$$\sigma = k_m \cdot k_a \cdot p \quad (2.1)$$

where  $p$  is the flatjack pressure required to restore the gage points to their initial distance,  $k_m$  is the calibration constant of the flatjack, and  $k_a$  is the ratio of measured area of the flatjack to the average measured area of the slot. Both  $k_m$  and  $k_a$  are constants lower than one.

The double flatjack test (Figure 2.1b) can be performed right after a single flatjack test. Indeed, after the unloading of the first flatjack, a second cut is made, parallel to the first one, and a second flatjack is inserted at a distance of at least five courses of masonry from the previous one. The two flatjacks delimit a masonry portion of appreciable size on which a uniaxial compression stress can be applied. In this way, a compression test is carried out on an undisturbed sample. Linear Variable Differential Transformers (LVDTs) are used to measure vertical and lateral displacements, allowing for the calculation of the elastic modulus and the Poisson's ratio of masonry. Several loading-unloading cycles may be performed at increasing

stress levels in order to study the stress-strain behavior of the masonry during loading and unloading phases. The maximum value of the stress reached by the last loading cycle can also be used to roughly estimate the compressive strength of masonry, if the portion of wall above the cut is able to provide a sufficient contrast to the applied forces.

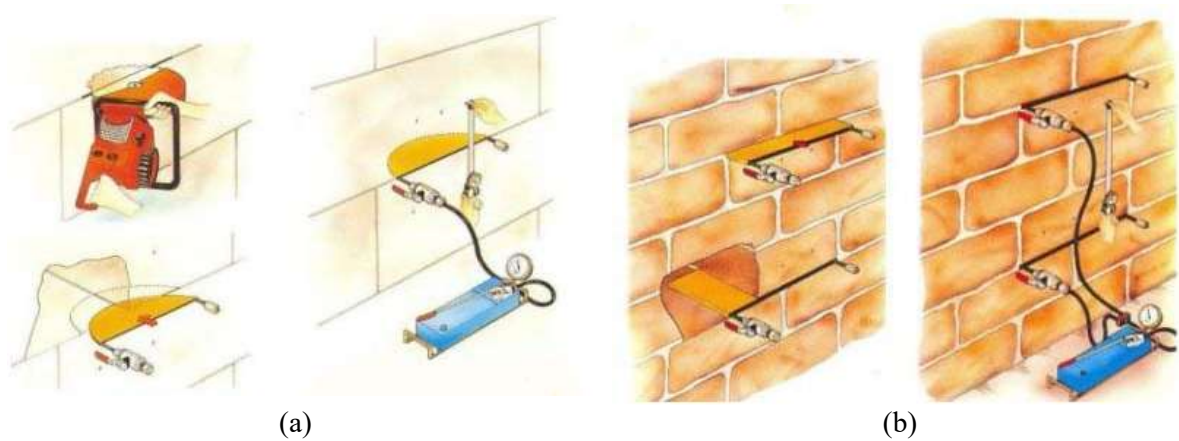


Figure 2.1. Flatjack test testing procedure: a) single flatjack test; b) double flatjack test.

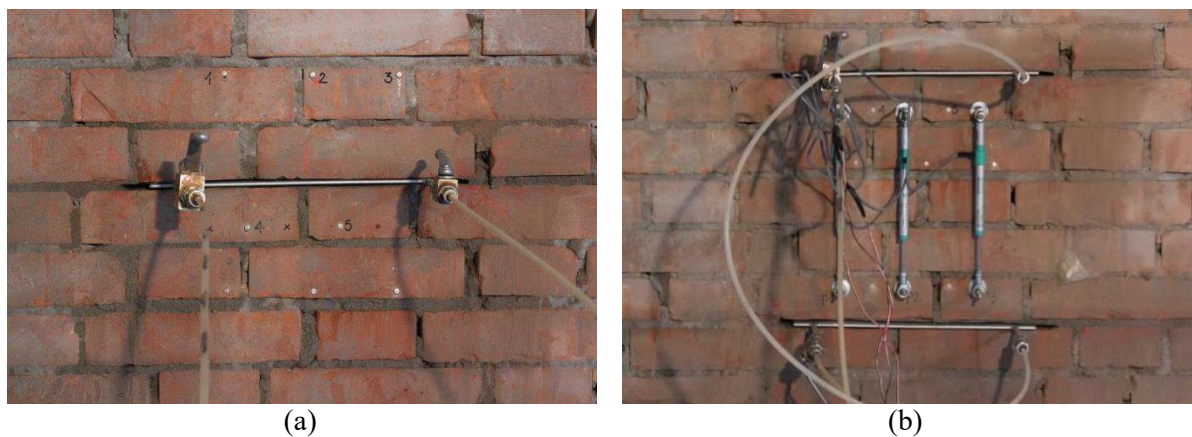


Figure 2.2. Single (a) and double (b) flatjack test setups.

### 2.1.2 Shove test

The shove test, as reported in the standard ASTM C1531-16, is aimed at evaluating an index of the in situ, horizontal shear resistance of mortar joints in unreinforced masonry. It consists, indeed, in producing the sliding of a brick with respect to the surrounding masonry, along two horizontal mortar joints. The test can be performed according to three different methods (Figure 2.3), which basically differ one from the other depending on the way in which the vertical compression is controlled or applied. Indeed, in *Method A*, the vertical compression is directly applied by means of two flatjacks, positioned above and below the test unit, while in *Method B* and *C*, the vertical stress is evaluated through an estimation of the acting dead and live loads.

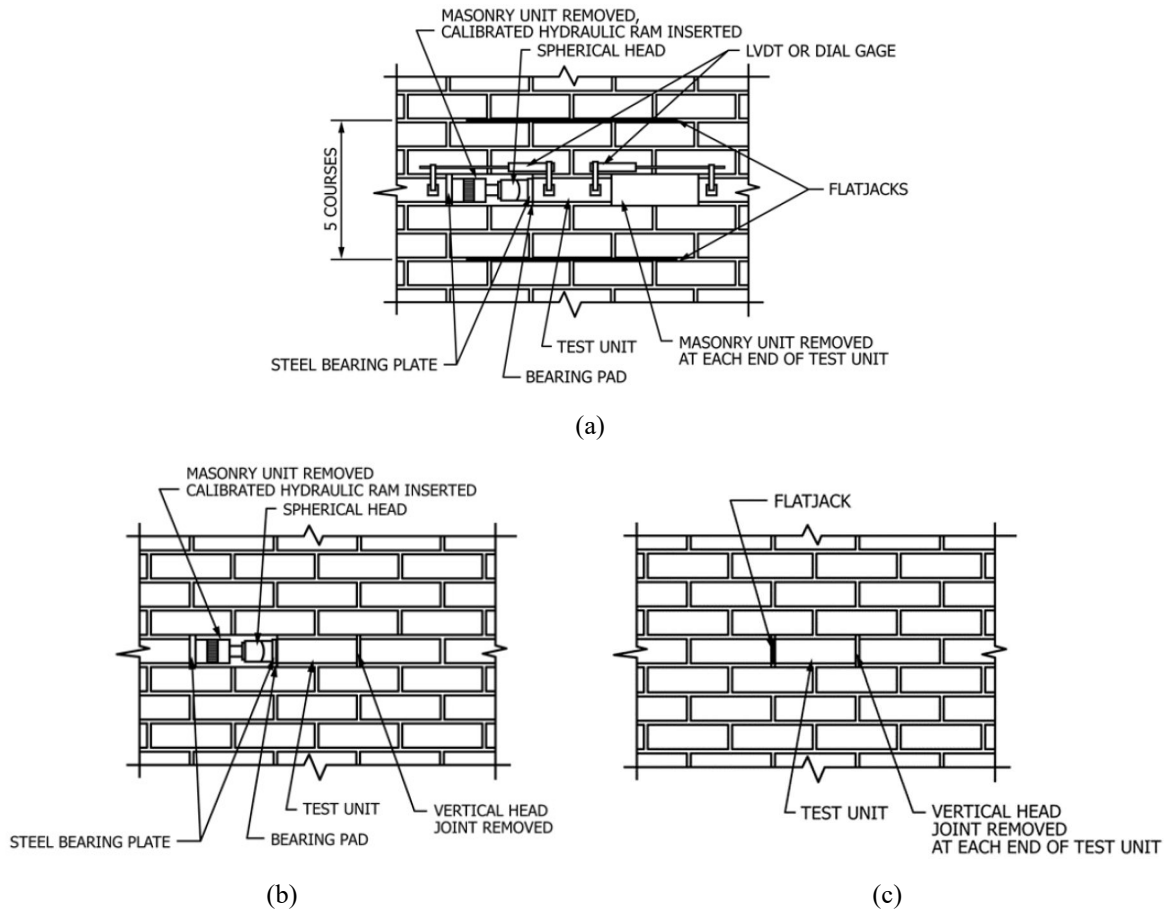


Figure 2.3. Shove test setups: (a) Method A; (b) Method B; Method C.

The testing procedure for *Method A* is more complicated than the one for *Method B* and *C*. However, the compressive stress level is controlled for the entire duration of the test and, if single and double flatjack tests are executed, the state of stress and the deformability properties of masonry can be evaluated as well. After the seating of the flatjacks, a single masonry block and a head joint have to be removed from opposite ends of the chosen test unit. At the beginning of the shove test, the pressure in the two flatjacks have to be set at a very low value ( $\sigma_1=0.07$  MPa). Then, the pressure in the horizontal jack is increased gradually until the sliding failure of the joint is reached. During the tests, horizontal displacements should be measured using LVDTs. After the obtainment of this first sliding, the pressure in the flatjacks is increased and the sliding produced again. This process can be repeated several times and the shear strength at each level of normal compressive stress can be obtained:

$$\tau_i = \frac{F_{max,i}}{A_j} \quad (2.2)$$

where  $F_{max,i}$  is the maximum shear load at the  $i$ -th level of normal compressive stress, and  $A_j$  is the gross area of upper and lower bed joints.

According to the Standard, the coefficient of friction  $\mu$  and the initial shear strength  $c_0$  can be determined by a linear interpolation of the failure points  $(\sigma_i; \tau_i)$  at each compressive stress level, plotted in a shear strength versus normal compressive stress diagram. As an example, results obtained by Atkinson et al. (1988), who were the first researchers working on this topic, are reported in Figure 2.4.

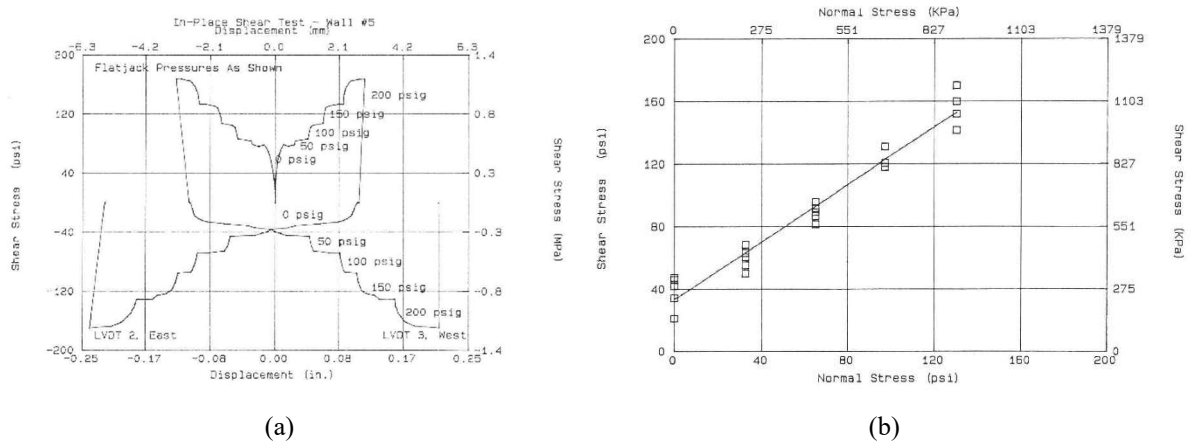


Figure 2.4. Typical shove test results (*Method A*): (a) load-displacement curve; (b) Coulomb friction failure domain. (Atkinson et al. 1988)

For *Method B* (Figure 2.5), a single masonry block and a head joint have to be removed from opposite ends of the chosen test unit, which is then displaced horizontally using a hydraulic jack. The horizontal force required to produce the first displacement of the brick provides a measure of the mortar joint shear strength. In this case, only one failure point is obtained. Therefore, in order to calibrate a Coulomb friction failure domain, assumptions on the friction coefficient should be made.

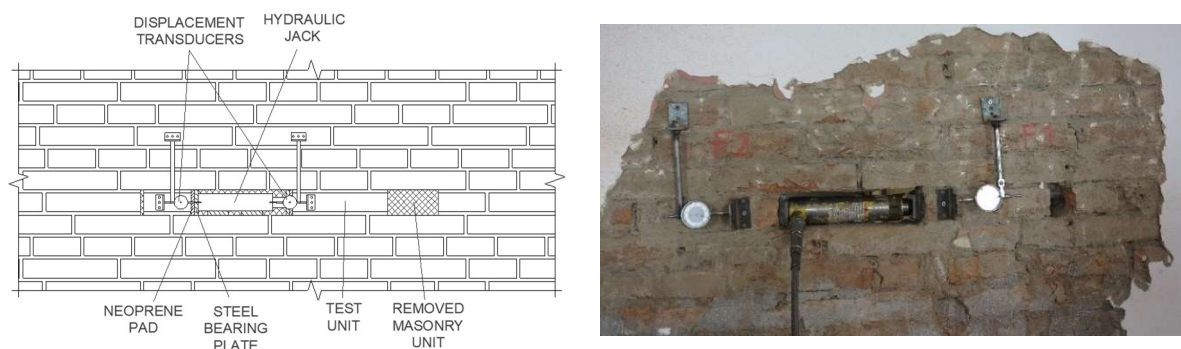


Figure 2.5. Setup of the shove test, *Method B*.

In *Method C*, which will not be analyzed here, only two vertical joints at the opposite sides of the test unit are removed and a vertical flatjack is inserted in one of these joints to produce the sliding of the brick.

Advantages of *Method A* with respect to *Method B* are related to the possibility of performing the test more than one time on a single location. In this way, a reliable estimation of the failure criterion can be obtained. Moreover, if the masonry quality is quite uniform throughout the building, the execution of the test according to *Method A* is the same as performing many shove tests with *Method B* at different elevations (i.e. at different compressive stress levels) in the building (Noland et al. 1988). However, the execution of the test is more complex and creates a greater disturbance of the stress state due to execution of the flatjack slots.

Two main issues should be highlighted regarding the execution of the test and the elaboration of the results. Firstly, for both test methods, there are uncertainties about the determination of the normal compressive stress acting on the test unit. Indeed, the actual stress distribution could significantly differ from the assumed uniform one imposed by the flatjacks (*Method A*) or estimated with load analysis (*Method B*). This can be due to several factors, such as the wall geometry (e.g. single-wythe or double-wythe), the removal of lateral bricks, the dilatant behavior of masonry, etc. For these reasons, the Standard suggests, only for *Method A*, the use of a modification factor, to be determined case by case, to convert the flatjack stress into normal stress on the test unit. Secondly, for *Method A*, it is not well specified in the Standard that the first failure point is associated with an initial Coulomb friction failure criterion while the subsequent ones – with increased normal compressive stress – describe a pure frictional behavior of the bed joints and have to be associated to a residual Coulomb friction domain. The two mentioned issues will be discussed and analyzed in Section 6.

### 2.1.3 *Splitting test on masonry cores with inclined mortar joint*

The splitting test on masonry cores with inclined mortar joint was introduced as a slightly-destructive technique for the determination of the masonry shear strength, to be applied on samples extracted from masonry walls (Benedetti et al. 2008, Braga et al. 1993). The aim of this test is to simulate a sliding failure mechanism along the mortar joint, that can be interpreted by a Mohr-Coulomb's failure criterion. The cores are tested under compression – force orthogonal to the core axis – with different inclinations of the mortar layer with respect to the horizontal direction (Figure 2.6).

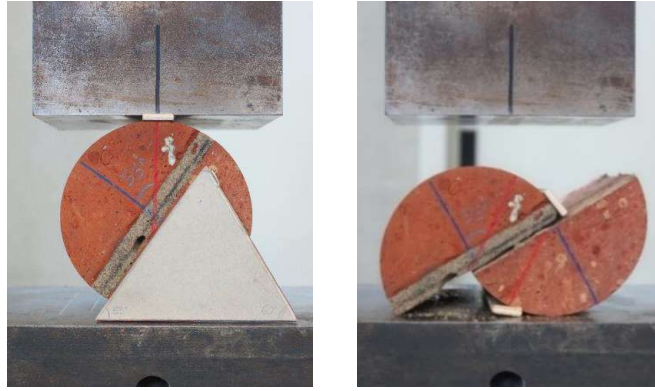


Figure 2.6. Splitting test on a masonry core with inclined mortar joint.

Due to the inclination of the mortar joint, the state of stress along it (which is typically the sliding surface) can be assumed as a combination of compressive and tangential stresses. In recent researches (Marastoni et al. 2016, Pelà et al. 2015), the existence of a triaxial state of stress in the mortar joint has been investigated and the use of a *continuum model* for the interpretation of the splitting test has been analyzed, also taking into account the confinement effect given by the segments of bricks on the mortar layer. However, a simplified approach is used here to interpret the sliding behavior of bricks as rigid elements and considering the mortar layer as an interface – assuming an infinitesimal thickness – on which the stress components act. According to this model, the stress state can be represented by a single point in the Mohr plane.

The stress components are therefore assumed to be uniform on the joint surface and equal to:

$$\sigma_{f,c} = \frac{F_{\max}}{A} \cdot \cos \alpha \quad (2.3)$$

$$\tau_{f,c} = \frac{F_{\max}}{A} \cdot \sin \alpha , \quad (2.4)$$

where  $F_{\max}$  is the maximum load registered during the test,  $A$  and  $\alpha$  are the sliding surface area and the inclination of the mortar joint, respectively. For each mortar layer inclination, values of  $\sigma_{f,c}$  and  $\tau_{f,c}$  measured at failure can be drawn as points in the  $\sigma$ - $\tau$  stress plane. In order to cover a wide range of compression and shear stresses in the Mohr plane, at least three different inclinations  $\alpha$  should be used. Regarding the choice on the mortar layer inclinations, previous researches showed that, for cores tested with inclinations equal to  $45^\circ$ ,  $50^\circ$  and  $55^\circ$ , the desired sliding failure can be obtained (Mazzotti et al. 2014). Indeed, for inclinations lower than  $40^\circ$ , a splitting failure mode was noticed, while for values higher than  $60^\circ$  the failure mode was driven by the detachment of a brick wedge just below the strip where the force was applied.

## 2.2 Destructive tests

### 2.2.1 Diagonal compression test

The diagonal compression test consists in applying a compressive load along one diagonal of a square masonry sample. The in-situ procedure has been adapted from the standard laboratory test (ASTM E519-15) according to proposals from previous experimental campaigns (Chiostrini et al. 2000, Corradi et al. 2003, Borri et al. 2011).

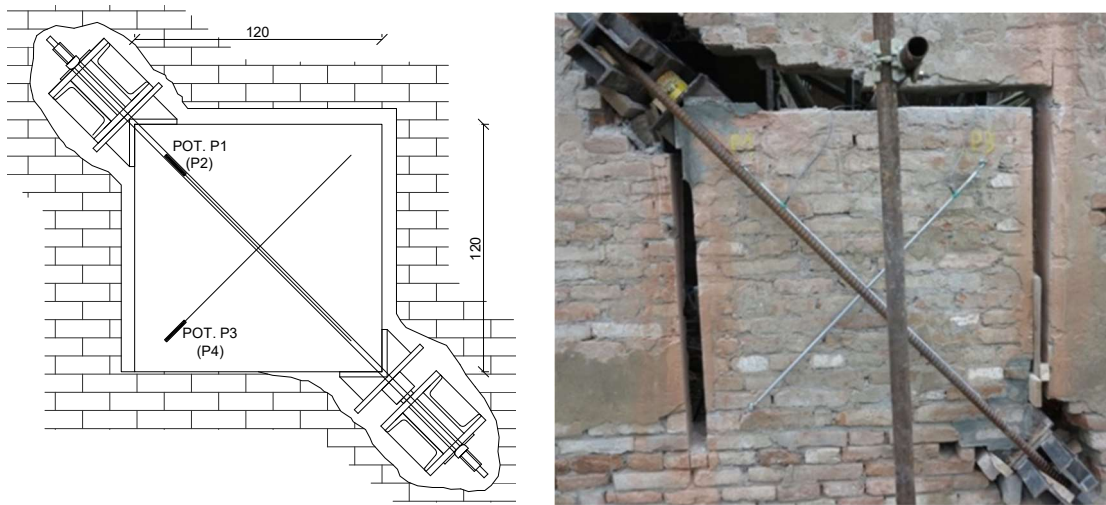


Figure 2.7. Setup of the diagonal compression test.

The panel, having dimensions  $120 \times 120 \text{ cm}^2$ , is separated from the surrounding masonry on three sides, while it remains anchored to the rest of the wall, on the fourth side, for approximately 60 cm. The compressive load is applied monotonically up to failure and the diagonal displacements (along both diagonals), on both sides, can be measured using linear potentiometers (Figure 2.7) or LVDTs.

The interpretation of results from this test is not unique and still rises some uncertainties. On one hand, the standard ASTM E519-15 assumes that in the center of the panel a pure shear stress state can be found. Accordingly, the corresponding Mohr circle is centered in the origin of the stress plane (continuous line of Figure 2.8) and the principal stress directions coincide with the two diagonals of the panel. Therefore, the shear strength without compression  $\tau_0$  and the principal tensile strength  $f_t$  are equal and can be calculated according to the expression:

$$f_{t,CD,ASTM} = \tau_0 = 0.707 \frac{P_f}{A_n}, \quad (2.5)$$

where  $P_f$  is the load at failure and  $A_n$  is the net area of the panel.

An alternative interpretation of the test was initially proposed by Frocht (1931), who studied the stress state in the diagonal compression test through photoelasticity. Later on, similar findings were obtained by other authors, who performed linear elastic analysis of the masonry panel modelled as an isotropic and homogeneous material (Calderini et al. 2010, Borri et al. 2013). In the followings, this interpretation will be referred to as the elastic interpretation. The stress state in the center of the panel, in this case, is not a pure shear stress state but can be described by the Mohr circle drawn with the dashed-line in Figure 2.8, where axial stress is also present along the horizontal and vertical arrangements. Accordingly, the principal stresses lay along the diagonal directions and can be expressed as a function of the applied load:

$$\sigma_{I,El.} = -0.5 \frac{P}{A_n} \quad (2.6)$$

$$\sigma_{II,El.} = 1.62 \frac{P}{A_n}. \quad (2.7)$$

Correspondingly, the diagonal tensile strength of masonry ( $f_{t,CD,El.}$ ) can be obtained from Eq. (2.6) by introducing the failure load  $P_f$ .

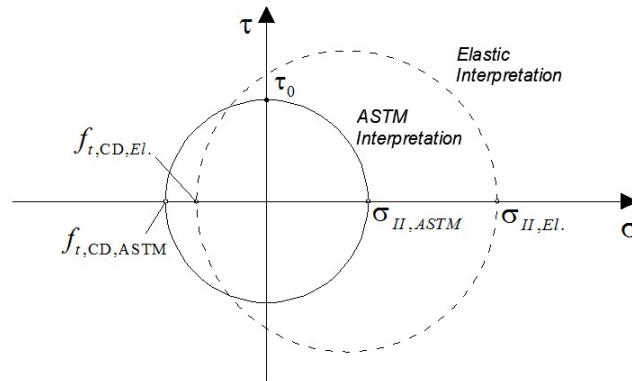


Figure 2.8. Mohr circles for the two different interpretations of the stress state in the diagonal compression test.

### 2.2.2 Shear compression test

The shear-compression test consists in applying an increasing shear load to a masonry wall subjected to a constant level of vertical compression. The main goal of this test is to study the shear behavior of masonry and to obtain the shear strength for assigned values of axial stress. The in-situ version of the test has not been standardized yet and two different setups have been proposed in literature (Chiostriini et al. 2000, Corradi et al. 2003). The test, indeed, can be performed either separating the panel from the surrounding masonry (laterally and above) and applying a known level of compression – *Setup A* (Figure 2.9) – or leaving the continuity along the vertical direction, thus considering the actual compression given by the dead loads acting

on the sample, determined through load analysis or by performing single flatjack tests – *Setup B* (Figure 2.10).

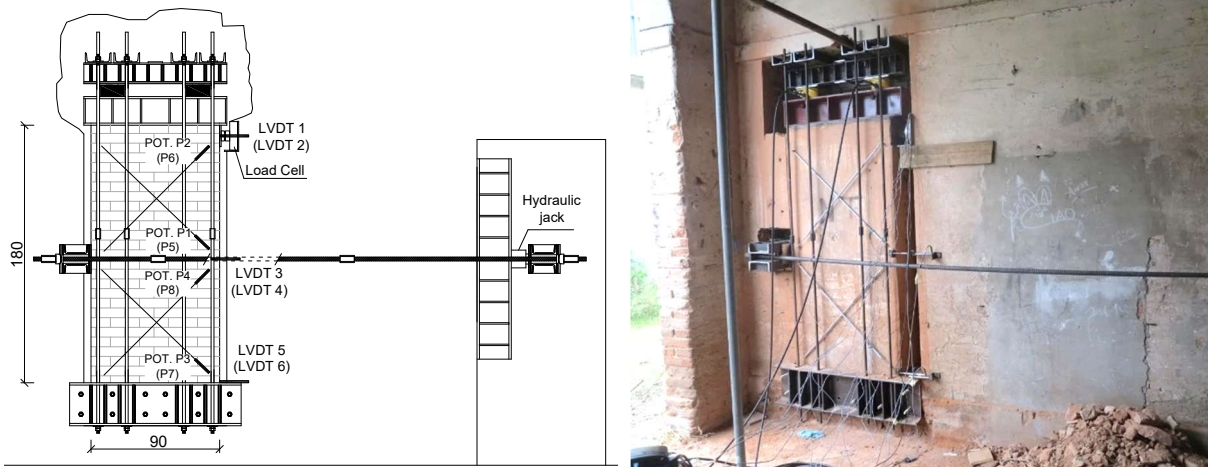


Figure 2.9. Shear-compression test: Setup A.

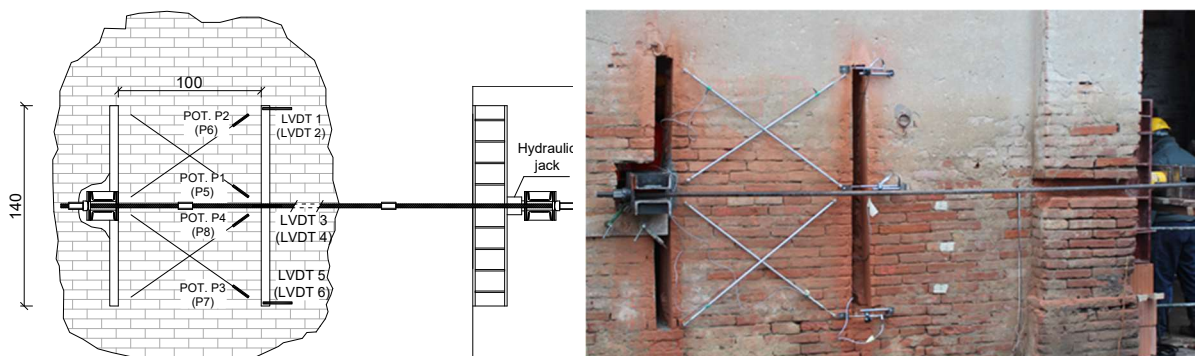


Figure 2.10. Shear-compression test: Setup B.

In both cases, the shear load is applied in the centre of the panels up to failure. During the test, the diagonal displacements in the upper and lower halves of the panels are measured, together with the horizontal in-plane displacements in correspondence of the upper, lower and central cross sections of the samples.

The shear stress acting on the panels has to be calculated according to the different structural schemes (Figure 2.11). In *Setup A*, the mean tangential stress can be calculated in the upper and lower half of the panel with the following formulas, considering a perfectly clamped edge at the bottom and an elastic support at the top:

$$\tau_{sup} = \frac{R}{A} \quad (2.8)$$

$$\tau_{inf} = \frac{T - R}{A}, \quad (2.9)$$

where  $T$  is the shear force applied,  $A$  is the cross section area of the panel and  $R$  is the horizontal reaction at the top of the panel, recorded through a load cell.

In *Setup B*, the panel can be considered clamped on both sides, so the mean tangential stress  $\tau$  can be evaluated as:

$$\tau = \frac{T}{2A} \quad (2.10)$$

The main advantage of *Setup B* is to have a symmetric configuration for upper and lower panels, thus leading to a more robust and reliable interpretation of the results. This behaviour, as will be shown in Section 3, was also confirmed by the entity of the lateral displacements measured during the tests at the top, at the bottom and in the centre of the specimens. In *Setup A*, on the contrary, there are uncertainties on the level of constraint at the top of the panel, where horizontal and rotational displacements can be present. However, the drawback of the *Setup B* is related to the estimation of the vertical load, which cannot be measured like in *Setup A*.

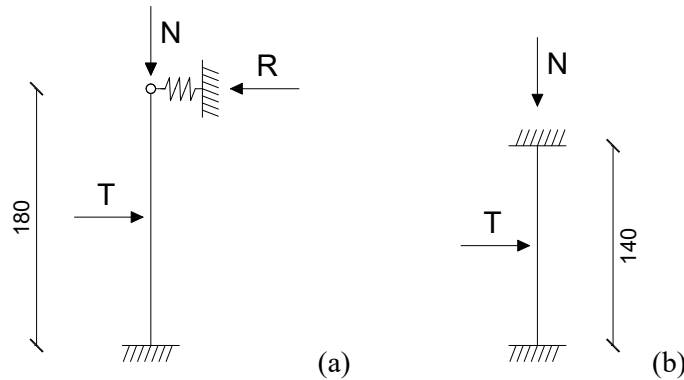


Figure 2.11. Structural schemes of the shear-compression test: (a) *Setup A*; (b) *Setup B*.

The state of stress in the centre of the lower panel, for a general instant of the test, can be represented with the Mohr circle depicted in grey in Figure 2.12, in which the points  $A(\sigma_n, b \cdot \tau_n)$  and  $B(0, -b \cdot \tau_n)$ , considered for the construction of the circle, and the centre  $C(\sigma_n/2, 0)$ , are indicated. The stresses  $\sigma_n$  and  $\tau_n$  are the mean compressive stress and the mean tangential stress applied to the cross section of the panel, respectively. Since the shear stress distribution across the cross-section is not uniform, the maximum shear stress applied to it can be defined as  $b \cdot \tau_n$ . The  $b$  factor, indeed, takes into account the distribution of the shear stresses over the cross section of the panel.

Given the constant vertical load applied to the sample and increasing the shear force, the diagonal cracks will finally occur when the masonry diagonal tensile strength in the centre of the half-panel will be reached. Adopting a criterion defining the failure in terms of maximum tensile stress, which is the case for the Turnšek and Čačovič's criterion, the limit state for the panel corresponds to the Mohr circle depicted in black (Figure 2.12), in which the principal

tensile stress  $\sigma_t$  reaches the masonry diagonal tensile strength  $f_{t,NT}$ . The principal direction is inclined with respect to the vertical direction of an angle  $\alpha$ .

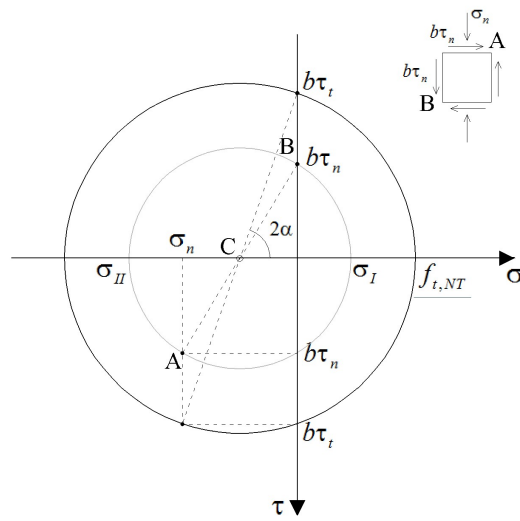


Figure 2.12. Shear-compression test: Mohr circle at failure.

### 3 Experimental campaign on rural masonries in Emilia-Romagna

The seismic events that struck Italy in recent years highlighted the great vulnerability of existing masonry buildings. The 2012 Emilia earthquake, indeed, have shown the great deficiencies of existing constructions, often built without following the “Rule of the Art” and not designed at all to withstand seismic actions. In various works, the seismic vulnerability of historic monumental masonry buildings – such as churches, towers, city halls, etc. – was analyzed (Cattari et al. 2012, Parisi & Augenti 2013, Milani 2013, Cattari et al. 2014). However, limited studies were conducted on rural constructions (Sorrentino et al. 2014), which constitute a quite significant portion of the building stock in Emilia Romagna and resulted severely damaged by the earthquake as well. In the followings, a particular attention will be devoted to these construction typologies.

The Emilia countryside, rather homogeneous concerning the geography, the social and economic development, is characterized by the presence of a large number of isolated buildings, which show similar features. In many cases, a courtyard is characterized by the presence of both a residential building and one or more adjacent constructions, used in the past as stable or barn. Despite the various functions of the buildings, the main differences were not observed in the constituent materials (bricks and lime-based mortar) but in the regularity (or irregularity) of the masonry texture and in their state of conservation. As mentioned, these construction typologies were significantly affected by the seismic events of May 2012. Indeed, after the seismic events, the damage surveys performed on these construction typologies revealed structural problems associated with both out-of-plane and in-plane mechanisms.

Concerning out-of-plane failure modes, the typical observed structural deficiencies associated to these mechanisms were: lack of interlocking between orthogonal walls (eg. at building corners) and between pillars and partition walls (Figure 3.1*a*), absence of adequate connections between floors and vertical structural elements, associated with high flexibility and low robustness of timber floors (Figure 3.1*b*), absence of transverse walls, presence of thrusting roofs (Figure 3.1*c*). Particular failure mechanisms were also associated to the seismic behavior of masonry columns in stables and barns (Figure 3.1*d*). In presence of multi-wythes masonry walls, the lack of transversal connections between the wall leaves (sometimes associated to the presence of voids and rubble materials in the cross section of the wall panels), determined out-of-plane collapses, especially when the horizontal structural elements rested on the internal leaf only.

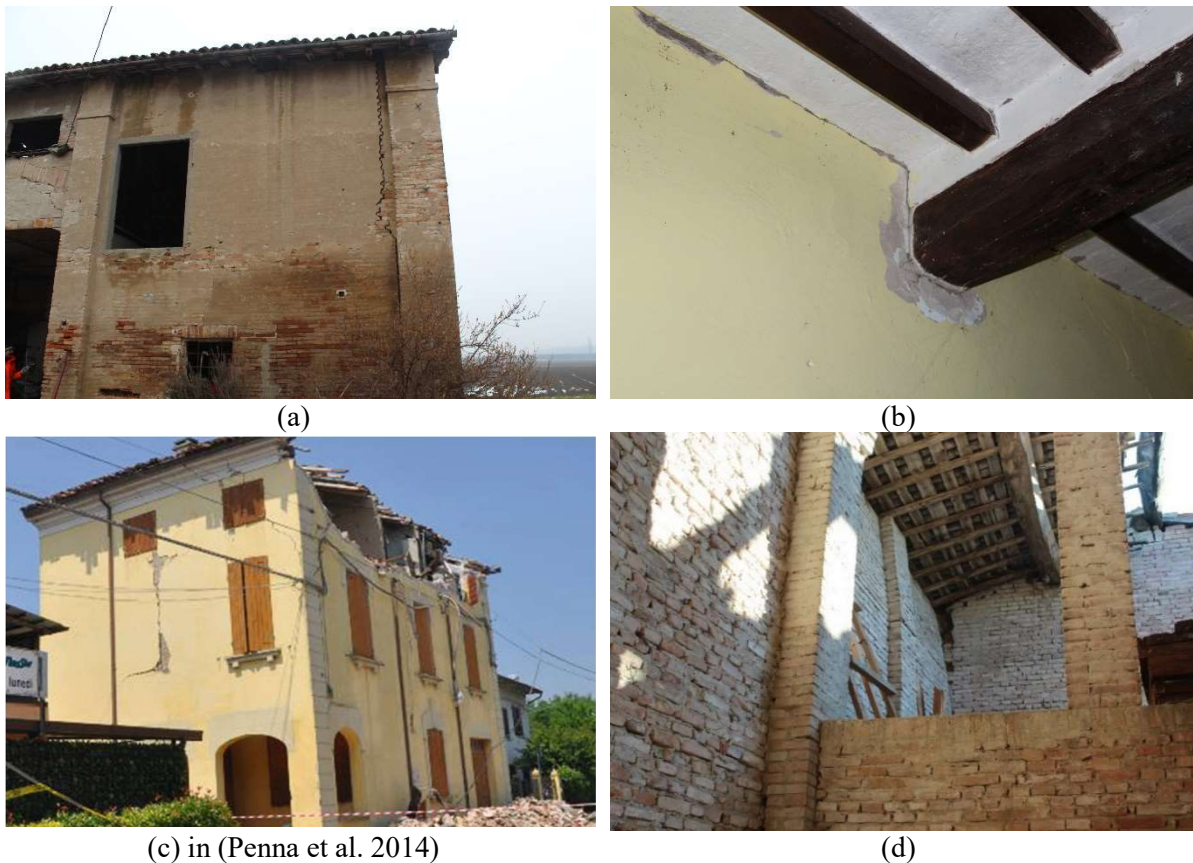


Figure 3.1. Structural deficiencies associated to out-of-plane mechanisms.

Buildings which did not suffer out-of-plane damages, generally exhibited a mainly global behavior governed by the in-plane wall response. The damages associated to in-plane failure mechanisms can be observed especially in piers and spandrels (Figure 3.2*a-b*). Typical diagonal cracks were observed in masonry piers, but also spandrel elements, sometimes considered of secondary importance, appeared to be rather vulnerable and suffered of both flexural and shear damages (Penna et al. 2014). Damages in masonry lintels were also observed (Figure 3.2*c*), which have a strong influence in the global in-plane seismic behavior of façades. Openings positioned too close to the corners of the building (Figure 3.2*d*) strongly weakened the connection between orthogonal walls. Moreover, their vertical misalignment could determine irregular paths for the transfer of the horizontal actions to the foundations.

In-plane failure modes can be usually associated to the quality of masonry, which is strictly connected to the quality of the constituent materials and to the bond pattern. The very low quality of mortars seemed to be a great issue in many cases, since it was often characterized by a low lime content and by a sever degradation (Sorrentino et al. 2014). The use of adobe bricks was also detected in some cases, especially in rural zones, where the use of easily available and poor-quality materials was more frequent (Borri et al. 2013).

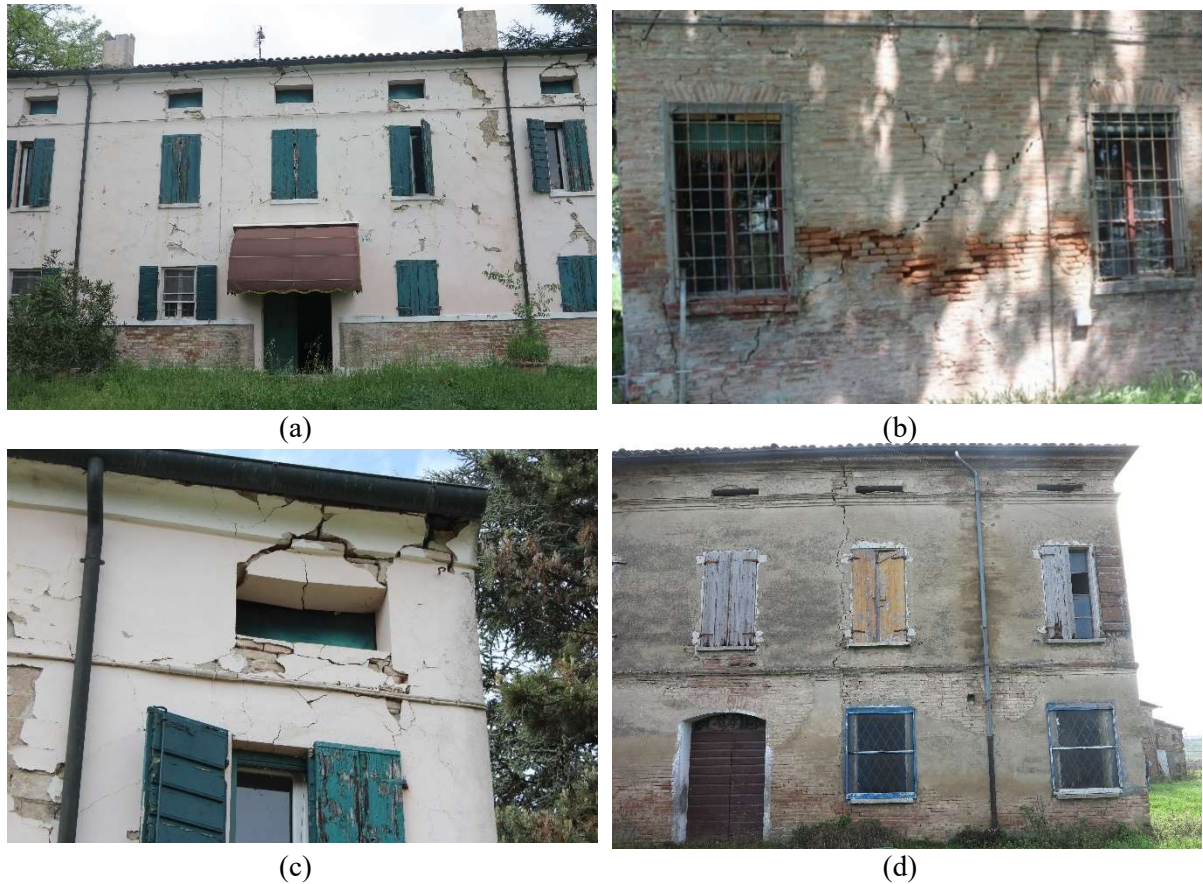


Figure 3.2. Structural deficiencies associated to in-plane mechanisms.

In this framework, being crucial the study of the mechanical properties of masonry structures, an extended in-situ experimental campaign was conducted on rural masonry buildings in the zones most affected by the earthquake. In particular, with the objective of analyzing the shear behavior, slightly-destructive and destructive tests were performed on eight masonry buildings (or portions of them), located in Emilia Romagna region and seriously damaged by the 2012 Emilia earthquake.

In this Chapter, the experimental program will be presented, and the experimental results will be analyzed and discussed. The comparison between the results of the different considered techniques is reported both in terms of obtainable masonry mechanical parameters and of failure criteria that could interpret the observed failure modes.

### 3.1 Experimental Program

The experimental program presented in this Section aimed to investigate the shear behavior and to evaluate the mechanical parameters of rural masonry in Emilia Romagna (Italy). Different types of tests, both slightly-destructive and destructive, were applied on eight rural masonry buildings in order to discuss and compare the results in terms of shear strength. In particular, the sliding shear and the diagonal cracking failure modes were considered and in depth analyzed.

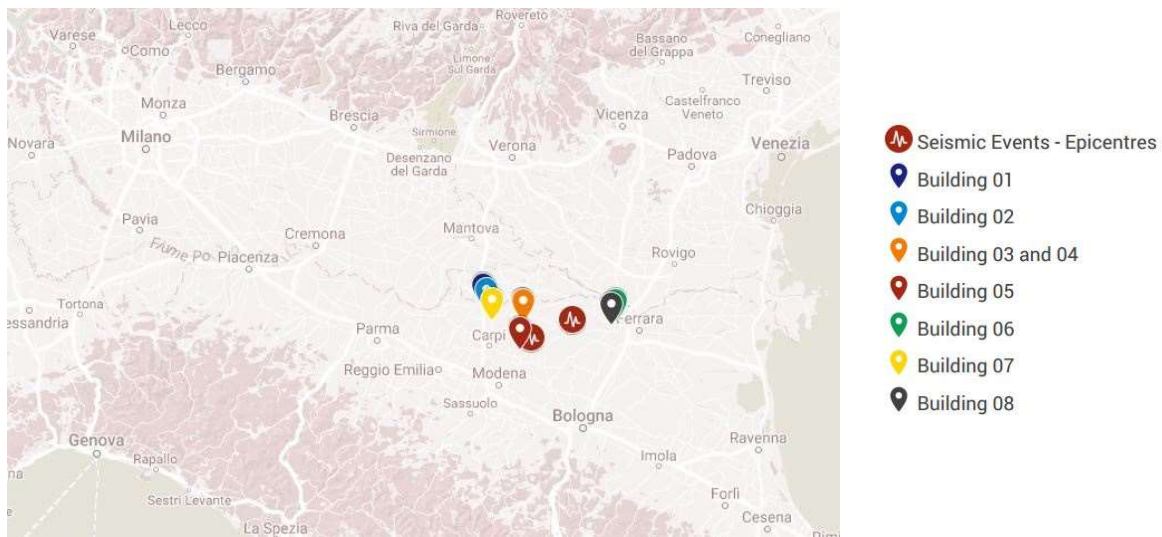


Figure 3.3. Location of the investigated buildings.

The eight buildings were located in the rural area of the provinces of Ferrara, Modena and Reggio Emilia, the areas most affected by the seismic events (Figure 3.3). These buildings (numbered from 01 to 08) had similar characteristics and, in general, a simple configuration, consisting of rectangular or square plan and two or three floors above ground (Figure 3.4). The vertical structural elements were double-wythe, brick-masonry walls, with or without transversal connections (“diatoni”). The walls were characterized by the frequent presence of irregular bricks and by the use of poor-quality, lime-based mortars, sometimes containing traces of clay. The state of conservation of the materials was found to be very different from building to building and from wall to wall as well. The different exposition of the walls, indeed, played a crucial role in the mortar degradation, as observed during the experimental campaign, where the walls facing North experienced the highest materials degradation.



Figure 3.4. Investigated masonry buildings.

The investigated buildings, were severely damaged and intended to be demolished, thus a huge number of experimental tests could be executed, as reported in Table 3.1. In particular, as slightly-destructive techniques, shove tests and splitting tests on cores with inclined mortar joints were chosen and diffusely applied throughout the constructions; as destructive

techniques, diagonal compression and shear-compression tests were executed. On each building, one diagonal compression and one shear-compression tests were performed on masonry panels belonging to the same wall or, if not possible, having at least similar characteristics in terms of texture and constituent materials. A total of about 200 slightly-destructive tests and of 16 destructive tests were conducted.

Table 3.1. Number of performed tests.

Building Code	Splitting tests on cores	Shove tests	Diagonal compression test (CD)	Shear-compression test (NT)
B01	34	5	1	1
B02	18	6	1	1
B03	25	5	1	1
B04	14	2	1	1
B05	20	6	1	1
B06	13	6	1	1
B07	8	8	1	1
B08	14	6	1	1

The planning phase, through which define locations of the tests, was essential for the efficacy of the experimental program. For each building, initially the walls subjected to destructive tests were accurately selected, avoiding already damaged walls or modified ones. Then, the slightly-destructive tests were performed in portions of them or in adjacent walls with similar characteristics. As an example, the locations of the tests conducted on building B01 are shown in Figure 3.5, where two internal walls were selected for destructive tests (CD and NT) and cores were extracted from the same walls. Moreover, extraction of cores and shove tests were conducted in the external walls of the building to evaluate the homogeneity of the masonry throughout the construction.

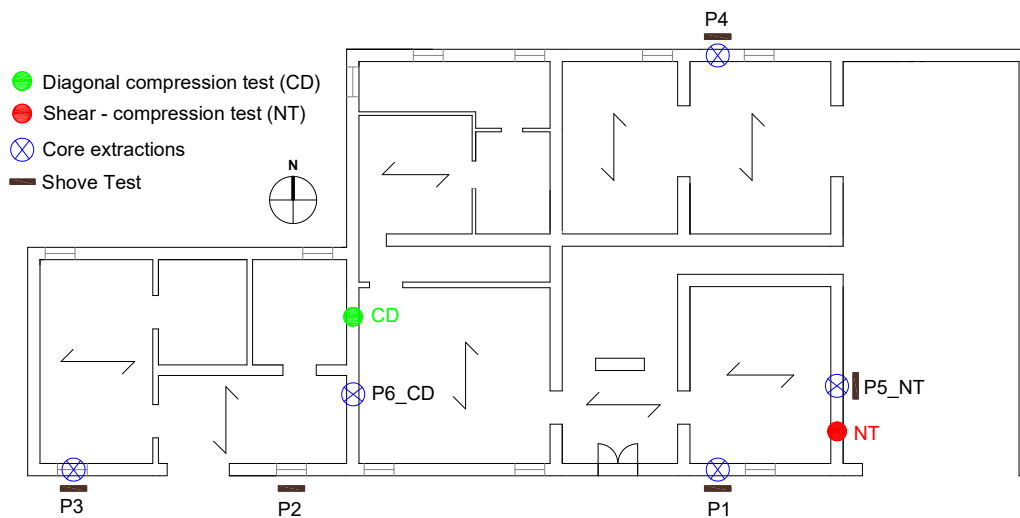


Figure 3.5. Location of the experimental tests, building B01.

In the followings, the interpretation of the different types of tests, together with the failure modes observed, will be discussed and compared with the aim of providing indications on the use of the most appropriate shear failure criteria based on the test typologies. A brief review of these criteria has been already presented in Section 1.2, highlighting their main features with the objective of determining their ability to describe the shear behavior experimentally identified. Indeed, the aim of the experimental campaign is to build a failure domain for the masonry walls of each building investigated, starting from the results of the slightly-destructive tests and the destructive tests. On the one hand, a failure domain describing the sliding failure mode is built based on the results of the splitting tests on cores and the shove tests. On the other hand, a failure criterion describing the diagonal cracking failure mode is built starting from the result of the diagonal compression test. Then, the reliability of the latter calibrated failure criterion is evaluated by taking into account the result of the shear-compression test.

### 3.2 Slightly-destructive tests

With regards to the shear-sliding behavior of masonry, two types of slightly-destructive tests were performed to calibrate a Mohr-Coulomb's criterion for the masonry typologies of the investigated buildings. In particular, splitting tests on masonry cores with inclined mortar joint and shove tests were performed. Cores were extracted from the bearing walls of the investigated buildings and then tested in laboratory (Figure 3.6a). The shove test, instead, was directly executed in situ (Figure 3.6b).

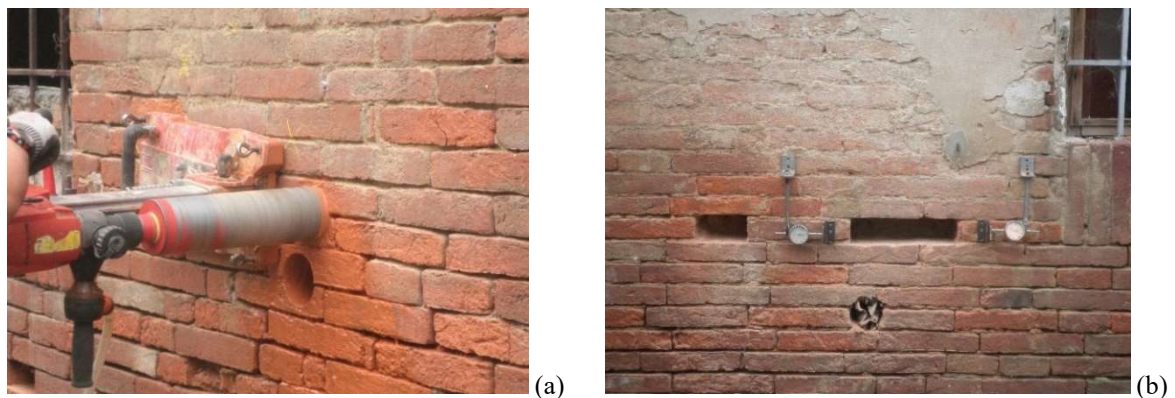


Figure 3.6. Slightly-destructive tests: (a) core extraction; (b) preparation for the shove test.

#### 3.2.1 *Splitting test on masonry cores with inclined mortar joint*

In the experimental campaign, the splitting tests were conducted on masonry cores with a 100-mm diameter. They were properly drilled so to obtain a central diametric mortar layer, avoiding vertical joints. According to the testing procedure, described in detail in Section 2.1.3, the cores

were tested with mortar layer inclinations equal to 45°, 50° and 55° and the corresponding failure states of stress were evaluated:

$$\sigma_{f,c} = \frac{F_{\max}}{A} \cdot \cos \alpha \tag{3.1}$$

$$\tau_{f,c} = \frac{F_{\max}}{A} \cdot \sin \alpha , \tag{3.2}$$

In the data elaborations, the results for each inclination were analyzed and their mean value was estimated with the aim to define a failure criterion suitable for each selected building. In order to obtain a statistical estimation of the mean values for the three inclinations, a significant number of cores were tested for each building, as reported in Table 3.1.

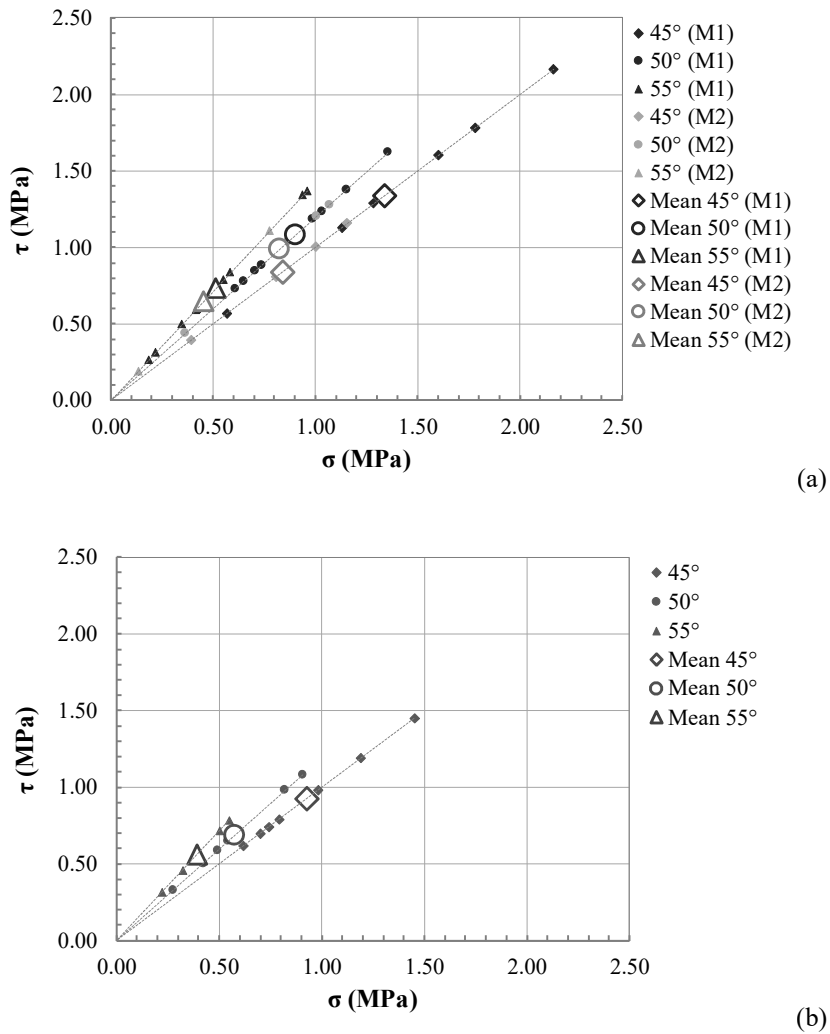


Figure 3.7. Splitting test on masonry cores with different mortar layer inclinations: (a) building B01; (b) building B02.

After the initial visual inspections, in some of the buildings different masonry typologies were identified. The differences observed were mainly associated to the age, degradation and exposition of the materials (e.g. walls facing North). In these cases, mean values for each masonry typology were calculated. In general, one or two masonry typologies (denoted in the followings as M1 and M2) were identified in a single building. As an example, in Figure 3.7 the results of the splitting tests performed on buildings B01 and B02 are reported, together with the mean values calculated for each inclination. In B01, two distinct masonry typologies were identified, while B02 was characterized by a unique masonry type. Despite the distinction of two masonry typologies for B01, the high scatter of experimental results can be graphically observed.

### 3.2.2 Shove test

The shove test was performed in the experimental campaign according to *Method B* proposed in the Standard (ASTM C1531-16). As reported in Section 2.1.2, in order to seat the horizontal hydraulic jack, a single masonry block adjacent to the test unit was removed. On the opposite side, a portion of brick was also removed to be sure that the test unit was free to move.

The shove tests were conducted on masonry portions representative of the state of conservation of the building, with different level of compressive stress acting – e.g. at the ground floor (maximum stress - Figure 3.8a) or below openings (almost zero vertical stress - Figure 3.8b). During the test, the horizontal displacements of both the test unit and the brick behind the jack were measured.



Figure 3.8. Shove test: (a) at ground floor (max vertical stress); (b) below window openings (zero vertical stress)

According to the standard interpretation of the test, the shear strength  $\tau_{f,s}$  can be calculated from the maximum horizontal force  $F_{max}$  resisted by the test unit:

$$\tau_{f,s} = \frac{F_{max}}{A_b}, \quad (3.3)$$

where  $A_b$  is the gross area of upper and lower bed joints, along which the sliding failure occurs.

Considering the compressive stress acting on the tested brick, estimated through a load analysis or evaluated with a single flatjack test, the couples of values  $(\sigma_{f,s}; \tau_{f,s,max})$  at failure were found not to be compatible with the results from the splitting tests on cores, although the two tests were intended to reproduce the same sliding phenomenon. At the same time, those shear capacities ( $F_{max}$  in Figure 3.9) were attained at very high values of non-linear shear slips, which are hardly compatible with the brittle nature of shear failure. This type of behavior occurred since the low mechanical strength of mortar, together with the uneven thickness of the mortar beds and the dimensions of the aggregates, led to some interlocking effects during the sliding mechanism. Therefore, the reaching of very high values of the failure loads could be associated to a dilatant behavior of masonry. For these reasons, a different interpretation of the results from the shove test is here proposed: the onset of the shear failure is attained with a force value smaller than the maximum ever reached during the test. In particular, the shear capacity is assumed to be equal to the force  $F_{sliding}$  in correspondence of which the  $F$ - $\delta$  curve deviates from the initial pseudo-elastic branch (Figure 3.9). After that point, crack propagation can be observed with a macroscopic sliding taking place. The couples of stresses  $(\sigma_{f,s}; \tau_{f,s,slide})$  so determined can be represented as single points in the Mohr plane.

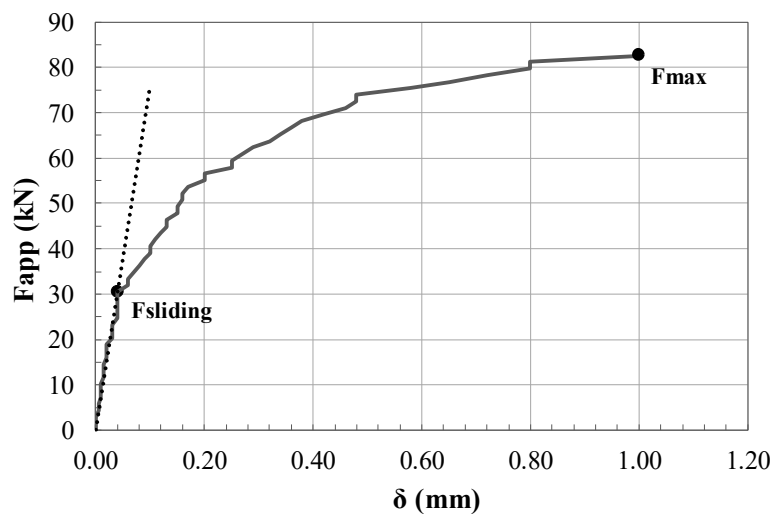


Figure 3.9. Shove test: load-displacement curve with the identification of the first sliding load.

### 3.2.3 Calibration of Mohr-Coulomb's failure domain through slightly-destructive test results

In order to define the failure domain for the masonry typologies of a single building, the results of the shove tests and the splitting tests on cores with inclined mortar joint (Table 3.2 and Table 3.3) are here used together. Concerning the splitting tests, the mean value for each inclination angle was determined, as already explained in Section 3.2.1, excluding the results of few tests in which the cores failed with a mechanism different from sliding.

Table 3.2. Slightly-destructive tests: results and Mohr-Coulomb's failure domain parameters, buildings B01-B04.

Building	Masonry Typology	Test Type	N° of tests	$\sigma_f$ (MPa)	$\tau_f$ (MPa)	$c$ (MPa)	$\mu$	$R^2$	
B01	M1	Cores (45°)	7	1.34	1.34	0.28	0.83	0.99	
		Cores (50°)	8	0.91	1.08				
		Cores (55°)	9	0.52	0.74				
		Shove Test	3	0.08	0.35				
				0.09	0.38				
	M2				0.09	0.29			
		Cores (45°)	4	0.84	0.84	0.16	0.93	0.96	
		Cores (50°)	4	0.83	0.99				
		Cores (55°)	2	0.46	0.65				
		Shove Test	2	0.00	0.10				
		0.00	0.19						
B02	M1	Cores (45°)	7	0.92	0.92	0.26	0.71	0.92	
		Cores (50°)	6	0.58	0.69				
		Cores (55°)	5	0.39	0.56				
		Shove Test	6	0.10	0.26				
				0.09	0.40				
			0.00	0.35					
			0.00	0.32					
			0.07	0.24					
			0.08	0.23					
	B03	M1	Cores (45°)	3	0.55	0.55	0.19	0.73	0.91
Cores (50°)			3	0.53	0.63				
Cores (55°)			3	0.20	0.28				
Shove Test			2	0.11	0.32				
M2					0.13	0.28			
		Cores (45°)	6	0.48	0.48	0.08	0.93	0.86	
		Cores (50°)	5	0.35	0.42				
		Cores (55°)	5	0.34	0.49				
Shove Test	3	0.00	0.09						
		0.10	0.05						
		0.00	0.15						
B04	M1	Cores (45°)	5	0.60	0.60	0.11	0.91	0.96	
		Cores (50°)	4	0.53	0.64				
		Cores (55°)	5	0.28	0.40				
		Shove Test	2	0.14	0.21				
				0.11	0.20				

Table 3.3. Slightly-destructive tests: results and Mohr-Coulomb's failure domain parameters, buildings B05-B08.

Building	Masonry Typology	Test Type	N° of tests	$\sigma_f$ (MPa)	$\tau_f$ (MPa)	$c$ (MPa)	$\mu$	$R^2$	
B05	M1	Cores (45°)	3	1.15	1.15	0.18	0.90	0.92	
		Cores (50°)	5	0.67	0.80				
		Cores (55°)	4	0.58	0.83				
		Shove Test	3	0.03	0.36				
				0.00	0.05				
	M2				0.14	0.20	0.23	0.88	0.92
		Cores (45°)	3	1.04	1.04				
		Cores (50°)	2	0.81	0.97				
		Cores (55°)	3	0.74	1.05				
		Shove Test	3	0.13	0.22				
B06	M1			0.00	0.31	0.05	0.80	0.88	
				0.13	0.33				
		Cores (45°)	5	0.30	0.30				
		Cores (50°)	4	0.23	0.28				
		Cores (55°)	4	0.15	0.21				
	M2	Shove Test	6	0.18	0.15	0.45	0.71	0.87	
				0.09	0.12				
				0.00	0.04				
				0.17	0.16				
				0.17	0.18				
B07	M1			0.00	0.08	0.45	0.71	0.87	
				0.15	0.63				
				0.15	0.31				
		Cores (45°)	4	1.18	1.18				
		Cores (50°)	1	1.07	1.27				
	M2	Cores (55°)	1	0.75	1.07	0.11	0.09	0.05	
		Shove Test	3	0.00	0.55				
				0.15	0.63				
				0.15	0.31				
				-	-				
B08	M1	Cores (45°)	-	-	-	0.00	0.82	0.82	
		Cores (50°)	1	0.13	0.15				
		Cores (55°)	1	0.12	0.18				
		Shove Test	5	0.37	0.14				
				0.23	0.15				
	M2				0.18	0.05	0.13	0.69	0.75
					0.19	0.13			
					0.00	0.09			
		Cores (45°)	3	0.04	0.04				
		Cores (50°)	1	0.01	0.01				
M2	Cores (55°)	-	-	-	0.13	0.69	0.75		
	Shove Test	3	0.14	0.12					
			0.11	0.12					
			0.10	0.06					
			0.23	0.23					
		0.27	0.32						
		0.25	0.36						
		0.04	0.16						
		0.01	0.20						
		0.00	0.08						

For each building, the points  $(\sigma_f; \tau_f)$  obtained from the slightly-destructive tests at failure can be reported in a  $\sigma - \tau$  plane. With a linear interpolation of the results, the Mohr-Coulomb's failure criterion can be calibrated, thus obtaining the parameters  $c$  and  $\mu$  for each specific masonry typology within the building. In B01, B03, B05, B07, and B08, two distinct masonry typologies were identified and consequently two failure criteria were built. In B02, B04, and B06, instead, the masonry was quite uniform throughout the building, so only one criterion was calibrated. As an example, in Figure 3.10 the results of the slightly-destructive tests and the failure domains obtained for buildings B01 and B02 are reported.

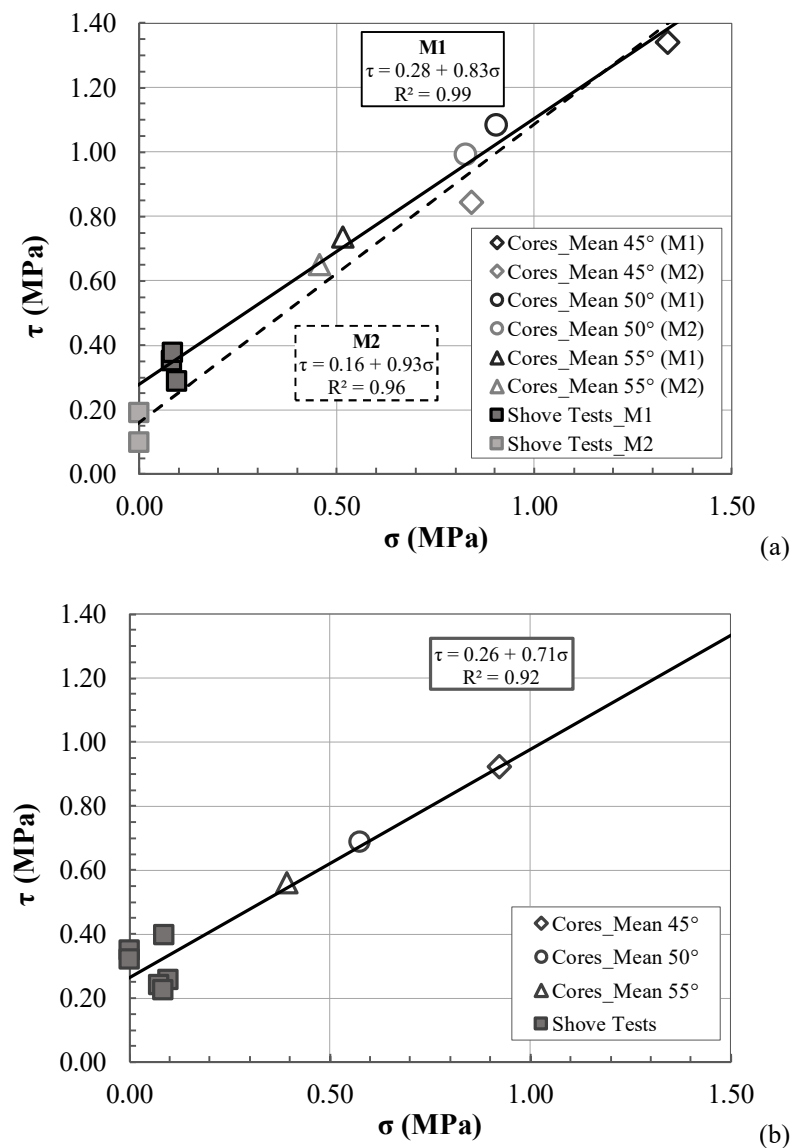


Figure 3.10. Determination of the Mohr-Coulomb's failure domain: (a) building B01, (b) building B02.

Both types of selected tests are fundamental for the determination of the parameters  $c$  and  $\mu$ , since they cover a wide range of possible compressive stress. In particular, given the quite low vertical stress present in situ, the points coming from the shove tests are close to the  $\tau$  axis, while the points obtained from tests on cores are usually characterized by values of  $\sigma$  significantly higher. For these reasons, the results of the shove tests are more representative for what concerns the shear strength without compression (cohesion  $c$ ), while the results of the splitting tests are of great help in order to determine the slope of the domain (friction coefficient  $\mu$ ).

In Table 3.2 and Table 3.3 values of the cohesion  $c$  and the friction coefficient  $\mu$  are reported for each masonry typology, together with the coefficient of determination  $R^2$ . As expected, given the local nature of these tests, a significant difference in the results among the different masonries and different buildings is observed, especially for the cohesion. However, for the single masonry typology, the linear model shows a good match with the experimental results, given the quite high values of the  $R^2$  coefficient (in the range of 0.75-0.99 and higher than 0.90 for more than half of the masonry typologies). A poor correlation was found in building B07 for the M2 masonry typology, partially because only two intact cores were extracted and tested.

Concerning the cohesion  $c$ , very low values were obtained for the masonry typologies B03\_M2, B06\_M1 and B08\_M1, which experienced a severe degradation of the mortars, resulting in the almost complete absence of binder. A very high value of the cohesion was found for B07\_M1, which probably underwent some restoration processes of bed joints in the past years. Intermediate values, still quite scattered (from 0.11 MPa to 0.28 MPa), were obtained for the remaining masonry typologies. It is worth noting that cohesion values higher than 0.20 MPa were obtained only for well-preserved masonries, usually covered by plaster.

Focusing on the friction coefficient  $\mu$ , the obtained values range from 0.69 to 0.93, excluding the non-reliable result of B07\_M2. Differently from the cohesion parameter, it is more difficult to relate the values of the friction coefficient to the masonry quality since the frictional behavior is mainly dependent on the characteristics of the surfaces along which the sliding occurs, i.e. along the areas of adhesion between mortar and bricks or inside the mortar. However, at low compressive stress, a variation of the values of the friction coefficient has a lower influence on the shear strength than a variation of the cohesion values. It should also be highlighted that for all the masonry typologies, the value of the friction coefficient is much greater than the one suggested by the Eurocode and the Italian Code, equal to 0.4.

One of the drawbacks of the splitting tests on cores was the fact that, in some cases, cores could not be tested because they were already detached after the extraction procedure. Thus,

the obtained results from remaining cores could overestimate to some extent the mechanical properties of the masonry typologies since it is impracticable to perform the mean value between results from tested cores and detached ones (not tested).

### 3.3 Destructive tests

With the aim of investigating the diagonal shear failure mechanism of the analyzed rural masonries, two types of destructive tests were performed on full-scale samples: diagonal compression and shear-compression tests. The choice of the appropriate panels to be tested was anything but trivial due to the state of damage and the inhomogeneity of the masonry walls throughout the buildings. Indeed, samples should not present cracks or evident modifications occurred in time (e.g. traces of pre-existing openings) and should be representative of the seismic resistant walls of the building.

#### 3.3.1 Diagonal compression test

In the experimental program, eight diagonal compression tests, one for each building, were carried out on double-wythe masonry walls. The panels, having dimensions 120 x 120 cm<sup>2</sup>, were separated from the surrounding masonry on three sides, while they remained anchored to the rest of the wall, on the fourth side, for approximately 60 cm. The compressive load was applied by means of a 500 kN hydraulic jack positioned on one corner of the panel and interposed between a loading shoe, in contact with the samples, and a steel profile. The steel profile was connected with two steel bars to a similar element on the opposite corner of the panel. The load was applied monotonically up to failure. Linear potentiometers positioned, with a gage length of 120 cm, along the compressed and the tensioned diagonals of the panels, on both sides, allowed the measurements of the diagonal displacements of the samples during the test (Figure 3.11 - Figure 3.12).

The results of the diagonal compression tests, in terms of ultimate load  $P_f$ , failure state of stress and diagonal tensile strength, considering both the ASTM ( $f_{i,CD,ASTM}$ ) and the elastic ( $f_{i,CD,El.}$ ) interpretation, are reported in Table 3.4. The differences in the results are related to the variety of the masonry typologies, which were found to be quite significant even if the buildings belonged to a small geographic area. More in details, two panels, B03\_CD and B07\_CD, showed high capacity while for the panel B02\_CD a very low value of the ultimate load was registered. These differences are related to the quality of the masonry: very good in the first cases while quite poor in the latter case, with special reference to the state of conservation of

the mortar. These remarks were also confirmed by the results of the slightly-destructive tests conducted on the same walls.

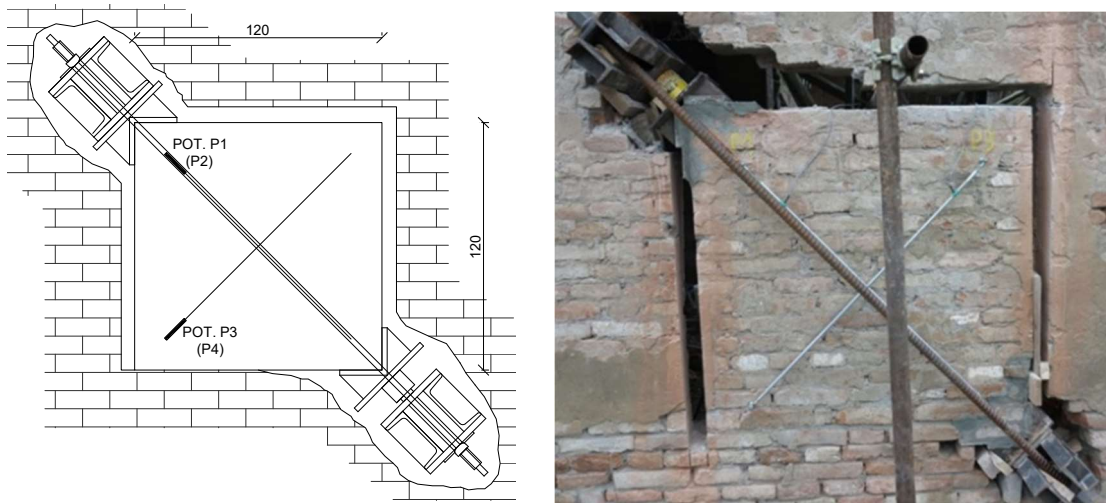


Figure 3.11. Setup of the diagonal compression test.



Figure 3.12. Setup of the diagonal compression test, details.

Table 3.4. Diagonal compression test (CD): results.

Sample code	Masonry Typology	Cross section dimensions (cm <sup>2</sup> )	$P_f$ (kN)	Failure Mode	ASTM interpretation			Elastic interpretation		
					$\sigma_{f,CD}$ (MPa)	$\tau_{f,CD}$ (MPa)	$f_{t,CD,ASTM}$ (MPa)	$\sigma_{f,CD}$ (MPa)	$\tau_{f,CD}$ (MPa)	$f_{t,CD,El.}$ (MPa)
B01_CD	M2	120 x 35	34.0	M	0.00	0.06	0.06	0.05	0.09	0.04
B02_CD	M1	120 x 32	15.2	M	0.00	0.03	0.03	0.02	0.04	0.02
B03_CD	M1	120 x 30	119.8	M	0.00	0.24	0.24	0.19	0.35	0.17
B04_CD	M1	120 x 29	63.4	M	0.00	0.13	0.13	0.10	0.19	0.09
B05_CD	M1	120 x 31	73.1	M	0.00	0.14	0.14	0.11	0.21	0.10
B06_CD	M1	120 x 28	47.5	M	0.00	0.10	0.10	0.08	0.15	0.07
B07_CD	M1	120 x 27.5	210.0	B	0.00	0.45	0.45	0.36	0.67	0.32
B08_CD	M2	120 x 27	41.9	M	0.00	0.09	0.09	0.07	0.13	0.06

The load - mean diagonal deformations curves are reported in Figure 3.13 for all the tested panels: elongations are considered positive. A similar behavior can be found along the two

diagonals until the applied force is small. Then, elongations, as expected, increase more and faster due to the opening of cracks. As a general remark, a more evident nonlinear behavior can be noticed for panels made of poor-quality materials, which also showed a larger peak deformation. In most cases, panels did not experience a fragile collapse: after the diagonal cracking and the reaching of the peak load, they did not completely lose their bearing capacity and, in some tests, a load increase was registered. This behavior can be explained considering that after the crack development (peak), and the correspondent drop in the load bearing capacity, the wall self-weight produced residual strength through frictional sliding mechanisms.

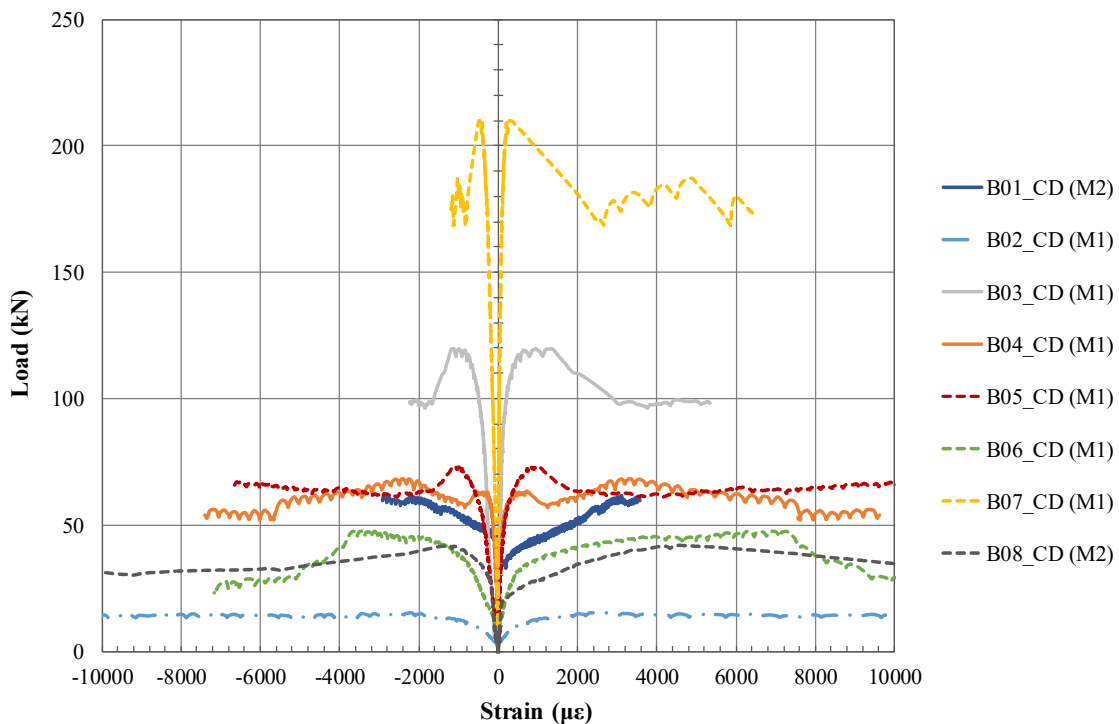


Figure 3.13. Diagonal compression test: mean diagonal deformations.

The typical failure modes of the masonry panels, presented in Figure 3.14 for three buildings only, were generally characterized by the appearance of a crack along the compressed diagonal. The crack, which started from the center of the panel and then propagated towards the corners, involved mainly the mortar joints (failure mode *M*), thus confirming the poor quality of the mortar with respect to bricks. The only panel showing a different behavior was B07\_CD, in which the tensile failure of few bricks along the compressed diagonal was observed (failure mode *B*). This can be attributed, as already noticed, to the good quality of the mortar.

Since the “stair-stepped crack path” (failure mode *M* in Figure 3.14) was activated by a splitting mechanism along the diagonal under traction (onset of cracking), it seems consistent to consider the failure (peak load) driven by the reaching of the tensile strength of the material

in the center of the sample. Therefore, in the followings, the value of the diagonal tensile strength here obtained will be used to calibrate the Turnšek and Čačovič's failure domain for each building, according to Eq. (1.2). The diagonal tensile strength is, indeed, the only mechanical parameter needed to set this criterion. The different interpretations of the test (ASTM and elastic) will be both considered in Section 3.4, where the failure criteria calibrated for each building will be presented.

Sample code	Failure Mode	Detail of the crack
B04_CD (Failure Mode <i>M</i> )		
B05_CD (Failure Mode <i>M</i> )		
B07_CD (Failure Mode <i>B</i> )		

Figure 3.14. Diagonal compression test: failure modes.

### 3.3.2 Shear-compression test

In the experimental campaign, eight shear-compression tests were conducted, one for each investigated building. In particular, tests were performed according to both the setups presented in Section 2.2.2: *Setup A* (Figure 3.15) for buildings B01 and B02 and *Setup B* (Figure 3.16) for the other buildings. A compressive load was directly applied at the top of the panels in *Setup A*, while the compressive stress level was only estimated for *Setup B*. In both cases, the shear load was applied in the center of the panels by means of a 500 kN hydraulic jack positioned in between two steel profiles, one acting as a contrast and in contact with the masonry, the other connected, by means of two steel bars, with another steel profile positioned in correspondence of the center line of the panels. During the test, the diagonal displacements in the upper and lower halves of the panels were measured using 8 linear potentiometers. The horizontal in-plane displacements, instead, were measured by means of 6 linear variable displacement transducers (LVDT) positioned, on each side, in correspondence of the upper, lower and central cross sections of the samples.

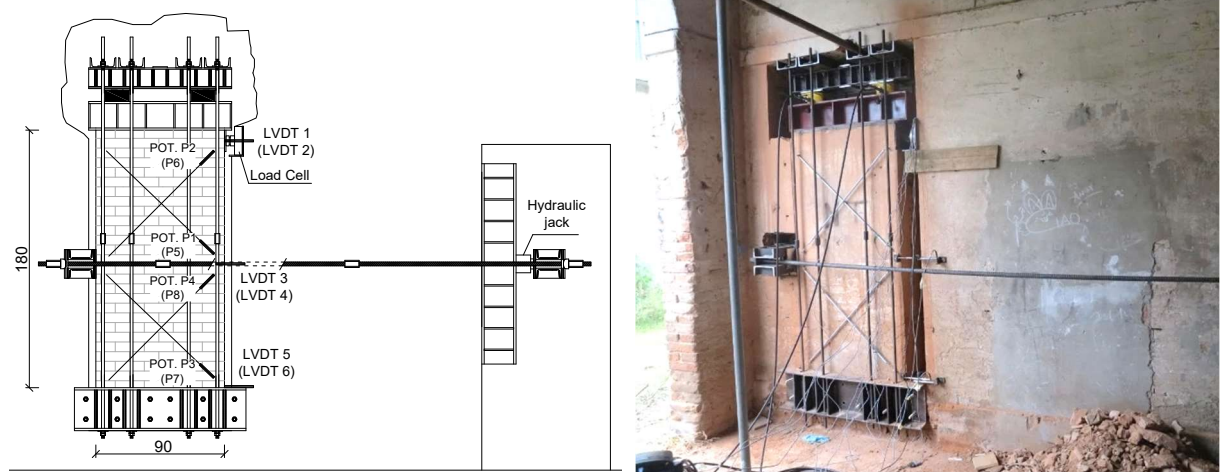


Figure 3.15. Shear-compression test: Setup A.

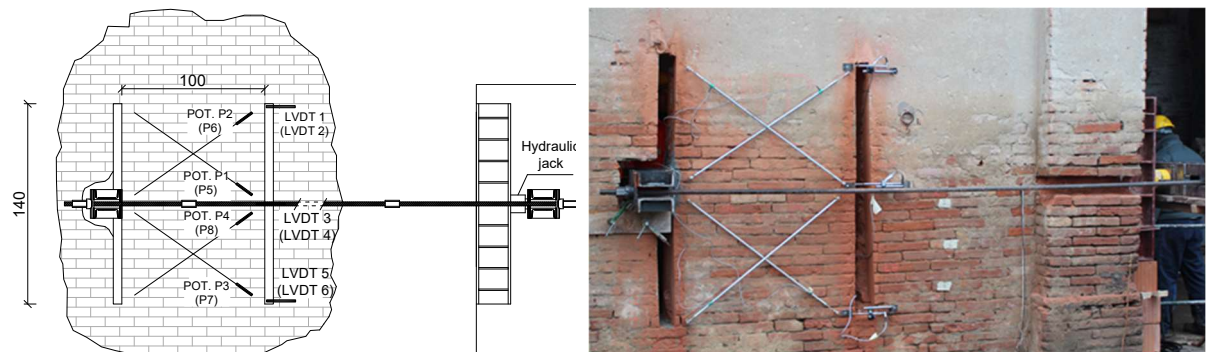


Figure 3.16. Shear-compression test: Setup B.

In addition to the differences regarding the boundary conditions and the level of compressive stress applied, also the geometry of the samples changed in the two setups. More in details, the size of the panels was chosen to be equal to 90 x 180 cm<sup>2</sup> in *Setup A* and to 100 x 140 cm<sup>2</sup> in *Setup B*. On the one hand, the dimensions of the samples in *Setup A* are the most common ones proposed in literature. On the other hand, the modified geometry in *Setup B* was chosen to reduce the slenderness of the panels in order to induce a proper diagonal shear failure and to avoid the flexural one, given the very low value of actual compressive stress (0.10-0.20 MPa).

The results of the shear compression tests are reported in Table 3.5 in terms of mean vertical and shear stresses at failure ( $\sigma_{f,NT}; \tau_{f,NT}$ ). It can be observed that, except from buildings in which *Setup A* was used, the values of the estimated compressive stress acting on the panel were quite low (in the range of 0.13 MPa – 0.22 MPa) since buildings had usually one or two floors only. The choice of the value of the compressive stress to be applied in tests with *Setup A* (approximately equal to 0.3 MPa) was made in order to give a vertical load comparable to the one present in situ (service life), but not too low, so to induce a diagonal cracking shear failure.

Table 3.5. Shear-compression test (NT): results.  
(FF: Flexural Failure, DSF: Diagonal Shear Failure)

Sample code	Masonry Typology	Cross section dimensions (cm <sup>2</sup> )	$\sigma_{f,NT}$ (MPa)	$\tau_{f,NT}$ (MPa)	Failure Mode
B01_NT_A	M1	90 x 35	-	-	FF
B02_NT_A	M1	90 x 32	0.34	0.30	FF-DSF
B03_NT_B	M1	100 x 15	0.21	0.35	DSF
B04_NT_B	M1	100 x 29	0.13	0.30	DSF
B05_NT_B	M1	100 x 32	0.14	0.34	DSF
B06_NT_B	M1	100 x 30	0.17	0.25	DSF
B07_NT_B	M2	100 x 29	0.22	0.09	DSF
B08_NT_B	M1	100 x 31	0.14	0.14	DSF

In Figure 3.17 the typical failure modes observed for the masonry panels are reported, for both the setups. It has to be highlighted that in shear-compression tests with *Setup A* (B01\_NT\_A and B02\_NT\_A) a flexural behaviour was observed, with the appearance of a horizontal crack in the central cross section of the sample. In the test B01\_NT\_A, after the first cracking, the specimen was unloaded and reloaded in shear with an increased value of the compressive stress applied (up to 0.67 MPa). Despite this, the desired shear failure was not obtained. The results of this test, therefore, are not included in further discussions. Instead, in the test B02\_NT\_A, after the horizontal cracking, the panel continued to carry the shear load until the formation of

an inclined crack in the lower half of the panel. Because of the flexural behaviour observed during these two tests and the uncertainties on the level of constraint at the top, it was decided to change the geometry of the panels and to perform shear-compression tests with *Setup B*. With this change, the observed failure modes were characterized by the presence of diagonal cracks, both in the upper and lower half-panels (Figure 3.17). These cracks developed along the compressed diagonals and ran mainly through mortar joints, given the poor-quality of mortars already observed in the diagonal compression tests. Focusing on the details in Figure 3.17, differently to what happened in the diagonal compression tests, along the surface of the cracks only a horizontal displacement occurred.

Sample code	Failure Mode	Detail of the crack
B01_NT_A (Flexural Failure)		
B02_NT_A (Mixed Failure)		
B04_NT_B (Diagonal Shear Failure)		

Figure 3.17. Shear-compression test: failure modes.

The mean diagonal deformations registered during the tests in the lower half of the panels are presented in Figure 3.18, with elongations considered positive. In general, also in this case, it can be observed that the deformations, in tension and in compression, are comparable in the first part of the tests. Then, the elongations become higher because of the cracking of the specimens. For the sample B01\_NT\_A the diagonal deformations are very low, confirming the predominant flexural behaviour of the panel. In Figure 3.19, the corresponding shear stress vs slip curves are presented. As also evidenced from the diagonal compression tests, the nonlinear behavior of the samples was quite apparent and, in most cases, failure was not so fragile. Furthermore, it can be observed that at higher compressive stresses do not always correspond higher ultimate loads due to the differences of the masonry quality among the investigated typologies.

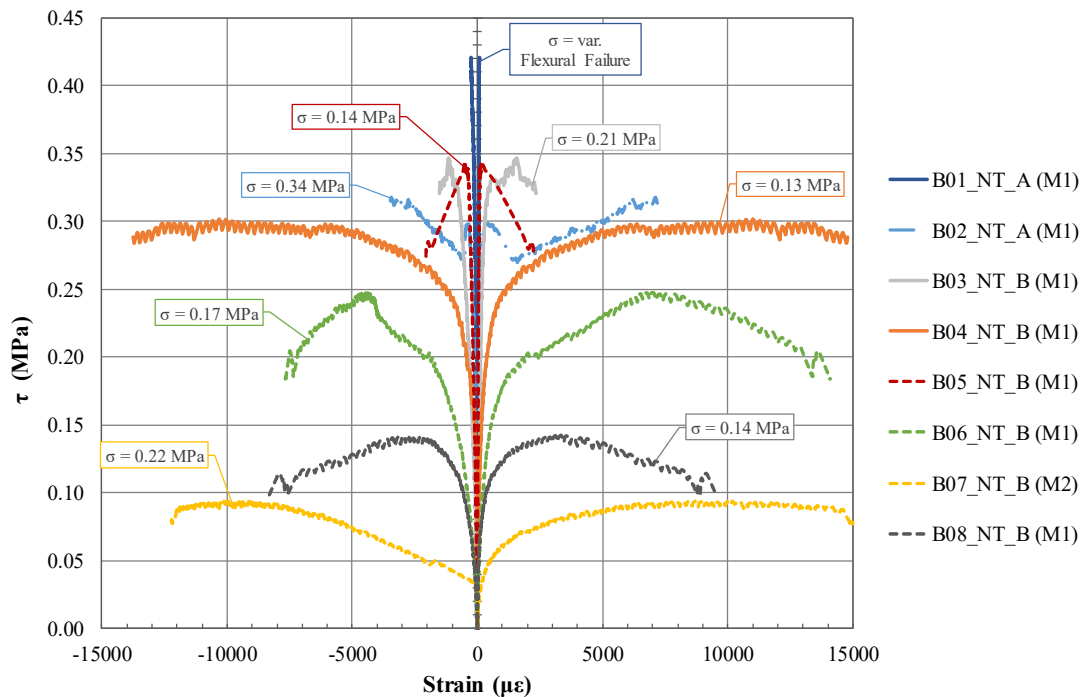


Figure 3.18. Shear-compression test: mean diagonal deformations in the lower half of the masonry panel.

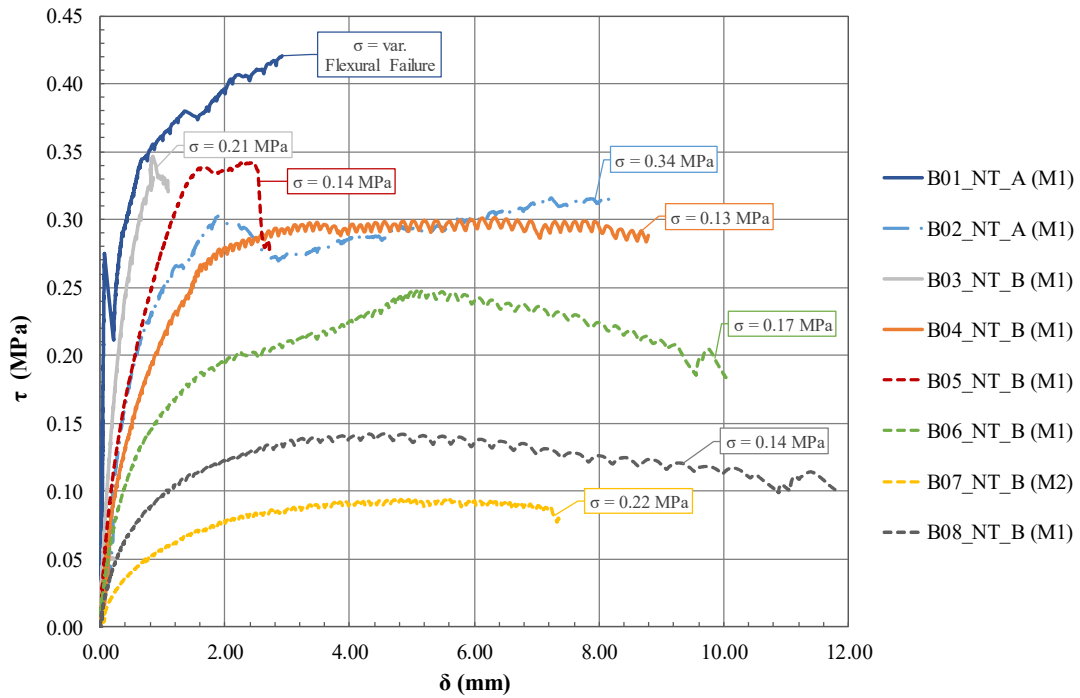


Figure 3.19. Shear-compression test: shear stress vs horizontal displacement in the lower half of the masonry panel.

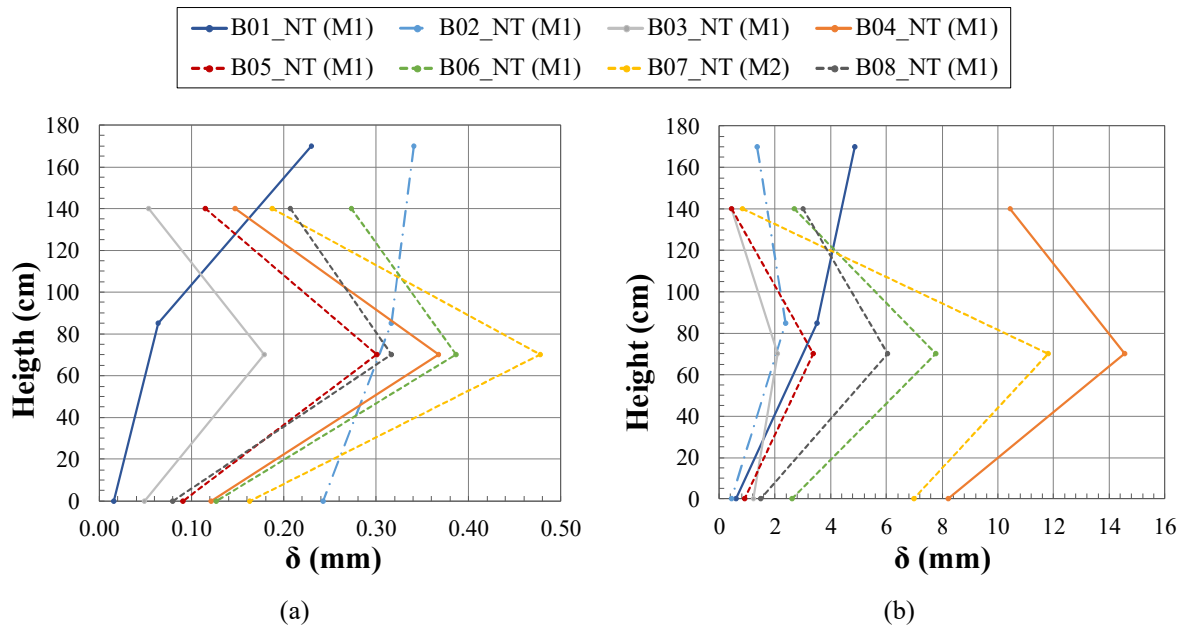


Figure 3.20. Shear-compression test - Deformed shapes of the panels: (a) elastic phase; (b) maximum load.

Considering the absolute displacements measured by the LVDTs, the deformed shapes of the samples in the first pseudo-elastic phase (at approximately 1/3 of the ultimate load) and in correspondence of the peak load are represented in Figure 3.20. The trend of the majority of the curves confirms the symmetric behaviour of upper and lower panels for the entire duration of

the test and validates the assumption of the structural scheme considered in *Setup B*. For the panel B01\_NT\_A and B02\_NT\_A, instead, the deformed shapes in the elastic phase evidence the issues already highlighted regarding the level of constraint at the top of the panel. However, at the maximum load, the sample B02\_NT\_A shows an almost symmetric deformed shape, probably consistent with the transition from flexural to shear failure observed during the test.

### 3.4 Discussion on the calibrated failure criteria

The objective of this section is to analyze the different failure criteria available and calibrated with slightly-destructive tests or diagonal compression tests results, and to check their agreement with the experimental results coming from the shear-compression tests. The failure domains obtained by slightly-destructive tests and diagonal compression tests will be analyzed separately and then compared when referred to the same type of masonry. Due to the variability of the masonry constructions, observed during the in-situ inspections and confirmed also by the experimental results, the buildings will be analyzed one by one.

In Figure 3.21, the failure criteria selected for describing the behavior observed during the tests are reported in a  $\sigma - \tau$  plane for each building. In Figure 3.21f two Mohr-Coulomb's failure domains are reported (M1 and M2), corresponding to the two masonry types characterizing walls where destructive tests were conducted (CD and NT respectively). Together with the Mohr-Coulomb's criterion, the Turnšek and Čačovič's failure domains are also reported and the Mann and Müller's criterion is introduced. Data from buildings B01 and B07 are not presented. Indeed, no conclusions can be drawn for these buildings since a shear failure was not obtained in the shear-compression test for B01 and in B07 the quality of the panels in the two destructive tests was not comparable at all.

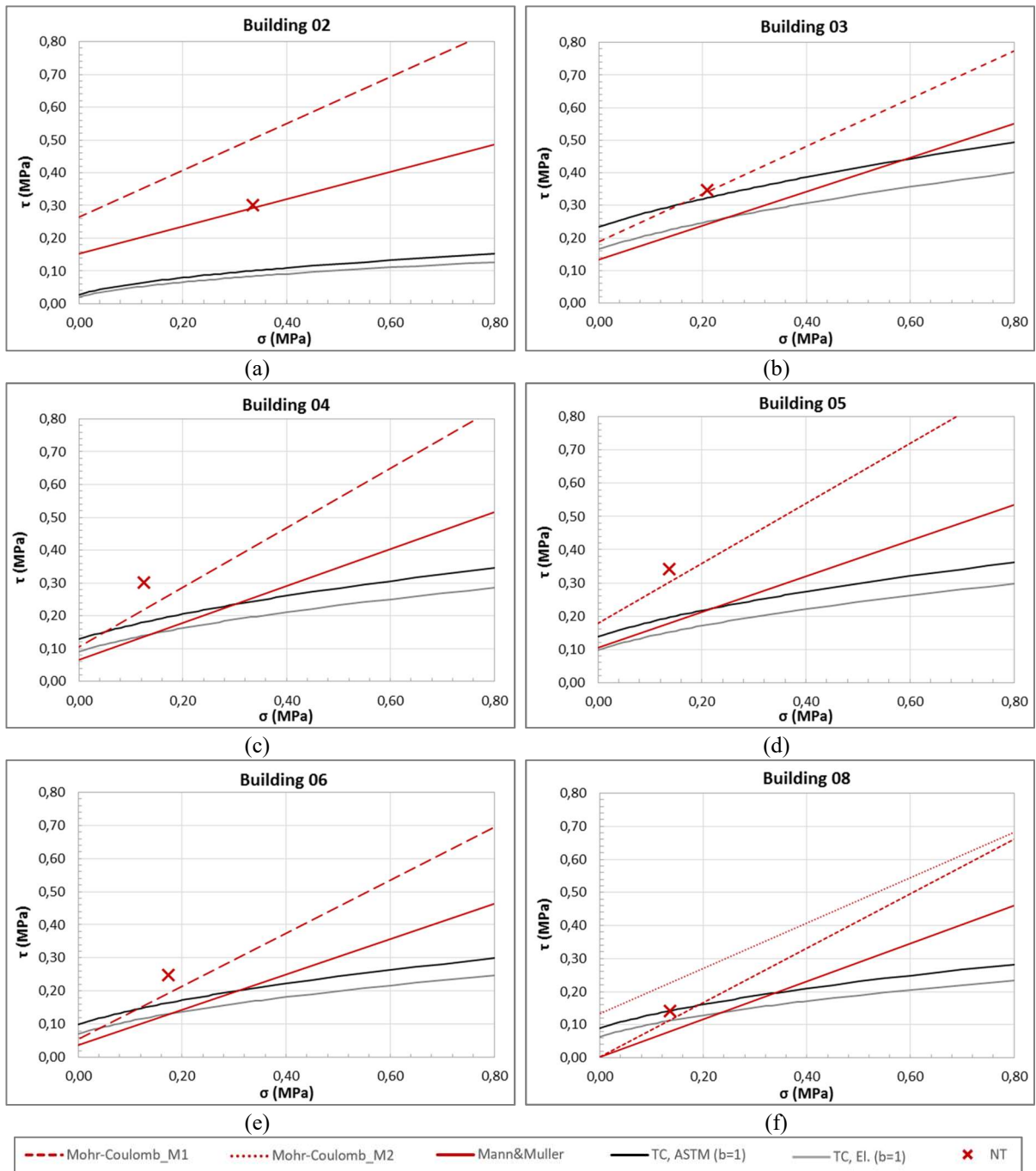


Figure 3.21. Comparison of failure criteria for the investigated buildings.

### 3.4.1 Mohr-Coulomb's failure criterion from slightly-destructive tests

The Mohr-Coulomb's failure criterion has confirmed to be a good model for the interpretation of the results coming from the shove tests and the splitting tests on cores, since it describes a sliding behavior which is the one observed during both the tests. More in details, the combination of the results of the two slightly-destructive tests and the alternative interpretation used for the shove test helped in obtaining reliable strength parameters. The drawbacks of using these slightly-destructive techniques for the calibration of the model are: (i) the need of

performing a great number of tests in order to get reliable results; (ii) the fact that the weakest cores, already split into two parts after the extraction procedure, are not tested and are excluded in the elaboration of the data, thus leading to a possible overestimation of the parameters  $c$  and  $\mu$  because of the use of the strongest cores only for their evaluation.

### 3.4.2 Turnšek and Čačovič's failure criterion for destructive tests

For the calibration of the Turnšek and Čačovič's failure criterion, the first issue to deal with is related to the different interpretations of the state of stress in the diagonal compression test, presented in Section 2.2.1. Some drawbacks of the two interpretations should be highlighted: on the one hand, the elastic interpretation is based on assumptions – isotropic, linear, elastic masonry – which may not be suitable in case of strong nonlinear behavior of the material, observed in the tests; on the other hand, the ASTM interpretation could not adequately describe the actual stress state during the test. In this work, both interpretations were used to estimate the tensile strength  $f_{l,CD,ASTM}$  and  $f_{l,CD,EL}$ , respectively, and the value of the parameter  $b$  was set equal to 1 according to the proposal of Benedetti and Tomažević (1984). The two curves are reported for each type of masonry in Figure 3.21, where a reduced difference between them can be found with respect to the distance from the results of the shear-compression tests. Nevertheless, it can be noticed how the point  $(\sigma_{f,NT}; \tau_{f,NT})$  from the shear-compression test (NT) is closer to the Turnšek and Čačovič's criterion calibrated with  $f_{l,CD,ASTM}$  and  $b=1$ , and almost aligned with it for building B03. In many cases, the distance between the shear-compression test result and the Turnšek and Čačovič's criterion can be quite significant (independently from the criterion applied). This can be explained bearing in mind, on the one hand, the intrinsic heterogeneity of the masonries, even if belonging to the same masonry typology, and, on the other hand, the differences between the two destructive tests. These differences can be attributed to various aspects: in the diagonal compression test the panel can be considered a free body since it is almost completely detached from the surrounding masonry, while in the shear-compression test it is more restrained. This aspect is consistent with the observed failure modes, one characterized by a splitting failure along the diagonal and the other characterized by a horizontal sliding after the appearance of the fracture. Then, the geometry of the samples, the texture and the state of stress have an influence on the crack inclination and, consequently, on the direction of the principal tensile stress, which is different in the two tests (Figure 3.22). Therefore, the anisotropy of masonry can surely be a further explanation of the differences encountered in the results of the destructive tests here presented. Finally, the stress state at failure is far away from being in the elastic range and this is in contrast with the main hypothesis

of both the elastic interpretation of the diagonal compression test and the Turnšek and Čačovič's formulation. This is especially true for this type of poor masonry.

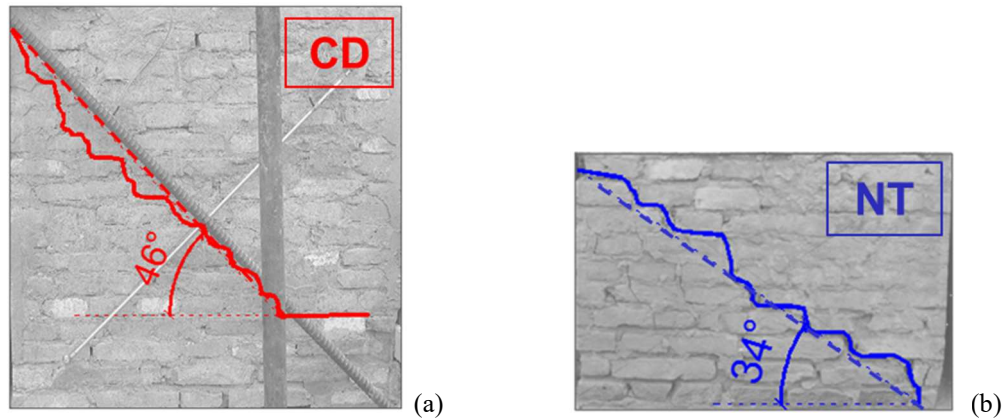


Figure 3.22. Comparison between crack inclinations for building B04: (a) CD test; (b) NT test.

### 3.4.3 Mann and Müller's failure criterion for destructive tests

From the observations on the sliding phenomenon occurred in the shear-compression tests and considering the issues introduced in the previous section, an additional failure criterion is here presented: the Mann and Müller's formulation (Eq. (1.3)). It is based on the evaluation of the “global” parameters of the masonry (Table 3.6), by knowing the values of the “local” parameters obtained from slightly-destructive tests (Table 3.2 and Table 3.3) and of the coefficient  $\varphi$  (Eqs. (1.4) and (1.5)). Even if the texture of masonry was quite regular, in the present case  $\varphi$  was determined by looking at the path of the actual crack, thus it could be calculated as the tangent of the angle of its inclination, as suggested by Calderini et al. (2010) for irregular patterns (Figure 3.23).



Figure 3.23. Definition of the parameter  $\varphi$  for different type of masonry (Calderini et a. 2010)

Table 3.6. Mann and Müller’s failure domain parameters.

Building	$\varphi$	$\tilde{c}$ (MPa)	$\tilde{\mu}$
B02	1.00	0.15	0.42
B03	0.55	0.13	0.52
B04	0.68	0.07	0.56
B05	0.75	0.11	0.54
B06	0.63	0.04	0.53
B08	0.53	0.00	0.57

The Mann and Müller’s criterion just introduced is plotted together with the previous ones for sake of comparison (Figure 3.21). In most of the cases, it can be observed that for low compressive stresses, the Mann and Müller’s domain lies below the Turnšek and Čačovič’s criteria, at least below the one calibrated with the ASTM interpretation. Moreover, it is worth noting that this domain, even if theoretically suitable in case of “stair-stepped” cracks, in most cases underestimates significantly the shear strength with respect to the result of the shear-compression test. An exception is represented by building B02, where the Mann and Müller’s criterion is higher than the parabolic failure domain by Turnšek and Čačovič. In particular, the domain is very close to the result of the shear-compression test. However, in this building, the behavior of the panel was slightly different with respect to the others, with the appearance of a flexural crack followed by the shear failure.

#### 3.4.4 Comparison between failure criteria and shear-compression test results

All calibrated failure criteria will be considered together in this section and compared with the results of the shear-compression tests, with the aim of determining which one is more appropriate for interpreting the shear behavior observed in the tests. With reference to Figure 3.21, it is possible to notice that the Mohr-Coulomb’s criterion is the closest to the results of the shear-compression tests for all buildings, except B02. Indeed, as already observed, the Turnšek and Čačovič’s criterion underestimates significantly the experimental capacities. The better agreement of the Mohr-Coulomb’s criterion with the shear-compression test results could confirm the important role of the sliding behavior, occurred after the diagonal cracking, in assessing the shear capacity of the masonry panels, at least of the poor-quality masonry considered in the paper. Even if introduced for describing a failure mode similar to the one observed in the tests, the Mann and Müller’s criterion does not fit effectively the experimental results. As a possible explanation of this aspect, the presence of very poor-quality mortars in the panels subjected to shear-compression tests, could have determined a behavior more

influenced by the local properties of the materials than by the features of the structural elements. In this way, a local criterion can be used to predict the structural capacity of the masonry.

### 3.5 Conclusions

In the present Chapter, the results of an extensive experimental campaign on rural masonry buildings were presented. Slightly-destructive tests (*shove tests* and *splitting tests* on cores with inclined mortar joint) and destructive tests (*diagonal compression* and *shear-compression* tests) were conducted on eight existing buildings with the scope of studying the masonry shear behavior. The poor-quality masonry, with a weak degraded lime mortar, led usually to failure of the specimens driven by the latter. The execution of both slightly-destructive and destructive tests allowed to compare their results in terms of shear strength, through different failure criteria. First of all, an attempt of identifying the most suitable formulation, for the different techniques, was made. On the one hand, the Mohr-Coulomb's failure criterion was determined with the results of slightly-destructive tests for the different masonry typologies. On the other hand, the Turnšek and Čačovič's failure domain was calibrated with the masonry diagonal tensile strength, evaluated through diagonal compression test, for the interpretation of the diagonal cracking failure mode observed in the destructive tests. Then, a comparison between the cited failure criteria was presented. For most buildings, the results were in line with the expected masonry behavior, with a sliding failure mode characterizing panels with low compressive axial stress applied and a diagonal cracking failure mode at higher axial stress values.

The execution of two destructive tests on a single building could not be sufficient for the accurate determination of a failure criterion for masonry. However, these kinds of results are quite rare and, when destructive tests are performed on an existing building, their number is often very limited. From here, the need of verifying the correspondence of the existing failure criteria with the results of the destructive tests for each single construction investigated. Indeed, understanding how the results from these tests could be used is of great help in the engineering practice. In particular, the definition of the diagonal tensile strength from the results of the diagonal compression test seemed quite accurate, given the failure modes observed in the tests and considering that the panels were almost completely detached from the surrounding masonry. However, the choice about the interpretation to be used for the diagonal compression test is still controversial. This of course affects the calibration of the Turnšek and Čačovič's criterion, which in most cases underestimated the results of the shear-compression test,

especially when the elastic interpretation of the diagonal compression test was taken into account.

With reference to the shear-sliding observed in the shear-compression test after cracking, the use of the Mann and Müller's formulation was also investigated. From a theoretical point of view, differently from the local Mohr-Coulomb's domain, the criterion should take the characteristics of the entire wall (in terms of geometry, texture, etc.) into account and should be adequate to describe this failure mode. However, when compared to the experimental results, in most cases it did not match adequately the stress state of the shear-compression tests at failure. Instead, the Mohr-Coulomb's criterion, calibrated from local tests, gave better correspondence with the results from destructive tests. Therefore, also compared to the Turnšek and Čačovič's domain, it seems to be the most suitable for describing the shear behavior of the masonry typologies investigated, characterized by very poor-quality mortars. These conclusions cannot be extended to other different types of masonry, where possibly a stronger mortar or a different brick arrangement could modify the failure mode and the prediction capability of considered criteria. Nevertheless, it seems credible to consider these results as representative of the mechanical behavior of masonry buildings located in the rural areas of Emilia Romagna (Italy).

The testing procedures and typologies here presented can be applied in the seismic vulnerability assessments for the evaluation of the materials mechanical properties. It should be stressed, on the basis of the results obtained, that the execution of a limited number of in-situ tests often implies the obtainment of highly scattered results, which may not provide adequate strength parameters for the investigated masonry. Therefore, the accurate planning of an experimental campaign is fundamental and different type of tests should be executed on the same masonry typology in order to get more reliable results.

## 4 Numerical studies on the shear-sliding behavior of masonry

The shear failure modes of a masonry structural element – toe crushing associated to rocking, sliding or diagonal cracking – depend mainly on its geometry, boundary conditions, level of compression applied, quality of the component materials and texture (Magenes & Calvi 1997, Calderini et al. 2009). Regarding brick masonry, the presence of horizontal and vertical mortar joints surely affects the shear response of a masonry pier. Indeed, they constitute a major source of nonlinearities and, in many cases, they represent planes of weakness along which the failure can occur (Lourenço 1996, Rots 1997).

In a masonry panel subjected to shear, the typical sliding failure mode is characterized by a horizontal crack in a bed joint, located usually at the bottom of the pier. However, the activation of a sliding mechanism could also take place in presence of a stair-stepped diagonal crack, as evidenced in the experimental campaign performed on existing constructions. In this case, the diagonal cracking failure mode is the leading collapse mechanism and the crack formation could be associated to the reaching of the masonry diagonal tensile strength in the center of the panel. Then, in presence of a stair-stepped crack passing mainly through the joints, that is a typical situation when dealing with poor-quality mortars, the activation of a sliding mechanism could be identified and can influence, to some extent, the lateral capacity of the masonry panel. For this reason, the following Sections will be devoted to the study of the aspects and parameters which can affect the shear-sliding behavior of masonry.

The sliding failure mode can usually be described by a Coulomb friction model. Thus, the local properties of the mortar joints, in terms of initial shear strength and friction coefficient, are the most important parameters to be evaluated. Experimental tests may be performed with this purpose, and if a displacement controlled procedure is applied, the sliding along mortar joints can be characterized both in the pre-peak, at failure and in the post-peak phase. For a complete understanding of this nonlinear behavior, together with experimental tests, on a different – but complementary – level, numerical simulations should also be carried out.

The experimental tests, executed in laboratory or in situ, consist in producing the sliding failure along a mortar joint in a specimen, composed by two or more bricks, subjected to a certain value of orthogonal pre-compression. To ensure the reliability of the results in a compression-shear test, various aspects have to be taken into account (Riddington et al. 1997). First of all, normal and shear stress distributions should be uniform along the sliding mortar joint. Secondly, the failure should initiate far away from the joint edges and should propagate

quickly on the entire length of the joint. Finally, the presence of tensile stresses should be checked and avoided since they could affect the test outcomes.

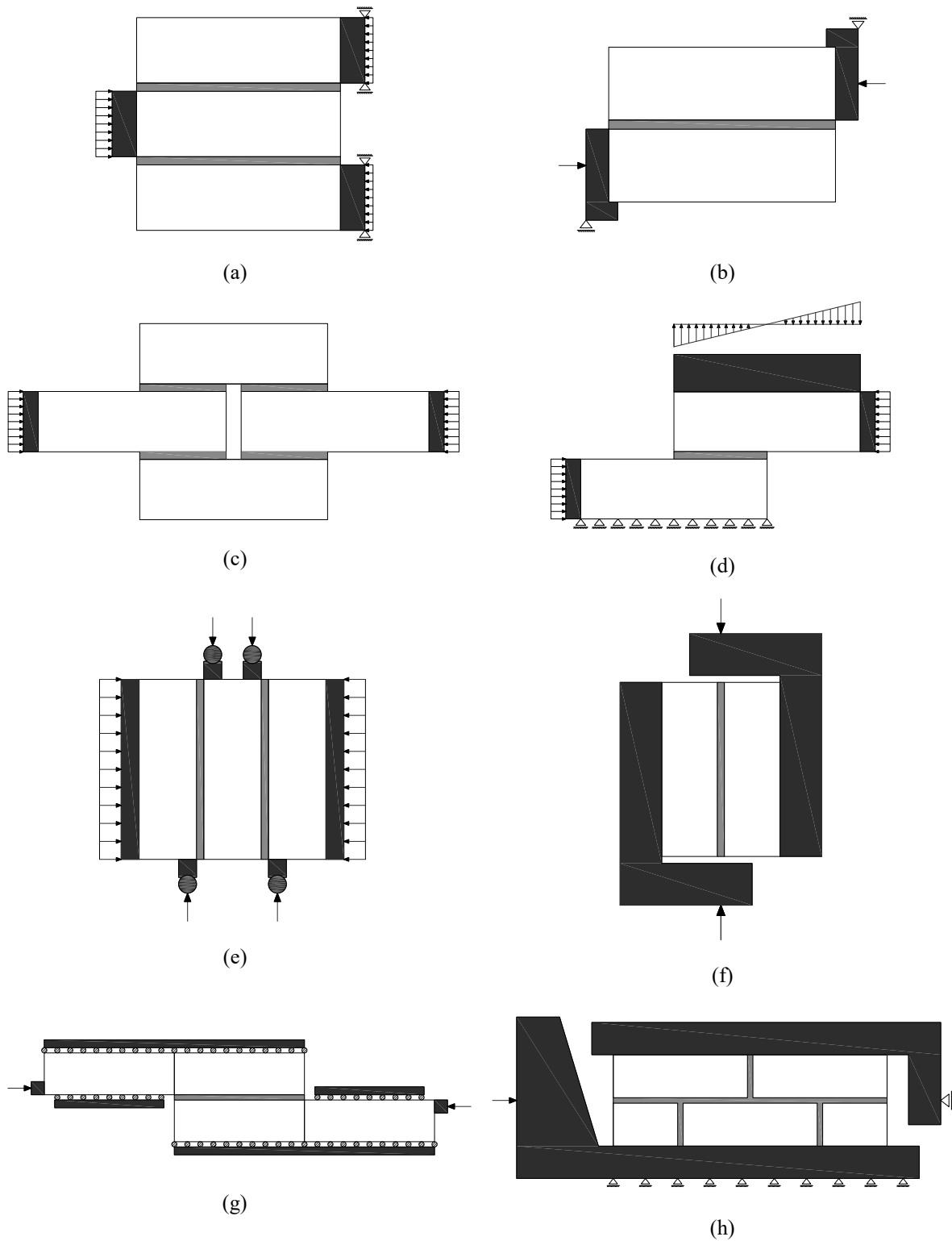


Figure 4.1. Shear test setups for the evaluation of the masonry shear strength: (a) Schubert test; (b) DIN test; (c) Hamid & Drysdale test; (d) Hoffman & Stöckl test; (e) Triplet test, Riddington & Jukes; (f) Van der Pluijm test; (g) Popal & Lissel test; (h) Atkinson test.

Due to the difficulty in finding a testing procedure satisfying all the criteria, many different laboratory test methods have been proposed and studied in the past (Schubert 1978, DIN 18555: Part 5, Drysdale et al. 1979, Stöckl et al. 1990, Riddington & Jukes 1994, Van der Pluijm 1993, Popal & Lissel 2010). They basically differed one from another in the geometry of the specimen – e.g. considering one or more bed joints – and in the loading arrangement (Figure 4.1). They were aimed at obtaining reliable results in terms of initial shear strength and friction coefficient, maintaining the test setup as simple as possible. Few test methods included the presence of head joints (Atkinson et al. 1989).

Finite element analyses were also carried out to investigate peculiar aspects of the different methodologies, highlight their advantages and disadvantages and propose new test methods (Jukes & Riddington 2000, Van Zijl 2004b, Popal & Lissel 2010). It was observed that none of the test methods was capable to completely fulfill all the Riddington's criteria and could not, therefore, be considered as an ideal test (Riddington et al. 1997). In particular, one of the most crucial aspect, observed in almost all the tests, was the unevenness of stress distributions along the sliding mortar joint, especially the normal stress one (Stöckl et al. 1990). Indeed, it was affected by the presence of bending moment along the joint and stress concentrations were detected close to the loading plates (Montazerolghaem & Jaeger 2014).

A particular focus is here devoted to the triplet test, as proposed by Riddington & Jukes (1994) and adopted by the Standard EN 1052-3 (Figure 4.3a). The specimen, composed by three bricks arranged with a stacked bond, is subjected to a constant axial pre-compression, while shear load is applied to the central brick to produce its sliding. This test is really common since it does not need any specific or complex equipment (if compared to other testing methods) and, above all, it was found to be adequate to provide reliable results (Vermeltoort, 2010). By performing the test with pre-compression, the presence of tensile stresses in the joints could be avoided. Moreover, the position of the support in the standard setup ensure the minimum bending moment inside the joints (Jukes & Riddington 2001).

By performing a shear test, such as the triplet test, the following properties may be determined (Figure 4.2), which are very useful for the characterization of masonry and for the numerical modeling (Rots 1997):

- Shear strength  $\tau_{max}$ , which is dependent on the acting compressive stress;
- Shear stiffness  $G$  of the mortar joint;
- Mode-II fracture energy  $G_f^{II}$ , defined as the amount of energy that is needed to create a unit area of a shear crack;

- Angle of dilatancy  $\psi$  between the relative transverse (orthogonal) displacement  $u$  and the relative tangential displacement  $v$ :

$$\tan \psi = \frac{\Delta u_{pl}}{\Delta v_{pl}}. \quad (4.1)$$

where  $\Delta u_{pl}$  and  $\Delta v_{pl}$  are the plastic normal and tangential relative displacements on the interface.

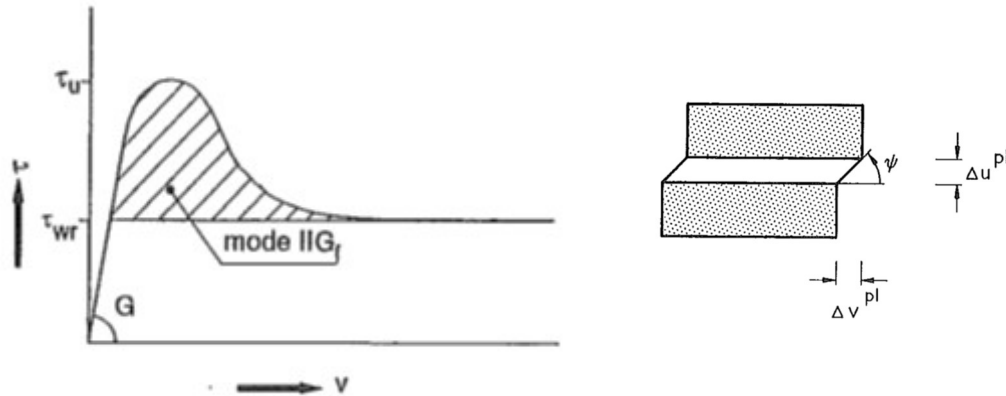


Figure 4.2. Shear test: typical diagram and mechanical properties to be derived. (Rots 1997)

The dilatancy angle  $\psi$  represents a relevant feature of masonry and indicates the volume change upon shearing. Usually, the dilatancy angle is positive, indicating expansion, but tends to zero upon increasing shear displacement and increasing normal confining stress (Lourenco et al. 2004). Dilatancy is highly relevant in case of confinement. Indeed, if the volume increase is prevented, a wedging effect is created, which causes an increase in the compressive stress. For materials characterized by pressure-dependent strength, this phenomenon can lead to a significant strength increase (Rots 1997, Van Zijl 2004a). Therefore, the accurate study of the dilatant behavior of masonry is a very important aspect when performing shear tests.

In parallel to the aforementioned tests, in-situ slightly-destructive techniques were also developed in order to evaluate the masonry mortar joint shear strength. Indeed, given the difficulties in extracting undamaged samples from in-situ masonry walls, laboratory techniques can hardly be performed on existing masonry. According to the Standard ASTM C1531-16, one of the tests which can be carried out with this purpose is the shove test (Figure 4.3b), already presented and described in Section 2.1.2. Even if the shear resistance of a single unit is not, strictly speaking, the same as the shear resistance of a masonry wall, the shove test still yields the most accurate and direct approximation of the in-situ shear strength (Noland et al. 1988).

The scope of the work presented in Chapters 4, 5 and 6 is to investigate the factors that could affect the shear-sliding behavior of masonry, by performing numerical simulations of the triplet

test and the shove test. Many parameters play a role in the sliding behavior observed in the mentioned experimental tests, such as the boundary conditions, the uniformity of the stress distributions along the mortar joints, the cracking formation and evolution, the dilatancy.

Moreover, different outcomes from the two experimental tests could be observed. Typically, higher results were found for the shove test with respect to the triplet test, for the same nominal value of compressive stress applied to the sliding brick. This is basically related to the evaluation of the compressive state of stress on the bed joints during the shove test (Atkinson et al. 1988, Rossi et al. 2015), which will be discussed in the followings. Indeed, since these tests were introduced to capture the same shear-sliding behavior, there is the need of assessing which factors, and to what extent, determine these discrepancies in the tests outcomes.

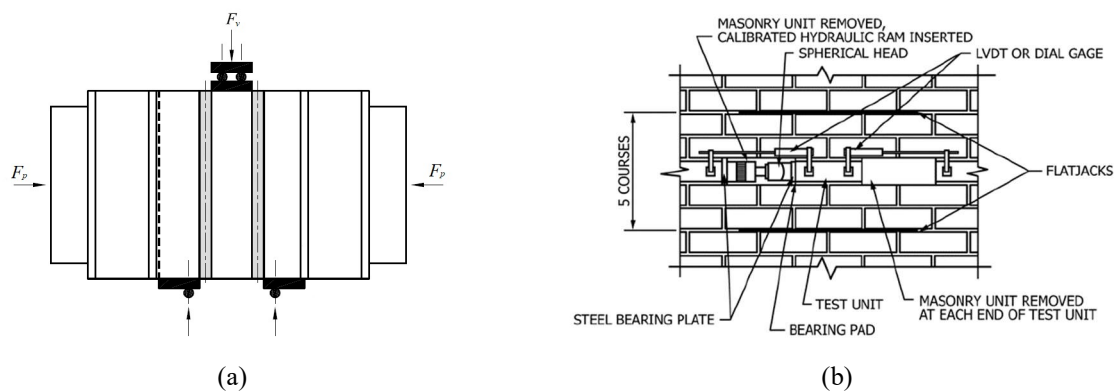


Figure 4.3. Shear tests: (a) triplet test (EN 1052-3); (b) shove test (ASTM C1531).

## 4.1 Numerical modeling of masonry

Masonry is a composite, non-homogeneous and anisotropic material, which exhibits a strong nonlinear behavior. Due to its intrinsic complexity, there is often the need of using robust numerical tools to study and analyze the behavior of masonry elements, both in the pre-peak and post-peak phase. In this framework, different modeling strategies and different constitutive models have been proposed and developed in the past (Anthoine 1992). The attention will be focused in the followings on the nonlinear analysis of masonry structures which can be approximated as being in a state of plane stress. The finite element method offers a variety of possibilities concerning the description of the masonry structures within the framework of detailed nonlinear analyses (Roca et al. 2010).

### 4.1.1 Modeling strategies

Among the modeling strategies that can be found in literature for the modeling of masonry structures (Rots 1991, Lourenço et al. 1995, Rots 1997, Roca et al. 2010), it is basically possible

to distinguish between micro-modeling and macro-modeling approaches, depending on the way in which the constituents (units and mortar) and their interactions are considered (Figure 4.4). On the one hand, if a very accurate representation of masonry is needed – e.g. for small scale problems or for the study of local phenomena – a micro-modeling approach can be used, in which the single components are separately modeled. In this case, a very detailed description of the material is needed, and the mechanical properties required as input parameters in the numerical models have to be obtained from laboratory tests on the constituents or on small scale samples. On the other hand, the macro-modeling strategy can be adequate to study the global behavior of masonry structural elements. Indeed, this approach does not make any distinction between bricks and mortar and masonry is modeled as a fictitious homogeneous continuum. The computational effort can, therefore, be significantly reduced. In this case, the mechanical properties to be assigned to the continuum should be determined by performing experimental tests on specimens of sufficient size subjected to homogeneous states of stress.

Within the framework of micro-modeling, two different strategies can be adopted: the detailed micro-modeling (Figure 4.4b) and the simplified micro-modeling (Figure 4.4c). The detailed micro-modeling is probably the most accurate tool to simulate the real behavior of masonry (Roca et al. 2010). The single components (bricks and mortar) are separately modeled with continuum elements and the brick-mortar interface is modeled with discontinuous elements. In the simplified micro-modeling, masonry is considered as a set of elastic blocks bonded by potential fracture/slip planes in the joints. Indeed, units are modeled with continuum elements, while the mortar joint and the brick-mortar interface are lumped and modeled with discontinuous elements (Lourenço 1996).

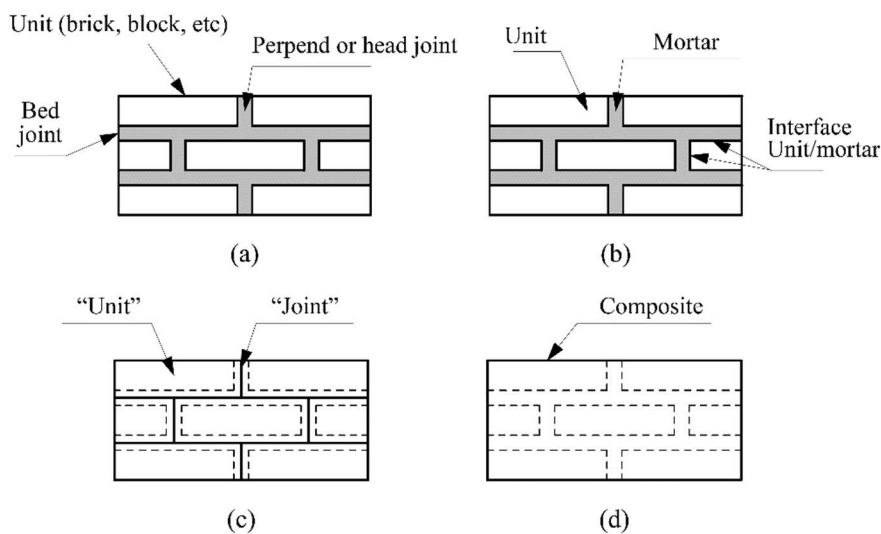


Figure 4.4. Modeling strategies for masonry structures: (a) masonry sample; (b) detailed micro-modeling; (c) simplified micro-modeling; (d) macro-modeling. (Lourenço 1996)

With the aim of studying the shear-sliding behavior along a mortar joint in triplet and shove tests, a high level of accuracy is needed. Therefore, given also the relatively small dimensions of the specimens in the two tests considered, a micro-mechanical model was chosen. Moreover, the simplified micro-modeling strategy was considered adequate to capture the shear behavior observed in the tests, also allowing for the reduction of the computational effort, and was adopted in this research. According to this strategy, the mortar joints were modeled as zero-thickness interface elements and the units were modeled using continuum elements with expanded geometry, so to maintain the overall dimensions of the sample unchanged.

#### 4.1.2 Constitutive models

The shear-sliding failure mode, intended to be reproduced in the numerical simulations, was characterized by a sliding mechanism taking place along the brick-mortar interfaces. Therefore, bricks were modeled as a linear, elastic and isotropic material and the nonlinear behavior was only assigned to the interface elements along which the sliding failure was expected to take place. In the followings, the constitutive models assigned to the plane-stress elements (bricks) and to the interface elements (joint) will be described. More details about the modeling of the triplet test and the shove test will be presented in the dedicated Sections 5 and 6, respectively. In the linear elastic range, the constitutive law for plane stress elements reads:

$$\begin{bmatrix} \sigma_x \\ \sigma_y \\ \tau_{xy} \end{bmatrix} = \frac{E_b}{1-\nu_b^2} \cdot \begin{bmatrix} 1 & \nu_b & 0 \\ \nu_b & 1 & 0 \\ 0 & 0 & \frac{1-\nu_b}{2} \end{bmatrix} \cdot \begin{bmatrix} \varepsilon_x \\ \varepsilon_y \\ \gamma_{xy} \end{bmatrix}, \quad (4.2)$$

where  $E_b$  and  $\nu_b$  are the elastic modulus and the Poisson's ratio of the bricks, respectively.

The constitutive behavior of the interface elements can be described through a relationship between the stresses and the relative displacements along the interface. In the linear elastic range, it is possible to express it as:

$$\begin{bmatrix} \sigma \\ \tau \end{bmatrix} = \begin{bmatrix} k_n & 0 \\ 0 & k_t \end{bmatrix} \cdot \begin{bmatrix} u \\ v \end{bmatrix}, \quad (4.3)$$

where  $\sigma$  and  $\tau$  are the compressive and shear stresses along the interface,  $k_n$  and  $k_t$  are the normal and shear elastic stiffness components, respectively, and  $u$  and  $v$  are the normal and tangential relative displacements on the interface.

As introduced in Section 4.1.1, in the simplified micro-modeling strategy, a modified geometry of the masonry elements is considered, with zero-thickness mortar joints and blown-

up units. Therefore, the elastic stiffness parameters of the brick-mortar interfaces should be evaluated according to Eq.(4.4) and Eq. (4.5) (Rots 1997):

$$k_n = \frac{E_b E_m}{t_m (E_b - E_m)} \quad (4.4)$$

$$k_t = \frac{G_b G_m}{t_m (G_b - G_m)} \quad (4.5)$$

where  $E_b$  and  $G_b$  are the elastic and shear moduli of the bricks,  $E_m$  and  $G_m$  are the elastic and shear moduli of the mortar, and  $t_m$  is the mortar joint thickness.

To mortar joints on which the sliding failure could occur, a nonlinear behavior is assigned, considering a composite interface model. It was formulated in the context of multi-surface plasticity by Lourenço (1996). As mentioned in his numerous publications on the topic, the theory of plasticity is a natural constitutive description for metals, but it can also be used for quasi-brittle materials in shear-compression problems where plastic irreversible strains are observed. Due to the incapability of the theory to reproduce elastic stiffness degradation, it cannot be used for cyclic loads, but good results have been found for monotonic loading conditions (Feenstra 1993, Lourenço 1995). The fundamental notion in the plasticity theory is the existence of a yield function bounding the elastic domain. In the considered interface model, a composite yield surface is defined, including all failure mechanisms which characterize the masonry behavior: tensile failure (Mode I), shear failure (Mode II), and compressive failure. A Coulomb friction failure criterion is assumed for shear, with a tension cut-off and an elliptical compressive cap (Figure 4.5). Both the tensile failure mode and the shear failure mode are characterized by a post-peak softening behavior (Figure 4.6a-b), observed in experimental tests, which is considered in the model. The compressive failure, instead, is characterized by a hardening-softening behavior (Figure 4.6c).

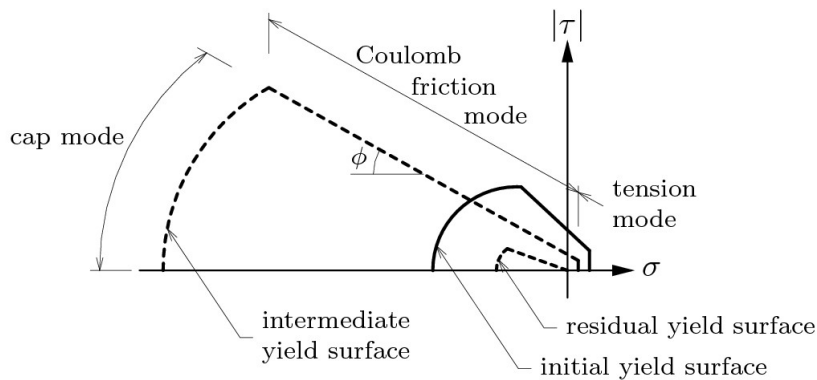


Figure 4.5. Combined cracking-shearing-crushing model for nonlinear interface elements. (Diana Manual).

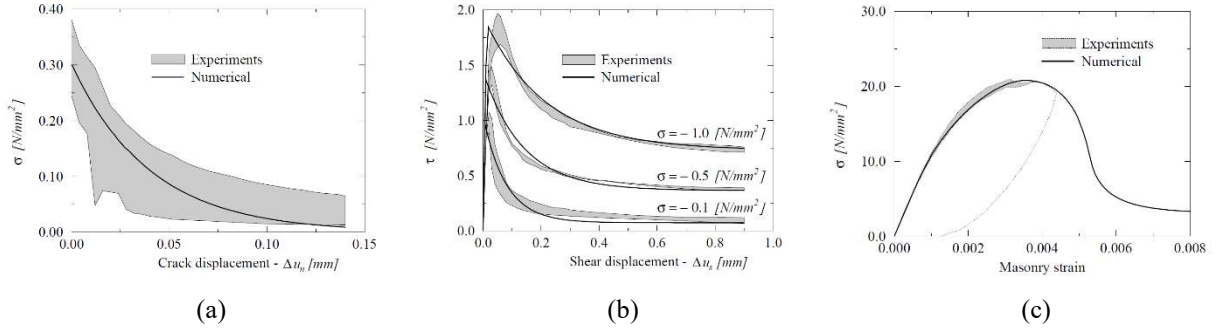


Figure 4.6. Stress-displacement diagrams for interface elements according to the different failure modes: (a) tensile behavior; (b) shear behavior; (c) compressive behavior. (Lourenço, 1996).

For the complete description of the numerical implementation of the composite interface model refer to Lourenço & Rots (1996) and Van Zijl (2004a). In the followings, the yielding functions are reported for each failure mode, together with the functions defining the post-peak behavior. Since the focus of the present work is the shear-sliding behavior of masonry, a more detailed description of the Coulomb friction mode will be reported.

#### Tension mode (Mode I)

The yield function for the tension mode reads:

$$f(\sigma, \kappa_1) = \sigma - \bar{\sigma}_1(\kappa_1) \quad (4.6)$$

Exponential softening is considered, according to the following expression:

$$\bar{\sigma}_1(\kappa_1) = f_t \exp\left(-\frac{f_t}{G_f^I} \kappa_1\right) \quad (4.7)$$

where  $f_t$  is the tensile strength of masonry,  $G_f^I$  is the mode-I fracture energy and  $\kappa_1$  is the plastic normal displacement. An associated flow rule and a strain softening hypothesis are considered.

#### Coulomb friction mode (Mode II)

The Coulomb friction yield criterion, describing the shear slip along the interface, reads:

$$f(\sigma, \kappa_2) = |\tau| + \sigma \tan \phi(\kappa_2) - c(\kappa_2). \quad (4.8)$$

The cohesion and friction softening are defined according to the following expressions:

$$c(\kappa_2) = c_0 \cdot \exp\left(-\frac{c_0}{G_f^{II}} \kappa_2\right) \quad (4.9)$$

$$\tan \phi(\kappa_2) = \tan \phi_0 + (\tan \phi_{res} - \tan \phi_0) \frac{c_0 - c(\kappa_2)}{c_0}. \quad (4.10)$$

In the previous equations,  $c_0$  is the cohesion of the brick-mortar interface,  $\phi_0$  and  $\phi_{res}$  are the initial and the residual friction angle, respectively,  $G_f^{II}$  is the mode-II fracture energy, and  $\kappa_2$  is the shear plastic displacement. Exponential softening is assumed for both the cohesion and the friction angle. In particular, the friction softening is taken proportional to the cohesion softening. Under these hypothesis, the expression for the mode-II fracture energy, determined by appropriate integration of the stress-crack width response, results:

$$G_f^{II*} = G_f^{II} \left( 1 + \frac{\sigma}{c_0} (\tan \phi_{res} - \tan \phi_0) \right), \quad (4.11)$$

which shows the linear relation between the mode-II fracture energy and the normal compressive stress, also found experimentally (Rots 1997).

Non-associated plasticity (Vermeer & De Borst 1984) is here considered, given that masonry joints are characterized by a dilatancy angle which is usually significantly lower than the internal friction angle. Therefore, a non-associated plastic potential  $g_2$  is defined, with a dilatancy angle  $\psi$  and a strain softening hypothesis:

$$g_2 = |\tau| + \sigma \tan \psi - c. \quad (4.12)$$

In the computational implementation of the model, according to the proposal by Van Zijl (2004a), who improved the previous formulations by Lourenço (1996) and Giambanco et al. (2001), a variable dilatancy is considered. This was done to capture the pressure buildup and shearing resistance increase accurately. Results of shear experiments (Figure 4.7) showed that the plastic normal displacement  $u_{pl}$  component depends on the confining stress  $\sigma$  and the plastic shear slip  $v_{pl}$ .

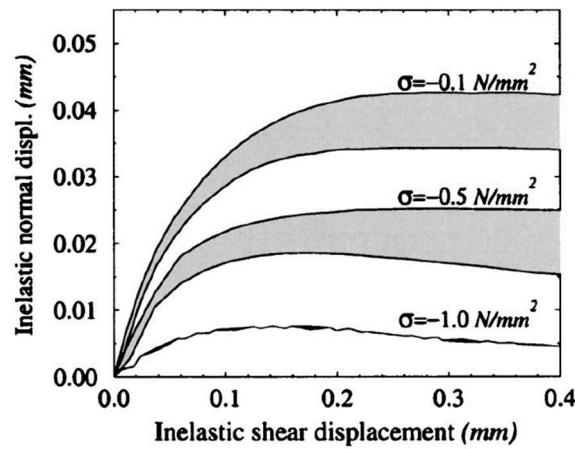


Figure 4.7. Dilatant displacement normal to the joint upon plastic shear displacement – Curves from experiments by Van der Pluijm. (Van Zijl 2004a)

The functions defining the plastic normal displacement upon shearing and, consequently, the dilatancy angle are the followings:

$$u_{pl} = \frac{\Psi_0}{\delta} \left\langle 1 - \frac{\sigma}{\sigma_u} \right\rangle (1 - e^{-\delta \cdot v_{pl}}) \quad (4.13)$$

$$\Psi = \Psi_0 \left\langle 1 - \frac{\sigma}{\sigma_u} \right\rangle e^{-\delta \cdot v_{pl}}, \quad (4.14)$$

where  $\Psi_0 = \tan \psi_0$  is the dilatancy at zero confining stress and shear-slip,  $\sigma_u$  is the confining compressive stress at which the dilatancy becomes zero, and  $\delta$  is the dilatancy shear slip degradation coefficient. From these expressions, which reflects experimental observations, it can be noticed that a linear dependence is assumed between plastic normal displacement and plastic shear slip. Moreover, given a constant confining pressure, the rate of plastic normal displacement decreases exponentially with plastic shear slip.

### Compressive mode (Mode III)

The compressive cap is defined through an elliptic function:

$$f(\sigma, \kappa_3) = C_{mm} \cdot \sigma^2 + C_{ss} \cdot \tau^2 + C_n \cdot \sigma - (\bar{\sigma}_3(\kappa_3))^2, \quad (4.15)$$

where  $C_{mm}$  and  $C_n$  are parameters controlling the center of the cap and its intersection with the positive  $\sigma$ -axis (tensile stresses),  $C_{ss}$  is a parameter controlling the contribution of shear stresses to the failure, and  $\kappa_3$  is the plastic compressive displacement.

For the hardening-softening behavior, the following laws are adopted:

$$\bar{\sigma}_a(\kappa_3) = \bar{\sigma}_i + (f_c - \bar{\sigma}_i) \cdot \sqrt{\frac{2\kappa_3 - \kappa_3^2}{\kappa_p - \kappa_p^2}}, \quad \text{for } 0 \geq \kappa_3 \geq \kappa_p \quad (4.16)$$

$$\bar{\sigma}_b(\kappa_3) = f_c + (\bar{\sigma}_m - f_c) \cdot \left( \frac{\kappa_3 - \kappa_p}{\kappa_m - \kappa_p} \right)^2, \quad \text{for } \kappa_p \geq \kappa_3 \geq \kappa_m \quad (4.17)$$

$$\bar{\sigma}_c(\kappa_3) = \bar{\sigma}_r + (\bar{\sigma}_m - \bar{\sigma}_r) \cdot \exp \left( 2 \left( \frac{\bar{\sigma}_m - f_c}{\kappa_m - \kappa_p} \right) \cdot \left( \frac{\kappa_3 - \kappa_m}{\bar{\sigma}_m - \bar{\sigma}_r} \right) \right), \quad \text{for } \kappa_3 \geq \kappa_m. \quad (4.18)$$

In these equations,  $f_c$  is the compressive strength of masonry,  $\bar{\sigma}_i$  is the initial yield value (corresponding to 1/3 of the compressive strength),  $\bar{\sigma}_m$  is the medium yield value (equal to half the compressive strength),  $\bar{\sigma}_r$  is the residual yield value (corresponding to 1/7 of the compressive strength),  $\kappa_p$  is the plastic displacement at the peak, and  $\kappa_m$  is the plastic displacement associated with  $\bar{\sigma}_m$ .



## 5 Numerical simulations of triplet test

In the triplet test (EN 1052-3), a sliding failure is reproduced, in which the mortar joints are subjected to a prescribed level of axial compression (orthogonal to the bed joints) and to an increasing tangential shear load. The Standard prescribes the execution of at least three tests at three different pre-compression levels, typically equal to 0.20 MPa, 0.60 MPa and 1.00 MPa. By performing the triplet test using a displacement controlled procedure, all properties characterizing the nonlinear shear-sliding behavior of mortar joints, according to a Coulomb friction model, can be derived: shear strength, cohesion and friction softening, mode-II fracture energy, dilatancy. The typical shear load vs tangential relative displacement relationship (Figure 5.1) is characterized by an initial almost linear behavior up to the peak load, followed by a softening branch and a residual tail, corresponding to a dry friction condition. Sometimes, a degradation of stiffness can be recognized just before the peak load.

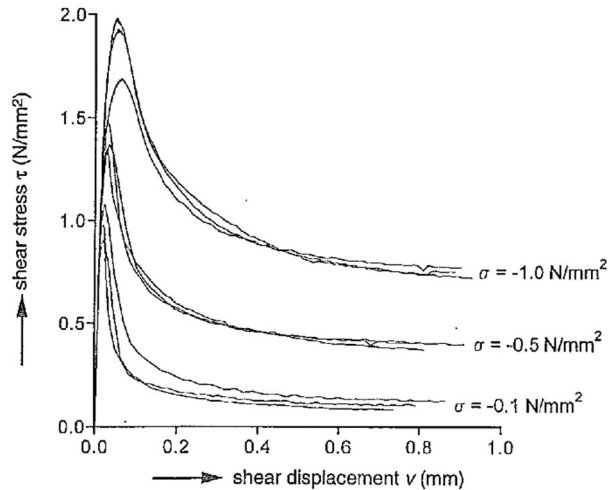


Figure 5.1. Typical shear stress vs shear displacement curves for different values of pre-compression applied. (Rots 1997)

By plotting the peak shear strength  $\tau$  against the normal compressive stress  $\sigma$  for each pre-compression level, it is possible to calibrate the Coulomb friction failure criterion:

$$\tau = c_0 + \sigma \tan \phi_0, \quad (5.1)$$

where  $c_0$  is the cohesion or initial shear strength, and  $\phi_0$  is the friction angle. In a similar way, by plotting the residual shear strength  $\tau_{res}$  against the normal compressive stress  $\sigma$  and performing a linear interpolation, the residual failure criterion could be evaluated as well. It is characterized by a residual shear strength  $c_{res}$  and by a residual friction angle  $\phi_{res}$ .

The standard triplet specimen (EN 1052-3) is composed by three bricks, arranged with a stacked bond pattern (Figure 5.2a). However, considering a typical masonry pattern, the situation in which two bricks slide one over the other is not common. A more representative condition is the one in which also head joints are included. In order to study the influence of the vertical mortar joints on the sliding failure of masonry, modified triplet specimens can also be considered, characterized by a running bond pattern (Figure 5.2b).

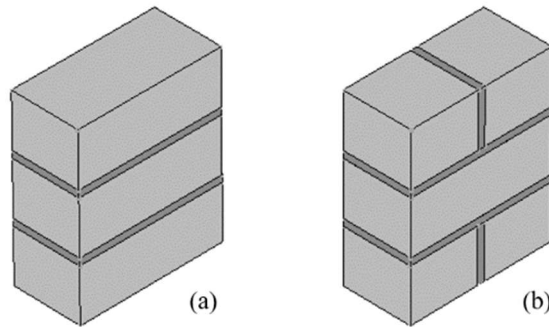


Figure 5.2. Specimen geometry: (a) standard triplet specimen (stacked bond); (b) modified triplet specimen (running bond).

With the objective of investigating the shear properties of bed joints in calcium silicate brick masonry, a laboratory experimental campaign was carried out at Delft University of Technology on replicated masonry samples (Jafari & Esposito 2016). Both geometries were considered. Accordingly, numerical simulations of the standard triplet test and the modified triplet test were carried out, and will be presented in Sections 5.1 and 5.2, respectively. In particular, the results of the experimental tests on standard triplets allowed to calibrate the input parameters for the numerical model, which was then applied also to the modified triplet test geometry. Comparisons between numerical and experimental results were carried out to validate the model.

## 5.1 Standard triplet test

### 5.1.1 Experimental campaign

Standard triplet specimens were built using calcium silicate bricks (dimensions: 214x102x72 mm<sup>3</sup>) and pre-mixed cementitious mortar (class M5), with joint thickness of 10 mm. The mechanical properties of the materials, summarized in Table 5.1, were determined through standard laboratory tests on the components and on masonry wallets (Jafari & Esposito 2016).

Table 5.1. Mechanical properties of calcium silicate masonry.

Property	Symbol	Unit	Value
Compressive strength of bricks	$f_b$	MPa	13.26
Elastic modulus of bricks	$E_b$	MPa	10000
Compressive strength of mortar	$f_m$	MPa	7.57
Flexural strength of mortar	$f_{m,fl}$	MPa	3.21
Compressive strength of masonry	$f_M$	MPa	6.35
Elastic modulus of masonry	$E_M$	MPa	4972
Poisson's ratio of masonry	$\nu_M$	-	0.16
Mode-I fracture energy	$G_f^c$	N/mm	20.0

The triplet test setup is presented in Figure 5.3. At the beginning of the test, the pre-compression was applied by means of a manually operated hydraulic jack (load controlled) and kept constant. The lateral steel plates ensured the diffusion of the compressive load on the entire lateral surfaces of the sample. The shear load was then applied, along the vertical direction, to the intermediate brick, by using a displacement controlled apparatus composed of a 100 kN hydraulic jack and of a spherical joint. The assigned shear displacement rate was equal to 0.005 mm/s during the loading phase and to 0.05 mm/s in the unloading phase. During the test, displacements tangential and orthogonal to the mortar joints were continuously measured with Linear Variable Differential Transformers (LVDT), positioned on both sides of the specimen. Nine specimens were tested at three levels of pre-compression: 0.20 N/mm<sup>2</sup>, 0.60 N/mm<sup>2</sup> and 1.20 N/mm<sup>2</sup>. Moreover, one sample was tested with a pre-compression equal to 0.05 N/mm<sup>2</sup>, to better estimate the initial shear strength. For all the pre-compression levels, after the attainment of the first sliding, the pre-compression load was increased and the sliding produced again. This procedure was repeated several times to obtain a better estimation of the residual strength criterion.



Figure 5.3. Standard triplet test: experimental setup.

The observed failure modes were all characterized by a sliding failure along the area of adhesion between bricks and mortar (Figure 5.4). In few cases, at high pre-compression stress levels, the shear failure involved also the mortar, with a diffuse crack pattern (Figure 5.5).



Figure 5.4. Standard triplet test: typical failure mode.



Figure 5.5. Standard triplet test: shear failure involving mortar.

The results of the triplet tests are reported in Figure 5.6a in terms of shear stress vs tangential-displacement. As in the typical relationship shown in Figure 5.1, it can be observed that the curves are characterized by a first peak, followed by a softening branch and then by a plateau, in correspondence of large sliding displacements ( $>0.5$  mm). The resistance in this last phase can be associated to friction only.

The results of the tests were plotted together in a shear stress vs compressive stress diagram (Figure 5.6b). By performing a linear interpolation of the so obtained points, both at the peak load and in the residual phase, the initial and the residual failure criteria could be evaluated, as already mentioned. The obtained domains are shown in Figure 5.6b and the values of the mechanical properties are reported in Table 5.2. It is worth noting that the friction coefficients of the initial and residual failure criteria are very similar. Moreover, it is possible to observe

that the residual failure criterion, as expected, is characterized by a zero cohesion, thus confirming the pure frictional behavior after the attainment of the first sliding.

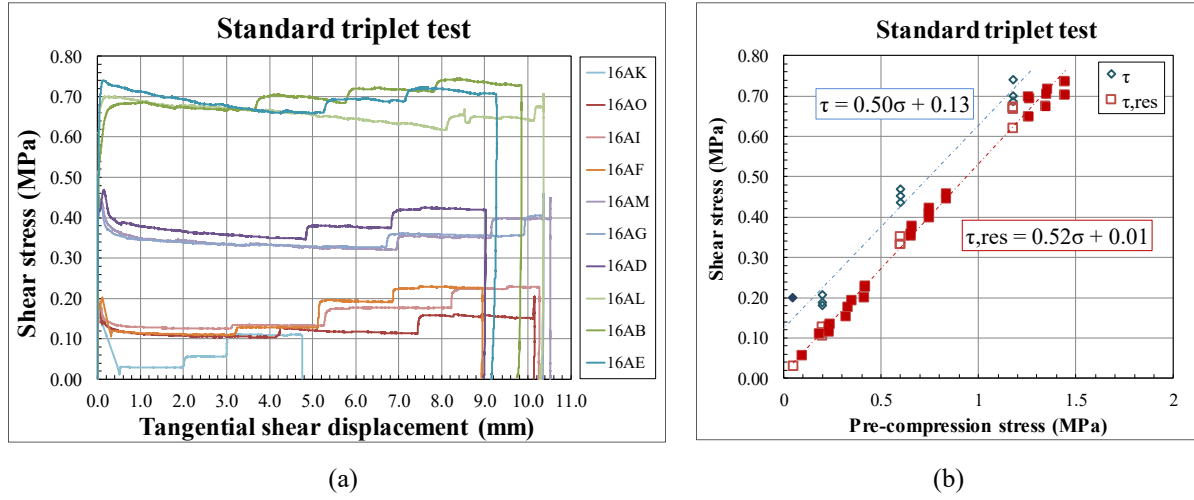


Figure 5.6. Standard triplet test results: (a) shear stress vs relative displacement of the central brick (LVDTs readings); (b) shear stress vs pre-compression stress.

Table 5.2. Shear properties of standard triplets.

Property	Symbol	Unit	Value
Initial shear strength	$c_0$	MPa	0.13
Coefficient of friction	$\mu$	-	0.50
Friction angle	$\phi_0$	rad	0.463
Residual shear strength	$c_{res}$	MPa	0.01
Residual friction coefficient	$\mu_{res}$	-	0.52
Residual friction angle	$\phi_{res}$	rad	0.480

The mode-II fracture energy  $G_f^{II}$  was calculated for each test and the mean value for each pre-compression stress level was evaluated. According to previous researches (Rots 1997, Van der Pluijm 2000), its linear dependence on the pre-compression level can be described by the following equation:

$$G_f^{II} = a\sigma + b = 0.114\sigma + 0.011 \quad (5.2)$$

where  $a$  and  $b$  were determined from linear regression of experimental data (Figure 5.7).

$\sigma$ (Mpa)	$G_f^{II}$ (N/mm)
0.05	0.035
0.2	0.019
0.6	0.069
1.2	0.155

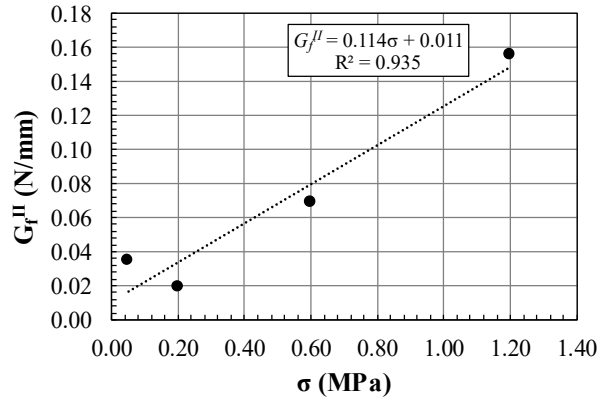


Figure 5.7. Standard triplet test results: mode-II fracture energy vs pre-compression stress.

Transverse expansion upon shearing was observed during experimental tests, as can be noticed from Figure 5.8, where the graphs of normal displacement  $\delta_u$  vs tangential displacement  $\delta_v$  are presented. Very low values – almost null – of normal displacements can be noticed for a pre-compression level of 0.60 N/mm<sup>2</sup>, while, for a pre-compression level of 1.20 N/mm<sup>2</sup>, negative normal displacements were registered, associated to a shear failure involving mortar. Parameters governing the dilatant behavior of mortar joints were evaluated by least-squares fitting of experimental data, according to the variable formulation for dilatancy (Van Zijl 2004), presented in Section 4.1.2. Their values are reported in Table 5.3.

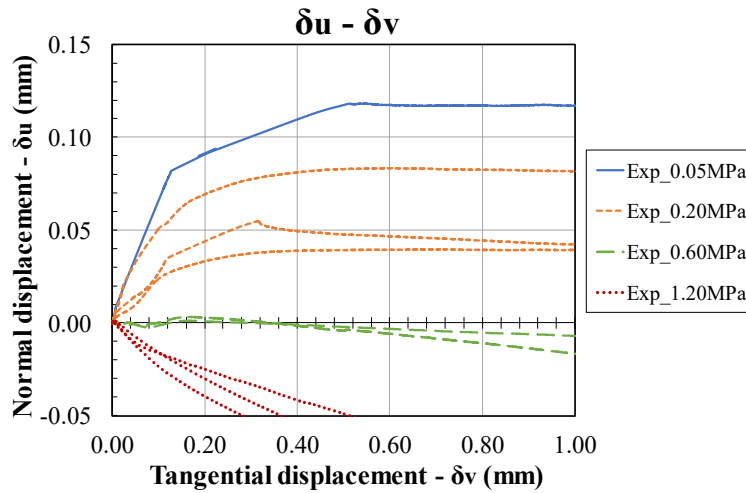


Figure 5.8. Standard triplet test results: normal displacement vs tangential displacement.

Table 5.3. Standard triplet test results: dilatancy parameters.

Parameter	Symbol	Unit	Value
Dilatancy angle	$\psi_0$	rad	0.374
Confining normal stress	$\sigma_u$	N/mm <sup>2</sup>	0.58
Exp. degradation coeff.	$\delta$	-	9.63

### 5.1.2 Numerical model

The detail of the mesh used in the numerical model is shown in Figure 5.9. A 2D model was adopted and, making use of symmetry, only half of the sample was considered. According to the simplified micro-modeling approach, bricks were modeled using quadratic 8-noded plane stress elements, while zero-thickness mortar joints were modeled using line 3-noded interface elements, both based on quadratic interpolation. The DIANA finite element software (Release 10.1) was used for the numerical analyses.

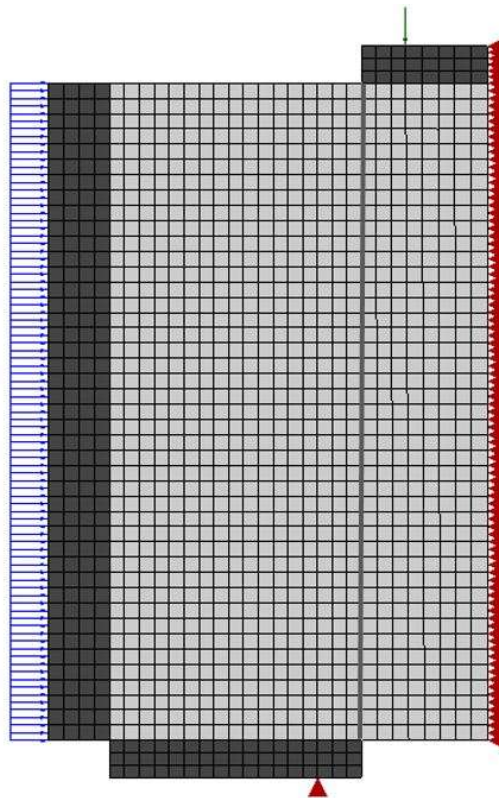


Figure 5.9. Standard triplet test: finite element model.

A linear elastic behavior was considered for plane stress elements (bricks), with the typical stress-strain relations for continuum elements. For interface elements, the elastic constitutive behavior described in Section 4.1.2 was adopted. Since the sliding failure was expected to take place along the bed joint, the nonlinear behavior was only assigned to this failure plane.

The input parameters used in the numerical models for masonry are reported in Table 5.4, where distinction is made between parameters obtained directly from tests and calibrated ones. Concerning calibrated parameters, tensile strength and mode-I fracture energy were determined as a fraction of the cohesion and mode-II fracture energy, respectively (Rots 1997). The parameters for the Coulomb friction model were calibrated from standard triplet tests results, as explained in Section 5.1.1.

To entirely reproduce the test setup, the loading steel plates were also modeled using quadratic plane stress elements, with a linear elastic behavior. The elastic modulus  $E_s$  and the Poisson's ratio  $\nu_s$  for steel were equal to 210000 N/mm<sup>2</sup> and 0.30, respectively. Interface elements were adopted for the brick-to-steel contact surfaces. These elements were modeled as a no-tension material, with a dummy value for the normal stiffness in compression, to allow both the transfer of compressive stress and the separation between steel plates and bricks in presence of tensile stresses. A very low value (10 N/mm<sup>3</sup>) was given to the shear stiffness to avoid lateral confinement of bricks.

Numerical simulations were performed with the finite element software DIANA FEA (Release 10.1), at 4 different pre-compression levels  $\sigma_p$  (0.05 – 0.20 – 0.60 – 1.20 N/mm<sup>2</sup>), to reproduce the loading conditions of the experimental tests. The numerical simulations were carried out by imposing an increasing vertical displacement to the top plate. Regular Newton-Raphson method was adopted to solve the nonlinear problem.

Table 5.4. Input parameters for masonry.

	Description	Symbol	Units	Value
Parameters from tests	Elastic modulus of brick	$E_b$	N/mm <sup>2</sup>	10000
	Poisson's ratio of brick	$\nu_b$	-	0.16
	Elastic modulus of mortar	$E_m$	N/mm <sup>2</sup>	1088
	Poisson's ratio of mortar	$\nu_m$	-	0.20
	Cohesion	$c_0$	N/mm <sup>2</sup>	0.13
	Friction angle	$\phi_0$	rad	0.463
	Residual friction angle	$\phi_{res}$	rad	0.463
	Compressive strength	$f_c$	N/mm <sup>2</sup>	6.35
	Compr. fracture energy	$G_f^c$	N/mm	20
	Equiv. plastic shear displ.	$\kappa_p$	-	0.005
Calibrated Parameters	Interface normal stiffness	$k_n$	N/mm <sup>3</sup>	122.1
	Interface shear stiffness	$k_t$	N/mm <sup>3</sup>	50.7
	Tensile strength	$f_t$	N/mm <sup>2</sup>	0.09
	Mode-I fracture energy	$G_f^I$	N/mm	0.01
	Dilatancy angle	$\psi_0$	rad	0.374
	Confining normal stress	$\sigma_u$	N/mm <sup>2</sup>	0.58
	Exp. degradation coeff.	$\delta$	-	9.63
	Mode-II fracture energy ( $G_f^{II} = a\sigma + b$ )	$a$ $b$	mm N/mm	0.114 0.011

### 5.1.3 Numerical results

The results of the numerical simulations for standard triplet tests, at each pre-compression level, are reported in Figure 5.10 and Figure 5.11 in terms of shear stress  $\tau$  vs tangential

displacement  $\delta_v$  and normal displacement  $\delta_u$  vs tangential displacement  $\delta_v$ , respectively. They are compared with experimental results. Concerning  $\tau$ - $\delta_v$  diagram, it can be noticed how numerical results are in good agreement with the experimental ones, for all pre-compression levels. The presence of multiple peaks in some of the experimental curves could indicate that the failure was not activated at the same time on both mortar joints. However, given the symmetric model considered, this aspect is not studied here.

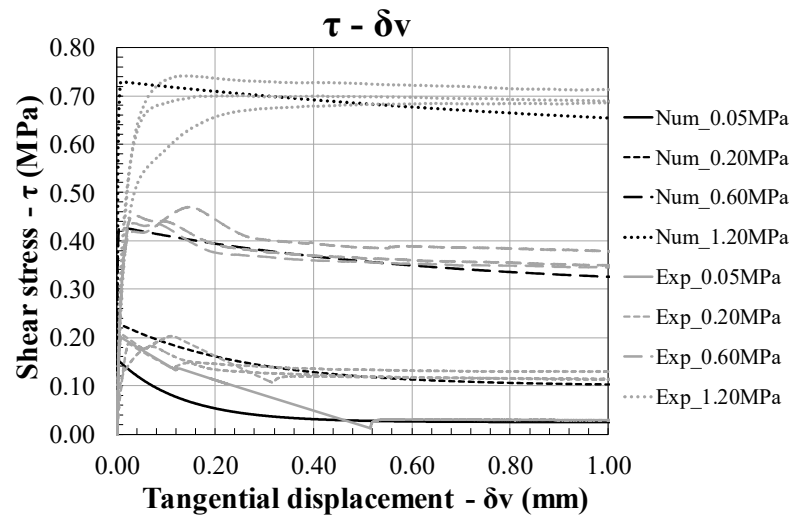


Figure 5.10. Standard triplet test, shear stress vs tangential displacement.

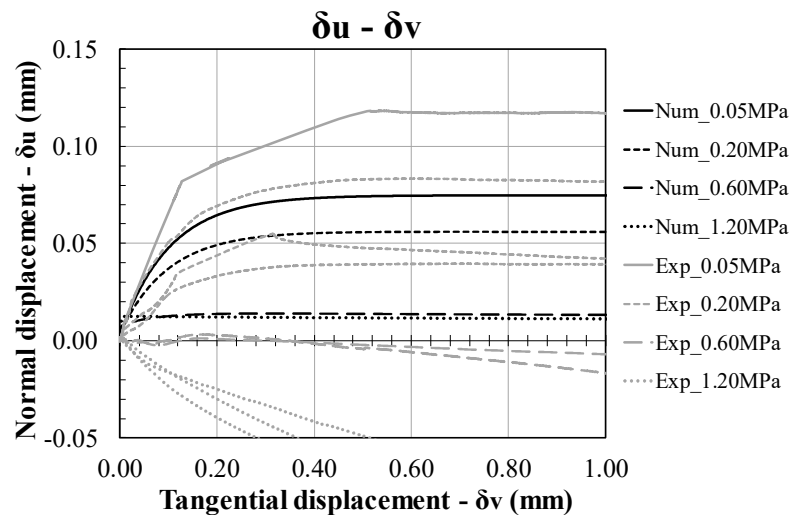


Figure 5.11. Standard triplet test, normal displacement vs tangential displacement.

Looking at Figure 5.11, it can be noticed that, for pre-compression levels of 0.60 N/mm<sup>2</sup> and 1.20 N/mm<sup>2</sup>, the experimental curves show a compression orthogonal to the bed joint which is not well captured by the numerical results. This can be explained by some setup features – e.g. lateral loading plate not free to displace at high pre-compression stress levels – or by considering that the failure mode observed in these experimental tests, especially for the pre-

compression level of  $1.20 \text{ N/mm}^2$ , was not a pure sliding failure along the brick-mortar interface but involved the mortar itself. Indeed, cracking in the mortar occurred along the compression lines, especially close to the upper joint edge. In order to capture the very low – even negative – values of normal displacements  $\delta_u$ , variations to the numerical model could be made. On the one hand, a modification of the boundary conditions could be considered, as will be discussed in detail in Section 5.1.4. On the other hand, to properly describe the mortar failure, a detailed micro-modeling strategy, not reported in this work, could be adopted.

The principal stress distributions in Figure 5.12, reported as an example for a pre-compression level of  $0.20 \text{ N/mm}^2$ , show high stress concentrations close to the loading plates and the presence of a compressed strut.

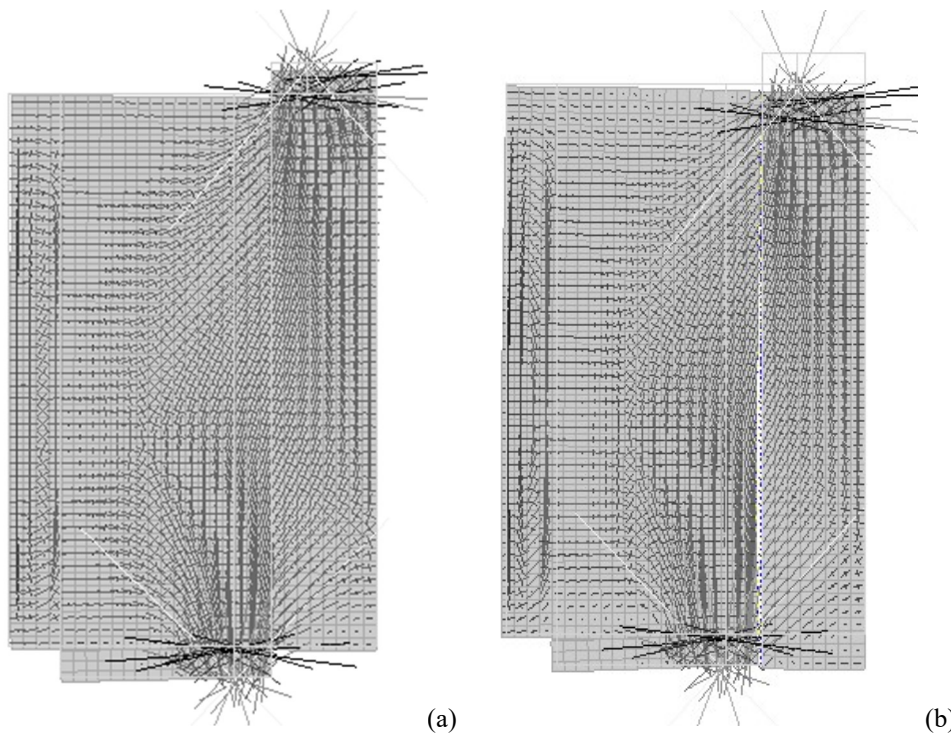


Figure 5.12. Standard triplet test at pre-compression  $0.20 \text{ N/mm}^2$  – Principal stress distributions: (a) pre-peak ( $\delta_v = 0.02 \text{ mm}$ ); (b) post-peak ( $\delta_v = 0.08 \text{ mm}$ ).

Considering the results of the nonlinear analyses for standard triplet specimens, it is interesting to investigate the development of the stress distributions along the joint and the propagation of the failure, given that they could influence the reliability of the results, as mentioned at the beginning. In Figure 5.13 and Figure 5.14 the stress evolution along the sliding failure plane is shown, both for normal and tangential stresses, at pre-compression equal to  $0.20 \text{ N/mm}^2$ . It can be noticed that the stress distributions are not uniform along the joint and that concentrations of stresses occur at the joint edges, as already observed. Due to the diffusion of the shear load, in the first part of test, the normal compression increases at the joint extremities (always greater

at the top), while it decreases in the middle of the specimen. In the post-peak phase, instead, the normal compression is greater at mid-height than at the extremities. The shear stress distributions develop accordingly.

Failure did not initiate far away from the joint edges but close to the bottom extremity and then propagated upwards. Nevertheless, a shear displacement increase of less than 0.01 mm was needed for it to propagate along the entire joint length.

Similar results were obtained in previous researches, where finite element analyses of different shear tests were performed, and stress distributions compared (Riddington et al. 1997, Stöckl et al. 1990). In almost all shear tests, except the one proposed by Van der Pluijm (1999), non-uniform stress distributions were observed and peak stresses at the joint extremities were quite high.

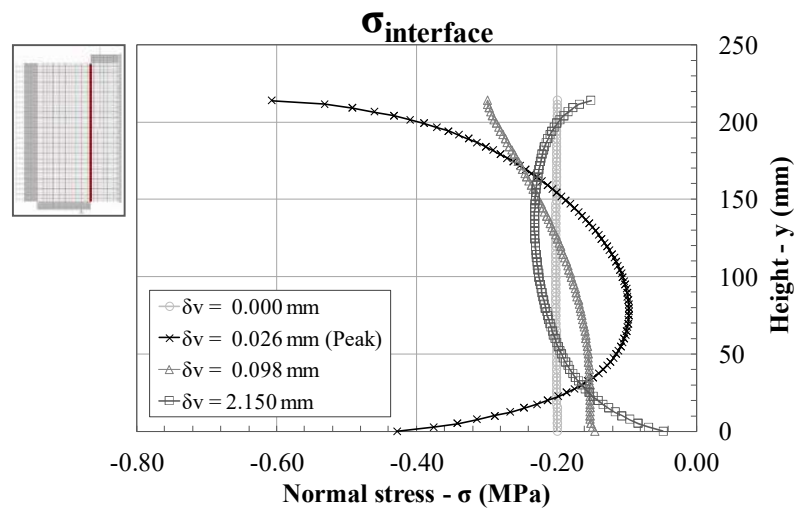


Figure 5.13. Standard triplet test at pre-compression  $0.20 \text{ N/mm}^2$ , normal stress evolution along the nonlinear interface.

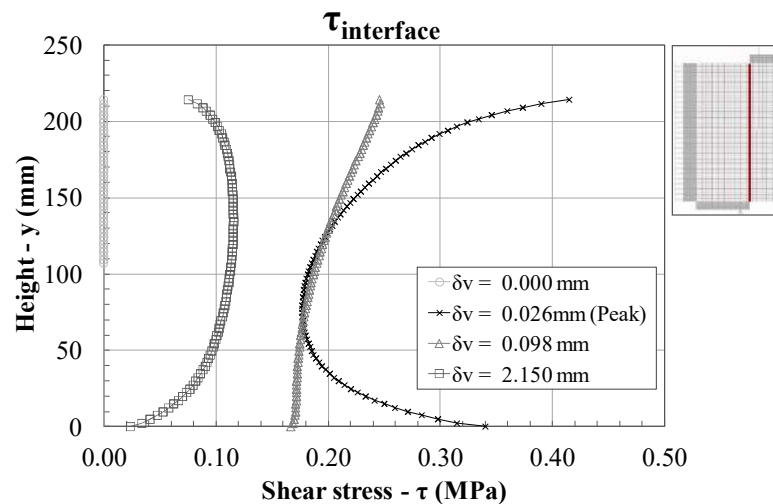


Figure 5.14. Standard triplet test at pre-compression  $0.20 \text{ N/mm}^2$ , tangential stress evolution along the nonlinear interface.

#### 5.1.4 Influence of boundary conditions

Dilatancy is one of the most important parameters governing the sliding failure of mortar joints. Indeed, the dilatant behavior of masonry could affect the results in two different ways, depending on the boundary conditions of the triplet tests. It could either produce an increase in the peak load, in case of restrained lateral displacement, or an increase in the displacements orthogonal to the bed joint, if the specimen is free to displace laterally. In particular, an increase in the shear capacity is determined by the fact that, during the sliding, when the transverse expansion is restrained, the pre-compression level on the joint increases, which consequently leads to higher peak loads. Therefore, the way in which the pre-compression is applied to the sample plays a crucial role in the outcomes of the test.

To study the influence of the boundary conditions, additional numerical simulations were performed, in which the pre-compression load was applied as a constant lateral displacement, i.e. to reproduce the restrained displacements condition. The mechanical properties and the pre-compression levels considered were the same of the previous analyses. The results of the numerical simulations for the laterally restrained model are here reported for standard triplet tests only.

The shear stress  $\tau$  vs tangential displacement  $\delta_v$  diagrams are reported in Figure 5.15. It can be stated that the laterally restrained condition is not representative of standard triplet tests at low pre-compression stress levels, i.e.  $0.05 \text{ N/mm}^2$  and  $0.20 \text{ N/mm}^2$ . Indeed, differently to what can be observed in Figure 5.10, the numerical curves do not correspond at all to the experimental ones. On the opposite, for higher pre-compression levels ( $0.60 \text{ N/mm}^2$  and  $1.20 \text{ N/mm}^2$ ), there is a good agreement between numerical and experimental results. This is related to the fact that, in these latter cases, dilatancy is playing a very marginal role, given the high compression acting on the joint.

The normal displacement  $\delta_u$  vs tangential displacement  $\delta_v$  diagrams are reported in Figure 5.16 for triplet tests at  $0.60 \text{ N/mm}^2$  and  $1.20 \text{ N/mm}^2$ . Here, the results already presented for standard triplets with free lateral displacements are reported as well. The portion of the diagram for low values of tangential displacements is considered, since it is the most interesting part, corresponding to the activation of the sliding failure and the reaching of the peak load. It can be noticed that for the restrained displacement condition, the normal displacement is considerably low. However, the behavior of the samples at high pre-compression levels is still not properly captured. Indeed, as already observed, the simplified micro-modeling seems to be not adequate to reproduce the failure modes observed in these tests, and detailed micro modeling is probably needed.

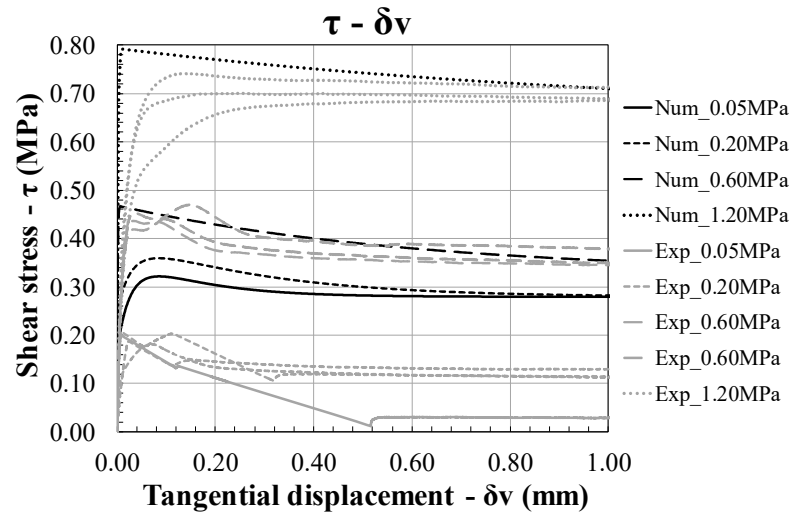


Figure 5.15. Standard triplet test with restrained lateral displacement, shear stress vs tangential displacement.

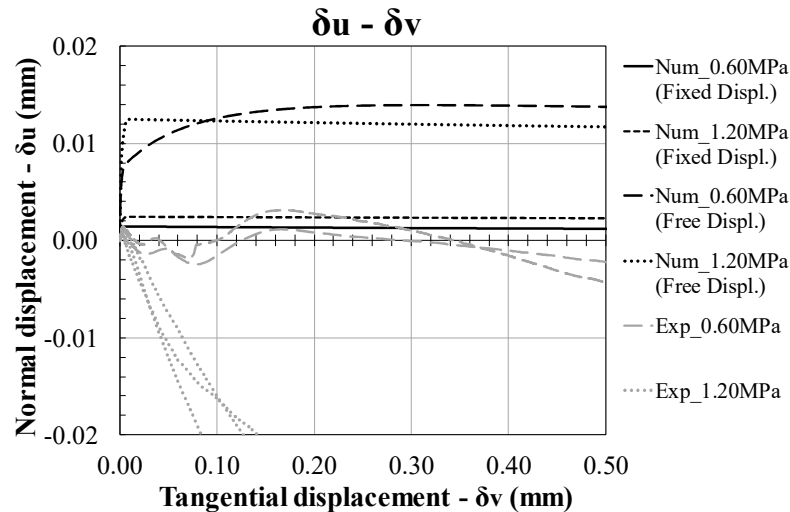


Figure 5.16. Standard triplet test, shear stress vs tangential displacement – Free vs restrained lateral displacement conditions.

## 5.2 Modified triplet test

### 5.2.1 Experimental campaign

The modified triplet test specimens were built using the same materials (calcium silicate bricks and cementitious mortar) adopted for standard triplet specimens. Their mechanical properties can be found in Table 5.1. The test setup is presented in Figure 5.17. The only difference with respect to the setup used for standard triplet tests is the presence of two additional LVDTs per side, positioned across the head joint, to check relative displacements between the lateral units.

Nine specimens were tested at three levels of pre-compression: 0.20 N/mm<sup>2</sup>, 0.60 N/mm<sup>2</sup> and 1.20 N/mm<sup>2</sup>. Moreover, one sample was tested with a pre-compression equal to 0.05 N/mm<sup>2</sup>, to better estimate the initial shear strength. For all the pre-compression levels, after the

attainment of the first sliding, the pre-compression load was increased and the sliding produced again. This procedure was repeated several times to obtain a better estimation of the residual strength criterion.



Figure 5.17. Modified triplet test: experimental setup.

The observed failure modes were all characterized by a sliding failure along the area of adhesion between bricks and mortar (Figure 5.18). In some cases, a “bridging” failure was identified: the sliding surface was located on one side of the sliding joint in the upper portion of the specimen and on the other side of the joint in the lower portion (Figure 5.19). Only in two tests, the head joint was involved in the failure process (Figure 5.20). As in standard triplet tests, at high pre-compression stress levels, the shear failure involved also the mortar, with a diffuse crack pattern.



Figure 5.18. Modified triplet test: typical failure mode.



Figure 5.19. Modified triplet test: “bridging” failure mode.



Figure 5.20. Modified triplet test: shear failure involving the head joint.

The results of the modified triplet tests are reported in Figure 5.21a in terms of shear stress vs tangential-displacement. As in the typical relationship shown in Figure 5.1, it can be observed that the curves are characterized by a first peak, followed by a softening branch and then by a plateau, in correspondence of large sliding displacements ( $>0.5$  mm). The resistance in this last phase can be associated to friction only.

The results of the tests were plotted together in a shear stress vs compressive stress diagram (Figure 5.21b). By performing a linear interpolation of the so obtained points, both at the peak load and in the residual phase, the initial and the residual failure criteria could be evaluated, as already mentioned. The obtained domains are shown in Figure 5.21b and the values of the mechanical properties are reported in Table 5.5. It is worth noting that the friction coefficients of the initial and residual failure criteria are equal. Moreover, it is possible to observe that the residual failure criterion, as expected, is characterized by a zero cohesion, thus confirming the pure frictional behavior after the attainment of the first sliding.

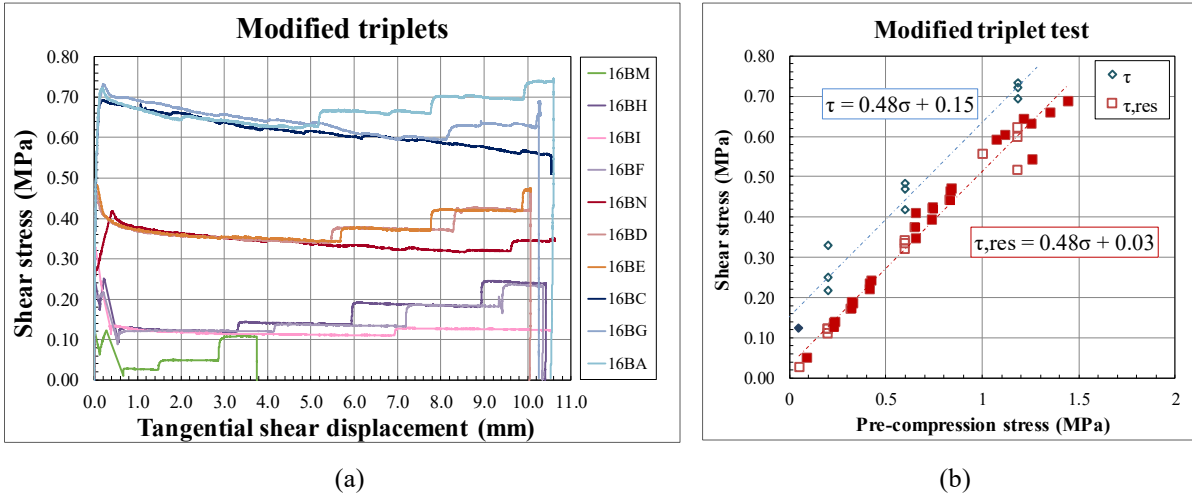


Figure 5.21. Modified triplet test results: (a) shear stress vs relative displacement of the central brick (LVDTs readings); (b) shear stress vs pre-compression stress.

Table 5.5. Shear properties of modified triplets.

Property	Symbol	Unit	Value
Initial shear strength	$c_0$	MPa	0.15
Coefficient of friction	$\mu$	-	0.48
Friction angle	$\phi_0$	rad	0.448
Residual shear strength	$c_{res}$	MPa	0.03
Residual friction coefficient	$\mu_{res}$	-	0.48
Residual friction angle	$\phi_{res}$	rad	0.448

The mode-II fracture energy  $G_f^{II}$  was calculated for each test and the mean value for each pre-compression stress level was evaluated, as already done for standard triplet tests. The linear dependence on the pre-compression level can be described by the following equation:

$$G_f^{II} = a\sigma + b = 0.179\sigma + 0.014 \tag{5.3}$$

where  $a$  and  $b$  were determined from linear regression of experimental data (Figure 5.22).

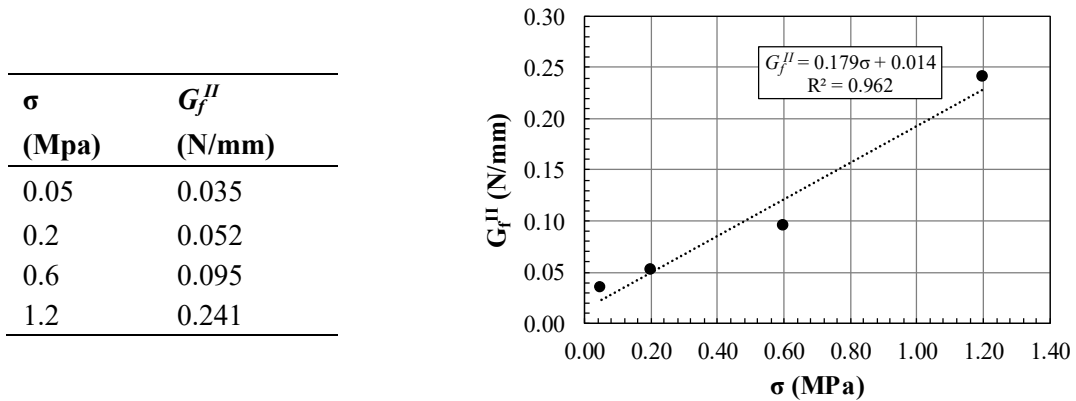


Figure 5.22. Modified triplet test results: mode-II fracture energy vs pre-compression stress.

Transverse expansion upon shearing was observed during experimental tests, as can be noticed from Figure 5.23, where the graphs of normal displacement  $\delta_u$  vs tangential displacement  $\delta_v$  are presented. In this case, positive values of the normal displacements can be noticed also at high pre-compression stress level, at the beginning of the test. Afterwards, in most of the cases, negative normal displacements were registered, indicating a shear failure involving the mortar, as already observed for standard triplet tests. Due to the high dispersion of the results, especially for the pre-compression level of 0.20 N/mm<sup>2</sup>, the parameters governing the dilatant behavior of mortar joints, evaluated by least-squares fitting of experimental data, were found not to be reliable and, therefore, are not reported here.

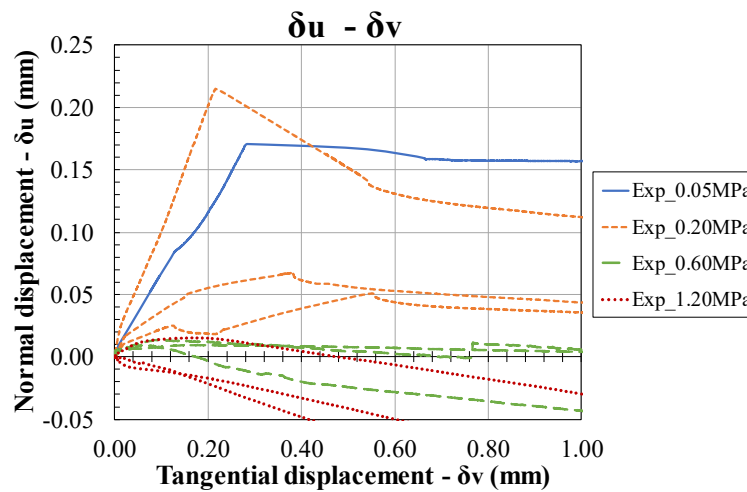


Figure 5.23. Modified triplet test results: normal displacement vs tangential displacement.

### 5.2.2 Numerical model

The detail of the mesh used in the numerical model is shown in Figure 5.24. A 2D model was adopted and, making use of symmetry, only half of the sample was considered. According to the simplified micro-modeling approach, bricks were modeled using quadratic 8-noded plane stress elements, while line 3-noded interface elements were adopted to model the zero-thickness mortar joints.

A linear elastic behavior was considered for plane stress elements (bricks), with the typical stress-strain relations for continuum elements. For interface elements, the elastic constitutive behavior described in Section 4.1.2 was adopted. Since the sliding failure was expected to take place along the bed joint, the nonlinear behavior was only assigned to this failure plane. The head joint was supposed to remain elastic during the shear failure. The steel plates were modeled as already described for standard triplet tests.

In the numerical simulations, the input parameters calibrated for standard triplet tests (Table 5.4) were adopted to validate the model. The nonlinear analyses were carried out with the finite element software DIANA FEA (Release 10.1), considering 4 different pre-compression levels  $\sigma_p$  (0.05 – 0.20 – 0.60 – 1.20 N/mm<sup>2</sup>), to reproduce the loading conditions of the experimental tests. The numerical simulations were carried out by imposing an increasing vertical displacement to the top plate. Regular Newton-Raphson method was adopted to solve the nonlinear problem.

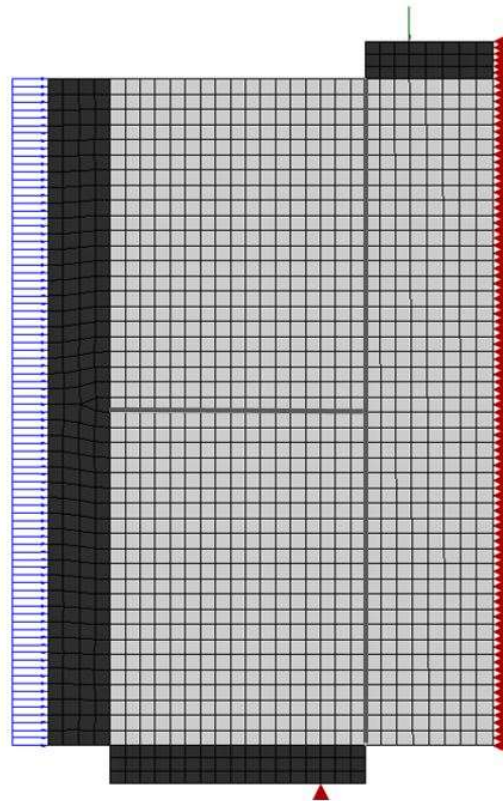


Figure 5.24. Modified triplet test: finite element model.

### 5.2.3 Numerical results

The results of the numerical simulations for modified triplet tests are reported in terms of shear stress  $\tau$  vs tangential displacement  $\delta_v$  (Figure 5.25) and in terms of normal displacement  $\delta_u$  vs tangential displacement  $\delta_v$  (Figure 5.26). Experimental results are also included. It can be noticed a good agreement between numerical and experimental results, especially in the  $\tau$ - $\delta_v$  diagram. In the  $\delta_u$ - $\delta_v$  diagram, their agreement is quite good for almost all pre-compression levels, especially in correspondence of low tangential displacement values. Exceptions are represented by the sample tested at 0.05 N/mm<sup>2</sup> and by one specimen at 0.20 N/mm<sup>2</sup>, which showed a great expansion upon shearing. The issue previously highlighted for standard triplets

– which registered negative  $\delta_u$  values for high pre-compression stresses – is here present only for two samples at pre-compression equal to  $1.20 \text{ N/mm}^2$ .

The results of the numerical analysis for modified triplet specimens are satisfactory if compared with experimental results, even if the numerical model was calibrated with results from standard triplet tests. This fact could be explained by considering the failure modes observed in modified triplet tests. Indeed, in the majority of the cases, the sliding failure involved the brick-mortar interface close to the central brick. Only in few cases, the mortar continuity between the head and bed joint was damaged. Therefore, the presence of the head joint, for the masonry typology investigated, did not seem to have a great influence on the outcomes of the tests, especially in terms of peak and residual shear loads.

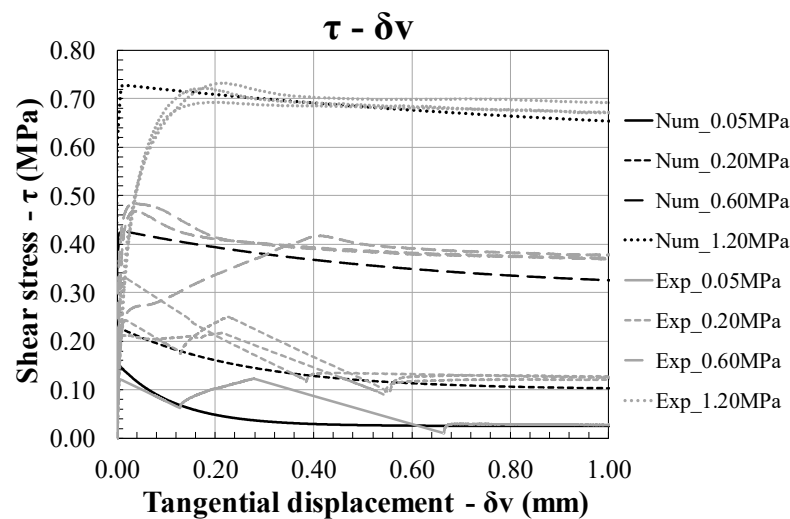


Figure 5.25. Modified triplet test, shear stress vs tangential displacement.

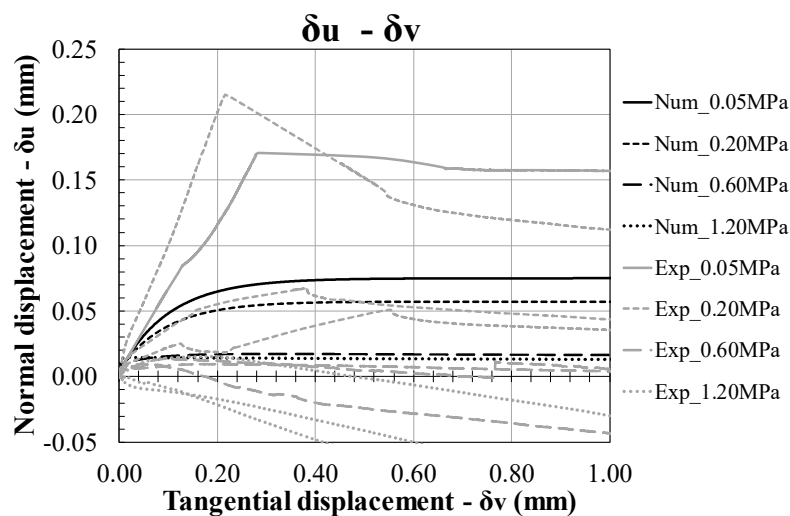


Figure 5.26. Modified triplet test, normal displacement vs tangential displacement.

Figure 5.27 and Figure 5.28 show the stress evolution along the sliding failure plane of the vertical joint for increasing values of shear slip, both for normal and tangential stresses, at a pre-compression of  $0.20 \text{ N/mm}^2$ . As already observed for standard triplet tests, the stress distributions are not uniform along the joint and concentrations of normal stresses are present at the joint extremities. The jump in the stress distributions in correspondence of the head joint can be explained by considering that the upper left brick was subjected to a variable lateral shortening (prevalent at the top) and a clockwise rotation. With respect to the stress distributions for the standard triplet tests (Figure 5.13 and Figure 5.14), these movements caused, along the upper portion of the sliding surface, higher peak stresses at the top and reduced stresses in the middle, even leading to tensile normal stresses in a small portion of the sliding interface.

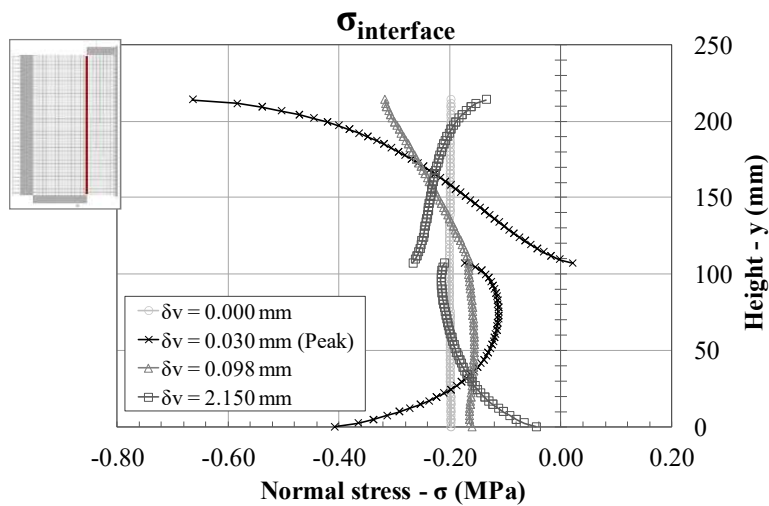


Figure 5.27. Modified triplet test at pre-compression  $0.20 \text{ N/mm}^2$ , normal stress evolution along the nonlinear interface.

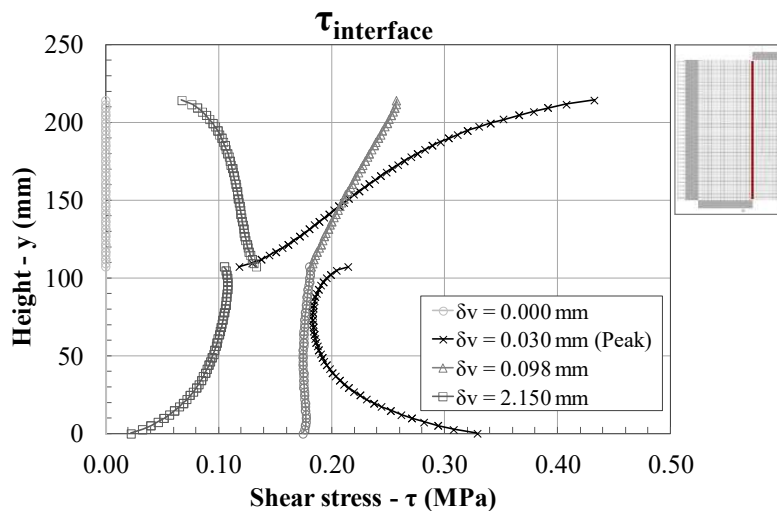


Figure 5.28. Modified triplet test at pre-compression  $0.20 \text{ N/mm}^2$ , tangential stress evolution along the nonlinear interface.

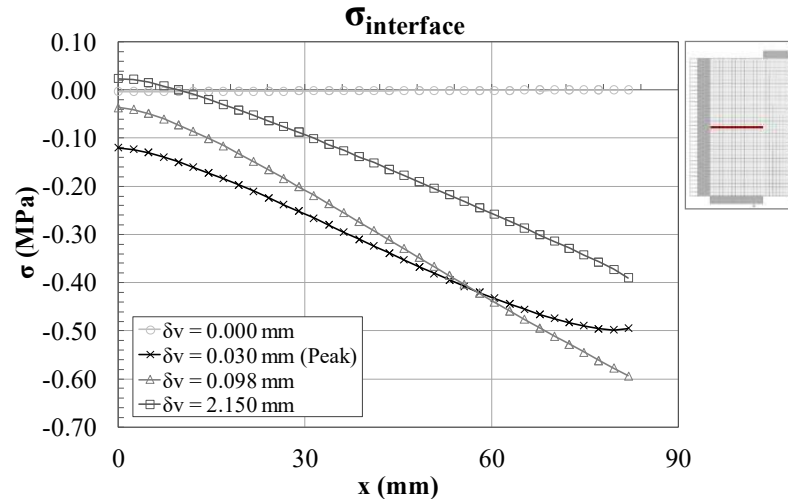


Figure 5.29. Modified triplet test at pre-compression  $0.20 \text{ N/mm}^2$ , normal stress evolution along the head joint.

The normal stress evolution on the head joint is presented in Figure 5.29. Maximum values of compressive stresses are located at the right-end side, close to the sliding failure plane. This is consistent with the diffusion of the shear load inside the specimen and with the clockwise rotation of the upper left brick. With the failure propagation, the reduction of the compressive stresses along the head joint can be related to the reduction of the upper left brick deformation due to the lateral relaxation of the sample in the softening phase.

#### 5.2.4 Influence of dilatancy parameters

The uplift upon shearing is governed by the dilatancy function (Eq. (4.14)) and, therefore, by the parameters  $\psi_0$ ,  $\sigma_u$  and  $\delta$ . In this context, parametric studies were performed for models with free lateral displacements, varying the values of these parameters. In the followings, results of numerical simulations for modified triplet tests are shown, where increased values of  $\psi_0$  and  $\sigma_u$  were considered (Table 5.6). Indeed, experimental results showed that modified triplet specimens were characterized by higher normal displacements  $\delta_u$  with respect to standard triplets. Given the observations reported in Section 5.1.4, the results were not expected to be different from the previous models in terms of shear capacity, but in terms of normal displacements. Figure 5.30 shows an increase in the normal uplift for all tests, except for the case with pre-compression equal to  $1.20 \text{ N/mm}^2$ . Comparing it with Figure 5.26, it is possible to observe that a better agreement between numerical and experimental results is found, especially at low pre-compression levels.

Table 5.6. Modified dilatancy parameters.

Parameter	Symbol	Value
Dilatancy angle	$\psi_0$ [rad]	0.561 (+50%)
Confining normal stress	$\sigma_u$ [N/mm <sup>2</sup> ]	0.70 (+20%)
Exp. degradation coeff.	$\delta$	9.63

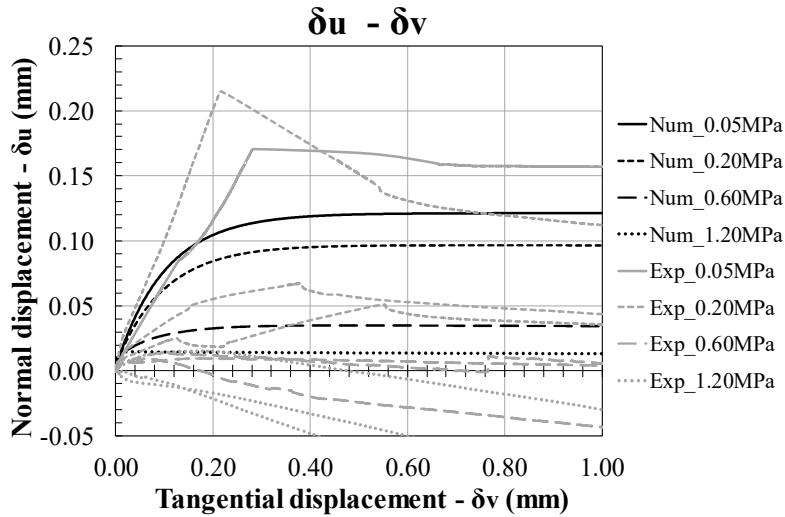


Figure 5.30. Modified triplet test, normal displacement vs tangential displacement.

### 5.2.5 Influence of the elastic properties of the head joint

With reference to the modified triplet specimens, parametric studies were carried out on the elastic stiffnesses of the head joint. Indeed, in the engineering practice, it is quite common to deal with masonry structures in which head joints have lower mechanical properties than bed joints. This is due to construction reasons and, moreover, to the fact that head joints are not subjected to compression during the curing. Therefore, imperfections or microcracks are often present. To simulate this situation, the elastic modulus of mortar was reduced by 50% and the elastic stiffness parameters of the interface elements were modified accordingly. Results are here reported in terms of normal stresses for the pre-compression level of 0.20 N/mm<sup>2</sup> (Figure 5.31). Distributions at peak load and in the residual phase are shown and results from Figure 5.29 are also included. In presence of weak head joint, a 20% compressive stress reduction can be observed on the right-end side of the joint, in correspondence of the peak load ( $\delta_v = 0.030$  mm), as expected. In the residual phase, instead, where the shear load has already been transferred and a pure friction behavior can be observed, the two stress distributions are almost coincident.

Differences were not observed neither in terms of peak and residual shear load nor in terms of orthogonal displacements. Similar observations can be done for the other pre-compression levels, which are not reported here, for sake of brevity.

The variation of the elastic properties of the head joint was not sufficient to influence the sliding failure during the triplet test. In order to consider different behaviors, e.g the failure within the head joint or in the contact point between head and bed joint, the use of a detailed micro-modeling strategy could be useful, in which nonlinearities could be assigned to the head joint. However, these variations were not considered here, given that the head joint was almost never involved in the sliding failure during experimental tests.

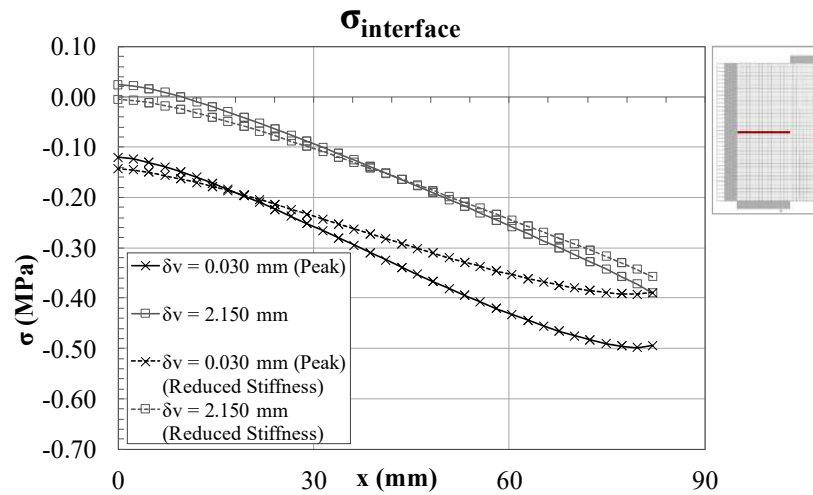


Figure 5.31. Modified triplet test at pre-compression  $0.20 \text{ N/mm}^2$ , normal stress evolution – Intact vs weak head joint.

### 5.3 Discussion

The numerical simulations of triplet tests presented were carried out to study the shear-sliding behavior of calcium silicate brick masonry. Two different geometries were considered: the standard triplet specimen and the modified one, characterized by a running bond pattern. A simplified micro-modeling strategy was adopted. The models were calibrated with results of standard triplet tests and then validated through comparisons between numerical and experimental results.

The obtained numerical results allowed to understand which aspects could most affect the outcomes of the triplet tests. In particular, the influence of dilatancy and the boundary conditions were analyzed.

The influence of dilatancy on the results of the triplet test is strongly associated to the boundary conditions of the test itself. On the one hand, in case of restrained lateral

displacements, an overestimation of the shear capacity was observed for samples at pre-compression equal to  $0.05 \text{ N/mm}^2$  and  $0.20 \text{ N/mm}^2$ . At higher pre-compression levels, instead, the restrained displacements condition could partially capture the very low values registered for normal displacements. On the other hand, in case of free lateral displacements, the dilatancy can affect the values of the normal displacements along the sliding failure plane. To investigate this aspect, parametric studies were performed on the variables defining the dilatancy function. In particular, for modified triplet tests, in which the registered transverse displacement upon shearing was higher than in standard triplet tests, these parametric studies allowed to better capture the behavior of the samples, at least for low pre-compression levels.

The presence of a head joint did not have a great influence on the tests outcomes. This was confirmed both by numerical and experimental results and can be related to the specific masonry typology investigated. Indeed, the head joint was almost never involved in the failure process. Parametric studies were performed, reducing the normal and shear stiffness values, and the only difference in the results was represented by a change in the stress distributions along the head joint. In order to include failure modes involving the head joint, it is advisable to use a detailed micro-modeling strategy.

Aspects related to the triplet test setup and execution were analyzed and briefly discussed, such as the presence of non-uniform stress distributions along the sliding bed joint, the concentration of stresses at its extremities, the failure initiation and propagation. Even if the objective of the research was not to reduce or eliminate the influence that these aspects have on the test outcomes, they all represents intrinsic issues in the triplet test, which is important to be aware of.

In conclusion, the numerical simulations here presented allowed to gain a better understanding of the sliding failure in triplet tests. Future works can be done with the objective of better capturing the shear failure within the mortar at high pre-compression level. The detailed micro-modeling approach could be used to this purpose, in which failure inside the mortar can be included.

## 6 Numerical simulations of shove test

To investigate the shear-sliding behavior of existing masonry directly in situ, the shove test can be performed (ASTM C1531-16), according to one of the three methods presented in Section 2.1.2. It has been already discussed about the main advantages and disadvantages of each test setup. In the followings, a more detailed analysis of the differences between the proposed methods will be presented, by performing numerical simulations of the shove test. *Method A* and *Method B* will be considered.

The numerical analyses will be carried out considering a full-scale masonry panel, trying to reproduce as close as possible the in-situ conditions of the test. The wall geometry and the test setup were chosen to be equal to the ones adopted in an experimental campaign conducted at the Delft University of Technology on single-wythe calcium silicate brick masonry (Figure 6.1).

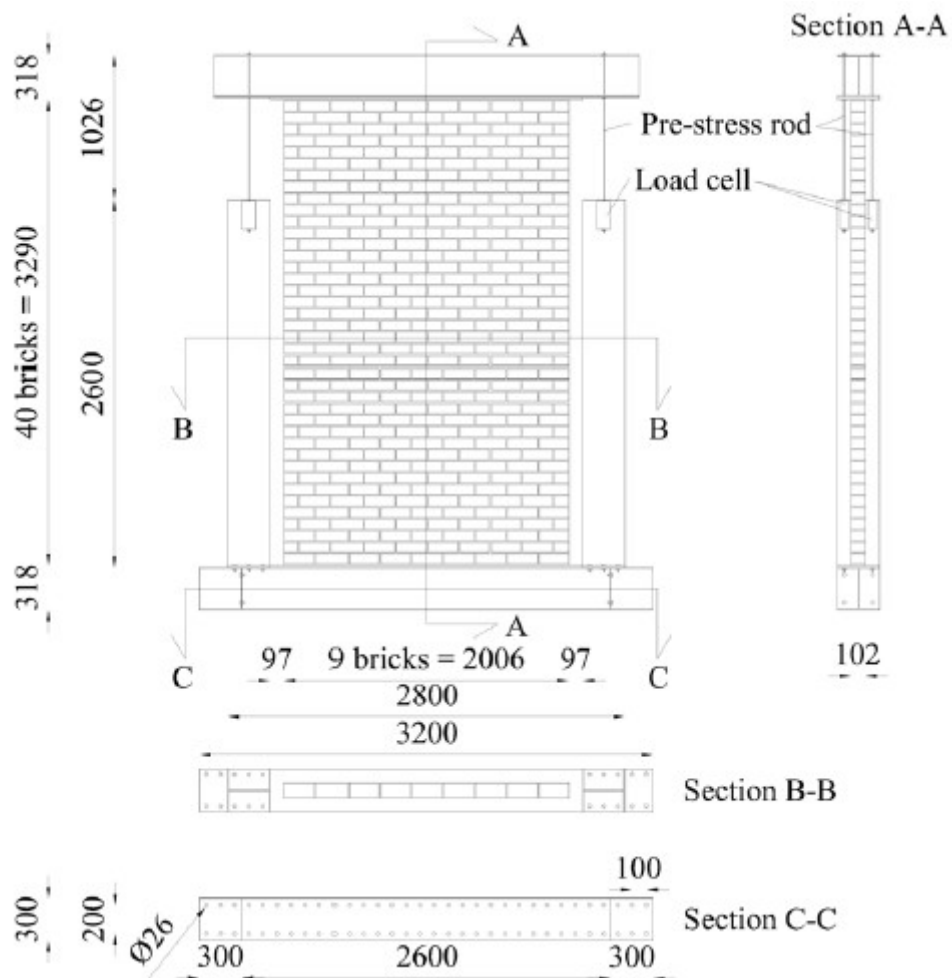


Figure 6.1. Shove test: wall geometry and test setup. (TUDelft)

Given that triplet tests were performed on the same masonry typology (Sections 5.1.1 and 5.2.1), the input parameters were calibrated with triplet test results and used also in the numerical models of the shove test, since the two tests aim at describing the same shear-sliding behavior. Factors influencing the sliding failure mechanism and the shear capacity in the shove test will be analyzed in detail with the objective of investigating the differences between the triplet and the shove test outcomes. Moreover, a validation of the numerical model used for the shove test will be carried out in Chapter 7, where a case study will be presented.

## 6.1 Shove test – Method A

### 6.1.1 Testing procedure

The testing procedure consists in applying a uniform distributed load at the top of the panel, reproducing the dead and live loads which can be present in situ. Then, the masonry unit to be subjected to the test is chosen and two cuts are executed in order to seat the flatjacks. The distance between the cuts and the tested unit shall be at least two masonry courses. Two bricks have then to be removed from the opposite end of the test unit. After setting the flatjack pressure to a very low value, the horizontal load is applied to the test unit by means of a hydraulic jack. The load is increased monotonically until the obtainment of the sliding failure of the brick. The geometry of the wall, with the identification of the test location, is reported in Figure 6.2.

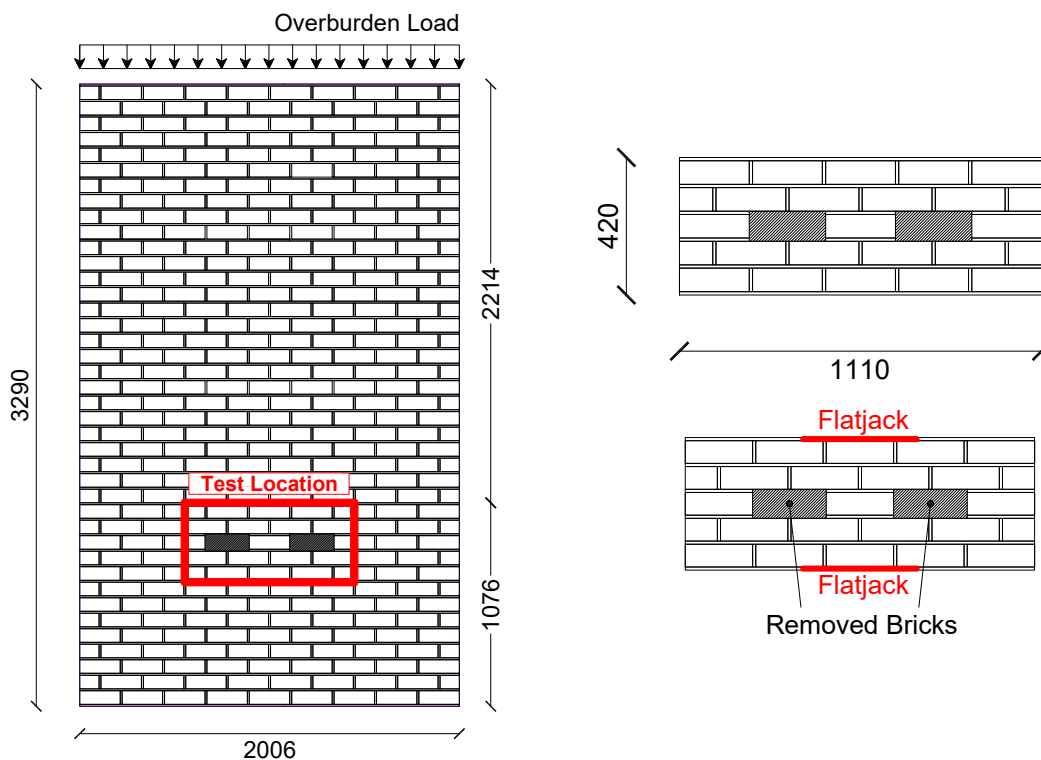


Figure 6.2. Shove test – *Method A*: wall geometry and test location.

### 6.1.2 Numerical model

The detail of the mesh used in the numerical model is shown in Figure 6.3. Given the geometry of the masonry panel, which was a single-wythe wall, a 2D model was considered adequate to reproduce the testing conditions. The simplified micro-modeling approach was adopted. Therefore, bricks were singularly modeled using 32 quadratic 8-noded plane stress elements, while line 3-noded interface elements were adopted to model the zero-thickness mortar joints, both vertical and horizontal.

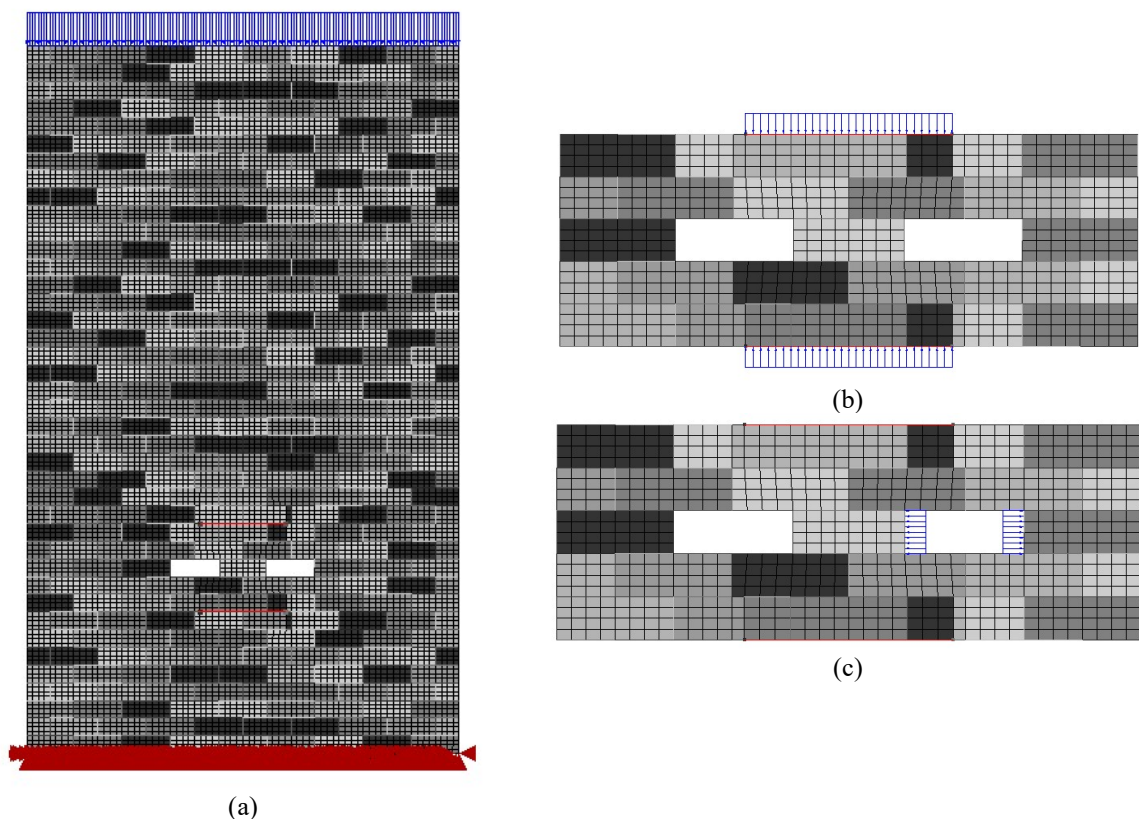


Figure 6.3. Shove test - *Method A*, finite element model: (a) entire wall panel; (b) detail of the flatjack pressure application; (c) detail of the shear load application.

The elastic constitutive behaviors presented in Section 4.1.2 for plane stress elements, modeling bricks, and for interface elements, modeling mortar joints, were considered. For horizontal mortar joints, a material behavior with a constant normal stiffness for compression and a stiffness reduction in tension was adopted. In particular, the normal stiffness coefficient was set to zero in correspondence of a tensile normal relative displacement equal to 0.001 mm. Vertical joints, instead, were modeled as a no-tension material. The choice of assigning weaker properties to the vertical joints is justified by considering that, during the construction process, a greater attention is paid to the realization of the horizontal mortar joints. Moreover, vertical joints are not subjected to vertical loads during the curing, thus micro-cracks or even loss of

bond between bricks and mortar are often more present in these joints. A nonlinear behavior with a composite interface model, whose description can be found in Section 4.1.2, was assigned to the mortar joints on which the sliding failure was expected to take place, i.e. upper and lower bed joints of the test unit. No connection was considered between the edges of the flatjack holes.

The beam at the top of the wall was not modeled as well as the loading steel plates used for the application of the shear load on the lateral surfaces of the brick. However, to take into account the presence of the steel elements, tyings (i.e. linear dependencies between nodal variables) were adopted to force the nodes along these edges to equally displace.

The input parameters used in the numerical models for masonry are the same used for the numerical simulations of the triplet test and have been reported in Table 5.4.

The finite element software DIANA FEA (Release 10.1) was adopted for the numerical simulations. Phased analyses were carried out to exactly reproduce the testing procedure:

- Phase 1: application of the self-weight and the overburden;
- Phase 2: execution of the first cut for the seating of the superior flatjack;
- Phase 3: execution of the second cut for the seating of the inferior flatjack;
- Phase 4: removal of bricks;
- Phase 5: application of the flatjack pressure;
- Phase 6: application of the shear load.

The nonlinear analyses were performed by imposing an increasing horizontal load both to the sliding and the contrast brick, to reproduce the presence of the horizontal hydraulic jack. Regular Newton-Raphson method and arc-length method were adopted to solve the nonlinear problem.

### 6.1.3 Numerical results

The results of three numerical simulations of the shove test, according to the procedure reported in the Standard for *Method A*, will be presented in this Section. Different loading conditions were considered, as reported in Table 6.1. In particular, the same flatjack pressure – set to a very low value, as suggested by the Standard – was considered, while three different overburden loads were applied at the top of the masonry wall to study the influence of the acting vertical load on the test outcomes.

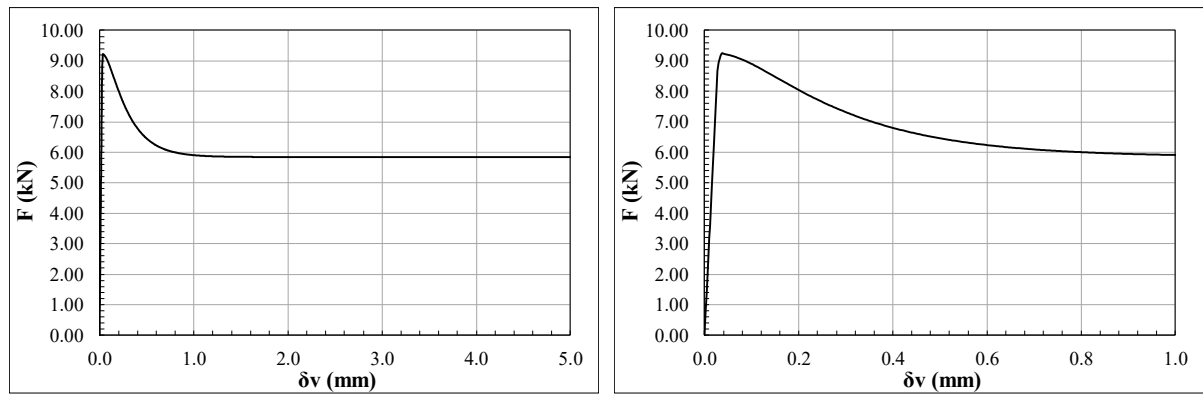
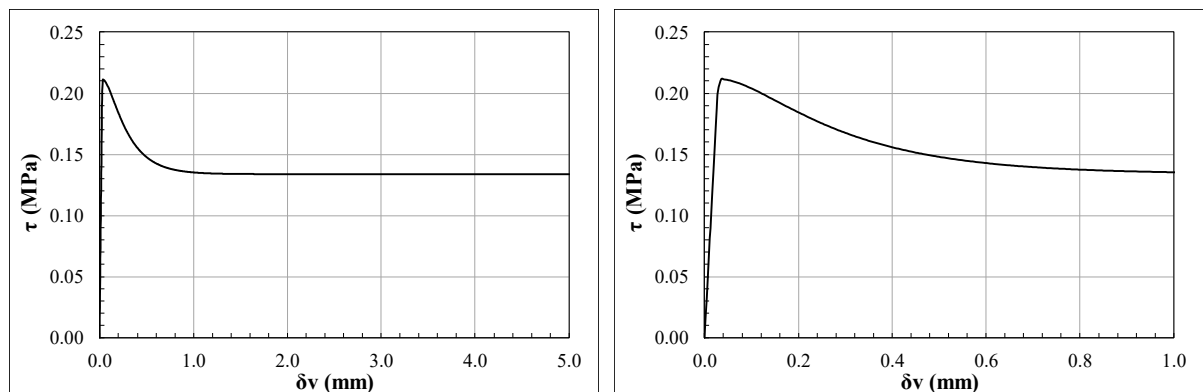
Table 6.1. Shove test – *Method A*: loading conditions for the numerical simulations.

Model	Overburden Load (kN)	Vertical compression* (MPa)	Flatjack pressure (Mpa)
A1	21.28	0.15	0.05
A2	41.74	0.25	0.05
A3	113.36	0.60	0.05

\*given by self-weight and overburden on the sliding brick at the beginning of the test

First of all, the results of Model A1 will be analyzed in detail to properly understand the shear-sliding behavior investigated in the shove test. Then, a comparison between the main outcomes of the three numerical simulations will be presented.

The shear load  $F$  vs tangential displacement  $\delta v$  curve and the shear stress  $\tau$  vs tangential displacement  $\delta v$  curve are presented in Figure 6.4 and Figure 6.5; respectively. They are both characterized by an initial linear behavior up to the peak load, followed by a softening branch and a residual phase, namely the dry-friction phase.

Figure 6.4. Model A1 – Numerical results: shear load  $F$  vs tangential displacement  $\delta v$  diagram.Figure 6.5. Model A1 – Numerical results: shear stress  $\tau$  vs tangential displacement  $\delta v$  diagram.

To investigate dilatancy, which could influence, to some extent, the shear capacity of masonry, the orthogonal displacement  $\delta u$  vs tangential displacement  $\delta v$  graph is reported in Figure 6.6. To evaluate the average orthogonal displacement  $\delta u$ , the differences between the vertical displacements of two pairs of points, positioned above and below the test unit, were considered. The presence of a positive displacement  $\delta u$  indicates a vertical expansion upon shearing, which could reveal that the uplift is not restrained. Therefore, the dilatant behaviour of masonry seems not to have an influence on the results in terms of shear capacity. Indeed, for this model, the failure load – corresponding to the point in which the failure domain is reached for all the integration points of the sliding surface – and the peak load coincide. This latter aspect will be discussed in the followings.

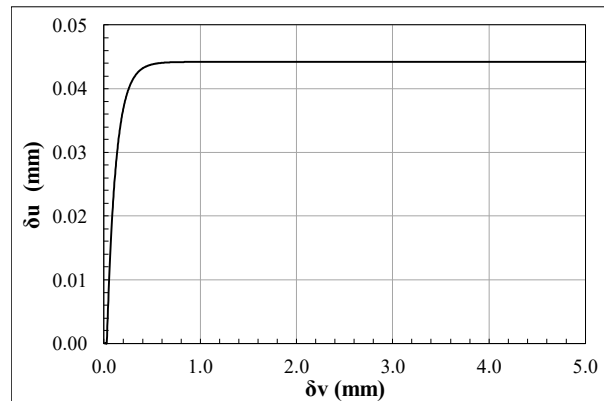


Figure 6.6. Model A1 – Numerical results: orthogonal displacements  $\delta u$  vs tangential displacement  $\delta v$ .

The evolution of the in-plane principal stress distributions on the masonry portion where the shove test is conducted is shown in Figure 6.7, Figure 6.8 and Figure 6.9. For each test phase, it is possible to recognize the following features:

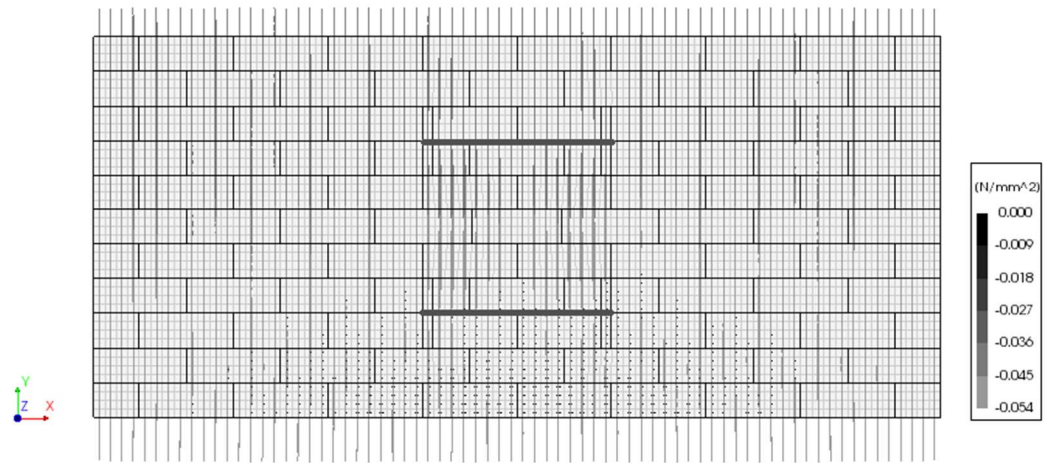
- Phase 1a - Self-weight of the wall panel (Figure 6.7a): the compression lines are vertical, and the in-plane principal compressive stresses are uniform on the cross section of the panel; the compressive stress due to vertical loads at the sliding brick height is 0.046 MPa.
- Phase 1b - Application of the overburden at the top of the wall (Figure 6.7b): the compression lines are vertical, providing a total uniform compressive stress at the sliding brick height equal to 0.15 MPa, including the self-weight.
- Phase 2 - Execution of the first cut for the seating of the superior flatjack (Figure 6.7c): due to the presence of the slot, the compression lines deviate from the vertical direction with an angle of approximately  $45^\circ$ , creating a parabolic unloaded area above and below the flatjack.

- Phase 3 - Execution of the second cut for the seating of the inferior flatjack (Figure 6.8a): as in the previous step, the compression lines deviate from the vertical direction with an angle of about 45°; the masonry portion between the flatjacks results almost unloaded.
- Phase 4 - Removal of the two bricks adjacent to the sliding brick (Figure 6.8b): the removal of two bricks produces a strong variation in the principal stress distribution. The vertical load given by the self-weight and the overburden partially deviates inwards on the tested brick, producing an increase in the compression stress and stress concentrations at the joint edges.
- Phase 5 - Application of the flatjack pressure (Figure 6.8c): due to the removal of the bricks, the compression lines between the two flatjacks are not vertical – this is particularly evident for low flatjack pressure values – but deviate partially on the sliding brick and partially outside the tested region, i.e. beyond the holes of the removed bricks. Also in this case, a stress concentration is evident at the joint edges of the sliding brick.
- Phase 6 - Application of the shear load (Figure 6.9): the in-plane principal stress distribution is strongly influenced by the presence of a shear load. Indeed, it produces lateral compression on the sliding brick, which is transferred with a diffusion cone, through the sliding joints, to the masonry above and below the test unit. The diffusion of the shear load inside the masonry produces also a variation in the compressive stress along the sliding joint. In Figure 6.9, three different steps of the analysis are considered: the application of the shear load (Figure 6.9a), the peak load (Figure 6.9b) and the residual phase (Figure 6.9c). The peak load obviously corresponds to the maximum shear stress sustained by the test unit. However, for Model A1, it also corresponds to the load step in which all the integration points reached the Coulomb friction failure domain. This aspect will be discussed later since it could be related, as already mentioned, to the identification of a dilatant behavior of masonry.

Focusing on the masonry portion between the two flatjacks, the in-plane principal stress distributions on the deformed configuration are shown in Figure 6.10, for three specific steps of the analysis:

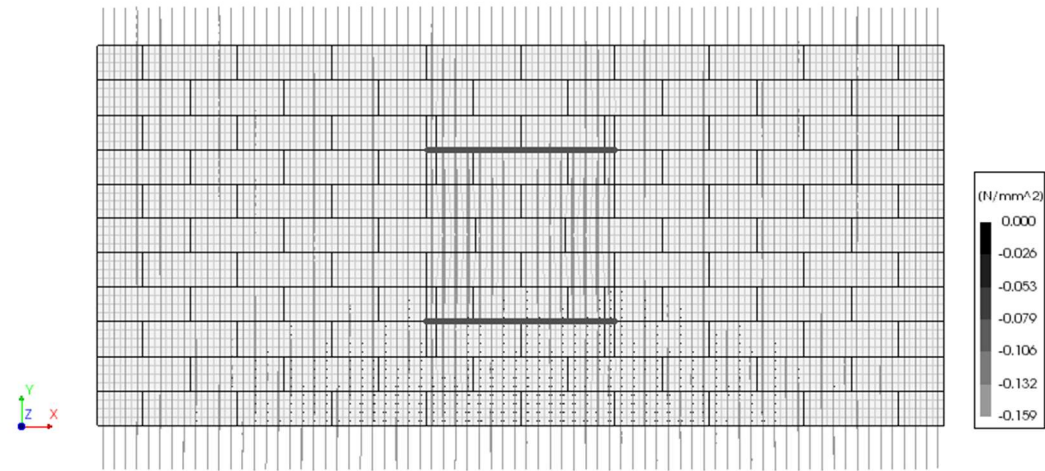
- Application of the flatjack pressure (Figure 6.10a);
- Peak shear load (Figure 6.10b): activation of the sliding along the entire interfaces and reaching of the maximum shear stress;
- Post-peak phase (Figure 6.10c): it is possible to observe the sliding of the brick with respect to the surrounding masonry and the dilatant behavior of the bed joints, i.e. the uplift upon shearing.

PhasedNL\_OB-015\_FJ005MPa  
 Phase1\_SWandOBApplication, Load-step 1, Load-factor 1.0000  
 Cauchy Total Stresses in-plane principal components



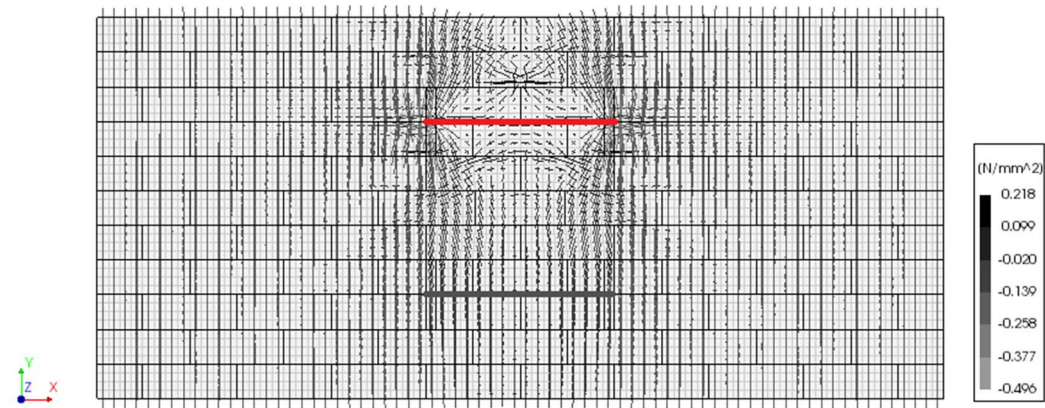
(a)

PhasedNL\_OB-015\_FJ005MPa  
 Phase1\_SWandOBApplication, Load-step 2, Load-factor 1.0000  
 Cauchy Total Stresses in-plane principal components



(b)

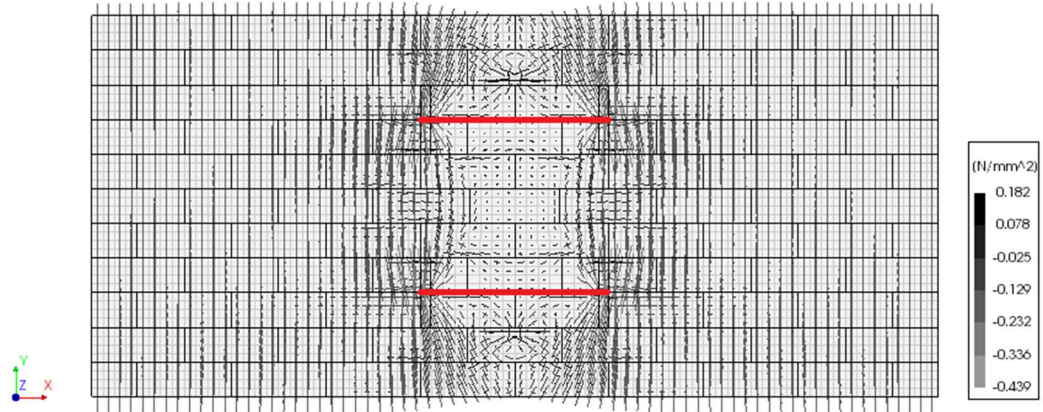
PhasedNL\_OB-015\_FJ005MPa  
 Phase2\_FirstCut, Start-step 1, Load-factor 1.0000  
 Cauchy Total Stresses in-plane principal components



(c)

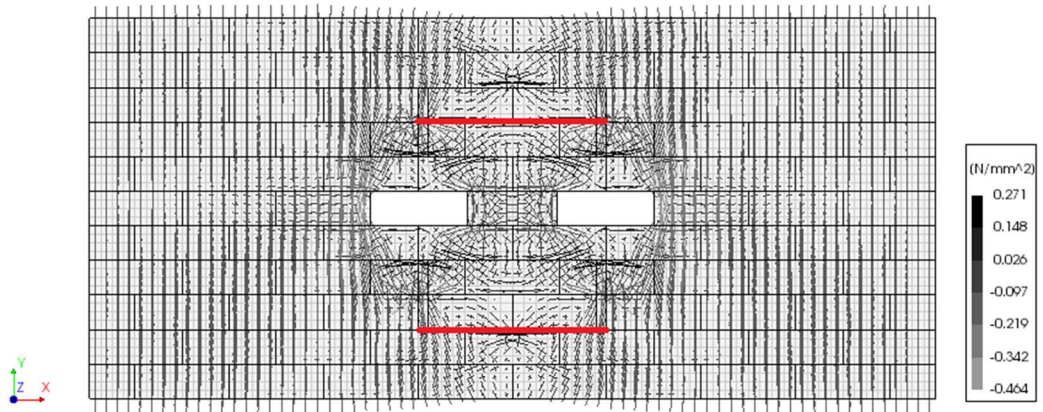
Figure 6.7. Model A1 – Principal stress distributions: (a) self-weight; (b) overburden application; (c) execution of the first cut.

PhasedNL\_OB-015\_FJ005MPa  
 Phase3\_SecondCut, Start-step 1, Load-factor 1.0000  
 Cauchy Total Stresses in-plane principal components



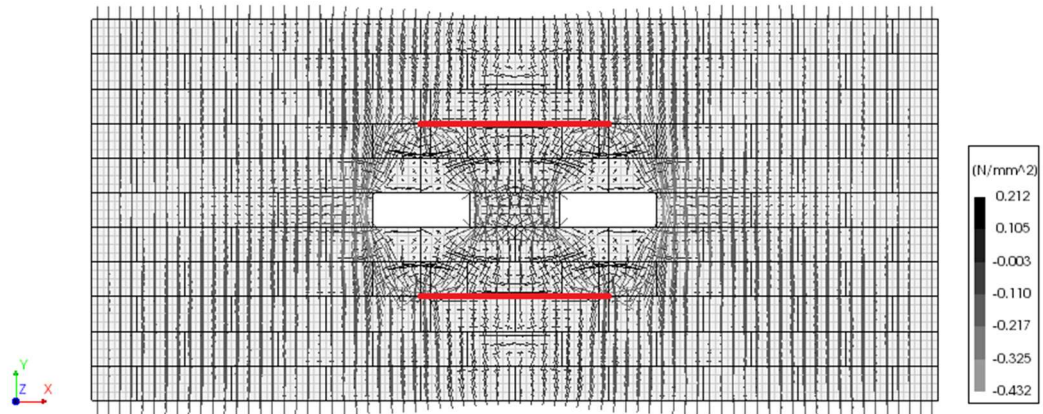
(a)

PhasedNL\_OB-015\_FJ005MPa  
 Phase4\_BricksRemoval, Start-step 1, Load-factor 1.0000  
 Cauchy Total Stresses in-plane principal components



(b)

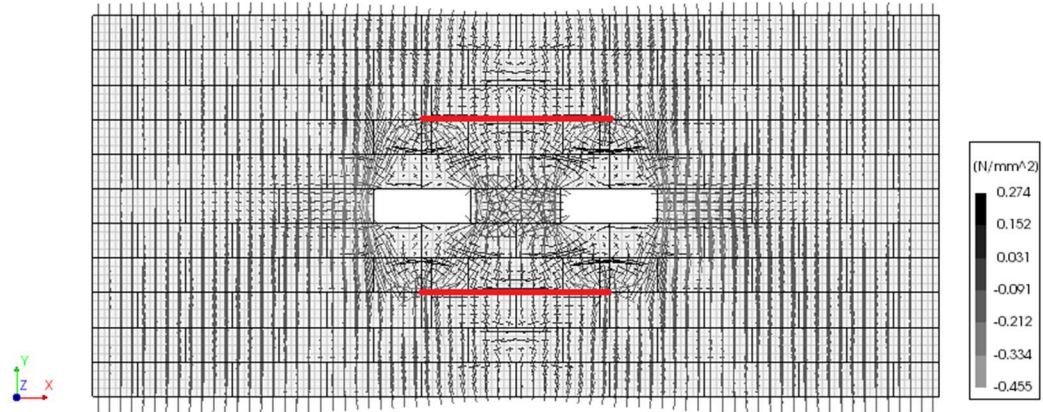
PhasedNL\_OB-015\_FJ005MPa  
 Phase5\_FJPressure, Load-step 1, Load-factor 1.0000  
 Cauchy Total Stresses in-plane principal components



(c)

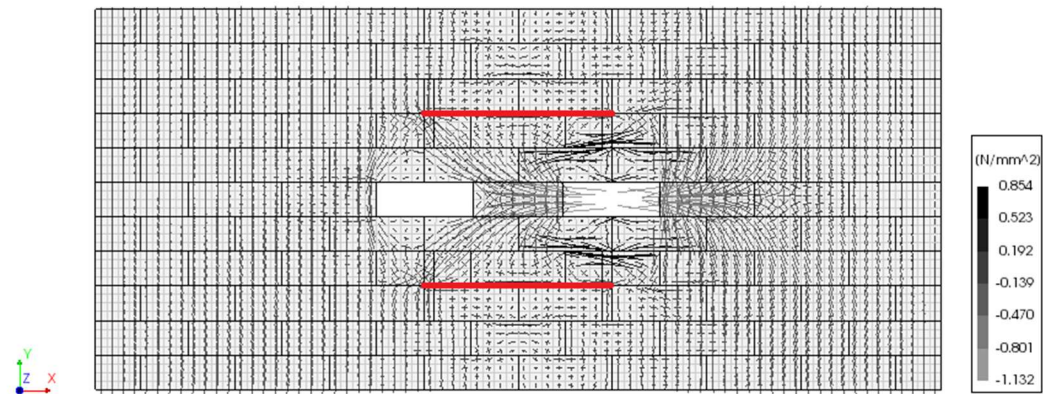
Figure 6.8. Model A1 – Principal stress distributions: (a) execution of the second cut; (b) removal of bricks; (c) application of the flatjack pressure.

PhasedNL\_OB-015\_FJ005MPa  
 Phase6\_Shear, Load-step 1, Load-factor 0.59182E-01  
 Cauchy Total Stresses in-plane principal components



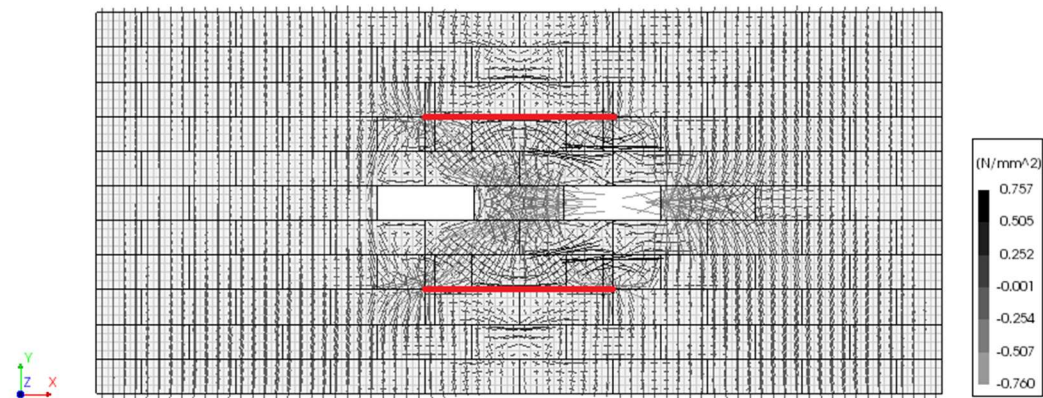
(a)

PhasedNL\_OB-015\_FJ005MPa  
 Phase6\_Shear, Load-step 14, Load-factor 0.75063  
 Cauchy Total Stresses in-plane principal components



(b)

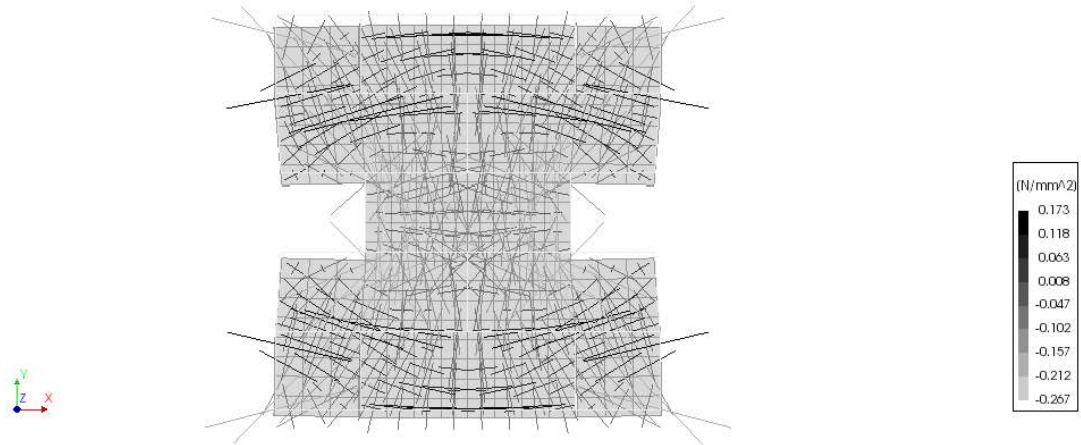
PhasedNL\_OB-015\_FJ005MPa  
 Phase6\_Shear, Load-step 400, Load-factor 0.47545  
 Cauchy Total Stresses in-plane principal components



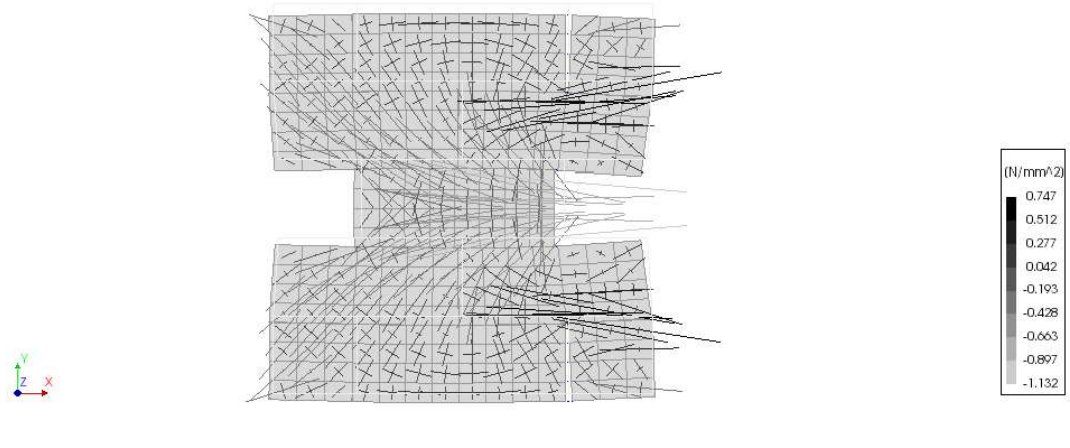
(c)

Figure 6.9. Model A1 – Principal stress distributions: (a) application of the shear load; (b) peak load; (c) residual branch.

PhasedNL\_OB-015\_FJ005MPa  
Phase5\_FJPressure, Load-step 1, Load-factor 1.0000  
Cauchy Total Stresses in-plane principal components



PhasedNL\_OB-015\_FJ005MPa  
Phase6\_Shear, Load-step 14, Load-factor 0.75063  
Cauchy Total Stresses in-plane principal components



PhasedNL\_OB-015\_FJ005MPa  
Phase6\_Shear, Load-step 42, Load-factor 0.63250  
Cauchy Total Stresses in-plane principal components

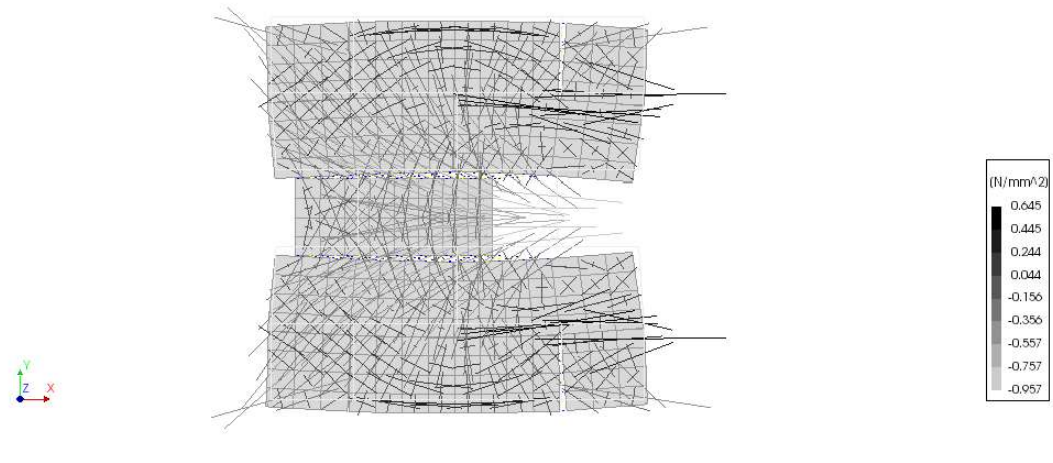


Figure 6.10. Model A1 – Principal stress distributions between flatjacks: (a) application of the flatjack pressure; (b) peak load; (c) post-peak phase.

The normal and tangential stress evolutions along the top and bottom sliding interfaces are reported in Figure 6.11 and Figure 6.12, respectively. The steps already analyzed for the in-plane principal stress distributions are here considered. For the tangential stresses, only the stress distributions at the peak load and in the residual phase are shown, given that they are null or negligible during the application of the vertical loads.

With reference to the normal stress evolutions on both the interfaces, uniform distributions are associated with the application of the self-weight and the overburden load, as expected. Then, relaxation of the masonry portion between the two cuts is registered, with decreasing compressive stresses along the interfaces, eventually going to zero after the execution of the second cut. Compressive stresses are slightly higher in this phase at the extremities of the sliding interfaces. Due to the bricks removal, the non-uniformity of the normal stress distributions becomes apparent, with quite high compressive stresses at the extremities of the joints. Analogous situation can be noticed in correspondence of the application of the flatjack pressure, which determines an increase of the compressive stress. When the shear load is applied – here the step corresponding to the peak load is considered – the compressive stresses increase significantly on the right-end side of the sliding interfaces, close to the application of the shear load. On the left-end side, instead, the state of stress remains almost unchanged with respect to the previous phase, where the flatjack pressure was applied. In the central portion of the joint, the discontinuity of the stress distributions is justified by the presence of the head joints above and below the superior and inferior interface, respectively. This determines, on one side of the head joint, a consistent decrease of the compressive stress, which results almost null or even positive; on the other side of the head joint, instead, a compression increase can be noticed. From a qualitative point of view, in correspondence of the peak load, the tangential stress distributions on both interfaces are similar to the normal stress ones, with higher shear stresses on the right-end side and a discontinuity in correspondence of the head joints. Smoother distributions can be observed in the residual phase, both for normal and tangential stresses.

The results presented for the Model A1 shows, in a quite evident manner, the extreme complexity connected to the execution of the shove test according to the *Method A* proposed by the ASTM Standard. In particular, great uncertainties are related to the estimation of the compressive stress acting on the joints during the entire duration of the test. The presence of the flatjacks, even if introduced to better control the state of stress on the tested brick, produces a great disturbance in the masonry wall – due to the cutting procedure – and strongly affects the in-plane stress distributions.

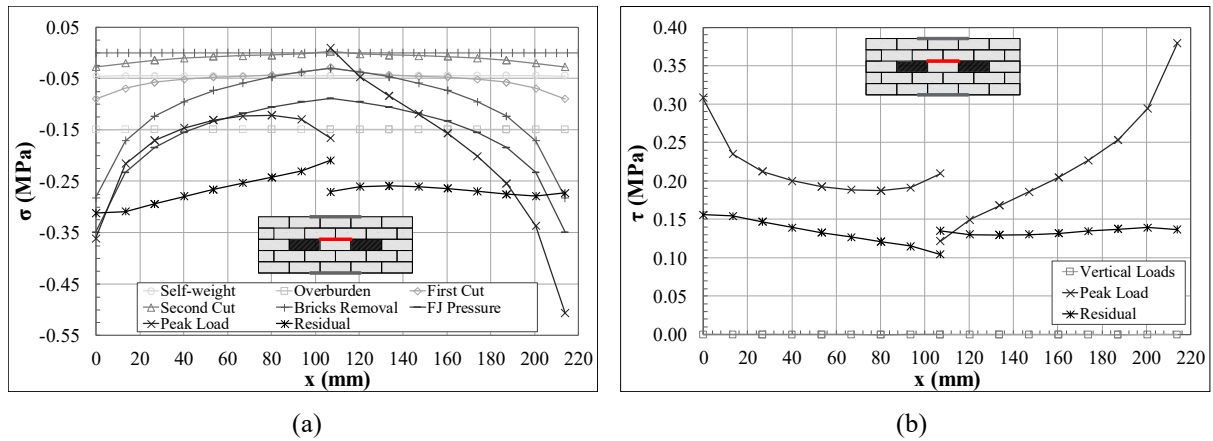


Figure 6.11- Model A1 – Stress evolution along the top sliding interface: (a) normal stress; (b) tangential stress.

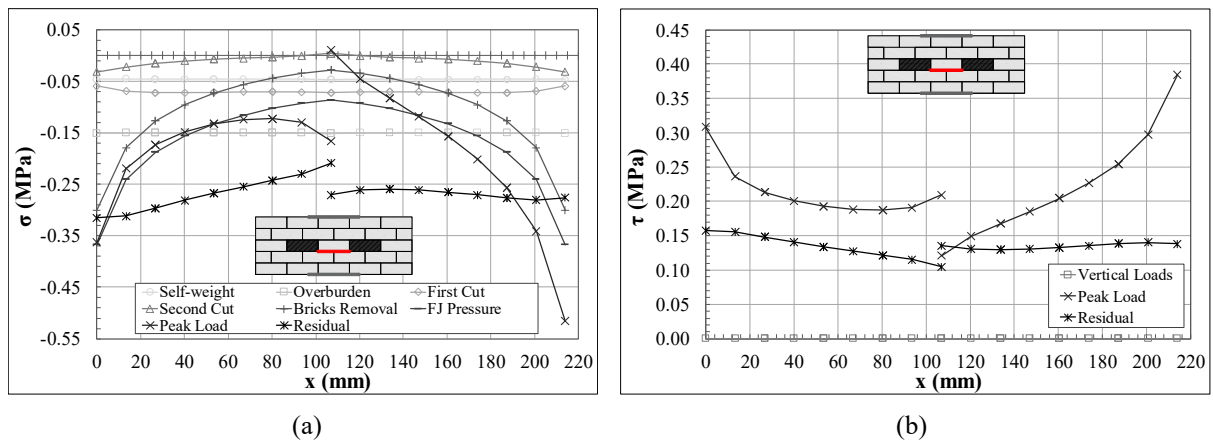


Figure 6.12- Model A1 – Stress evolution along the bottom sliding interface: (a) normal stress; (b) tangential stress.

The results of the numerical analyses for Model A1, A2 and A3 are reported together in Figure 6.13 and Figure 6.14 in terms of shear load  $F$  vs tangential displacement  $\delta v$  curves and shear stress  $\tau$  vs tangential displacement  $\delta v$  curves, respectively. The curves are all characterized by an initial almost linear branch up to the peak load, followed by softening and a residual phase, corresponding to the plateau. A smoother post-peak phase can be observed for Model A1 and A2. The increase of the overburden load in Model A2 and A3 determines an increase in the shear capacity of the tested brick. This is consistent with what observed for Model A1: due to the cutting of the slots for the seating of the flatjacks and the removal of bricks, the state of compression along the sliding interfaces is affected by the presence of the compressive stress given by the overburden, which partially goes on the test unit. In Figure 6.15, orthogonal displacement  $\delta u$  vs tangential displacement  $\delta v$  curves are reported. It is worth noting that the orthogonal displacement  $\delta u$  decreases as the overburden load, and consequently the

compressive stress on the test unit, increases. This is consistent with the dilatancy formulation presented in Section 4.

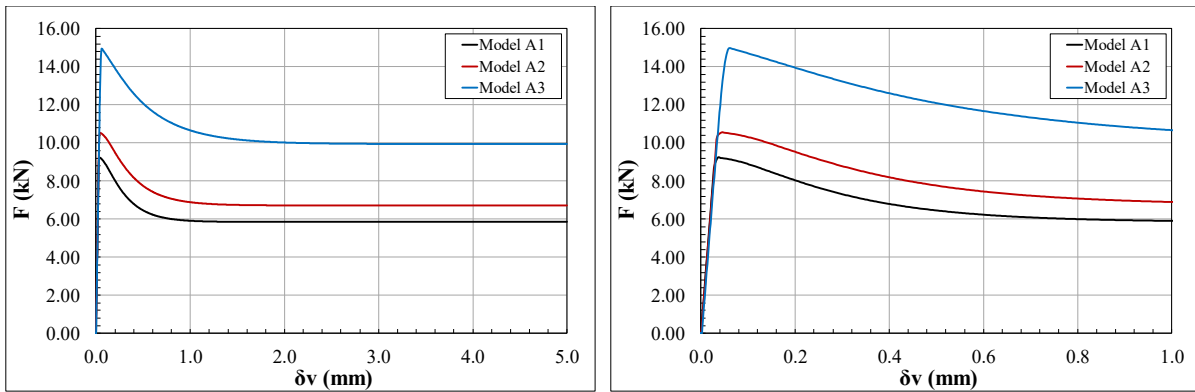


Figure 6.13. Numerical results – comparison: shear load  $F$  vs tangential displacement  $\delta v$  diagram.

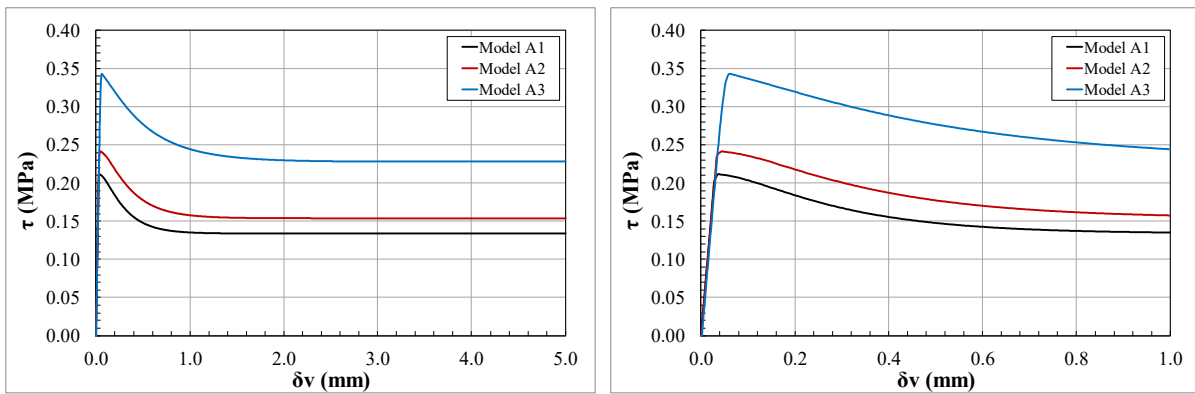


Figure 6.14. Numerical results - comparison: shear stress  $\tau$  vs tangential displacement  $\delta v$  diagram.

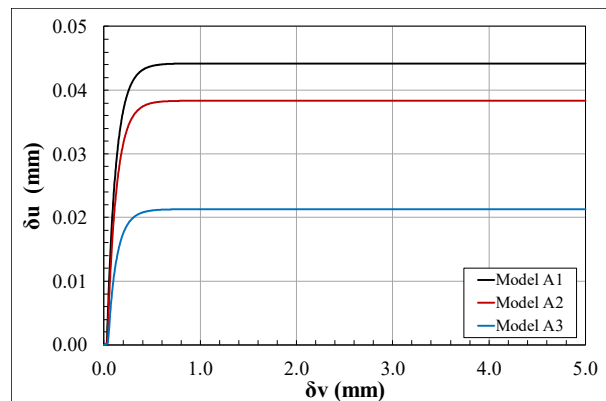


Figure 6.15. Numerical results - comparison: orthogonal displacements  $\delta u$  vs tangential displacement  $\delta v$ .

#### 6.1.4 Parametric studies on dilatancy

According to the variable formulation for dilatancy proposed by Van Zijl (2004) and used in this research, the dilatant behavior of masonry is governed by three parameters: the dilatancy angle at zero normal confining stress and shear slip ( $\psi_0$ ), the confining compressive stress at which the dilatancy becomes zero ( $\sigma_u$ ), and the dilatancy shear-slip degradation coefficient ( $\delta$ ). With the objective of analyzing the effect that each parameter can have on the shear-sliding response of a masonry unit in the shove test, parametric studies were performed by varying one parameter at a time, maintaining the others unchanged. In total, nine parametric analyses were carried out, as reported in Table 6.2, aimed at increasing the role of dilatancy for the considered models. In particular, greater values for  $\psi_0$  and  $\sigma_u$ , - considering the same increments - and lower values for  $\delta$  were chosen. In the followings, the results will be presented for Model A1 only, given that for lower acting compressive stresses, the effect of dilatancy is more evident.

Table 6.2. Shove test – *Method A*: parametric studies on dilatancy.

<b>Numerical simulation</b>	<b><math>\psi_0</math> (rad)</b>	<b><math>\sigma_u</math> (MPa)</b>	<b><math>\delta</math> (-)</b>
A1*	0.374	-0.58	9.63
A1_1b	0.561	-0.58	9.63
A1_1c	0.842	-0.58	9.63
A1_1d	1.262	-0.58	9.63
A1_2b	0.374	-0.87	9.63
A1_2c	0.374	-1.31	9.63
A1_2d	0.374	-1.96	9.63
A1_3b	0.374	-0.58	6.42
A1_3c	0.374	-0.58	4.28
A1_3d	0.374	-0.58	2.85

\*Reference parameters, calibrated through triplet test results.

In Figure 6.16, the plastic orthogonal displacement  $u_{pl}$  vs plastic tangential displacement  $v_{pl}$  curves are reported, for each set of parameters. These curves were not obtained from the numerical analyses, but were built according to Eq. (6.1), already introduced in Section 4.1.2, considering the average compressive stress  $\sigma$  present on the joint after the removal of the bricks in Model A1:

$$u_{pl} = \frac{\Psi_0}{\delta} \left( 1 - \frac{\sigma}{\sigma_u} \right) \left( 1 - e^{-\delta v_{pl}} \right). \quad (6.1)$$

Therefore, considering also that the compressive stress is variable during the test, they just provide general indications to be compared with the results of the parametric analyses. For a better comparison, the values of the plastic orthogonal displacement from Eq. (6.1) were doubled to account for the presence of both the joints along which the sliding occur. From Figure 6.16, it is possible to observe that the parameter influencing the most the value of the plastic orthogonal displacement is the initial dilatancy angle  $\psi_0$ . In the compressive stress range considered, variations of the confining stress  $\sigma_u$  do not seem to be relevant. The parameter  $\delta$ , instead, besides having a slight influence (if compared with  $\psi_0$ ) on the value of the plastic orthogonal displacement, affects more the position of the curve plateau, which is linked to a slower exponential decay of the function.

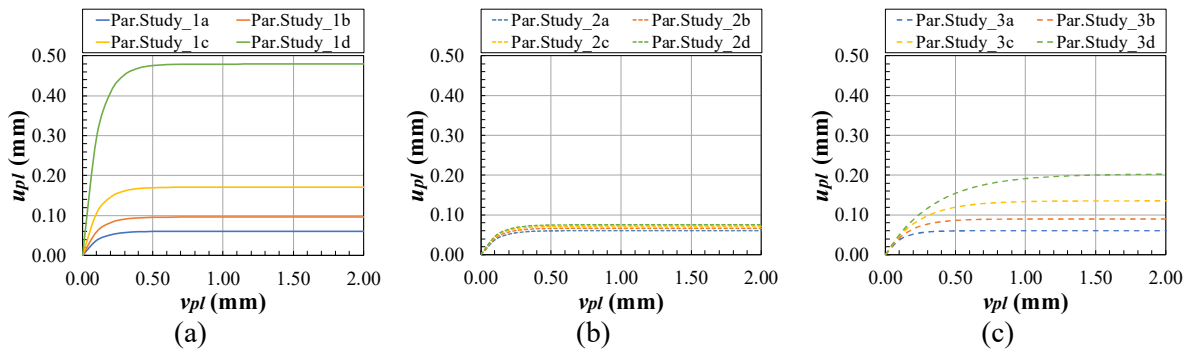


Figure 6.16. Theoretical plastic orthogonal displacement  $u_{pl}$  vs plastic tangential displacement  $v_{pl}$  curves: (a) parametric studies on  $\psi_0$ ; (b) parametric studies on  $\sigma_u$ ; (c) parametric studies on  $\delta$ .

Before analyzing the results of the parametric analyses, it should be noticed that, in the numerical model of the shove test, the vertical displacement cannot be considered completely free. Indeed, even if the vertical translation is not constrained at the top of the panel, the masonry outside the tested region could act as a sort of impediment to the uplift along the sliding joints. Consequently, if volume expansion is restrained to some extent, the orthogonal displacements registered are lower than the ones from the theoretical curves of Figure 6.16, and correspondent increases in the compressive stress state on the sliding interfaces can be observed, leading to an increase in the shear strength. Notice that in Figure 6.19, Figure 6.22, Figure 6.25, and Figure 6.28, total orthogonal ( $\delta u$ ) and tangential ( $\delta v$ ) displacements are reported, not their plastic components. Indeed, the displacement  $\delta u$  is calculated as the average of the differences between the vertical displacements of two pairs of points, positioned above and below the test unit, including both the joints involved in the sliding failure. This representation is more practical since it gives an average value of the orthogonal displacement, which can be directly compared with results from experimental tests.

The results of the parametric analyses are presented in Figure 6.17-Figure 6.25, in terms of: load  $F$  vs tangential displacement  $\delta v$ , shear stress  $\tau$  vs tangential displacement  $\delta v$ , and orthogonal displacement  $\delta u$  vs tangential displacement  $\delta v$ . In Figure 6.26-Figure 6.28, global comparisons are shown. In Table 6.3, a summary of the results is presented to quantitatively evaluate the differences between the considered models in terms of peak load ( $P_{peak}$ ), average shear strength ( $\tau_{max}$ ), average compressive stress at the peak ( $\sigma_{max}$ ), tangential displacement at the peak ( $\delta v_{peak}$ ), and orthogonal displacement at the peak ( $\delta u_{peak}$ ).

The parametric studies on  $\psi_0$  (Figure 6.17-Figure 6.19) shows significant increments in the shear capacity with respect to *Model A1* (up to 54%), which are obviously related to compressive stress increases. Indeed, in these cases, the orthogonal displacements registered are much smaller than the theoretical ones (Figure 6.16a), indicating that they are restrained due to the test conditions. Dilatancy is therefore playing a role and determines an increase in the peak load. The effect of dilatancy on the shear response is also visible looking at the  $F$ -  $\delta v$  and  $\tau$ -  $\delta v$  curves, where the failure load (corresponding to the point in which the failure criterion is reached in all the integration points of the interfaces) and the peak load can be distinctly identified. In particular, the failure load coincides with the peak of the curve for *Model A1* and it is the same in all the models. Beyond this point, the dilatant behavior of masonry, which plays a role in the nonlinear field, determines the mentioned increase in capacity.

For parametric studies on  $\sigma_u$  (Figure 6.20-Figure 6.22) it can be noticed how variations on this parameter do not produce significant changes in the sliding behavior during the shove test, except from a smoother transition between the peak load and the softening branch. Orthogonal displacements are slightly lower than the theoretical ones, but not as much as to produce an increase in the shear capacity. These observations are strictly connected to the compressive state of stress in the model considered, since it is the ratio  $\sigma/\sigma_u$  which governs the phenomenon.

The parameter  $\delta$ , looking at the results reported in Figure 6.23-Figure 6.25, rather than influencing the shear response in terms of capacity, affects the trend of the post-peak branch. The lower its value, the less steep is the softening branch, even reaching an almost constant plateau after the failure load for the lowest  $\delta$  value considered. Orthogonal displacements are globally lower than the theoretical ones for all the considered analyses, but no increases in the peak load are observed. This can be explained considering that the orthogonal displacements at the peak load, for *Model A1\_3b* and *A1\_3c*, are almost the same as for *Model A1* and equal to the theoretical ones. Therefore, an increase in the capacity could not be expected for these models.

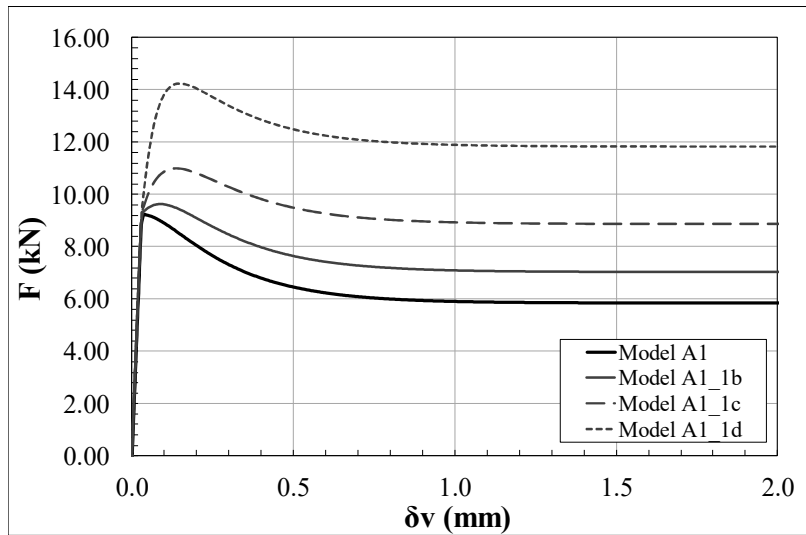


Figure 6.17. Parametric studies on  $\psi_0$ : shear load  $F$  vs tangential displacement  $\delta v$  diagram.

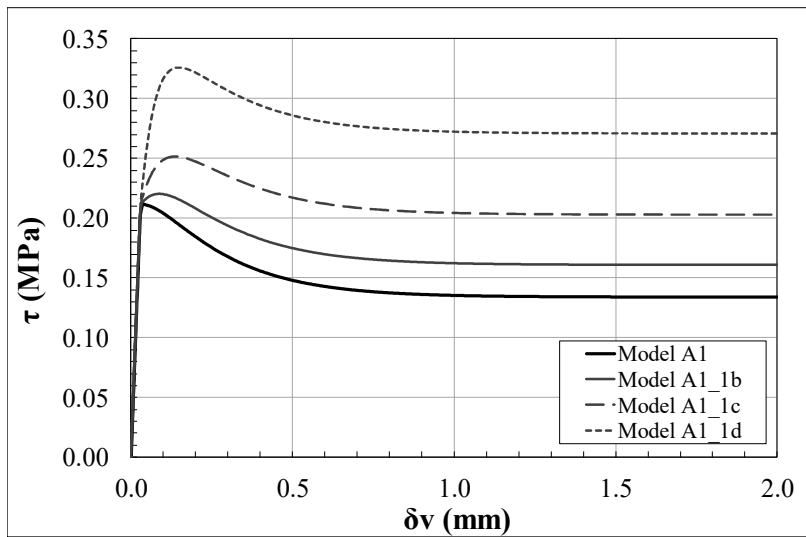


Figure 6.18. Parametric studies on  $\psi_0$ : shear stress  $\tau$  vs tangential displacement  $\delta v$  diagram.

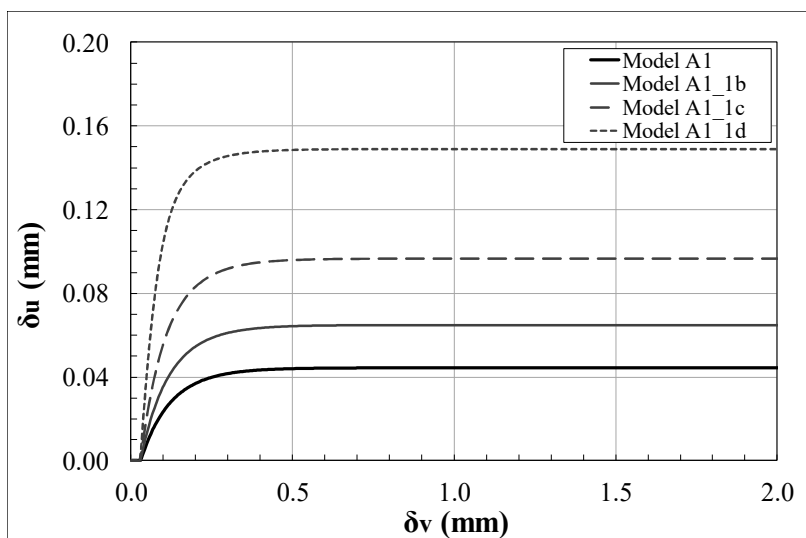


Figure 6.19. Parametric studies on  $\psi_0$ : orthogonal displacements  $\delta u$  vs tangential displacement  $\delta v$ .

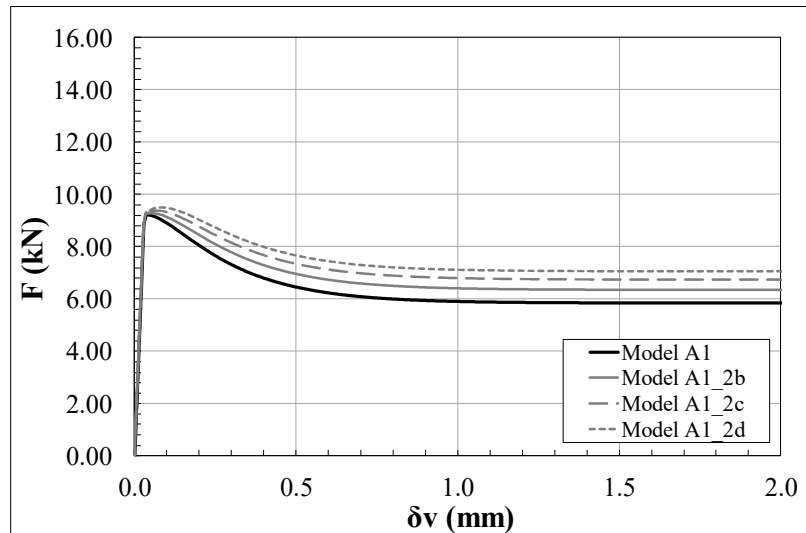


Figure 6.20. Parametric studies on  $\sigma_u$ : shear load  $F$  vs tangential displacement  $\delta v$  diagram.

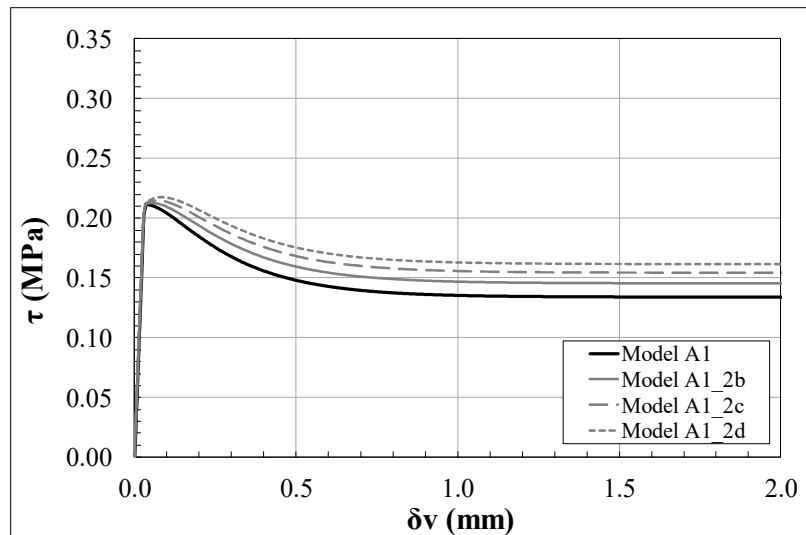


Figure 6.21. Parametric studies on  $\sigma_u$ : shear stress  $\tau$  vs tangential displacement  $\delta v$  diagram.

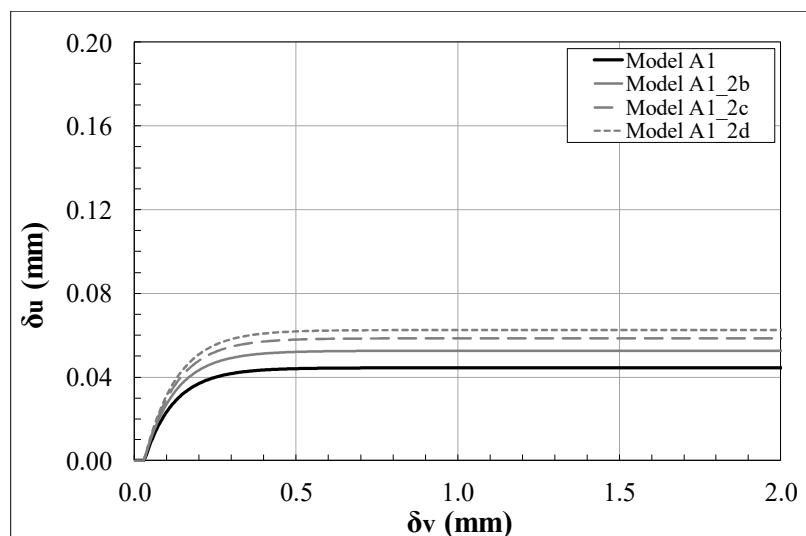


Figure 6.22. Parametric studies on  $\sigma_u$ : orthogonal displacements  $\delta u$  vs tangential displacement  $\delta v$ .

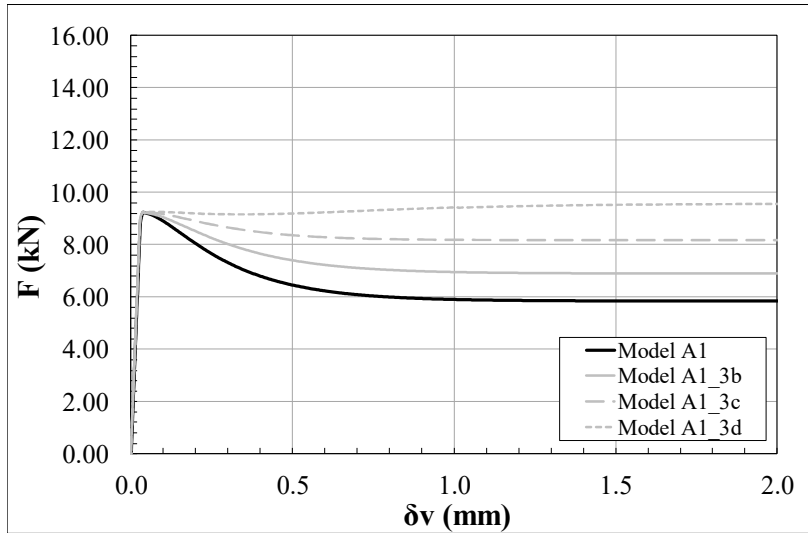


Figure 6.23. Parametric studies on  $\delta$ : shear load  $F$  vs tangential displacement  $\delta v$  diagram.

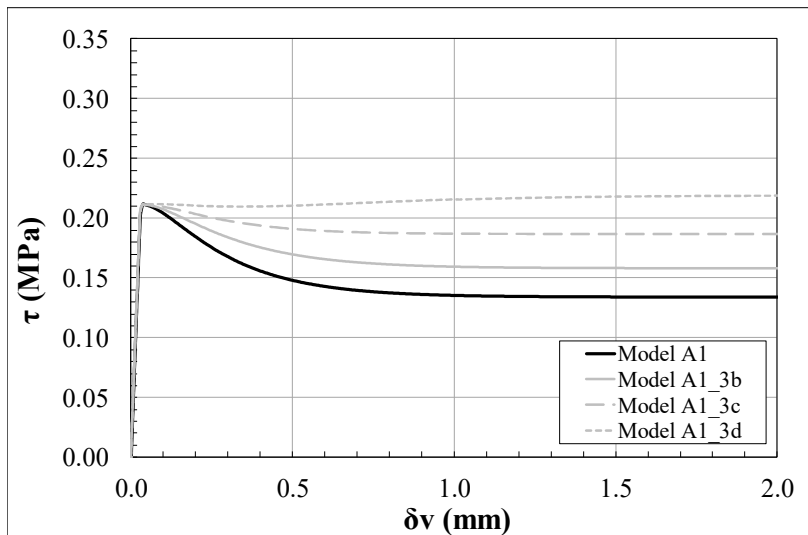


Figure 6.24. Parametric studies on  $\delta$ : shear stress  $\tau$  vs tangential displacement  $\delta v$  diagram.

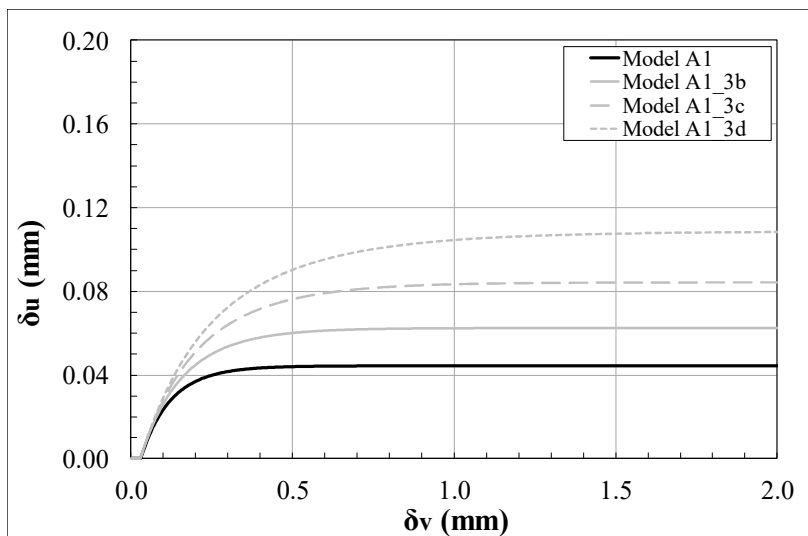


Figure 6.25. Parametric studies on  $\delta$ : orthogonal displacements  $\delta u$  vs tangential displacement  $\delta v$ .

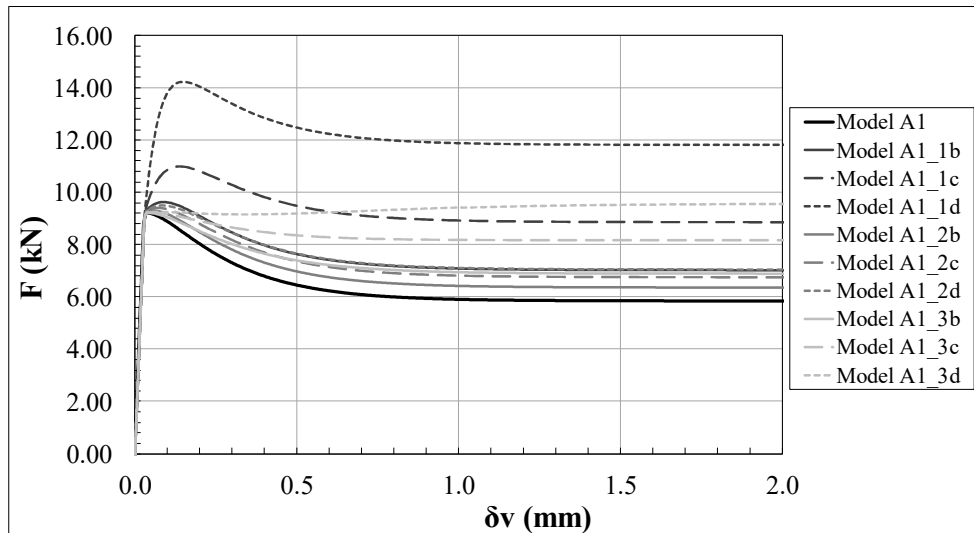


Figure 6.26. Parametric studies - comparison: shear load  $F$  vs tangential displacement  $\delta v$  diagram.

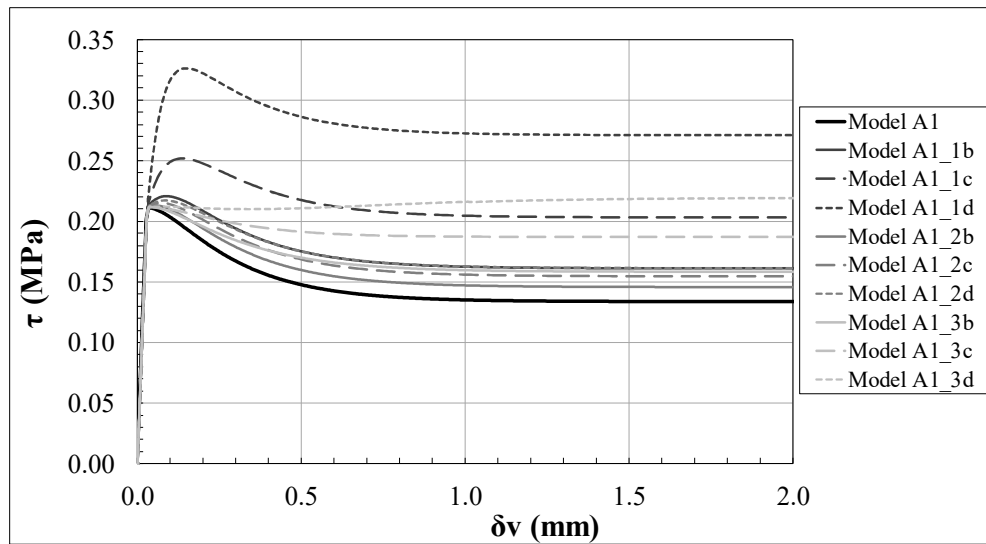


Figure 6.27. Parametric studies - comparison: shear stress  $\tau$  vs tangential displacement  $\delta v$  diagram.

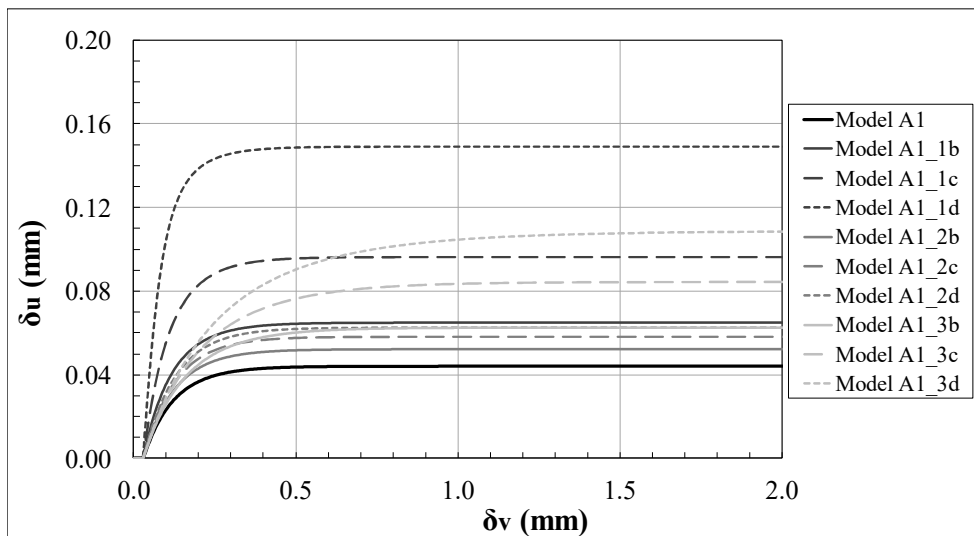


Figure 6.28. Parametric studies - comparison: orthogonal displacement  $\delta u$  vs tangential displacement  $\delta v$  diagram.

Table 6.3. Model A1 – Results of the parametric analyses.

<b>Model</b>	<b><math>\psi_0</math> (rad)</b>	<b><math>\sigma_u</math> (MPa)</b>	<b><math>\delta</math> (-)</b>	<b><math>P_{peak}</math> (kN)</b>	<b><math>\tau_{max}</math> (MPa)</b>	<b><math>\sigma_{max}</math> (MPa)</b>	<b><math>\delta v_{,peak}</math> (mm)</b>	<b><math>\delta u_{,peak}</math> (mm)</b>
Model A1	0.374	-0.58	9.63	9.23	0.211	0.163	0.036	0.003
Model A1_1b	0.561	-0.58	9.63	9.63	0.221	0.181	0.087	0.030
	50.0%	(-)	(-)	4.3%	4.3%	11.2%	140.6%	1021.2%
Model A1_1c	0.842	-0.58	9.63	11.00	0.252	0.244	0.138	0.068
	125.1%	(-)	(-)	19.1%	19.1%	49.7%	282.7%	2396.9%
Model A1_1d	1.262	-0.58	9.63	14.23	0.326	0.39	0.140	0.125
	237.4%	(-)	(-)	54.2%	54.2%	140.6%	289.7%	4512.8%
Model A1_2b	0.374	-0.87	9.63	9.29	0.215	0.17	0.054	0.011
	(-)	50.0%	(-)	0.6%	1.7%	4.5%	48.6%	316.2%
Model A1_2c	0.374	-1.31	9.63	9.39	0.215	0.17	0.071	0.020
	(-)	125.9%	(-)	1.7%	1.7%	4.5%	97.4%	626.9%
Model A1_2d	0.374	-1.96	9.63	9.49	0.217	0.17	0.083	0.025
	(-)	237.9%	(-)	2.8%	2.8%	7.3%	129.7%	833.3%
Model A1_3b	0.374	-0.58	6.42	9.23	0.212	0.16	0.037	0.003
	(-)	(-)	-33.3%	0.0%	0.0%	0.0%	2.9%	19.8%
Model A1_3c	0.374	-0.58	4.28	9.24	0.212	0.16	0.036	0.003
	(-)	(-)	-55.6%	0.1%	0.1%	0.1%	-0.2%	1.8%
Model A1_3d	0.374	-0.58	2.85	9.56	0.219	0.18	2.420	0.109
	(-)	(-)	-70.4%	3.6%	3.6%	9.3%	6615.8%	3907.5%

### 6.1.5 Correction factors for vertical loads

As introduced in previous Sections, the in-plane principal stress distributions and the compressive state of stress along the sliding joint could be strongly influenced, during the different phases of the test, by the presence of the slots for the seating of the flatjacks, by the removal of bricks, by the diffusion of the shear load, and by dilatancy. Therefore, the compressive stress acting on the sliding brick is far away from being equal to the pressure applied by flatjacks. In the model considered, given the reduced effect of dilatancy on the results, the actual value consists of basically two contributions: the first one is given by the vertical load acting on the wall, namely the self-weight and the overburden, the second one is given by the flatjacks. In order to evaluate these contributions, one possibility is to calibrate correction factors, given the stress distributions in the different phases of the test from the numerical model.

The characteristics of masonry surely affect the way in which vertical loads are deviated from the vertical direction, e.g. head joints not transmitting tensile stresses, etc. Therefore, in the followings, four different cases are considered for the evaluation of the above-mentioned correction factors:

- Elastic joints;

- No tension material for vertical and horizontal mortar joints with constant shear stiffness;
- No tension material for vertical and horizontal mortar joints with reduced shear stiffness (a reduction of 50% is considered);
- No tension material for vertical and horizontal mortar joints with zero shear stiffness.

The stress distributions are evaluated for top and bottom sliding joints, in each test phase. Then, the average compressive stress is calculated and compared with the nominal value applied (as overburden or as flatjack pressure) in that phase. In this way, by multiplying the correction factors and the nominal values of the overburden load and the flatjack pressure, the compressive stress acting on the sliding joint can be correctly evaluated. In Table 6.4-Table 6.7 are reported the results obtained in terms of average stresses in each phase, and in Table 6.8 is reported a summary of the correction factors. It can be noticed how, by decreasing the shear stiffness of the joints, the correction factor for vertical load decreases, while the correction factor for the flatjack pressure increases, which is consistent with the influence that the shear stiffness has on the diffusion of the stresses inside the masonry.

Table 6.4. Model A1 – Elastic joints: equivalent normal and tangential stresses.

Step	Top joint		Bottom joint		Mean	
	$\sigma_{equiv.}$ (MPa)	$\tau_{equiv.}$ (MPa)	$\sigma_{equiv.}$ (MPa)	$\tau_{equiv.}$ (MPa)	$\sigma_{equiv.}$ (MPa)	$\tau_{equiv.}$ (MPa)
1 - Self-Weight	-0.045	0.000	-0.046	0.000	<b>-0.045</b>	0.000
2 - Overburden	-0.149	0.000	-0.151	0.000	<b>-0.150</b>	0.000
3 - First cut	-0.059	0.000	-0.079	0.000	<b>-0.069</b>	0.000
4 - Second cut	-0.018	0.000	-0.018	0.000	<b>-0.018</b>	0.000
5 - Brick removal	-0.111	-0.006	-0.112	0.007	<b>-0.111</b>	0.000
6 - FJ Pressure	-0.166	-0.006	-0.167	0.006	<b>-0.166</b>	0.000

Table 6.5. Model A1 – No tension & constant shear stiffness: equivalent normal and tangential stresses.

Step	Top joint		Bottom joint		Mean	
	$\sigma_{equiv.}$ (MPa)	$\tau_{equiv.}$ (MPa)	$\sigma_{equiv.}$ (MPa)	$\tau_{equiv.}$ (MPa)	$\sigma_{equiv.}$ (MPa)	$\tau_{equiv.}$ (MPa)
1 - Self-Weight	-0.045	0.000	-0.046	0.000	<b>-0.045</b>	0.000
2 - Overburden	-0.149	0.000	-0.151	0.000	<b>-0.150</b>	0.000
3 - First cut	-0.052	0.000	-0.070	0.000	<b>-0.061</b>	0.000
4 - Second cut	-0.010	0.000	-0.010	0.000	<b>-0.010</b>	0.000
5 - Brick removal	-0.095	0.000	-0.097	0.000	<b>-0.096</b>	0.000
6 - FJ Pressure	-0.155	0.000	-0.157	0.000	<b>-0.156</b>	0.000

Table 6.6. Model A1 – No tension & reduced shear stiffness: equivalent normal and tangential stresses.

Step	Top joint		Bottom joint		Mean	
	$\sigma_{equiv.}$ (MPa)	$\tau_{equiv.}$ (MPa)	$\sigma_{equiv.}$ (MPa)	$\tau_{equiv.}$ (MPa)	$\sigma_{equiv.}$ (MPa)	$\tau_{equiv.}$ (MPa)
1 - Self-Weight	-0.045	0.000	-0.046	0.000	<b>-0.045</b>	0.000
2 - Overburden	-0.149	0.000	-0.151	0.000	<b>-0.150</b>	0.000
3 - First cut	-0.053	0.000	-0.068	0.000	<b>-0.060</b>	0.000
4 - Second cut	-0.010	0.000	-0.010	0.000	<b>-0.010</b>	0.000
5 - Brick removal	-0.094	0.000	-0.096	0.000	<b>-0.095</b>	0.000
6 - FJ Pressure	-0.155	0.000	-0.156	0.000	<b>-0.155</b>	0.000

Table 6.7. Model A1 – No tension &amp; zero shear stiffness: equivalent normal and tangential stresses.

Step	Top joint		Bottom joint		Mean	
	$\sigma_{equiv.}$ (MPa)	$\tau_{equiv.}$ (MPa)	$\sigma_{equiv.}$ (MPa)	$\tau_{equiv.}$ (MPa)	$\sigma_{equiv.}$ (MPa)	$\tau_{equiv.}$ (MPa)
1 - Self-Weight	-0.045	0.000	-0.046	0.000	<b>-0.045</b>	0.000
2 - Overburden	-0.149	0.000	-0.151	0.000	<b>-0.150</b>	0.000
3 - First cut	-0.056	0.000	-0.058	0.000	<b>-0.057</b>	0.000
4 - Second cut	-0.009	0.000	-0.011	0.000	<b>-0.010</b>	0.000
5 - Brick removal	-0.085	0.000	-0.087	0.000	<b>-0.086</b>	0.000
6 - FJ Pressure	-0.148	0.000	-0.150	0.000	<b>-0.149</b>	0.000

Table 6.8. Model A1 – Correction factors.

Model	Vertical loads*	Flatjack pressure
Elastic joints	0.74	1.10
No tension & constant shear stiffness	0.64	1.21
No tension & reduced shear stiffness	0.63	1.21
No tension & zero shear stiffness	0.58	1.25

\*self-weight and overburden

## 6.2 Shove test – Method B

### 6.2.1 Testing procedure

The testing procedure consists in applying a uniform distributed load at the top of a masonry panel, reproducing the dead and live loads which can be present in situ. Then, the masonry unit to be subjected to the test is chosen and two bricks have to be removed from its opposite ends. The horizontal load is applied to the test unit by means of a hydraulic jack. The load is increased monotonically until the obtainment of the sliding failure of the brick. The geometry of the wall, with the identification of the test location, which is the same considered for *Method A*, is reported in Figure 6.29.

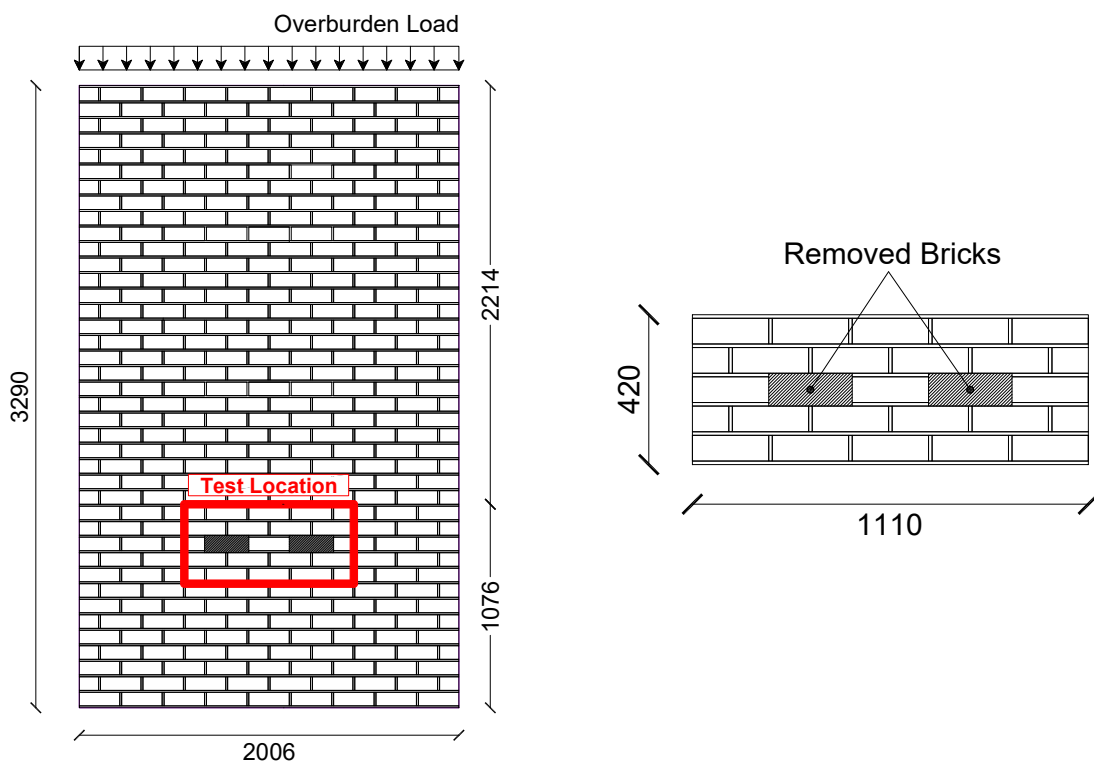


Figure 6.29. Shove test – *Method B*: wall geometry and test location.

### 6.2.2 Numerical model

The detail of the mesh used in the numerical model is shown in Figure 6.30. A 2D model and a simplified micro-modeling strategy were considered also in this case. The same modeling choices described for *Method A* in Section 6.1.2 were here adopted. The input parameters used in the numerical models for masonry are the same used for the numerical simulations of the triplet test and have been reported in Table 5.4.

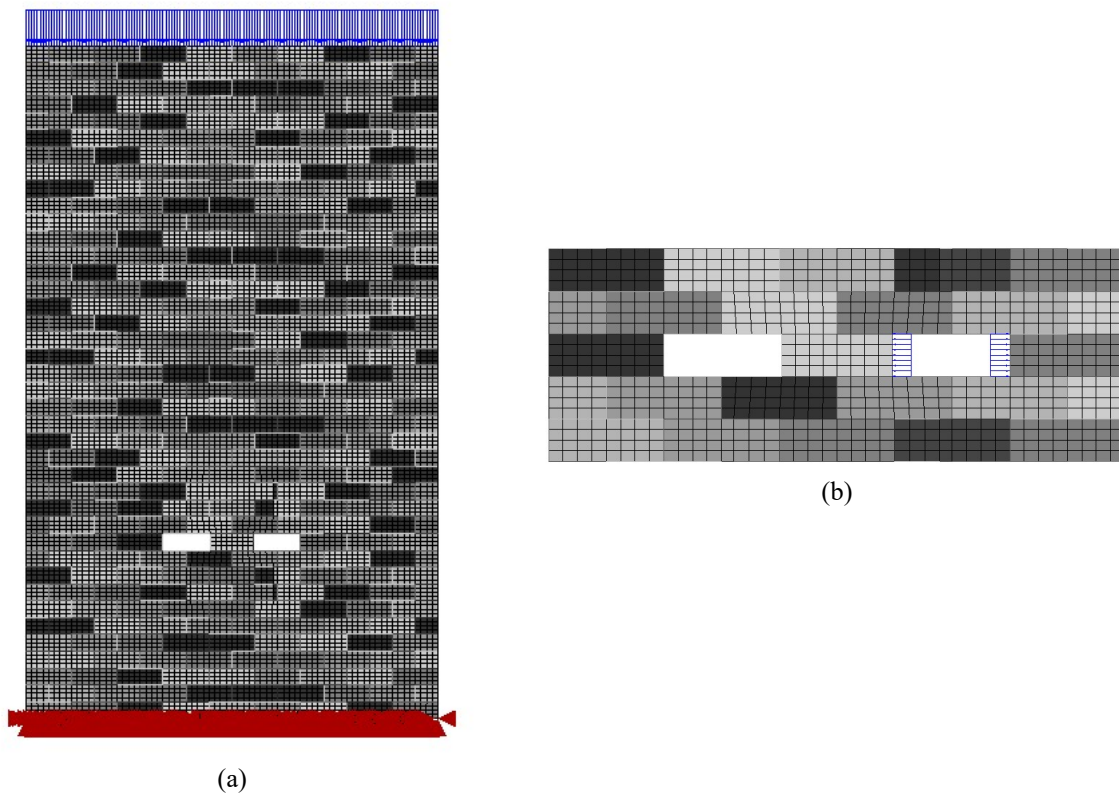


Figure 6.30. Shove test - *Method B*, finite element model: (a) entire wall panel; (b) detail of the shear load application.

The finite element software DIANA FEA (Release 10.1) was adopted for the numerical simulations. Phased analyses were carried out to exactly reproduce the testing procedure:

- Phase 1: application of the self-weight and the overburden;
- Phase 2: removal of bricks;
- Phase 3: application of the shear load.

The nonlinear analyses were performed by imposing an increasing horizontal load both to the sliding and the contrast brick, to reproduce the presence of the horizontal hydraulic jack. Regular Newton-Raphson method and arc-length method were adopted to solve the nonlinear problem.

### 6.2.3 Numerical results

The results of three numerical simulations of the shove test, according to the procedure reported in the Standard for *Method B*, will be presented in this Section. Different loading conditions were considered, as reported in Table 6.9. In particular, the same overburden loads considered in *Method A* were applied at the top of the masonry wall to provide a comparison of the two methodologies when the tests are executed on the same existing masonry wall.

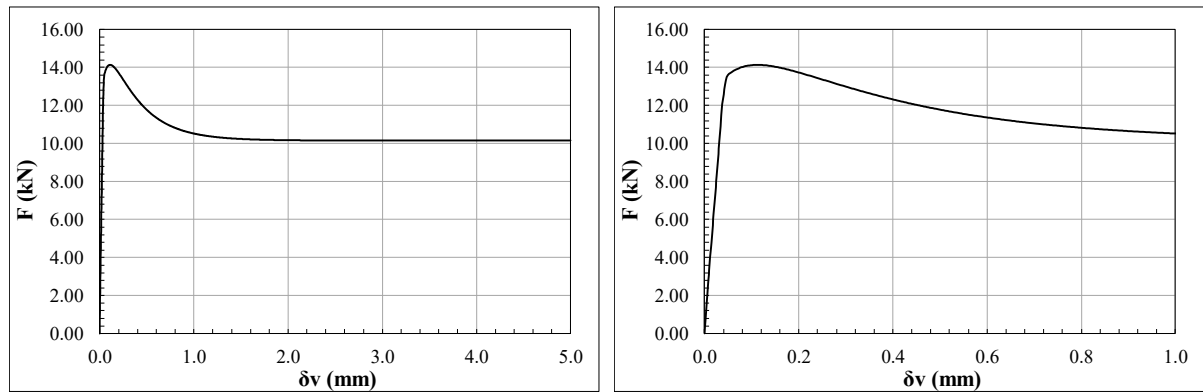
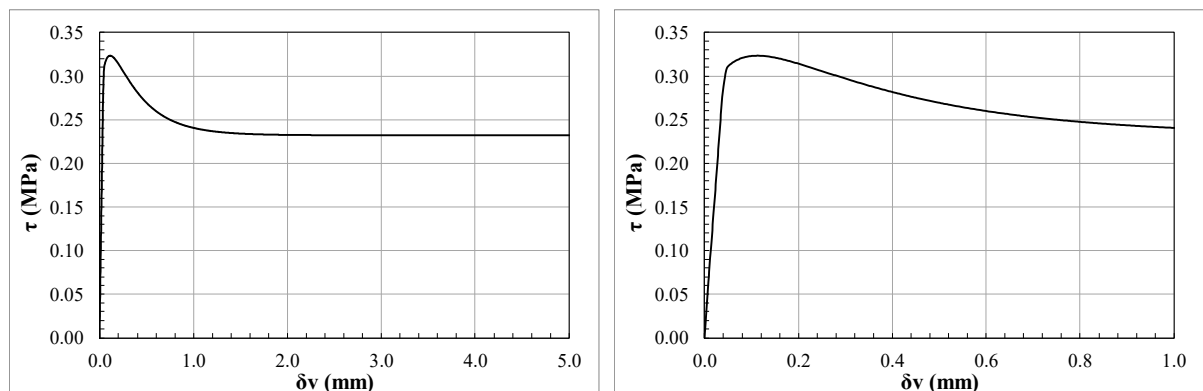
Table 6.9. Shove test – *Method B*: loading conditions for the numerical simulations.

Model	Overburden Load (kN)	Vertical compression* (MPa)
B1	21.28	0.15
B2	41.74	0.25
B3	113.36	0.60

\*given by self-weight and overburden on the sliding brick at the beginning of the test

First of all, the results of Model B1 will be analyzed in detail to properly understand the shear-sliding behavior investigated in the shove test. Then, a comparison between the main outcomes of the three numerical simulations will be presented.

The shear load  $F$  vs tangential displacement  $\delta v$  curve and the shear stress  $\tau$  vs tangential displacement  $\delta v$  curve are presented in Figure 6.31 and Figure 6.32; respectively. They are both characterized by an initial linear behavior up to the failure load, followed by a hardening phase, in which the peak load is reached, a softening branch and a residual phase, namely the dry-friction phase.

Figure 6.31. Model B1 – Numerical results: shear load  $F$  vs tangential displacement  $\delta v$  diagram.Figure 6.32. Model B1 – Numerical results: shear stress  $\tau$  vs tangential displacement  $\delta v$  diagram.

To investigate dilatancy, the orthogonal displacement  $\delta u$  vs tangential displacement  $\delta v$  graph is reported in Figure 6.33. Also in this case, to evaluate the average orthogonal displacement  $\delta u$ , the differences between the vertical displacements of two pairs of points, positioned above and below the test unit, were considered. It is possible to observe that, in the first part of the test, the masonry portion is subjected to compression. Then, as soon as the failure load is reached, the orthogonal displacement  $\delta u$  registered a positive increase, indicating a volume expansion during the sliding of the brick. Here, dilatancy seems to play a role in enhancing the shear capacity of masonry, with a little increase noticeable from the failure load to the peak load.

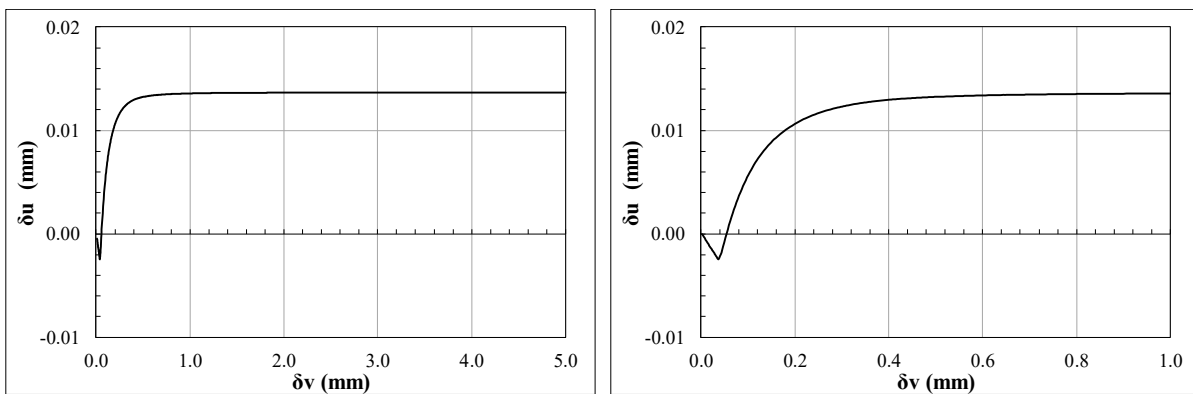


Figure 6.33. Model B1 – Numerical results: orthogonal displacements  $\delta u$  vs tangential displacement  $\delta v$ .

The evolution of the in-plane principal stress distributions on the masonry portion where the shove test is conducted is shown in Figure 6.34 and Figure 6.35. For each test phase, it is possible to recognize the following features:

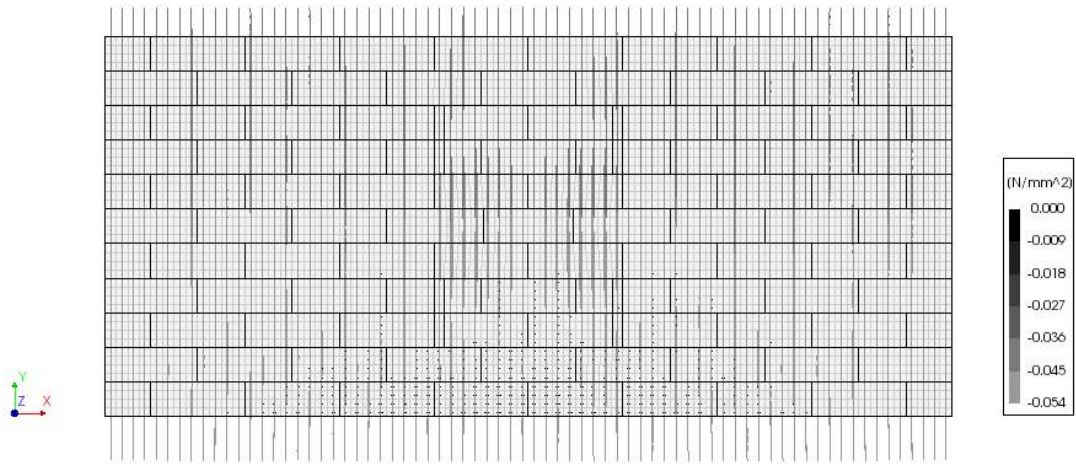
- **Phase 1a** - Self-weight of the wall panel (Figure 6.34a): the compression lines are vertical, and the in-plane principal compressive stresses are uniform on the cross section of the panel; the compressive stress due to vertical loads at the sliding brick height is 0.046 MPa.
- **Phase 1b** - Application of the overburden at the top of the wall (Figure 6.34b): the compression lines are vertical, providing a total uniform compressive stress at the sliding brick height equal to 0.15 MPa, including the self-weight.
- **Phase 2** - Removal of the two bricks adjacent to the sliding brick (Figure 6.34c): the removal of two bricks produces a strong variation in the principal stress distribution. The vertical load given by the self-weight and the overburden partially deviates inwards on the tested brick, producing a significant increase in the compression stress and stress concentrations at the joint edges.

- Phase 3 - Application of the shear load (Figure 6.35): the in-plane principal stress distribution is influenced by the presence of a shear load. Indeed, it produces lateral compression on the sliding brick, which is transferred with a diffusion cone, through the sliding joints, to the masonry above and below the test unit. The diffusion of the shear load inside the masonry produces also a variation in the compressive stress along the sliding joint. In Figure 6.35, three different steps of the analysis are considered: the application of the shear load (Figure 6.35a), the peak load (Figure 6.35b) and the residual phase (Figure 6.35c). The peak load obviously corresponds to the maximum shear stress sustained by the test unit. However, for Model B1, it does not correspond to the load step in which all the integration points reached the Coulomb friction failure domain (failure load).

Focusing on the tested masonry portion, the in-plane principal stress distributions on the deformed configuration are shown in Figure 6.36, for three specific steps of the analysis:

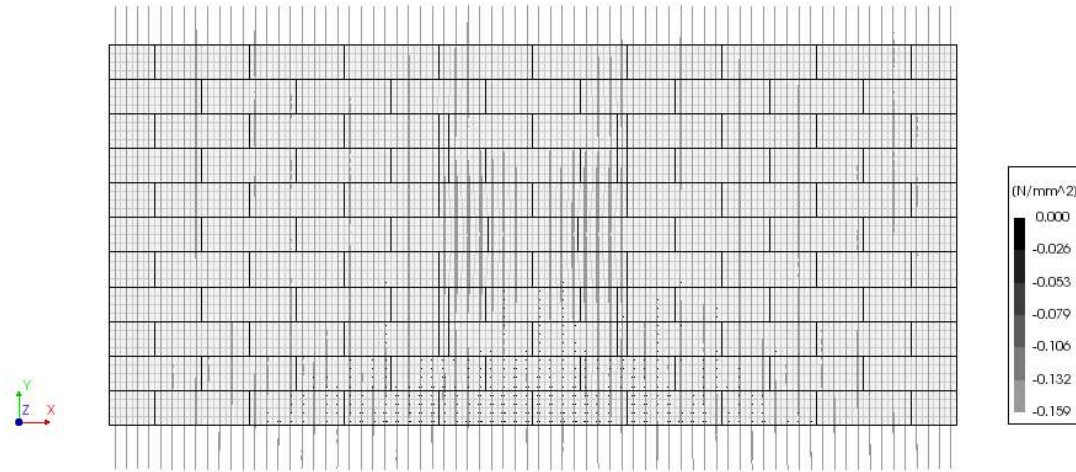
- Removal of bricks (Figure 6.36a);
- Peak shear load (Figure 6.36b): reaching of the maximum shear stress;
- Post-peak phase (Figure 6.36c): it is possible to observe the sliding of the brick with respect to the surrounding masonry; the dilatant behavior of the bed joints is not clearly visible here, since the orthogonal displacements are significantly lower than the ones observed for Model A1.

PhasedNL\_OB-015  
 Phase1\_SWandOBApplication, Load-step 1, Load-factor 1.0000  
 Cauchy Total Stresses in-plane principal components



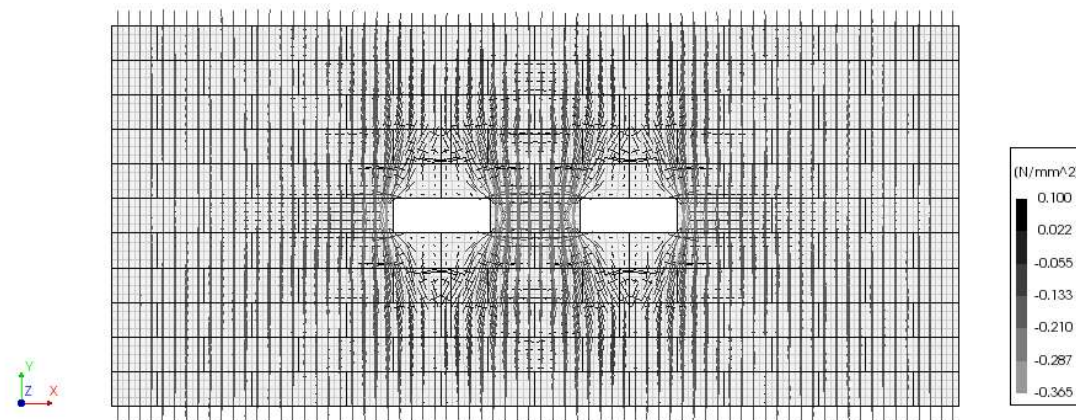
(a)

PhasedNL\_OB-015  
 Phase1\_SWandOBApplication, Load-step 2, Load-factor 1.0000  
 Cauchy Total Stresses in-plane principal components



(b)

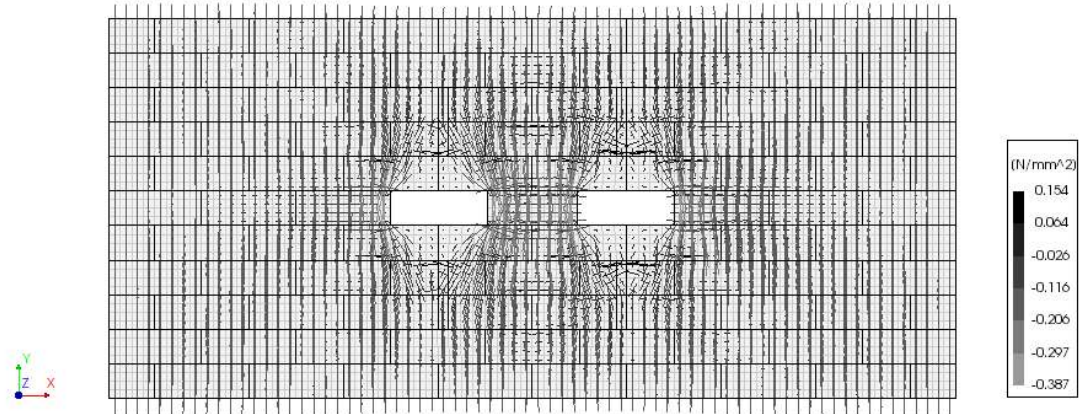
PhasedNL\_OB-015  
 Phase2\_BricksRemoval, Start-step 1, Load-factor 1.0000  
 Cauchy Total Stresses in-plane principal components



(c)

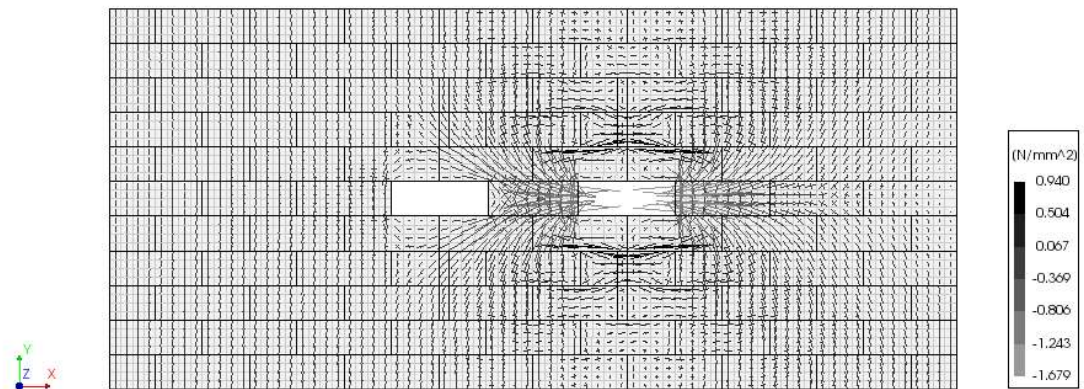
Figure 6.34. Model B1 – Principal stress distributions: (a) self-weight; (b) overburden application; (c) removal of bricks.

PhasedNL\_OB-015  
Phase3\_Shear, Load-step 1, Load-factor 0.59618E-01  
Cauchy Total Stresses in-plane principal components



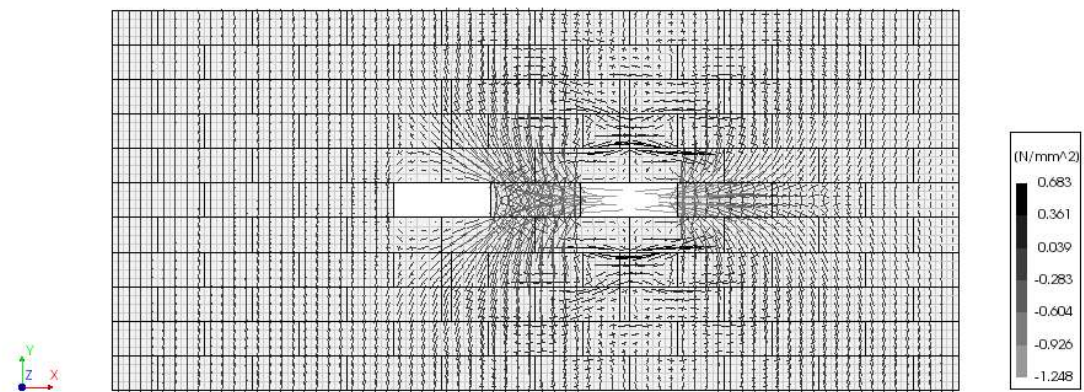
(a)

PhasedNL\_OB-015  
Phase3\_Shear, Load-step 24, Load-factor 1.1094  
Cauchy Total Stresses in-plane principal components



(b)

PhasedNL\_OB-015  
Phase3\_Shear, Load-step 400, Load-factor 0.82528  
Cauchy Total Stresses in-plane principal components



(c)

Figure 6.35. Model B1 – Principal stress distributions: (a) application of the shear load; (b) peak load; (c) residual branch.

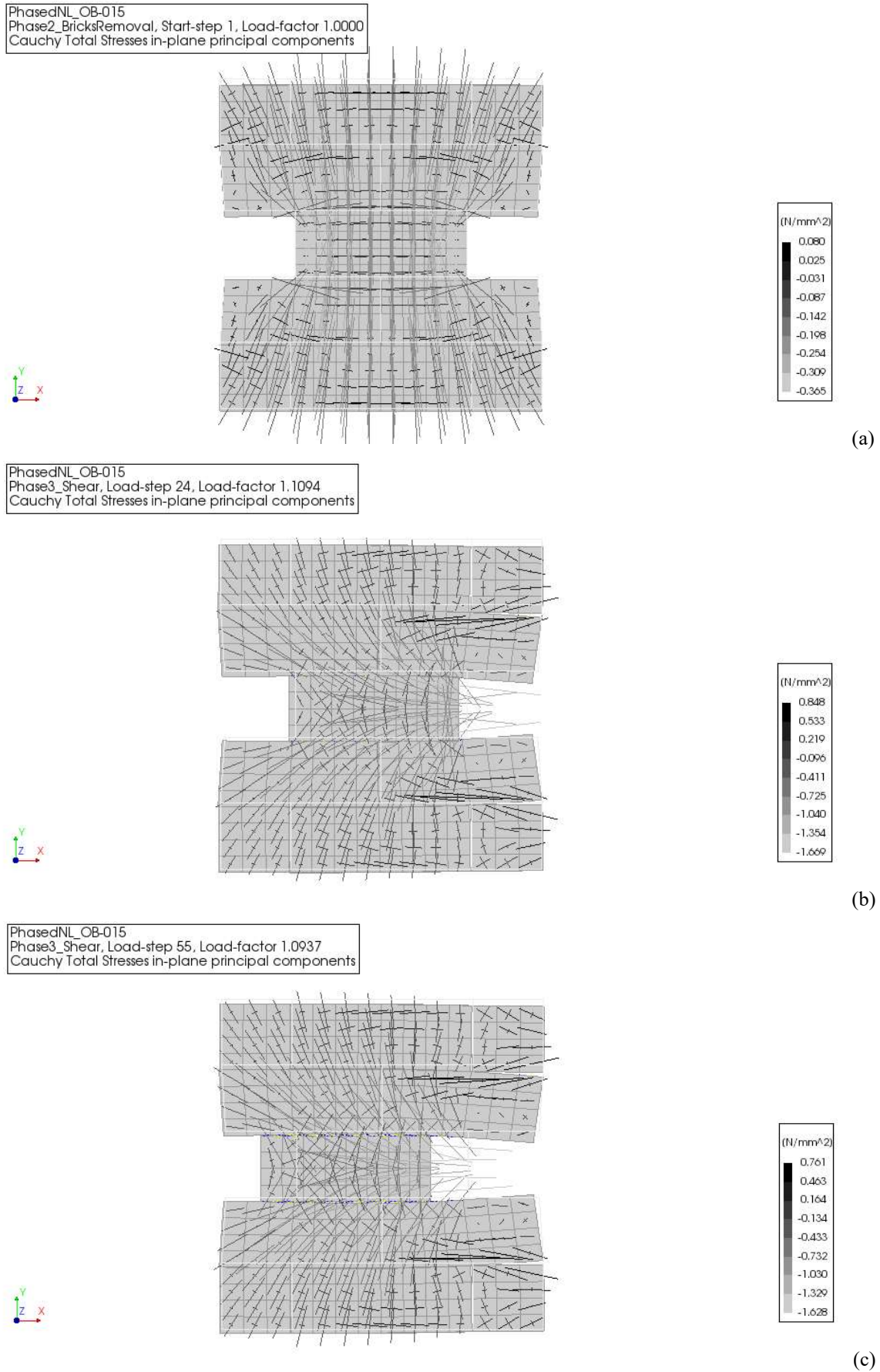


Figure 6.36. Model B1 – Principal stress distributions on the tested masonry portion: (a) application of the vertical load and removal of bricks; (b) peak load; (c) post-peak phase.

The normal and tangential stress evolutions along the top and bottom sliding interfaces are reported in Figure 6.37 and Figure 6.38, respectively. The steps already analyzed for the in-plane principal stress distributions are here considered. For the tangential stresses, only the stress distributions at the failure load, at the peak load, and in the residual phase are shown, given that they are null or negligible during the application of the vertical loads.

With reference to the normal stress evolutions on both the interfaces, uniform distributions are associated with the application of the self-weight and the overburden load, as expected. Then, due to the bricks removal, the non-uniformity of the normal stress distributions can be noticed, with quite high compressive stresses, especially at the extremities of the joints. With the application of the shear load, considering the step at failure, the compressive stresses increase significantly on the right-end side of the sliding interfaces, close to the application of the shear load. On the left-end side, instead, the state of stress remains almost unchanged with respect to the previous phase. In the central portion of the joint, the discontinuity of the stress distributions is justified by the presence of the head joints above and below the superior and inferior interface, respectively. This determines, on one side of the head joint, a consistent decrease of the compressive stress; on the other side of the head joint, instead, a compression increase can be noticed. Considering the step corresponding to the peak load, the compressive stress is still high on the right-end side of the joint, but a more uniform distribution can be recognized elsewhere. From a qualitative point of view, in correspondence of both the failure and the peak load, the tangential stress distributions on top and bottom interfaces are similar to the normal stress ones, with higher shear stresses on the right-end side and a discontinuity in correspondence of the head joints. Smoother distributions can be observed in the residual phase, both for normal and tangential stresses.

The results presented for the Model B1 shows the lower complexity of the shove test performed according to *Method B* with respect to *Method A* proposed by the ASTM Standard. However, also in this case, there are uncertainties related to the estimation of the compressive stress acting on the joints during the entire duration of the test. A major contribution to the compressive stress state is given by the vertical loads during the phase in which the bricks are removed.

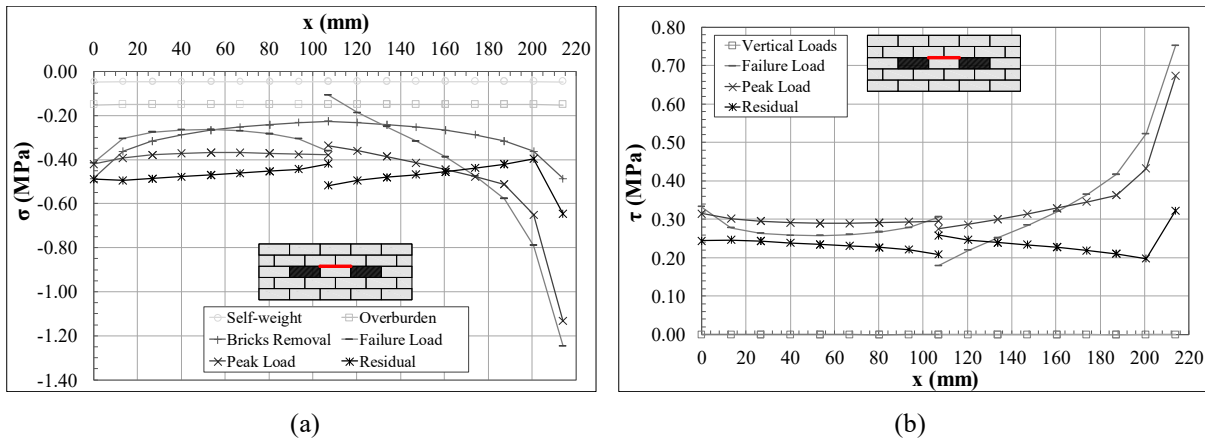


Figure 6.37- Model B1 – Stress evolution along the top sliding interface: (a) normal stress; (b) tangential stress.

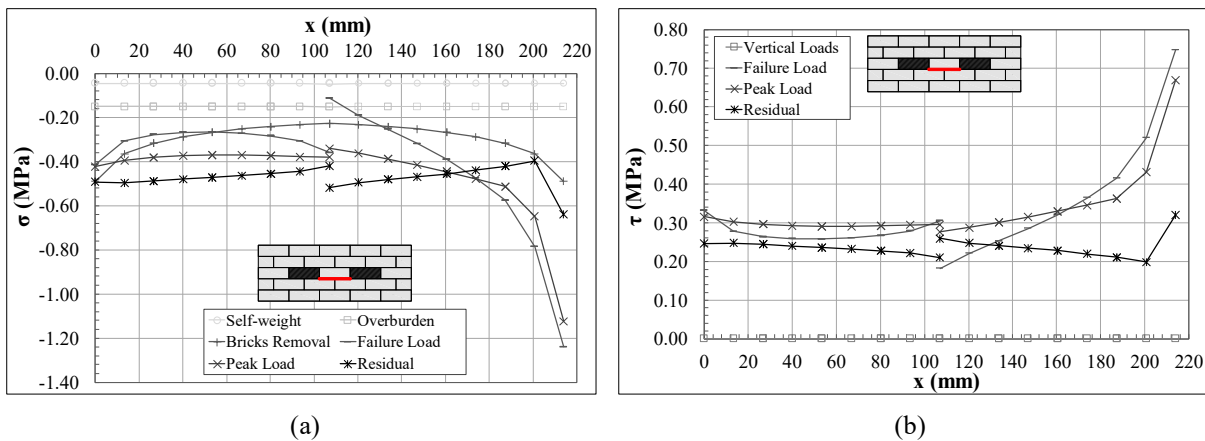


Figure 6.38- Model B1 – Stress evolution along the bottom sliding interface: (a) normal stress; (b) tangential stress.

The results of the numerical analyses for Model B1, B2 and B3 are reported together in Figure 6.39 and Figure 6.40 in terms of shear load  $F$  vs tangential displacement  $\delta v$  curves and shear stress  $\tau$  vs tangential displacement  $\delta v$  curves, respectively. The graphs are all characterized by an initial almost linear branch up to the failure load. For Model B2 and B3, the failure load and the peak load coincide, while for Model B1, as already observed, the peak load is greater than the failure load. In all cases, after the reaching of the peak load, a softening and a residual phase can be recognized. The increase of the overburden load in Model B2 and B3 determines a significant increase in the shear capacity of the tested brick. In Figure 6.41, orthogonal displacement  $\delta u$  vs tangential displacement  $\delta v$  curves are reported. It is worth noting that the orthogonal displacement  $\delta u$  decreases as the overburden load, and consequently the compressive stress on the test unit, increases. This is consistent with the dilatancy formulation presented in Section 4. In particular, for Model B3, in which the overburden is very high (higher

than the confining compressive stress  $\sigma_u$ ), the tested masonry portion is compressed for the entire duration of the test.

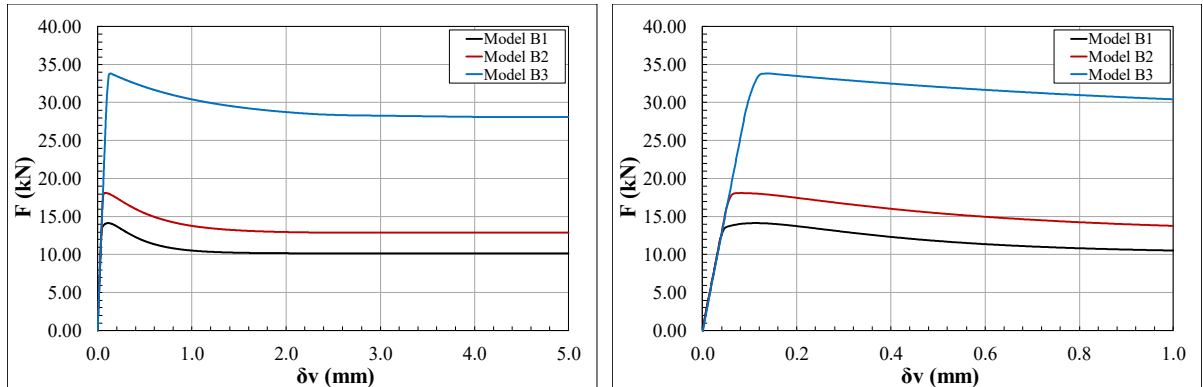


Figure 6.39. Numerical results – comparison: shear load  $F$  vs tangential displacement  $\delta v$  diagram.

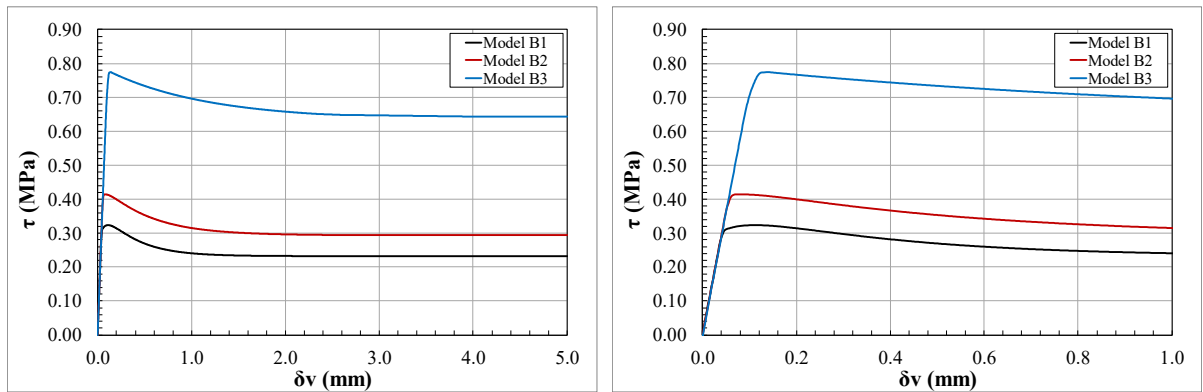


Figure 6.40. Numerical results - comparison: shear stress  $\tau$  vs tangential displacement  $\delta v$  diagram.

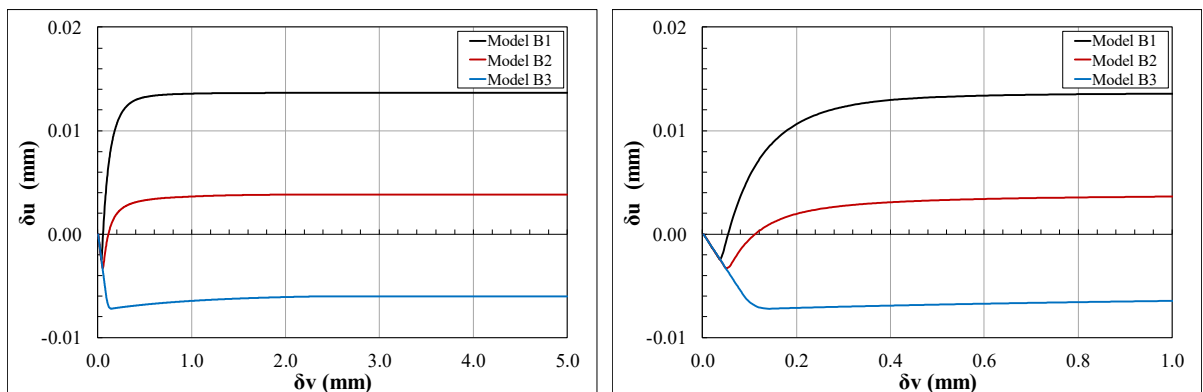


Figure 6.41. Numerical results - comparison: orthogonal displacements  $\delta u$  vs tangential displacement  $\delta v$ .

#### 6.2.4 Parametric studies on dilatancy

As already done in Section 6.1.4, parametric studies on dilatancy were performed for the *Method B* of the shove test. In total, nine parametric analyses were carried out, as reported in Table 6.10, aimed at increasing the role of dilatancy for the considered models. In particular, greater values for  $\psi_0$  and  $\sigma_u$ , - considering the same increments - and lower values for  $\delta$  were chosen. In the followings, the results will be presented for Model B1 only, given that for lower acting compressive stresses, the effect of dilatancy is more evident.

Table 6.10. Shove test – *Method B*: parametric studies on dilatancy.

<b>Numerical simulation</b>	<b><math>\psi_0</math> (rad)</b>	<b><math>\sigma_u</math> (MPa)</b>	<b><math>\delta</math> (-)</b>
B1*	0.374	-0.58	9.63
B1_1b	0.561	-0.58	9.63
B1_1c	0.842	-0.58	9.63
B1_1d	1.262	-0.58	9.63
B1_2b	0.374	-0.87	9.63
B1_2c	0.374	-1.31	9.63
B1_2d	0.374	-1.96	9.63
B1_3b	0.374	-0.58	6.42
B1_3c	0.374	-0.58	4.28
B1_3d	0.374	-0.58	2.85

\*Reference parameters, calibrated through triplet test results.

In Figure 6.42, the plastic orthogonal displacement  $u_{pl}$  vs plastic tangential displacement  $v_{pl}$  curves are reported, for each set of parameters. These curves were not obtained from the numerical analyses, but were built according to Eq. (6.2), already introduced in Section 4.1.2, considering the average compressive stress  $\sigma$  present on the joint after the removal of the bricks in Model B1:

$$u_{pl} = \frac{\Psi_0}{\delta} \left( 1 - \frac{\sigma}{\sigma_u} \right) \left( 1 - e^{-\delta \cdot v_{pl}} \right). \quad (6.2)$$

Therefore, considering also that the compressive stress is variable during the test, they just provide general indications to be compared with the results of the parametric analyses. For a better comparison, the values of the plastic orthogonal displacement from Eq. (6.2) were doubled to account for the presence of both the joints along which the sliding occur. Similarly to what observed in the parametric studies for *Method A*, from Figure 6.42, it is possible to notice that the initial dilatancy angle  $\psi_0$  influences the most the value of the plastic orthogonal

displacement, while variations of the confining stress  $\sigma_u$  do not seem to be very relevant. The parameter  $\delta$ , besides having a slight influence (if compared with  $\psi_0$ ) on the value of the plastic orthogonal displacement, affects more the position of the curve plateau, which is linked to a slower exponential decay of the function.

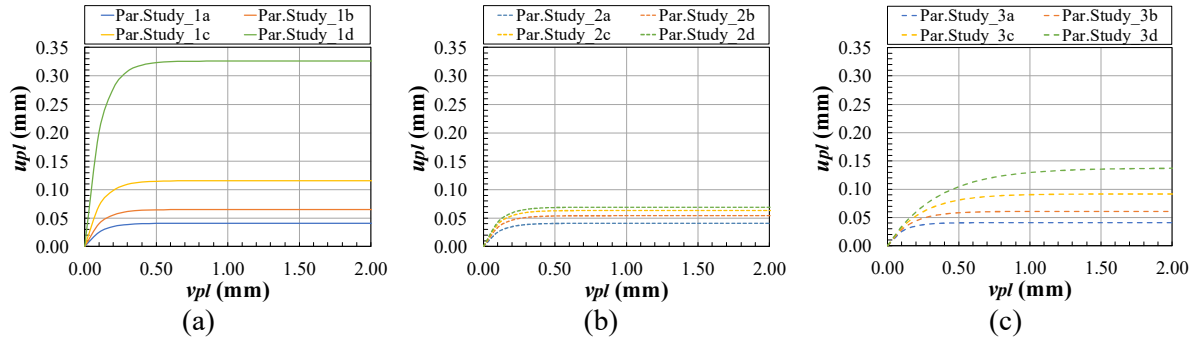


Figure 6.42. Theoretical plastic orthogonal displacement  $u_{pl}$  vs plastic tangential displacement  $v_{pl}$  curves: (a) parametric studies on  $\psi_0$ ; (b) parametric studies on  $\sigma_u$ ; (c) parametric studies on  $\delta$ .

Before analyzing the results of the parametric analyses, it is worth pointing out that, in the numerical model of the shove test according to *Method B*, the vertical displacements along the sliding interfaces cannot be considered completely free. Besides the impediment to the vertical uplift given by the surrounding masonry, already observed for *Method A*, the continuity of masonry (not disturbed by the presence of the flatjacks) can provide a greater confinement of the tested brick. Consequently, if volume expansion is restrained to some extent, the orthogonal displacements registered are lower than the ones from the theoretical curves of Figure 6.42, and correspondent increases in the compressive stress state on the sliding interfaces can be observed, leading to an increase in the shear strength. Moreover, it is also important to point out that, in correspondence of quite high values of the compressive stress  $\sigma$ , which is the case when performing the test with *Method B*, the ratio  $\sigma/\sigma_u$  in Eq. (6.2) can become the governing parameter and can have a higher effect on dilatancy. Indeed, in the parametric analyses here presented, the increase in the compressive stress due to dilatancy, with respect to Model B1, resulted to be quite high (10%-40%).

The results of the parametric analyses are presented in Figure 6.43-Figure 6.51, in terms of: load  $F$  vs tangential displacement  $\delta v$ , shear stress  $\tau$  vs tangential displacement  $\delta v$ , and orthogonal displacement  $\delta u$  vs tangential displacement  $\delta v$ . In Figure 6.52-Figure 6.54, global comparisons are shown. Notice that in Figure 6.45, Figure 6.48, Figure 6.51, and Figure 6.54, total orthogonal ( $\delta u$ ) and tangential ( $\delta v$ ) displacements are reported, not their plastic components. The displacement  $\delta u$  is calculated as already explained in previous sections. In Table 6.11, a summary of the results is presented to quantitatively evaluate the differences

between the considered models in terms of peak load ( $P_{peak}$ ), average shear strength ( $\tau_{max}$ ), average compressive stress at the peak ( $\sigma_{max}$ ), tangential displacement at the peak ( $\delta v_{peak}$ ), and orthogonal displacement at the peak ( $\delta u_{peak}$ ).

The parametric studies on  $\psi_0$  (Figure 6.43-Figure 6.45) shows significant increments in the shear capacity with respect to *Model A1* (up to 23%), which are obviously related to compressive stress increases. Indeed, in these cases, the orthogonal displacements registered are much smaller than the theoretical ones (Figure 6.42a), indicating that they are restrained due to the test conditions. Dilatancy is therefore playing a role and determines an increase in the peak load. The effect of dilatancy on the shear response is also visible looking at the  $F$ - $\delta v$  and  $\tau$ - $\delta v$  curves, where the failure load (corresponding to the point in which the failure criterion is reached in all the integration points of the interfaces) and the peak load can be distinctly identified. In particular, the failure load coincides with the point of the curve for *Model B1* from which the behavior is no more linear, and it is the same in all the models. Beyond this point, the dilatant behavior of masonry, which plays a role in the nonlinear field, determines the mentioned increase in capacity.

For parametric studies on  $\sigma_u$  (Figure 6.46-Figure 6.48) it can be noticed how variations on this parameter, differently to what expected by looking at the theoretical curves (Figure 6.42a), do produce significant changes in the sliding behavior during the shove test, with increases in the shear capacities (up to 25%) comparable to the ones observed from parametric studies on  $\psi_0$ . Trying to explain this apparent contradiction, it should be reminded that, being the other parameter constant, it is the ratio  $\sigma/\sigma_u$  which influences the most the phenomenon. This is the reason why the increments for these models are comparable with the ones observed in the parametric analyses on  $\psi_0$ . Indeed, in that case, given a constant  $\sigma_u$ , an increase in the compressive stress  $\sigma$ , associated to a confined dilatant behavior of masonry, counteract the increase that  $\psi_0$  can produce on the orthogonal displacement. Moreover, this is also the reason why the increments for these models are greater than the ones observed from parametric analyses for *Method A*. Therefore, in general, also the variation of the compressive stress  $\sigma$  have to be accurately taken into account.

The parameter  $\delta$ , looking at the results reported in Figure 6.49-Figure 6.51, rather than influencing the shear response in terms of capacity, affects the trend of the post-peak branch. The lower its value, the less steep is the softening branch. Orthogonal displacements are globally lower than the theoretical ones for all the considered analyses, but no significant increases in the peak load are observed.

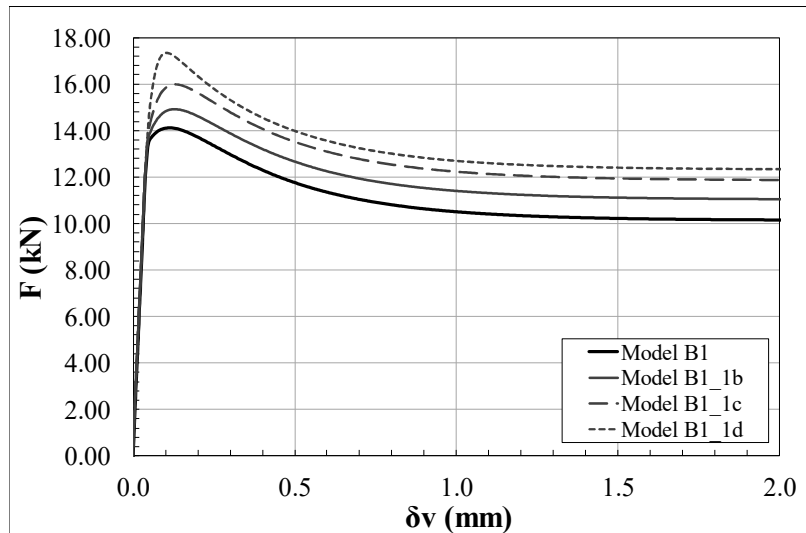


Figure 6.43. Parametric studies on  $\psi_0$ : shear load  $F$  vs tangential displacement  $\delta v$  diagram.

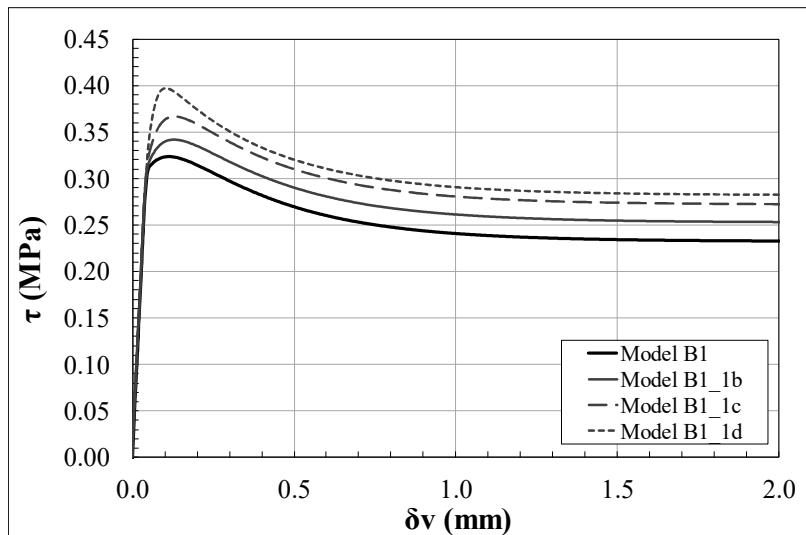


Figure 6.44. Parametric studies on  $\psi_0$ : shear stress  $\tau$  vs tangential displacement  $\delta v$  diagram.

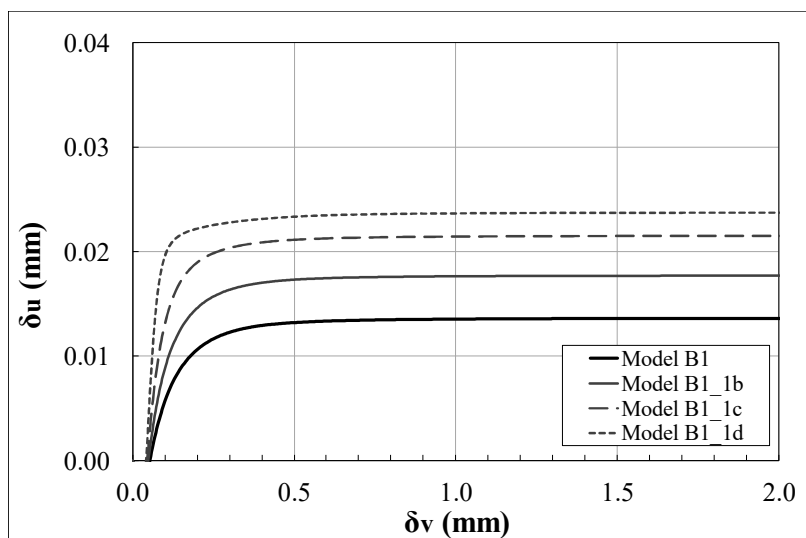
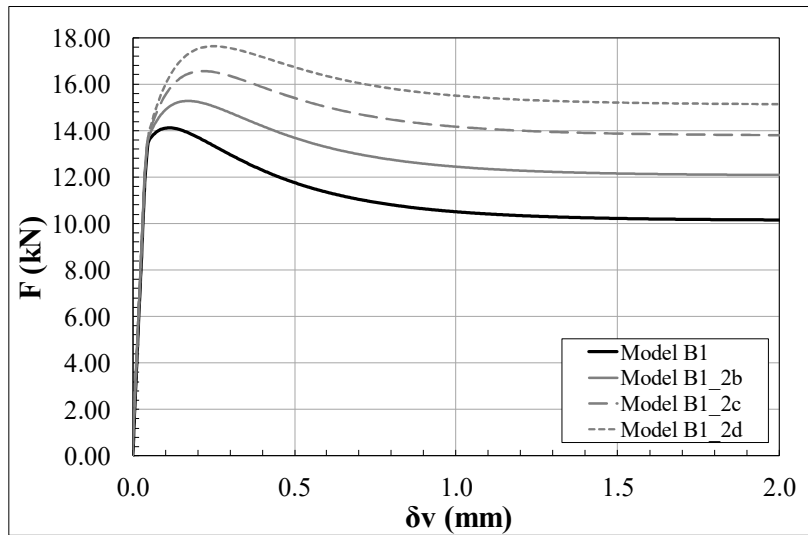
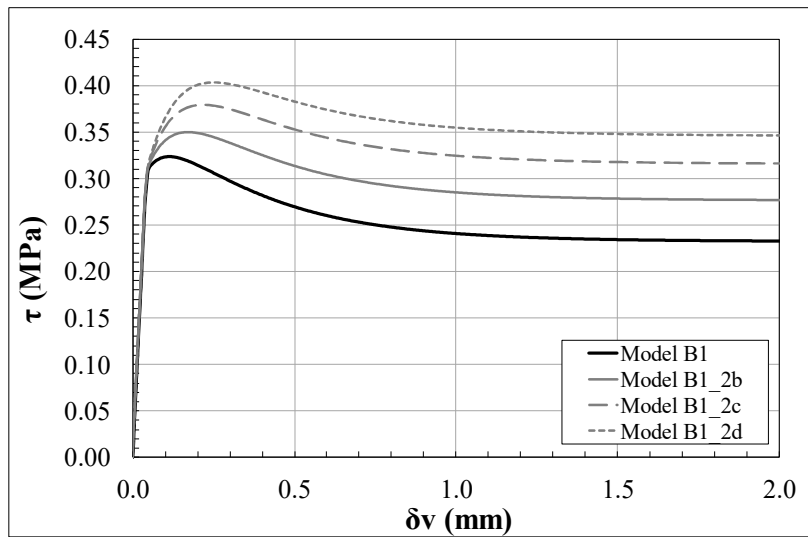
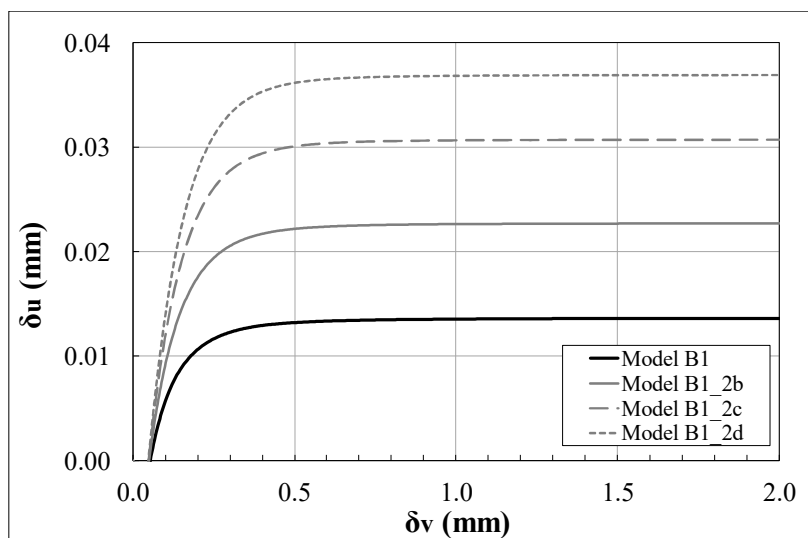


Figure 6.45. Parametric studies on  $\psi_0$ : orthogonal displacements  $\delta u$  vs tangential displacement  $\delta v$ .

Figure 6.46. Parametric studies on  $\sigma_u$ : shear load  $F$  vs tangential displacement  $\delta v$  diagram.Figure 6.47. Parametric studies on  $\sigma_u$ : shear stress  $\tau$  vs tangential displacement  $\delta v$  diagram.Figure 6.48. Parametric studies on  $\sigma_u$ : orthogonal displacements  $\delta u$  vs tangential displacement  $\delta v$ .

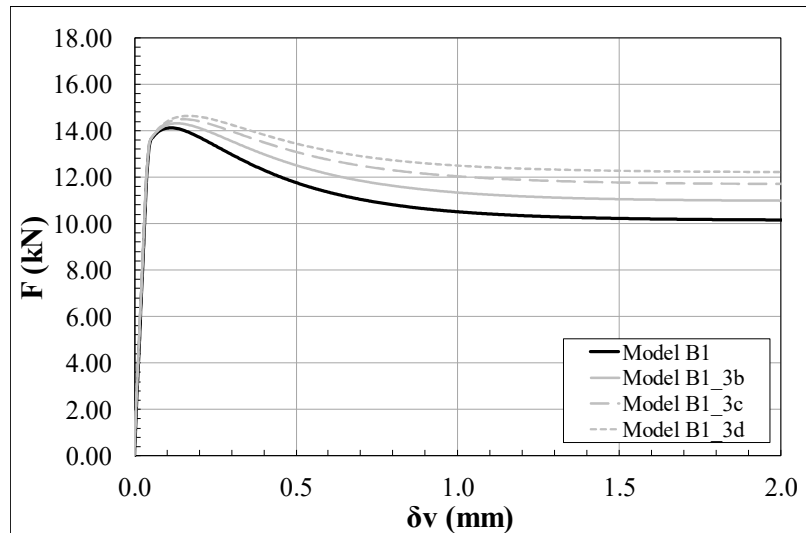


Figure 6.49. Parametric studies on  $\delta$ : shear load  $F$  vs tangential displacement  $\delta v$  diagram.

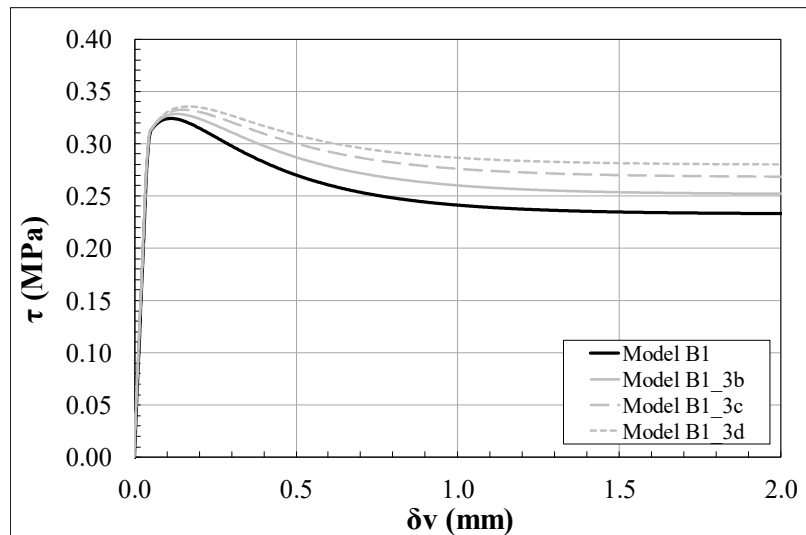


Figure 6.50. Parametric studies on  $\delta$ : shear stress  $\tau$  vs tangential displacement  $\delta v$  diagram.

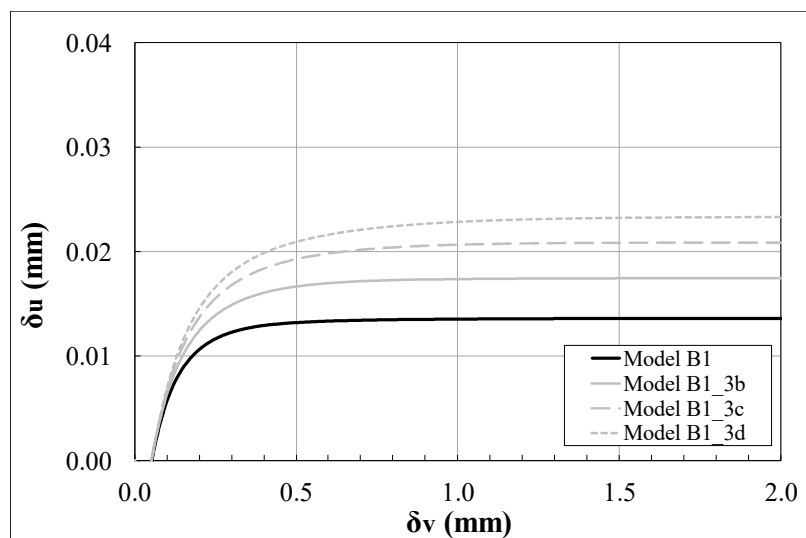


Figure 6.51. Parametric studies on  $\delta$ : orthogonal displacements  $\delta u$  vs tangential displacement  $\delta v$ .

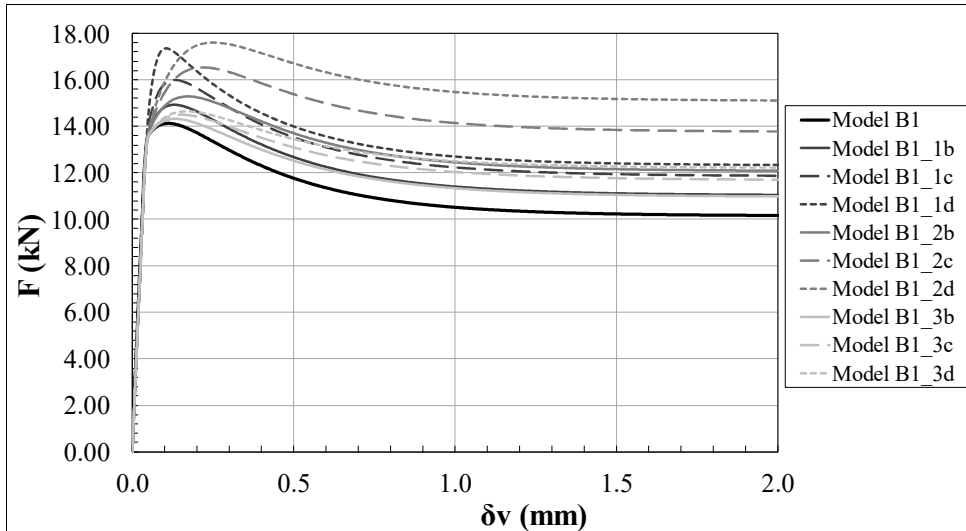


Figure 6.52. Parametric studies - comparison: shear load  $F$  vs tangential displacement  $\delta v$  diagram.

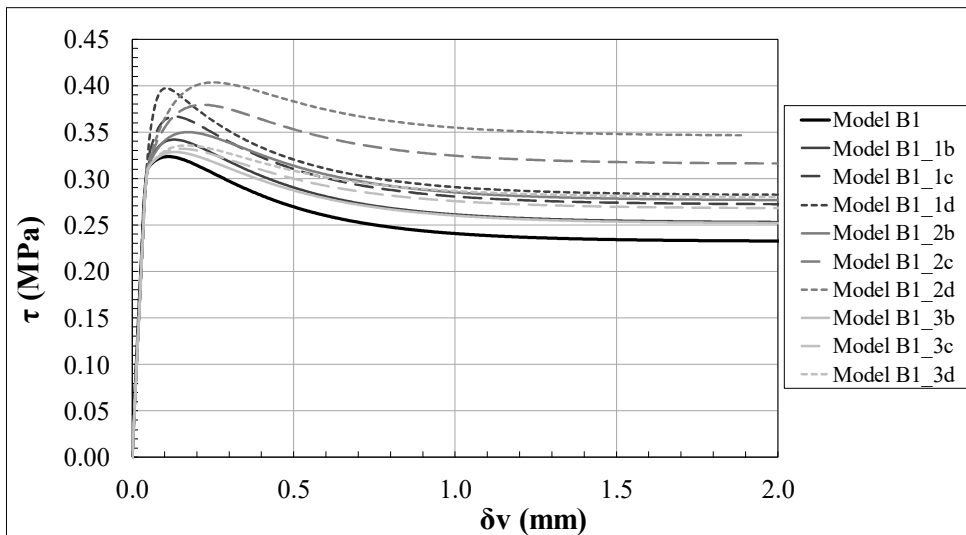


Figure 6.53. Parametric studies - comparison: shear stress  $\tau$  vs tangential displacement  $\delta v$  diagram.

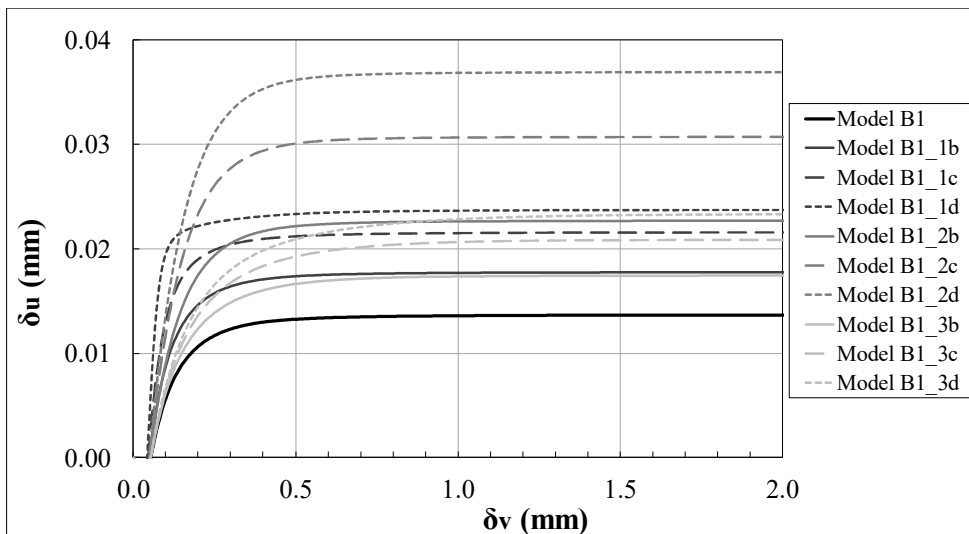


Figure 6.54. Parametric studies - comparison: orthogonal displacements  $\delta u$  vs tangential displacement  $\delta v$ .

Table 6.11. Model B1 – Results of the parametric analyses.

<b>Model</b>	$\psi_0$ <b>(rad)</b>	$\sigma_u$ <b>(MPa)</b>	$\delta$ <b>(-)</b>	<b>P<sub>peak</sub></b> <b>(kN)</b>	$\tau_{max}$ <b>(MPa)</b>	$\sigma_{max}$ <b>(MPa)</b>	$\delta v_{,peak}$ <b>(mm)</b>	$\delta u_{,peak}$ <b>(mm)</b>
Model B1	0.374	-0.58	9.63	14.13	0.324	0.387	0.113	0.007
Model B1_1b	0.561	-0.58	9.63	14.93	0.342	0.424	0.128	0.011
	50.0%	(-)	(-)	5.7%	5.7%	9.5%	12.8%	67.6%
Model B1_1c	0.842	-0.58	9.63	15.99	0.366	0.473	0.129	0.016
	125.1%	(-)	(-)	13.2%	13.2%	22.1%	14.4%	137.8%
Model B1_1d	1.262	-0.58	9.63	17.34	0.397	0.53	0.107	0.020
	237.4%	(-)	(-)	22.8%	22.8%	38.0%	-5.1%	200.2%
Model B1_2b	0.374	-0.87	9.63	15.28	0.350	0.44	0.173	0.016
	(-)	50.0%	(-)	8.2%	8.2%	13.6%	52.6%	138.9%
Model B1_2c	0.374	-1.31	9.63	16.54	0.379	0.50	0.218	0.024
	(-)	125.9%	(-)	17.1%	17.1%	28.6%	92.8%	266.1%
Model B1_2d	0.374	-1.96	9.63	17.61	0.403	0.55	0.253	0.031
	(-)	237.9%	(-)	24.7%	24.7%	41.2%	123.7%	367.8%
Model B1_3b	0.374	-0.58	6.42	14.32	0.328	0.40	0.135	0.009
	(-)	(-)	-33.3%	1.4%	1.4%	2.3%	19.7%	36.3%
Model B1_3c	0.374	-0.58	4.28	14.50	0.332	0.40	0.152	0.011
	(-)	(-)	-55.6%	2.6%	2.6%	4.4%	34.3%	64.6%
Model B1_3d	0.374	-0.58	2.85	14.65	0.336	0.41	0.169	0.013
	(-)	(-)	-70.4%	3.7%	3.7%	6.2%	49.2%	90.6%

### 6.2.5 Correction factors for vertical loads

As observed in previous Sections, the in-plane principal stress distributions and the compressive state of stress along the sliding joint could be strongly influenced, during the different phases of the test, by the removal of bricks, by the diffusion of the shear load, and by dilatancy. Therefore, the compressive stress acting on the sliding brick is far away from being equal to the overburden pressure. In the model considered, differently to what observed for *Method A*, the actual value consists of three contributions: the first one is given by the vertical load acting on the wall, namely the self-weight and the overburden, the second one is given by the diffusion of the shear load, and the third one is given by dilatancy. Ideally, all these contributions should be assessed to obtain a correct evaluation of the failure state of stress. However, here, a correction factor is calibrated for vertical loads only, as already done for *Method A*, for sake of comparisons.

The characteristics of masonry surely affect the way in which vertical loads are deviated from the vertical direction, e.g. head joints not transmitting tensile stresses, etc. Therefore, in the followings, four different cases are considered for the evaluation of the above-mentioned correction factor:

- Elastic joints;
- No tension material for vertical and horizontal mortar joints with constant shear stiffness;
- No tension material for vertical and horizontal mortar joints with reduced shear stiffness (a reduction of 50% is considered);
- No tension material for vertical and horizontal mortar joints with zero shear stiffness.

The stress distributions are evaluated for top and bottom sliding joints, in each test phase. Then, the average compressive stress is calculated and compared with the nominal pressure applied in that phase. In this way, by multiplying the correction factors and the nominal values of the self-weight and the overburden load, the compressive stress acting on the sliding joint, at least at the beginning of the test, can be correctly evaluated.

In Table 6.12-Table 6.15 are reported the results obtained in terms of average stresses in each phase, and in Table 6.16 is reported a summary of the correction factors, which basically are not influenced by the changes in the shear stiffness values.

Table 6.12. Model B1 – Elastic joints: equivalent normal and tangential stresses.

Step	Top joint		Bottom joint		Mean	
	$\sigma_{equiv.}$ (MPa)	$\tau_{equiv.}$ (MPa)	$\sigma_{equiv.}$ (MPa)	$\tau_{equiv.}$ (MPa)	$\sigma_{equiv.}$ (MPa)	$\tau_{equiv.}$ (MPa)
1 - Self-Weight	-0.045	0.000	-0.046	0.000	<b>-0.045</b>	0.000
2 - Overburden	-0.149	0.000	-0.151	0.000	<b>-0.150</b>	0.000
3 - Bricks removal	-0.285	-0.005	-0.286	0.005	<b>-0.285</b>	0.000

Table 6.13. Model B1 – No tension & constant shear stiffness: equivalent normal and tangential stresses.

Step	Top joint		Bottom joint		Mean	
	$\sigma_{equiv.}$ (MPa)	$\tau_{equiv.}$ (MPa)	$\sigma_{equiv.}$ (MPa)	$\tau_{equiv.}$ (MPa)	$\sigma_{equiv.}$ (MPa)	$\tau_{equiv.}$ (MPa)
1 - Self-Weight	-0.045	0.000	-0.046	0.000	<b>-0.045</b>	0.000
2 - Overburden	-0.149	0.000	-0.151	0.000	<b>-0.150</b>	0.000
3 - Bricks removal	-0.289	0.000	-0.290	0.000	<b>-0.290</b>	0.000

Table 6.14. Model B1 – No tension & reduced shear stiffness: equivalent normal and tangential stresses.

Step	Top joint		Bottom joint		Mean	
	$\sigma_{equiv.}$ (MPa)	$\tau_{equiv.}$ (MPa)	$\sigma_{equiv.}$ (MPa)	$\tau_{equiv.}$ (MPa)	$\sigma_{equiv.}$ (MPa)	$\tau_{equiv.}$ (MPa)
1 - Self-Weight	-0.045	0.000	-0.046	0.000	<b>-0.045</b>	0.000
2 - Overburden	-0.149	0.000	-0.151	0.000	<b>-0.150</b>	0.000
3 - Bricks removal	-0.289	0.000	-0.290	0.000	<b>-0.289</b>	0.000

Table 6.15. Model B1 – No tension &amp; zero shear stiffness: equivalent normal and tangential stresses.

Step	Top joint		Bottom joint		Mean	
	$\sigma_{equiv.}$ (MPa)	$\tau_{equiv.}$ (MPa)	$\sigma_{equiv.}$ (MPa)	$\tau_{equiv.}$ (MPa)	$\sigma_{equiv.}$ (MPa)	$\tau_{equiv.}$ (MPa)
1 - Self-Weight	-0.045	0.000	-0.046	0.000	<b>-0.045</b>	0.000
2 - Overburden	-0.149	0.000	-0.151	0.000	<b>-0.150</b>	0.000
3 - Bricks removal	-0.288	0.000	-0.289	0.000	<b>-0.289</b>	0.000

Table 6.16. Model B1 – Correction factors.

Model	Vertical loads*
Elastic joints	1.90
No tension & constant shear stiffness	1.93
No tension & reduced shear stiffness	1.93
No tension & zero shear stiffness	1.92

\*self-weight and overburden

### 6.3 Results comparison and discussion

The objective of this Section is to discuss the findings of the numerical analyses and provide some useful indications for the everyday practice, in which the studied experimental tests are actually applied to real structures. To this aim, comparisons between *Method A* and *Method B* of the shove test, and between shove test and triplet test, will be discussed.

#### 6.3.1 Shove test – *Method A* vs Shove test – *Method B*

The main advantages of *Method A* with respect to *Method B* are: the possibility to perform single and double flatjack test on the tested masonry portion, thus obtaining an estimation of the acting vertical loads and of the deformability properties of masonry, and the possibility to execute the shove test at different pre-compression levels. This is good to obtain an accurate estimation of the residual Coulomb friction criterion from a single test. However, in order to calibrate the initial failure criterion, without making any assumptions on the friction coefficient, the execution of more than one test (if possible, at least three tests on the same masonry typology) is needed. The drawback of *Method A* is the complexity of the test itself and the great uncertainties determined by the cutting of the flatjacks slots and the removal of bricks, which significantly influence the in-plane stress distributions and the compressive stress on the sliding brick. In practice, it can be quite difficult to correctly evaluate these contributions, because they substantially depend on the ability of masonry of transferring loads, which is extremely variable in existing, and maybe damaged or deteriorated, masonries. Moreover, in correspondence of very low flatjack pressures, the compressive stress state on the brick is much more influenced by the overburden load. Therefore, if a correct evaluation of the overburden contribution to the compressive stress state is not carried out, the results, in terms of failure state of stress, can lead to the calibration of an incorrect failure domain. Furthermore, when dilatancy is relevant for the shear-sliding response of masonry, which was not the case for the calcium silicate brick masonry here considered, the problem could become even more complex.

The main advantage of *Method B* is the quite simple and quick execution with respect to *Method A*, which are surely aspects to be taken into account when planning an experimental campaign on existing constructions. Moreover, a lower disturbance is created in the wall panel since the cuts for the seating of the flatjacks are not executed. To obtain information on the compressive state of stress of the wall prior to testing, single and double flatjack tests could be performed on the same masonry, close to the tested portion. In this way, less uncertainties will be related to the estimation of the compressive stress on the sliding brick. However, for *Method*

*B*, more than one test have be executed on the same masonry typology to calibrate both the residual and the initial Coulomb friction failure criterion.

Comparing the results of Models A1 and B1, it is evident that the shear capacity is greater in the latter case, due to the fact that a higher compressive stress state is present. Also, due to test conditions, vertical uplifts upon shearing are much more restrained for Model B1, and this can determine a greater impact of dilatancy on the shear capacity of masonry. From the performed numerical simulations, the diffusion of the shear load seems to have a greater influence on the compressive stresses for *Method B*. However, this latter observation could be also related to the features of the masonry considered and may not be generalized for different masonry typologies, eg. clay brick masonry, typical of many Italian regions.

To improve the testing procedures, for both methods, vertical LVDTs should be positioned in correspondence of the sliding brick. On the one hand, they can be useful to monitor the displacements during the removal of bricks in order to evaluate the average increase of the compressive stress in the tested masonry portion. In this way, it is possible to obtain information on the correction factor for vertical loads. On the other hand, they can be of great help in the detection of a dilatant behavior of masonry. To calibrate the Coulomb friction failure criterion, indeed, it is important to detect the failure load rather than the peak load. Indeed, the peak shear strength, if different from the failure one, is associated to an increase in the compressive stress due to dilatancy and should not be confused with the actual shear strength of the material. Using vertical LVDTs, the failure load can be identified as the point from which positive vertical displacements are registered.

### 6.3.2 *Shove test vs Triplet test*

Triplet tests are performed on small masonry samples and allow to identify the mechanical properties of masonry according to a Coulomb friction failure criterion. Since they are performed in laboratory, displacement controlled procedures may be used, even if requiring quite complex setup, and the post-peak phase can be characterized as well. This is very useful to obtain accurate input parameters to be used in the numerical simulations. On the contrary, with the shove test, which is executed in force control, the identification of the post-peak phase is really difficult and cannot be properly achieved. Even if the tests are executed with different control procedures, similar results in terms of calibrated failure criteria would be expected. However, differences can be detected both in the test setup and in the conditions of the samples, leading to different test outcomes.

First of all, the boundary conditions are not the same and they influence the stress distributions along the sliding joints. Being the non-uniformity of compressive and shear stresses one of the most important features of a shear test (Riddington et al. 1997), it is evident that this aspect can determine discrepancies in the triplet and shove test results.

Secondly, triplet tests are very small samples compared to the wall panels considered for the shove tests. Even if the presence of head joints is included in the triplet test specimens (i.e. modified triplet test), thus considering the same bond pattern of the shove test, the construction process of the triplet samples and their curing conditions (e.g. vertical loads to which they are subjected) are very different from the ones of the walls used for the shove test. Therefore, the presence of head joints above and below the sliding brick could determine a better performance of masonry in the shove test, differently to what happened in triplet tests, in which almost no differences were observed for standard and modified triplets.

Finally, the compressive stress state along the joints can be very different in the two tests. In the shove test, it is not simply the applied one, but it is influenced by many contributions, as previously described. Moreover, in the triplet test, the displacement orthogonal to the sliding joint is completely free while in the shove test, due to the test conditions already discussed, it is more restrained. Therefore, in the shove test, dilatancy could determine a further increase in compressive stress, while in the triplet test, dilatancy is only recognizable in terms of orthogonal displacements registered along the joints during the sliding failure.

The mentioned aspects should be taken into account when the results of the numerical analyses of the shove test, in which the model was calibrated with the triplet test results, are compared with the experimental results of a shove test, as will be done in Chapter 7 with a case study.

## 7 Case study

The case study here presented is part of an experimental campaign conducted at Delft University of Technology, in which the shove test was performed on a replicated single-wythe calcium silicate masonry wall, according to *Method A* of the ASTM Standard. For the construction of the wall, calcium silicate bricks (dimensions: 214x102x72 mm<sup>3</sup>) and cementitious mortar (joint thickness: 10 mm) were used. The mechanical parameters of the materials were the same presented for the triplet tests (Table 5.4). The geometry and the texture of the wall panel were chosen to reproduce a typical Dutch masonry wall, with one-storey height. Moreover, to simulate the in-situ state of stress, an overburden load was applied at the top of the wall, by pre-stressing four steel rods connected to a transverse beam. The shove test was performed in the lower portion of the wall, applying an overburden load such as to obtain a vertical compressive stress equal to 0.25 MPa at the single flatjack test height (Figure 7.1).

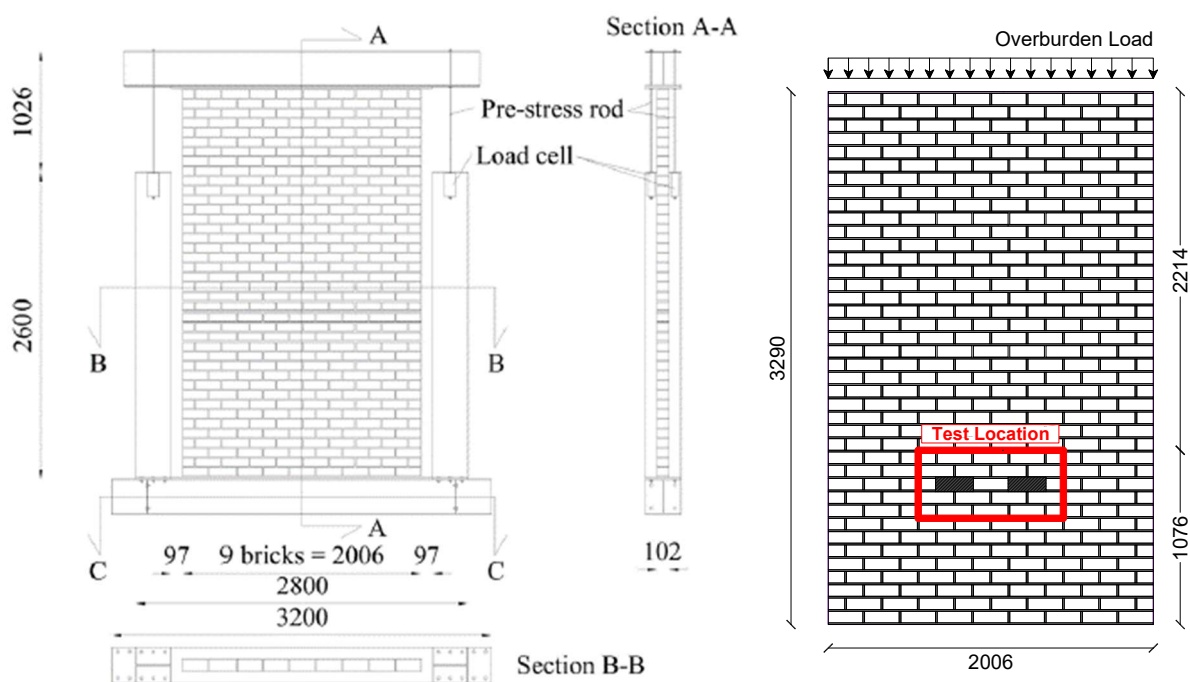


Figure 7.1. Case study: wall geometry and test setup. (TUDelft)

The test procedure consisted in: (i) selecting the masonry portion to be subjected to the test; (ii) performing a single and a double flatjack tests to estimate the compressive state of stress and the Young's modulus, respectively; (iii) removing of the two bricks adjacent to the sliding brick; (iv) performing a double flatjack test to evaluate the fictitious Young's modulus in this modified configuration, according to the proposal by Rossi et al. (2015); (v) apply a vertical

compressive stress by loading the flatjacks; (vi) increase the pressure in the horizontal jack to obtain the sliding failure of the tested unit. In the followings, the test setup and the results in each phase will be presented.

- Single flatjack test

By performing a single flatjack test, the compressive stress of masonry can be evaluated. In this case, the test was carried out to check the correspondence with the compressive stress state given by the self-weight and the overburden load. After the positioning of the gauge points and the measurements of their pre-cut distances, the cut was executed and the flatjack seated (Figure 7.2). Then, post-cut measurements were taken and the flatjack pressure was gradually increased to restore the initial distance between the gauge points. The result of the test, in terms of acting compressive stress, is reported in Table 7.1.



Figure 7.2. Case study – Single flatjack test: (a) execution of the cut; (b) seating of the flatjack.

Table 7.1. Case study – Single flatjack test results.

Single FJ test	Symbol	Unit	Value
Flatjack calibration factor	$k_m$	-	0.794
Flatjack area / Slot area	$k_a$	-	0.870
Flatjack pressure to restore the initial distance	$p$	bar	3.15-3.95
Average compressive stress	$\sigma$	MPa	0.22-0.27

- Double flatjack test (undisturbed masonry)

In order to perform the double flatjack test, a second cut was made, parallel to the the first one, at a distance of 5 courses. Four vertical LVDTs, with a gage length of 290 mm, were positioned for the measurement of the vertical displacements (Figure 7.3a). Four load cycles were performed, at 25%, 50%, 75% and 100% of the acting compressive stress. In Figure 7.3b, the compressive stress  $\sigma$  vs strain  $\varepsilon$  graph is shown. The elastic modulus  $E$  was evaluated and resulted to be equal to 9975 MPa, considering all the LVDTs, and 7945 MPa, considering the central LVDTs only.

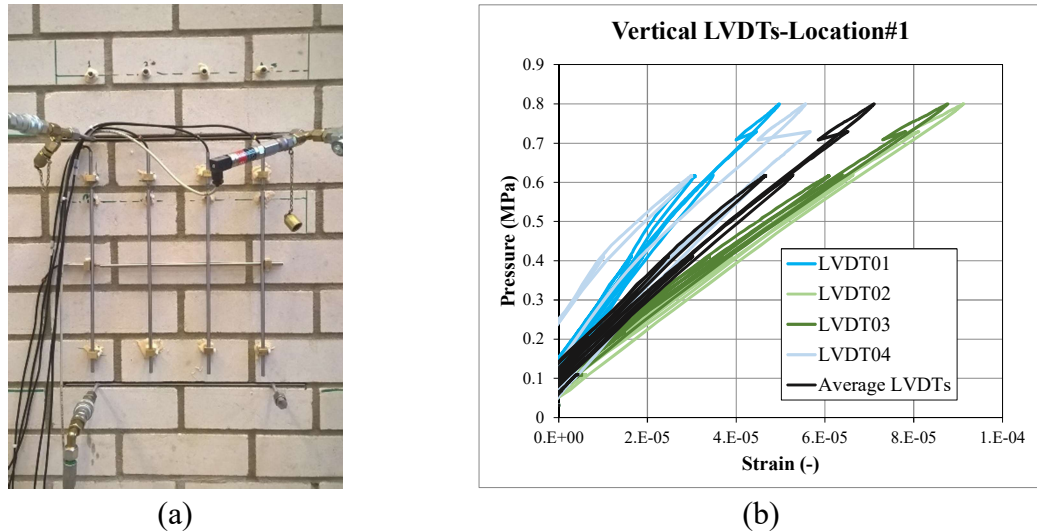


Figure 7.3. Case study – Double flatjack test (undisturbed masonry): (a) setup; (b)  $\sigma$ - $\varepsilon$  curves.

- Removal of bricks

The two bricks adjacent to the test unit and their mortar joints were accurately removed. Unfortunately, in this phase, the LVDTs were detached from the masonry surface in order not to damage them during the extraction procedure. Therefore, the increase in the compressive stress due to vertical load was not measured in this test.

- Double flatjack test (shove test configuration)

The double flatjack test was performed again after the removal of the bricks, in the shove test configuration, to determine a second elastic modulus  $E^*$  (Figure 7.4a). This was done according to the proposal by Rossi et al. (2015) in order to evaluate the jack to brick correction factor:

$$k_{bj} = \frac{\sigma_{brick,FJ}}{\sigma_{FJ}} = \frac{E}{E^*}, \quad (7.1)$$

where  $\sigma_{brick,FJ}$  is the vertical compressive stress on the brick,  $\sigma_{FJ}$  is the pressure applied by the flatjacks,  $E$  is the elastic modulus evaluated with the double flatjack test in the undisturbed configuration,  $E^*$  is the elastic modulus evaluated in the shove test configuration. In Figure 7.4b, the compressive stress  $\sigma$  vs strain  $\varepsilon$  graph is shown. The fictitious elastic modulus  $E^*$  was evaluated considering the two central LVDTs and was equal to 6750 MPa. Only the two central LVDTs were considered. Therefore, the value of the jack to brick correction factor  $k_{bj}$  resulted to be equal to 1.18.

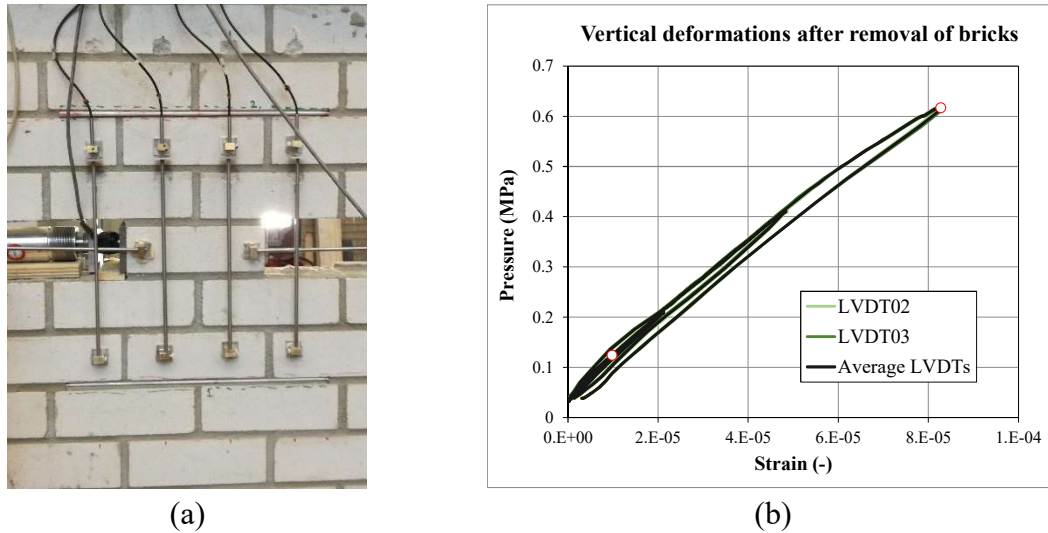


Figure 7.4. Case study – Double flatjack test (shove test configuration): (a) setup; (b)  $\sigma$ - $\epsilon$  curves.

#### - Shove test

The setup of the shove test is presented in Figure 7.5a. During the test, horizontal and vertical displacements were measured by means of LVDTs: two horizontal LVDTs were positioned on both sides of the sliding brick to measure its relative displacement with respect to the surrounding masonry, and two vertical LVDTs were positioned in correspondence of the sliding brick to monitor the displacements orthogonal to the mortar joint (dilatancy) during the sliding failure. Moreover, LVDTs were placed at the wall sides to check undesired failure modes, e.g. failure of the contrast portion behind the horizontal jack.

At the beginning of the test, the pressure in the two flatjacks was set at a very low value ( $\sigma_1=0.065$  MPa) and the shear force was applied monotonically by means of the horizontal jack. The failure mode (Figure 7.5b) was characterized by a sliding along the brick-mortar interface, with a “bridging” failure.

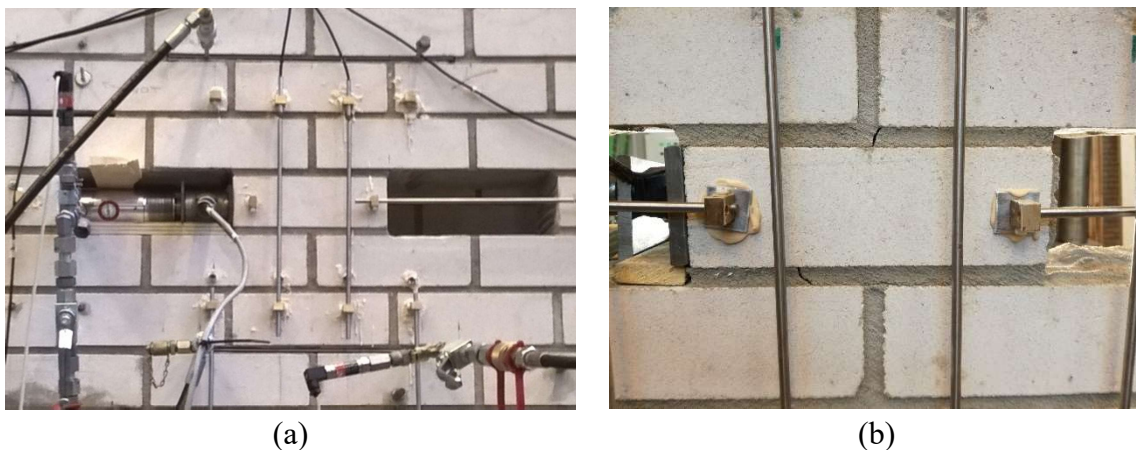


Figure 7.5. Case study – Shove test: (a) setup; (b) failure mode.

After the obtainment of this first sliding, the pressure in the flatjacks was increased and the sliding produced again. The results of the test, at each load step, are reported in Table 7.2, where:  $\tau$  is the maximum shear stress (only for the first step it is necessary to distinguish between the peak shear strength and the residual one),  $\sigma_{FJ}$  is the flatjack pressure,  $\sigma_{brick,FJ}$  is the vertical compressive stress on the brick due to the flatjack pressure (evaluated as  $\sigma_{FJ} * k_{bj}$ ), and  $\sigma_{real}$  is the compressive stress on the brick given by the sum of  $\sigma_{brick,FJ}$  and the contribution of the vertical load, evaluated using the correction factor for vertical loads (equal to 0.64) determined in Section 6.1.5.

Table 7.2. Case study – Shove test results.

Load Step	$\sigma_{FJ}$ (MPa)	$\sigma_{brickFJ}$ (MPa)	$\sigma_{Real}$ (MPa)	$\tau$ (MPa)
Load Step 1 - Peak	0.065	0.076	0.236	0.292
Load Step 1	0.065	0.076	0.236	0.087
Load Step 2	0.140	0.164	0.324	0.171
Load Step 3	0.272	0.320	0.480	0.256
Load Step 4	0.427	0.503	0.663	0.389
Load Step 5	0.565	0.665	0.825	0.398

The failure points obtained can be reported in a  $\sigma - \tau$  diagram for the evaluation of the residual criterion. From the diagram in Figure 7.6a, where the failure points were plotted considering  $\sigma_{brick,FJ}$  as the acting compressive stress on the brick, it is possible to notice that the residual failure criterion is not characterized, as it should be, by a zero cohesion. This can be explained considering that these values of the compressive stresses are not corrected accounting for the contribution of the vertical loads. Since this contribution was not experimentally determined, here the correction factor found for vertical loads in the numerical models (see Section 6.1.5) was used for a proper evaluation of the actual compressive stress on the brick. It can be seen that, plotting the  $(\sigma_{real}; \tau)$  points in the diagram (Figure 7.6b), an almost null cohesion is obtained. The value of the friction coefficient is 0.55, which is quite close to the value of the friction coefficient found in the experimental campaign on triplet tests (equal to 0.50). It is the same in both cases since, in the second graph, the points are simply translated to the right by the same quantity. It is worth pointing out that, with the corrections considered for the compressive stress values, it is tacitly assumed that dilatancy is not affecting the results in terms of capacity, as was found in the results for Model A1. Therefore, an increase in the compressive stress on the sliding brick is not expected due to dilatancy. With the execution of a single test, only one initial failure point is available. Therefore, an estimation of the cohesion cannot be provided.

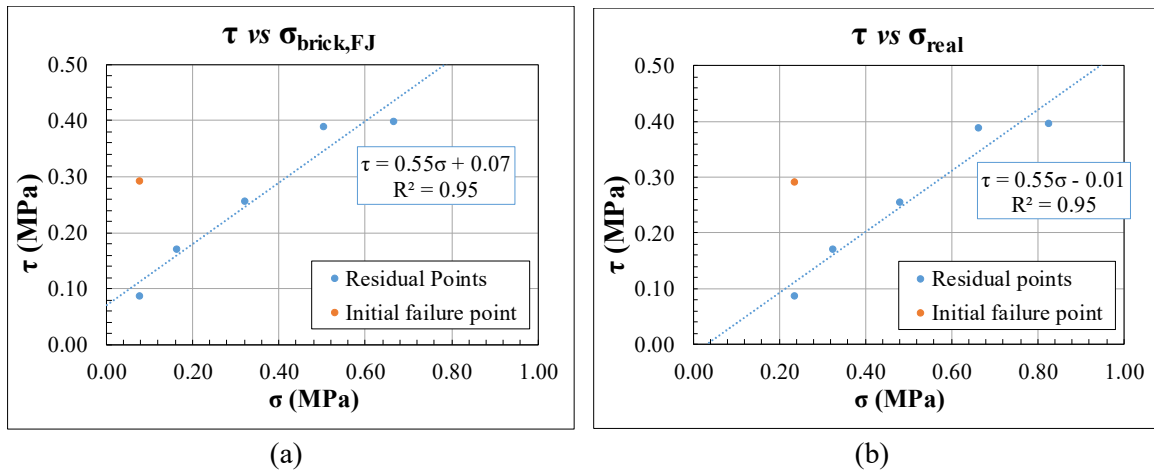


Figure 7.6. Case study – Shove test results:  $\sigma$ - $\tau$  diagrams.

In Figure 7.7, the experimental shear stress  $\tau$  vs tangential displacement  $\delta v$  and the orthogonal displacement  $\delta u$  vs tangential displacement curves  $\delta v$  are reported. The dashed line in the first step connected two consecutive registered points, highlighting the fact that the post-peak phase could not be correctly identified. The results of the numerical simulations, carried out as described in Section 6.1, are reported as well to compare the results and validate the model. In particular, in Figure 7.7b, only the first step is considered, given that dilatancy is effective for low values of the plastic tangential displacements, according to its definition. With reference to Figure 7.7a, it is possible to notice that, in the first step, a lower peak stress and a higher residual stress were obtained in the numerical analysis with respect to the experimental results. A slight difference in the failure criteria calibrated from triplet test and shove test results, in correspondence of a low compressive stress, can determine these discrepancies. In the subsequent load steps, instead, a better agreement was found, especially in the third and fourth steps. A very good agreement can be noticed in the first part of the graph of Figure 7.7b. However, in corresponding of the reaching of the peak load, the experimental orthogonal displacements are much higher than the ones obtained with the numerical analysis. This can be related to a dilatant behaviour which is not correctly taken into account in the model, or to the fact that during the experimental tests rigid movements of the sliding brick (e.g. rotation) influenced the final value of the orthogonal displacements. Despite this, the numerical model seems to be capable of reproducing the shear-sliding failure mode observed experimentally in the shove test and, moreover, reliable estimation of the actual compressive state of stress helped in the interpretation of the results and in the calibration of the residual failure criterion.

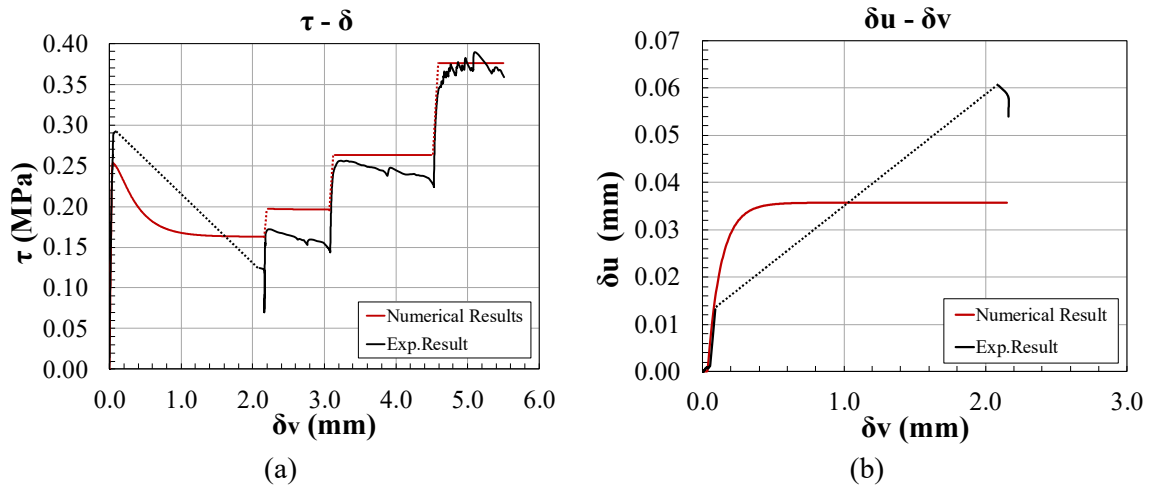


Figure 7.7. Case study – Shove test: experimental vs numerical results: (a) tangential stress  $\tau$  vs tangential displacement  $\delta v$ ; (b) orthogonal displacement  $\delta u$  vs tangential displacement  $\delta v$ .



## 8 Conclusions

### 8.1 Summary

The research work presented in this thesis was related to the investigation of the shear behavior of existing masonries, through experimental tests and numerical simulations. In particular, an experimental campaign was conducted on eight existing masonry buildings with the objective of identifying the most suitable techniques that can be used in the seismic vulnerability assessment procedures. Then, starting from the observations of the failure mechanisms obtained in the tests, a detailed study on the shear-sliding behavior of masonry was carried out, by performing numerical simulations of triplet tests and shove tests.

During the experimental campaign, slightly-destructive tests (*shove tests* and *splitting tests* on cores with inclined mortar joint) and destructive tests (*diagonal compression* and *shear-compression tests*) were conducted. Slightly-destructive tests were aimed at reproducing a sliding failure mode and, therefore, a Coulomb friction failure criterion was determined for the investigated masonry typologies. The combination of the two experimental slightly-destructive techniques was fundamental to provide a reliable calibration of the mechanical parameters of the criterion. A different interpretation of the results of the shove test was also proposed and resulted to be adequate to correctly evaluate the state of stress at failure. Destructive tests were conducted to analyze the diagonal cracking failure mechanism and to build Turnšek and Čačovič's failure domains. However, also in this case, a sliding mechanism was recognized after the formation of the diagonal crack, which was able to influence, to some extent, the shear capacity of the masonry panels. From the comparison of the outputs obtained from the slightly-destructive and destructive tests, in terms of failure state of stress and failure domains, the Coulomb friction criterion, calibrated with local tests, gave better correspondence with the results from destructive tests. Therefore, it seems to be the most suitable criterion for describing the shear behavior of the masonry typologies investigated, characterized by very poor-quality mortars. This confirms the important role of the sliding mechanism associated to the diagonal cracking failure mode.

The testing procedures and typologies presented can be applied in the seismic vulnerability assessments and it should be stressed, on the basis of the results obtained, that the execution of a limited number of in-situ tests often implies the obtainment of highly scattered results, which may not provide adequate strength parameters for the investigated masonry. Therefore, the

accurate planning of an experimental campaign is fundamental and different type of tests should be executed on the same masonry typology in order to get more reliable results.

The numerical simulations of triplet tests and shove tests allowed to understand which aspects could most affect the shear-sliding behavior of masonry. In particular, the influence of dilatancy was analyzed in both cases. It was observed that dilatancy can affect the results of the shove test in terms of shear capacity, while in the triplet tests, dilatancy have only an influence in terms of displacements orthogonal to the sliding joint, which were not restrained in the test. Aspects related to the test setup and execution were also discussed, such as the presence of non-uniform stress distributions along the sliding bed joints, the concentration of stresses, the failure initiation and propagation.

With reference to the shove test, the advantages and disadvantages of two test methods were deeply analyzed and various numerical simulations, including parametric studies on dilatancy, were performed. It was found that one of the most important aspect, when conducting a shove test, is the correct evaluation of the compressive state of stress acting on the sliding brick. Indeed, it can be influenced by the presence of the slots for the seating of the flatjacks, by the removal of bricks, by the diffusion of the shear load, and by dilatancy. The determination of these contributions is, therefore, fundamental. In the present research, correction factors for vertical load and for flatjack pressure were proposed for the masonry typology investigated. For the considered case study, given that dilatancy did not influence to a great extent the experimental results in terms of capacity, the evaluation of these two contributions only was sufficient for the correct estimation of the compressive stress state of the brick. Consequently, proposals for modifications of the test procedure and setup were made (e.g. additional LVDTs) with the objective of evaluating these contributions in situ. Comparisons between triplet test and shove test results confirmed that, if the correct failure state of stress is identified in the shove test, a quite good correspondence between the two tests can be found.

In conclusion, the numerical simulations allowed to gain a better understanding of the sliding failure in triplet and shove tests. From the comparisons between experimental and numerical results, it was noticed that the simplified micro-modeling strategy and the combined interface model are very adequate for the study of the shear-sliding phenomenon.

## **8.2 Future works**

Future works can be done, both from the experimental and the numerical point of view, on the following aspects:

- Experimental laboratory tests on clay brick masonries representative of the Italian existing constructions: it is believed that dilatancy would be more important in case of clay brick masonries rather than calcium silicate brick masonry, which was investigated with the experimental tests performed at TU Delft. Therefore, the calibration of the dilatancy parameters, together with parametric studies, could be of great help, also to confirm the interpretation of the shove test given in Section 3.2.2.
- For masonries characterized by a significant dilatant behavior, it would be important to calibrate correction factors or analytical formulations for the evaluation of the contribution given by dilatancy on the compressive state of stress of the sliding brick in the shove test.
- Numerical simulations of the shove test on 3D models: the redistribution of the stresses in double-wythe or multi-wythe masonry panels can be extremely different from the one in single-wythe walls and the effect of the collar joint could be studied as well. Moreover, detailed micro-modeling strategy can be adopted to model sliding failure mechanism occurring inside the mortar.
- Numerical and analytical studies on diagonal compression and shear compression tests, to better interpret the role of the sliding failure mechanism on the shear capacity of the masonry panel.



## Acknowledgements

The research reported in this thesis was carried out in the Department of Civil, Environmental and Material Engineering (DICAM) of the University of Bologna, with the support of the Department of Structural Engineering of Delft University of Technology, which is gratefully acknowledged for having provided the experimental results of triplet tests and shove tests.

The University of Bologna and the Marco Polo mobility program are also gratefully acknowledged for the financial support of this work.

The experimental campaign on existing constructions was financially supported by the Emilia Romagna region in the framework of the LARVUS Research Project and the Research Agreement: “Realizzazione di indagini sperimentali in situ su pareti di edifici in muratura nei comuni dell’Emilia colpiti dal Sisma del 2012” (CUP E49G13000640001). The financial support of the Italian Department of Civil Protection (ReLUIIS 2017 Grant – Innovative Materials) is gratefully acknowledged.

I would like to thank Prof. Marco Savoia and Prof. Barbara Ferracuti for the given opportunity to start a PhD research project on these very interesting and current topics. I am very grateful to Prof. Claudio Mazzotti, who assisted and guided me during the entire work. His precious suggestions and support helped me in maintaining a constant and focused motivation on the research.

I wish to thank all the friends and colleagues of the DICAM Department, with whom I shared positive and negative moments of these three years. A very special thank to all the CIRI guys I met and, especially, to Andrea, Anna V., Anna T., Ale, Vale, Dit, and Michele. They have been good travel companions and I learned a lot from them about testing.

I am very grateful to Prof. Jan G. Rots for the possibility of collaborating with the Delft University of Technology during my internship period abroad. Thanks for the willingness and for having introduced me to the topic of the numerical modeling of masonry structures. Thanks also to the people met in Delft, who have been precious during my stay in the Netherlands, both from the academic and the “everyday life” point of view.

My family deserves the most special thank for having supported me constantly during this adventure. Thanks to Luca, who is always on my side and believes in my capabilities. And thanks to the little Rachele, who gave a different light to these last months.



## References

- Alecci V., Fagone M., Rotunno T., De Stefano M. 2013. *Shear strength of brick masonry walls assembled with different types of mortar*. *Constr. Build. Mater.* 40:1038–1045.
- Anthoine A. 1992. *In-plane behavior of masonry: a literature review*. Report EUR 13840 EN, Commission of the European Communities, Joint Research Center – Institute for Safety and Technology, Ispra, Italy.
- ASTM C1196-14. 2014. *Standard Test Method for In Situ Compressive Stress Within Solid Unit Masonry Estimated Using Flatjack Measurements*. American Society of Testing Material.
- ASTM C1197-14. 2014. *Standard Test Method for In Situ Measurement of Masonry Deformability Properties Using the Flatjack Method*. American Society of Testing Material.
- ASTM C1531-16. 2016. *Standard Test Methods for In Situ Measurement of Masonry Mortar Joint Shear*. American Society of Testing Material.
- ASTM E519–15. 2015. *Standard Test Method for Diagonal Tension ( Shear ) in Masonry Assemblages*. American Society of Testing Material.
- Atkinson R.H. Kingsley G.R.; Saeb S., Amadei B., Sture S. 1988. *A laboratory and in situ study of the shear strength of masonry bed joints*. Proc. 8th Int. Brick/Block Masonry Conf., Dublin, October 1988.
- Atkinson R.H., Amadei B., Saeb S., Sture S. 1989. *Response of masonry bed joints in direct shear*. *Journal of Structural Engineering*, 115(9):2276-2296.
- Augenti N. 2000. *Il calcolo sismico degli edifici in muratura*. UTET.
- Benedetti A., Pelà L., Aprile A. 2008. *Masonry Properties Determination Via Splitting Tests on Cores With a Rotated Mortar Layer*. 8th Int. Semin. Struct. Mason.
- Benedetti D., Tomaževič M. 1984. *Sulla verifica sismica di costruzioni in muratura*. *Ing. Sismica*. 1: 9–16.
- Binda L., Tiraboschi C. 1999. *flatjack test as a slightly destructive technique for the diagnosis of brick and stone masonry structures*. *Int. Journal for Restoration of Buildings and Monuments*, pp.449-472.
- Binda L., Saisi A., Tiraboschi C. 2000. *Investigation procedures for the diagnosis of historic masonries*. *Constr. Build. Mater.* 14:199–233.
- Borri A., Castori G., Corradi M., Speranzini E. 2011. *Shear behavior of unreinforced and reinforced masonry panels subjected to in situ diagonal compression tests*. *Constr. Build. Mater.* 25: 4403–4414.
- Borri A., Cangi G., De Maria A. 2013. *Caratterizzazione meccanica delle murature (anche alla luce del recente sisma in Emilia) e interpretazione delle prove sperimentali a taglio*. ANIDIS Conference, Padova.
- Braga F., Dolce M., Masi A. 1993. *Interpretazione statistica di prove sperimentali per l'accertamento della resistenza a taglio della muratura di edifici esistenti*. 6° Convegno Naz. - L'ingegneria Sismica in Italia, pp.577–585.
- Calderini C., Cattari S., Lagomarsino S. 2009. *In-plane strength of unreinforced masonry piers*. *Earthquake Engineering and Structural Dynamics*, 38:243-267.
- Calderini C., Cattari S., Lagomarsino S. 2010. *The use of the diagonal compression test to identify the shear mechanical parameters of masonry*. *Constr. Build. Mater.* 24:677–685.
- Cattari S., Degli Abbati S., Ferretti D., Lagomarsino S., Ottonelli D., Rossi M., Tralli A. 2012. *The seismic behaviour of ancient masonry buildings after the earthquake in Emilia (Italy) on May 20<sup>th</sup> and 29<sup>th</sup>*. *Ing. Sismica*. 23:87-111.

- Cattari S., Degli Abbati S., Ferretti D., Lagomarsino S., Ottonelli D., Tralli A. 2014. *Damage assessment of fortresses after the 2012 Emilia earthquake*. Bull. Earthquake Eng. 12(5):2333-2365.
- Ceroni F., Pecce M., Sica S., Garofano A. 2012. *Assessment of Seismic Vulnerability of a Historical Masonry Building*, Buildings. 2:332–358.
- Chiostrini S., Galano L., Vignoli A. 2000. *On the Determination of Strength of Ancient Masonry Walls via Experimental Tests*. 12th World Conf. Earthq. Eng., Auckland, New Zealand, 30 January – 4 February 2000.
- Circolare 02/02/2009 n. 617. 2009. *Istruzioni per l'applicazione delle "Norme tecniche per le costruzioni" di cui al D.M. 14 gennaio 2008*.
- Corradi M., Borri A., Vignoli A. 2003. *Experimental study on the determination of strength of masonry walls*. Constr. Build. Mater. 17:325–337.
- Drysdale R.G., Vanderkeyl R., Hamid A.A. 1979. *Shear strength of brick masonry joints*. Proc. 5<sup>th</sup> Int. Brick and Block Mas. Conf., Washington D.C., 5-10 October 1979.
- DIN 18555-5. 1986. *Prüfung von Mörteln mit mineralischen Bindemitteln*. Festmörtel. Bestimmung der Haftscherfestigkeit von Mauermörteln, Berlin.
- D.M. 14 Gennaio 2008. *Nuove Norme Tecniche per le Costruzioni (NTC08)*. Italian Ministry of Infrastructure and Transportation, Rome.
- EN 1052-3:2002. *Method of test masonry – Part 3: Determination of initial shear strength*. European Standards (EN).
- EN 1998-3:2005. 2005. *Eurocode 8: Design of structures for earthquake resistance - Part 3: Assessment and retrofitting of buildings*.
- Frocht M. 1931. *Recent advances in photoelasticity*. ASME Trans. 55:135–153.
- Giambanco G., Rizzo S., Spallino R. 2001. *Numerical analysis of masonry structures via interface models*. Comput. Methods Appl. Mech. Eng. 190:6493-6511.
- Incerti A., Rinaldini V., Mazzotti C. 2016. *The evaluation of masonry shear strength by means of different experimental techniques : A comparison between full-scale and laboratory tests*. 16th Int. Brick Block Mason. Conf., Padova, Italy, pp. 1645–1652.
- Jafari S., Esposito R. 2016. *Material tests for the characterization of replicated calcium silicate brick masonry*. Delft University of Technology, Report number C31B67WP1-9, 14 November 2016.
- Jukes P., Riddington J.R. 2000. *Finite element prediction of block triplet shear strength*. Proc. 12<sup>th</sup> Int. Brick and Block Mas. Conf., Madrid, 25-28 June 2000.
- Jukes P., Riddington J.R. 2001. *The failure of brick triplet test specimens*. Masonry International, 15(1).
- Lenza P., Ghersi A. 2011. *Edifici in muratura alla luce della nuova normativa sismica*. Dario Flaccovio Editore,
- Lourenço P.B. 1996. *Computational strategies for masonry structures*. PhD thesis, Delft University of Technology.
- Lourenço P.B. 2014. *Masonry structures, overview*. Encyclopedia of Earthquake Engineering.
- Lourenço P.B., Barros J.O., Oliveira J.T. 2004. *Shear testing of stack bonded masonry*. Constr. Build. Mater. 18:125-132.
- Lourenço P.B., Rots J.G., Blaauwendraad J. 1995. *Two approaches for the analysis of masonry structures: micro and macro-modeling*. Heron, 40(4):313-340.
- Lourenço P. B., Rots J. G. 1997. *A multi-surface interface model for the analysis of masonry structures*. J. Struct. Eng., ASCE 123(7):660–668.
- Magenes G., Calvi G.M. 1997. *In-plane seismic response of brick masonry walls*. Earthquake Engineering and Structural Dynamics, 26:1091–1112.

- Magenes G., Bolognini D., Braggio C. 2000. *Metodi semplificati per l'analisi sismica non lineare di edifici in muratura*. CNR – Gruppo Nazionale per la Difesa dei Terremoti, Roma, Italy.
- Magenes G., Penna A. 2009. *Existing masonry buildings: general code issues and methods of analysis and assessment*. E. Cosenza (ed.), Eurocode 8 perspective from the Italian standpoint workshop, pp.185-198.
- Mann W., Muller H. 1980. *Failure of shear-stressed masonry - an enlarged theory, tests and application to shear walls*. Proc. Int. Symposium Load Bear. Brickwork, London.
- Marastoni D., Pelà L., Benedetti A., Roca P. 2016. *Combining Brazilian tests on masonry cores and double punch tests for the mechanical characterization of historical mortars*. Constr. Build. Mater. 112:112–127.
- Masciotta M.G., Roque J.C.A., Ramos L.F., Lourenço P.B. 2016. *A multidisciplinary approach to assess the health state of heritage structures: the case study of the Church of Monastery of Jerónimos in Lisbon*. Constr. Build. Mater. 116:169-187.
- Mazzotti C., Sassoni E., Pagliai G. 2014. *Determination of shear strength of historic masonries by moderately destructive testing of masonry cores*. Constr. Build. Mater. 54:421–431.
- Milani G. 2013. *Lesson learned after the Emilia Romagna, Italy, 20-29 May 2012 earthquakes: a limit analysis insight on three masonry churches*. Engineering Failure Analysis. 34:761-778.
- Montazerolghaem M., Jaeger W. 2014. *A comparative numerical evaluation of masonry initial shear test methods and modifications proposed for EN 1052-3*. Proc. 9<sup>th</sup> International Masonry Conference, Guimaraes, 2014.
- Noland J.L., Kingsley G.R., Atkinson R.H. 1988. *Utilization of non-destructive techniques into the evaluation of masonry*. Proc. 8th Int. Brick/Block Masonry Conf., Dublin, October 1988.
- Pagano M. 1968. *Teoria degli edifici – Vol. I, Edifici in muratura*. Liguori Editore, Napoli.
- Pagano M. 1990. *Costruire in muratura*. Liguori Editore, Napoli.
- Parisi F., Augenti N. 2013. *Earthquake damages to cultural heritage constructions and simplified assessment of artworks*. Engineering Failure Analysis. 34:735-760.
- Pelà L., Roca P., Benedetti A. 2015. *Mechanical Characterization of Historical Masonry by Core Drilling and Testing of Cylindrical Samples*. Int. J. Archit. Herit. pp.360–374.
- Penna A., Morandi P., Rota M., Manzini C.F., da Porto F., Magenes G. 2014. *Performance of masonry buildings during the Emilia 2012 earthquake*. Bull. Earthquake Eng. 12:2255-2273.
- Popal R., Lissel S.L. 2010. *Numerical evaluation of existing mortar joint shear tests and a new test method*. Proc. 8<sup>th</sup> International Masonry Conference, Dresden, 2010.
- Preite G. 1986. *Manuale delle costruzioni in muratura semplice e armata*. Ed. Scientifiche A. Cremonese, Roma.
- Regione Emilia Romagna. 2009. *Scheda raccolta dati per la qualificazione speditiva dei materiali*
- Regione Emilia Romagna. 2009. *Allegato 2 – Abaco delle tipologie murarie*.
- Reluis document. *Schede illustrative dei principali meccanismi di collasso locali negli edifici esistenti in muratura e dei relativi modelli cinematici di analisi*, Allegato a alle Linee Guida per la Riparazione e il Rafforzamento di elementi strutturali, Tamponature e Partizioni.
- Riddington J.R., Jukes P. 1994. *A masonry joint shear strength test method*. Proc. Instn Civ. Engrs Structs & Bldgs, 104:267-274.
- Riddington J.R., Fong K.H., Jukes P. 1997. *Numerical study of failure initiation in different joint shear tests*. Masonry International, 11(2).
- Roca P., Cervera M., Gariup G., Pelà L. 2010. *Structural analysis of masonry historical constructions. Classical and advanced approaches*. Arch. Comput. Methods Eng. 17:299-325.

- Rossi A., Graziotti F., Magenes G. 2015. A proposal for the interpretation of the in-situ shear strength index test for brick masonry. ANIDIS Conference, L'Aquila, Italy.
- Rots J.G. 1991. *Numerical simulation of cracking in structural masonry*. Heron, 36(2):49-63.
- Rots J.G. 1997. *Structural Masonry – An experimental/numerical basis for practical design rules*. Rotterdam: Balkema.
- Sassoni E., Mazzotti C. 2013. *The use of small diameter cores for assessing the compressive strength of clay brick masonries*. J. Cult. Herit. 14S:e95-e101.
- Schubert P., Glitza H. 1978. *Festigkeits und Verformungswerte von Mauermörtel und Wandbausteinen*. Institut für Bauforschung der RWTH Aachen, Bericht F 37.
- Sorrentino L., Liberatore L., Liberatore D., Masiani R. 2014. *The behaviour of vernacular buildings in the 2012 Emilia earthquakes*. Bull Earthquake Eng. 12(5):2367-2382.
- Stöckl S., Hofmann P., Mainz J. 1990. *A comparative finite element evaluation of mortar joint shear tests*. Masonry International, 3(3):101-104.
- TNO Building and Construction Research. 2017. *DIANA Finite Elements Analysis – Release 10.1*. User's Manual, The Netherlands.
- Tomažević M. 1999. *Earthquake-Resistant Design of Masonry Buildings*. Series on Innovation in Structures and Construction – Vol. 1. Imperial College Press.
- Turnsek V., Cacovic F. 1971. *Some experimental results on the Strength of Brick Masonry Walls*. Proc. 2nd Int. Brick Mason. Conf., Stoke-on-Trent, United Kingdom.
- Van der Pluijm R. 1992. *Material properties of masonry and its components under tension and shear*. Proceedings of the 6th Canadian Masonry Symposium, Saskatoon, Canada, pp. 675-686.
- Van der Pluijm R. 1999 *Out of plane bending of masonry*. Ph.D. Thesis. Eindhoven University of Technology, The Netherlands.
- Van der Pluijm R., Rutten H., Ceelen M. 2000. *Shear behavior of bed joints*. Proc. 12<sup>th</sup> Int. Brick and Block Mas. Conf., Madrid, 25-28 June 2000.
- Van Zijl G. 2004 (a). *Modeling masonry shear-compression: role of dilatancy highlighted*. Journal of Engineering Mechanics, 130(11):1289-1296.
- Van Zijl G. 2004 (b). *Masonry shear response characterization*. Masonry International, 17(1):26-32.
- Various Authors. 2016. *Next generation of Eurocode 8, masonry chapter*. Proc. 10<sup>th</sup> International Brick and Block Masonry Conference, Padova, Italy, 2016.
- Vermeer P.A., de Borst R. 1984. *Non-associated plasticity for soils, concrete and rock*. Heron 29(3):3-64.
- Vermeltoort A.T. 2010. *Variation in shear properties of masonry*. Proc. 8<sup>th</sup> International Masonry Conference, Dresden, 2010.